

BOSE-EINSTEIN CONDENSATES IN SYNTHETIC GAUGE FIELDS AND  
SPACES: QUANTUM TRANSPORT, DYNAMICS, AND TOPOLOGICAL  
STATES

A Dissertation

Submitted to the Faculty

of

Purdue University

by

Chuan-Hsun Li

In Partial Fulfillment of the  
Requirements for the Degree

of

Doctor of Philosophy

August 2019

Purdue University

West Lafayette, Indiana

**THE PURDUE UNIVERSITY GRADUATE SCHOOL  
STATEMENT OF DISSERTATION APPROVAL**

Dr. Yong P. Chen, Chair

School of Electrical and Computer Engineering and Department of Physics  
and Astronomy

Dr. Christopher H. Greene

Department of Physics and Astronomy

Dr. Daniel S. Elliott

School of Electrical and Computer Engineering and Department of Physics  
and Astronomy

Dr. Andrew M. Weiner

School of Electrical and Computer Engineering

**Approved by:**

Dr. Dimitrios Peroulis

Head of the Electrical and Computer Engineering Graduate Program

*To my family*

## ACKNOWLEDGMENTS

I would like to sincerely thank many people for their help, support, and encouragement. First, I would like to thank my adviser Prof Yong P. Chen for guiding me during my graduate study. When discussing with him, he is very patient and honest and would never make you feel that he knows and will be right about everything. Although he has been very busy, he tries to find time for discussion. I remember there were a few times that he was having lunch or dinner while discussing with me. I have learned a lot from him not only about physics but also tips for research. For example, it may be easy to learn and understand something by starting with a simple yet important example. When doing experiments, starting with a simple experiment/example to see if things work and to test whether they work correctly is important. Based on such a benchmark, more complicated experiments can be built. In addition to research, he always emphasizes the importance of writing a good scientific article. I could not remember how many times we have revised my first paper. But I have learned many tips from him. Hopefully, the number of revision for future papers will be notably reduced. I would also like to thank my graduate committee members Prof Chris Greene, Prof Daniel Elliott, and Prof Andy Weiner for their guidance and help during my graduate study. Their comments on my research projects are helpful and valuable.

Lab members are important to me. It is amazing that I have met so many kind and positive people during these years. Abraham Olson and Robert Niffenegger taught me many things about our Bose-Einstein condensate (BEC) machine. Abe was very patient in teaching me even the simplest stuff when I had no idea about many things. I think patience is a very important character for being a good mentor. I always keep this in mind if I have a chance to be someone's mentor. When I joined the lab, Abe along with Sourav Dutta instructed me to build an external cavity diode laser

(one of my first projects), which was used in our early experiments on synthetic gauge fields and was later used as a photoassociation laser. After about one semester, David Blasing joined the lab. After Abe and Bob graduated, David became my only lab partner working on BEC experiments for the rest of many years of my graduate study. It is unforgettable that we have faced many challenges and solved many problems together, such as replacing the laser diode in the DL-pro laser and then optimizing the Littrow configuration and aligning the downstream optics, designing new optical paths for seeding our home-built tapered amplifier and BoosTA, aligning the dipole trap for creating BECs after our IPG laser was repaired, improving the quality of our Raman laser such that the lifetime of BECs in the presence of Raman lasers can be greatly enhanced, fixing the BEC machine numerous times when it failed to work...and so on. I remember those happy timings when we finally fix something or make things work.

I would like to thank many undergrads who contributed to the lab. Ting-Wei Hsu (Wade Hsu) assisted in setting up the Raman laser system and built up a nice external cavity diode laser with home-built current and temperature controllers, and many other things. Dong Yan upgraded the power of our Raman laser. Zhenlin Wu set up a 1D optical lattice. Midhuna Duraisamy wrote a Labview code for controlling an arbitrary function generator and set up optics for creating a momentum-space lattice.

Around the time when David graduated, Esat Kondakci joined the lab as a post-doc. Esat is a sincere, patient, and humorous person with whom I enjoy discussing many things. In the last half year of my graduate study, new graduate student Shih-Wen Feng and undergrad Tianhui Wang joined the lab. Shih-Wen is a quick learner and is now capable of working on experiments independently. He is participating in the project of realizing a Hall cylinder that will be introduced in this thesis. Tianhui is passionate about doing research and is hard-working. I enjoy the happy dinner time with Shih-Wen and Tianhui.

I also enjoy the times with members in the nano group of Prof Yong Chen, especially Ting-Fung Chung (Jack Chung), Wonjun Park, and Nirajan Mandal. Jack is a very positive and humorous person. He can still make a joke even when he is tired and stressful. His attitude often cheers me up. Wonjun is a very sincere and kind person. I enjoy the times chatting with him and sharing our life experiences. Nirajan is a nice and patient person who is passionate in teaching students. I enjoy discussing physics and life with him. Communication with people in other labs is also pleasant. I particularly enjoy casual conversation/discussion with Tzu-Han Chang and Cheng-An Chen in Prof Chen-Lung Hung's group, and George Toh and Jungu Choi in Prof Elliott's group.

People in the labs always work hard and often face challenges and hard times. Perhaps one of the most important things I am learning from them is how to stay positive and happy while confronting difficulties. I really hope that these kind and positive people can reach their dreams.

I would also like to thank many friends outside the lab. They have played invaluable roles in my graduate student life.

For the project of spin transport in a spin-orbit-coupled BEC, I thank Bob for initiating the early experiments. I took over the project, taking all the experimental data presented in this thesis and the corresponding paper. We also thank many theorists who have provided several physical insights, including Chunlei Qu and Prof Chuanwei Zhang at University of Texas at Dallas, Su-Ju Wang and Prof Chris Greene and Prof Yuli Lyanda-Geller at Purdue University, Mingyuan He at Hong Kong University of Science and Technology and Prof Qi Zhou at Purdue University, and Prof Hui Zhai at Tsinghua University.

For the project of realizing a synthetic Hall cylinder, Prof Qi Zhou at Purdue University proposed the initial theoretical idea. I would like to thank Shih-Wen and David for their help in this experiment. This project is not fully completed at the moment. Currently, I am very happy to work with Shih-Wen who is now actively doing experiments with me. I also appreciate many helpful discussions with Yangqian Yan,

Sayan Choudhury, and Prof Qi Zhou, who always have insightful ideas and useful guidance for experiments.

For the projects of exploring rotational properties and scissors mode of a spin-orbit coupled BEC in a synthetic magnetic field, I would like to thank many theorists including Chunlei Qu at University of Colorado, Boulder, and Su-Ju Wang at Kansas state university, Yangqian Yan, and Prof Qi Zhou. I also want to thank David for his help in experiments.

I am really grateful for my family whose warm support and love are the reasons why I can conduct research and become a scientist. I appreciate my parents Mr. Kuang-Cheng Li and Mrs. Pai-Huang Huang and my brother Chuan-Jui Li, who are always there for me.

## TABLE OF CONTENTS

	Page
LIST OF TABLES . . . . .	xii
LIST OF FIGURES . . . . .	xiii
ABSTRACT . . . . .	xxix
1 INTRODUCTION . . . . .	1
1.1 Introduction to Bose-Einstein condensates . . . . .	1
1.2 Overview of the $^{87}\text{Rb}$ BEC machine at Purdue . . . . .	3
1.2.1 The laser systems for laser cooling and trapping . . . . .	4
1.2.2 The Raman laser system for creating synthetic gauge fields and synthetic spaces . . . . .	5
1.2.3 Microwave and radio frequency (RF) systems . . . . .	9
1.2.4 The vacuum side of the optical table . . . . .	12
2 ENGINEERING LIGHT-MATTER INTERACTIONS TO CREATE SYN- THETIC GAUGE FIELDS AND SPACES FOR NEUTRAL ATOMS . . . . .	13
2.1 Creating synthetic gauge fields using the Raman coupling scheme . . . . .	14
2.1.1 Calculation of the scalar and vector light shifts . . . . .	17
2.1.2 Calibrating the Raman coupling strength with resonant Raman- Rabi oscillations . . . . .	20
2.2 Synthetic vector potentials and synthetic electric and magnetic fields . . . . .	24
2.3 Synthetic spin-orbit coupling: spin-dependent vector potentials . . . . .	26
2.3.1 Phase transition diagrams at zero or finite temperatures . . . . .	28
2.3.2 Effects of the excluded $ m_F = +1\rangle$ state . . . . .	32
2.4 Spin-dependent synthetic electric and magnetic fields . . . . .	35
2.5 Synthetic spaces and synthetic gauge fields . . . . .	39
3 SPIN CURRENT GENERATION AND RELAXATION IN A QUENCHED SPIN-ORBIT-COUPLED BOSE-EINSTEIN CONDENSATE . . . . .	45

	Page	
3.1	Introduction and motivation . . . . .	45
3.2	Experimental setup and timing diagram . . . . .	48
3.2.1	Theoretical and experimental backgrounds . . . . .	51
3.3	Measurements of the spin-dipole mode (SDM) and its damping . . . . .	56
3.3.1	Analysis of momentum damping . . . . .	59
3.3.2	Control experiment 1: dipole oscillations of a SO-coupled BEC with a single dressed spin component in the $ \downarrow\rangle$ state . . . . .	61
3.3.3	Control experiment 2: common-mode dipole oscillations of two dressed spin components of a SO-coupled BEC . . . . .	62
3.4	Thermalization and spin current . . . . .	64
3.4.1	Analysis of condensate fraction . . . . .	66
3.4.2	Coherent spin current . . . . .	67
3.5	Observation of deformed atomic clouds and BEC shape oscillations . . . . .	68
3.5.1	Analysis of BEC shape oscillations . . . . .	70
3.5.2	Observation of the $m = 0$ quadrupole mode of a dressed BEC with another set of trap frequencies . . . . .	71
3.6	GPE simulations and interpretations . . . . .	73
3.6.1	Details in GPE simulations . . . . .	80
3.6.2	Different forms of energies in GPE simulations . . . . .	82
3.6.3	Calculation of nonorthogonality, effective interaction parameters, and immiscibility . . . . .	86
3.7	Control simulations, phase of BEC wavefunctions in SDM, and movies . . . . .	88
3.7.1	Effect of immiscibility on SDM . . . . .	88
3.7.2	Effect of interference on the relative motion between two colliding BECs . . . . .	90
3.7.3	Effect of turning off interactions on the relative motion between two colliding BECs . . . . .	92
3.7.4	Spatial modulation in the phase of BEC wavefunctions in SDM. . . . .	94
3.7.5	Movies of GPE simulations for the SDM . . . . .	94
3.8	Discussion and conclusion . . . . .	95

	Page
3.9 Note . . . . .	98
4 A BOSE-EINSTEIN CONDENSATE WITH EMERGENT TOPOLOGICAL LATTICES ON A SYNTHETIC HALL CYLINDER . . . . .	99
4.1 Introduction and motivation . . . . .	99
4.2 Experimental set-up for realizing a synthetic Hall cylinder . . . . .	100
4.3 The single-particle Hamiltonian $H$ for the synthetic Hall cylinder . . . . .	102
4.3.1 Derivation of the single-particle Hamiltonians $H$ and $H_{q_y}$ . . . . .	103
4.3.2 Symmetries of the Hamiltonian $H$ . . . . .	107
4.4 Quantum transport on a symmetry-protected Möbius strip in momentum space . . . . .	110
4.4.1 Importance of the synthetic magnetic flux threading the cylinder . . . . .	113
4.4.2 Calculations of BEC wavefunctions in the real space . . . . .	114
4.5 Quantum transport on a regular strip in momentum space . . . . .	117
4.5.1 Derivation of the Hamiltonians $H'$ and $H'_{q_y}$ . . . . .	120
4.6 Unzipping the Hall cylinder into a planar Hall strip . . . . .	120
4.6.1 Derivation of the Hamiltonian $H_{\text{unzip}}$ . . . . .	122
4.7 Details in experiments and calculations . . . . .	122
4.7.1 Initial state preparations for experiments in the previous sections . . . . .	122
4.7.2 Imaging analysis . . . . .	123
4.7.3 Calculated curves shown in figures in the previous sections . . . . .	124
4.8 Discussion and conclusion . . . . .	126
5 SCISSORS MODE AND ROTATIONAL PROPERTIES OF A SPIN-ORBIT-COUPLED BOSE-EINSTEIN CONDENSATE . . . . .	128
5.1 Introduction and motivation . . . . .	128
5.1.1 BECs versus superfluids . . . . .	130
5.1.2 Introduction to the scissors mode . . . . .	130
5.2 Experimental set-up and timing diagram . . . . .	134
5.3 Experimental and simulation results . . . . .	138

	Page
5.3.1 Experimental results . . . . .	138
5.3.2 Simulations . . . . .	141
5.4 Discussion and conclusion . . . . .	144
6 FUTURE DIRECTIONS . . . . .	147
6.1 Preliminary results of the ongoing projects . . . . .	148
6.1.1 Charge pumping of a BEC on a synthetic Hall cylinder . . . . .	148
6.1.2 Exploring interaction effects on the transport of a BEC in the momentum-space regular strip . . . . .	149
LIST OF REFERENCES . . . . .	152
VITA . . . . .	164

## LIST OF TABLES

Table	Page
<p>3.1 <b>Cases with different modified interaction parameters and the immiscibility metric.</b> For each case, the corresponding immiscibility metric <math>\eta = (g_{\uparrow\downarrow}^2 - g_{\uparrow\uparrow}g_{\downarrow\downarrow})/g_{\uparrow\uparrow}^2</math> is calculated. The corresponding simulated SDM for each case is shown in Fig. 3.12 above. . . . .</p>	89
<p>5.1 Physical velocity, physical linear momentum, physical angular momentum, and their canonical and spin-dependent contributions and their relations. SOC is along the <math>y</math> direction (see Eq. (5.1)). Physical quantities are indicated by a superscript “phy”. Canonical terms are indicated by a superscript “c”. Spin-dependent terms are indicated by a superscript “s”. <math>\langle \hat{p}_x \rangle = \langle \hbar \hat{q}_x \rangle</math>, <math>\langle \hat{p}_y \rangle = \langle \hbar \hat{q}_y \rangle</math>, <math>\langle \hat{p}_z \rangle = \langle \hbar \hat{q}_z \rangle</math> are canonical momenta (or quasi-momenta) respectively along the <math>x</math>, <math>y</math>, and <math>z</math>. . . . .</p>	145

## LIST OF FIGURES

Figure	Page
1.1 Behavior of a weakly-interacting bosonic gas at different temperatures. When the temperature of the gas is below the critical temperature $T_c$ , a BEC is formed. Reproduced from ref. [1]. . . . .	1
1.2 The laser side of the optical table for the BEC machine. . . . .	4
1.3 The Raman laser system for creating synthetic gauge fields and synthetic spaces for atoms. . . . .	5
1.4 Counter-propagating Raman lasers, detection laser, CCD camera, and MOT-B. . . . .	6
1.5 Measurement of the total atom number of a BEC versus hold time at various Raman couplings. . . . .	7
1.6 Measurement of the total atom number of a BEC versus hold time at various Raman couplings. This figure is the zoom-in of Fig. 1.5. . . . .	8
1.7 Measurement of the condensate fraction of a BEC versus hold time at various Raman couplings. Note that it can be challenging to extract the condensate fraction when the atom number is small (see Fig. 1.5), for example, when the hold time $> 700$ ms in the case of $7.5 E_r$ . Error bar is the standard error of the mean. . . . .	9
1.8 Circuit diagram of our microwave and RF systems. . . . .	10
1.9 A microwave horn and an RF loop antenna are placed near the vacuum chamber where we create BECs. . . . .	11
1.10 The vacuum side of the optical table for the BEC machine. . . . .	12
2.1 <b>Raman coupling scheme for generation of synthetic gauge fields.</b> (a) Counter-propagating Raman lasers with orthogonal linear polarizations couple the internal spin states of atoms. One polarization is parallel to and the other is perpendicular to the bias magnetic field $\mathbf{B}$ to satisfy the selection rules for such a Raman transition. The angular frequency difference between the Raman lasers is $\Delta\omega_R$ such that $\hbar\Delta\omega_R \sim \hbar\omega_Z$ . (b) Energy level diagram of a $^{87}\text{Rb}$ atom shows the Zeeman sublevels of the $F = 1$ hyperfine state. . . . .	15

Figure	Page	
2.2	Calculated magnitude of the scalar and vector light shifts for atoms in the $F = 1$ ground state as a function of the laser wavelength $\lambda_L$ . The calculation is performed using Eqs. (2.2-2.4). The scalar light shift vanishes around 790 nm, which is the magic wavelength. Note that for different wavelength $\lambda_L$ , $E_r = \hbar^2 k_r^2 / (2m)$ has different values because $k_r = 2\pi / \lambda_L$ . . . . .	19
2.3	Calculated magnitude of the vector light shift for atoms in the $F = 1$ or $F = 2$ ground states. The calculation is performed using Eqs. (2.2-2.4). In general, the vector light shift (responsible for the Raman coupling between different spin states in the same $F$ hyperfine manifold) for atoms in the $F = 1$ or $F = 2$ ground states may be different at a given laser wavelength $\lambda_L$ , because the corresponding laser detunings from the same excited state are different by $\approx 6.8$ GHz (the hyperfine splitting between the $F = 1$ or $F = 2$ ground states). However, when the laser detuning is much larger than the hyperfine splittings, the difference in the resulting vector light shift between $F = 1$ and $F = 2$ is negligible. . . . .	20
2.4	Measurement of the Raman detunings $\delta_{\text{res},0 \rightarrow -1}$ and $\delta_{\text{res},0 \rightarrow +1}$ for resonant Raman-Rabi oscillations. The peak population transfer from $ m_F = 0, 0\hbar k_r\rangle$ to $ m_F = +1, -2\hbar k_r\rangle$ reveals the SE corresponding to $\delta_{\text{res},0 \rightarrow +1}$ , and the peak population transfer from $ m_F = 0, 0\hbar k_r\rangle$ to $ m_F = -1, +2\hbar k_r\rangle$ reveals the SE corresponding to $\delta_{\text{res},0 \rightarrow -1}$ . SE is the voltage applied to the circuit for the magnetic coil to control the Zeeman splitting and thus the Raman detuning. See texts for details. . . . .	22
2.5	An example for resonant Raman-Rabi oscillations. (a) Select TOF images (where the labeled time is the pulse width) revealing the bare spin and mechanical momentum compositions of the BEC. (b) shows the analyzed relative population of $ m_F = +1, -2\hbar k_r\rangle$ (red scatters), $ m_F = 0, 0\hbar k_r\rangle$ (blue scatters), and $ m_F = +1, +2\hbar k_r\rangle$ (green scatters) versus the applied pulse width. Solid lines are fits to extract the Raman coupling strength. See texts for details. . . . .	23
2.6	An example of synthetic vector potentials. See texts for details. Reproduced from ref. [29]. . . . .	24
2.7	SO-coupled dispersion relations at various Raman coupling $\Omega$ at $\delta_R = 0$ in Eq. (2.8). The black arrow indicates increasing $\Omega$ , showing the evolution of double-minima structures to single-minimum structures. Reproduced from ref. [37]. . . . .	27

Figure	Page
2.8 Phase transition diagram of a stationary SO-coupled BEC at zero temperature. (a) The dispersion exhibits a double-minima structure within the region of dashed lines and otherwise a single-minimum structure. The gray area labeled as “b” is shown in (b) for details. (b) shows the metastable window within which both the energy minima of the dispersion may be simultaneously occupied by atoms. A miscible (phase mixed) to immiscible (phase separated) phase transition occurs around $0.2 E_r$ . (c) shows the phase mixed to phase separated transition with representative images revealing miscible or immiscible atomic clouds of different spin states. Reproduced from ref. [37]. . . . .	28
2.9 Phase transition diagram of a SO-coupled BEC at finite temperatures. There may be three possible scenarios for the finite-temperature phase transition diagram of a SO-coupled BEC. Experiment can determine (b1) to be the correct diagram based on the measurements of magnetic properties in ST and MG phases. ST: stripe, MG: magnetized, NM: non-magnetic. At zero temperature, $\Omega_1 \approx 0.2 E_r$ and $\Omega_2 \approx 4 E_r$ are respectively the Raman coupling for the ST-MG and MG-NM phase transitions. Reproduced from ref. [38]. . . . .	30
2.10 TOF images revealing bare spin and momentum compositions of a dressed BEC at varioud Raman coupling $\Omega$ with the corresponding dispersion relations. The double-minima to single-minimum transition observed in our lab occurs around $\sim 4.7 E_r$ when the quadratic Zeeman shift is $\hbar\epsilon \sim 0.45 E_r$ (the applied bias magnetic field is $\sim 5$ gauss). . . . .	32
2.11 The calculated quasimomentum of the energy minimum/minima (i.e. $\hbar q_{\sigma \min}$ ) of the SO-coupled dispersion relations at various Raman couplings. The calculated double-minima to single-minimum transition occurs around $4.7 E_r$ when the quadratic Zeeman shift $\hbar\epsilon \sim 0.45 E_r$ . . . . .	33
2.12 The calculated fractional population of the dominant bare spin component of the dressed state in the left or right minimum. . . . .	34
2.13 The calculated Raman detuning $\delta_R$ that can achieve the balanced double-minima dispersion at Raman coupling $\Omega$ when using the 3-state matrix in Eq. (2.8). . . . .	35
2.14 <b>Spin Hall effect of a BEC.</b> At the same side of Gaussian intensity distribution, the atomic cloud components of different dressed spin states have opposite tilt angles, reflecting the spin-dependent magnetic fields $\mathbf{B}_\sigma^*$ . At different sides of the Gaussian intensity distribution, atomic cloud components of the same dressed spin state have opposite tilt angles. The Raman coupling shown in each case refers to the coupling strength at the BEC’s center. . . . .	36

Figure	Page
2.15 <b>Spin Hall effect of a BEC.</b> Similar to Fig. 2.14 except that a dressed spin polarized BEC is used in this case. . . . .	38
2.16 (a) Spin Hall effect of a BEC. At the same side of the Gaussian intensity distribution of the Raman lasers, atomic cloud components from different dressed spin states have opposite tilt angles. (b) Measurement of the spin Hall shear coefficient (see texts) demonstrates the generation of spin-dependent synthetic magnetic fields and the spin Hall effect. . . . .	39
2.17 A synthetic 2D plane of a strip geometry subjected to a synthetic magnetic flux. Utilizing counter-propagating Raman lasers to Raman couple internal states ( $ 1\rangle$ and $ 2\rangle$ ) of atoms allows for creating synthetic magnetic flux in a synthetic two-dimensional plane composed of a synthetic dimension $\hat{w}$ and a real spatial dimension $\hat{y}$ . There are no edges in the $y$ direction, and there are only two sites in the $w$ direction with a hard-wall potential at the edges (an open boundary condition). See texts for details. . . . .	41
2.18 A Hall strip of lattice. A lattice with a strip geometry penetrated by a synthetic magnetic flux is realized using internal spin states ( $m = -1, 0, +1$ ) of atoms as a synthetic dimension and an optical lattice along a real spatial dimension. “ $j$ ” labels different lattice sites in the real spatial dimension. $t_s$ and $t_x$ are hopping amplitudes determined by the light couplings. Counter-propagating Raman lasers coupling $m = -1$ and $m = 0$ , and $m = 0$ and $m = +1$ , allow for generating an Aharonov-Bohm (AB) phase $\phi_{AB}$ corresponding to a synthetic magnetic flux for atoms. Reproduced from ref. [47]. . . . .	42
2.19 Using internal spin states (labeled as $ 1\rangle$ , $ 2\rangle$ , $ 3\rangle$ , $ 4\rangle$ , and $ 5\rangle$ ) of atoms as discrete sites allows for creating a synthetic circle in a curved synthetic dimension $\hat{w}$ . Hopping of atoms between different sites is induced by light (e.g. Raman, microwave, or RF couplings). . . . .	43
2.20 A 1D synthetic lattice is constructed using an atom’s different mechanical momentum states coupled by unique pairs of Bragg lasers. (a) Counter-propagating Bragg lasers are used to couple unique pairs of mechanical momentum states ( $p$ ) of atoms as shown in (b) to realize a 1D synthetic lattice shown in (c). Each hopping amplitude ( $t_{-2,-1,0,1}$ ) and the associated phase ( $\varphi_{-2,-1,0,1}$ ) can be individually controlled. See texts for details. Reproduced from ref. [45]. . . . .	44

**3.1 Experimental setup and timing diagram used for the spin-dipole mode (SDM) experiments.** (a) Linearly-polarized Raman beams with orthogonal polarizations (indicated by the double-headed arrows along  $\hat{z}$  and  $\hat{x}$ ) counter-propagating along  $\hat{y}$  couple  $m_F$  hyperfine sublevels (bare spin states) of  $^{87}\text{Rb}$  atoms. The sublevels are Zeeman split by  $\hbar\omega_Z \approx \hbar\Delta\omega_R = h \times (3.5 \text{ MHz})$  using a bias magnetic field  $\mathbf{B} = B\hat{z}$ , which controls the Raman detuning  $\delta_R = \hbar(\Delta\omega_R - \omega_Z)$ . (b) Experimental timing diagram: Raman coupling  $\Omega$  (with an experimental uncertainty of  $< 10\%$ ) is slowly ramped up in 80 ms to an initial value  $\Omega_I$  and held for 100 ms to prepare the BEC around the single minimum of the ground band at  $\Omega_I$  as shown in (c). Then,  $\Omega$  is quickly lowered to a final coupling  $\Omega_F$  in time  $t_E$  and held for some time  $t_{\text{hold}}$ , during which we study the dynamics of the BEC in the dipole trap. Subsequently, the atoms are released for absorption imaging after a 15 ms time of flight (TOF), at the beginning of which a Stern-Gerlach process is performed for 9 ms to separate atoms of different bare spin states. (c) The ground band (solid lines) of synthetic SOC is calculated for a few representative  $\Omega$  at  $\delta_R = 0$ . A higher band calculated for  $\Omega = 1.3 E_r$  is shown as dashed lines. The colors indicate the spin compositions, with red for  $|\downarrow\rangle$  and blue for  $|\uparrow\rangle$ . The ground band minima in quasimomentum marked by dots are identified with spin-dependent vector potentials ( $A_\sigma$ ), which shift in opposite directions as  $\Omega$  is lowered into the double minima regime during  $t_E$ . This generates spin-dependent synthetic electric fields  $E_\sigma$  and thus excites the SDM and an AC spin current along the SOC direction in a trapped BEC. The upper (lower) dashed circle represents the region around  $q_y = 0$  in the double minima band at an exemplary  $\Omega_F = 0$  ( $\Omega_F = 1.3 E_r$ ), from which the two (dressed) spin components of the BEC roll down towards the corresponding band minima in response to the application of  $E_\sigma$ . . . . .

- 3.2 SDM of a bare or a dressed BEC.** Select TOF images showing the bare spin and momentum compositions of atoms taken after applying spin-dependent synthetic electric fields  $E_\sigma$  with  $\Omega_F = 0$  (bare BEC) in (a) and  $\Omega_F = 1.3 E_r$  (SO-coupled BEC) in (b), followed by various hold times ( $t_{\text{hold}}$ ) in the dipole trap. The TOF images labeled by  $t_{\text{hold}} = -1$  ms are taken right before the application of  $E_\sigma$ . The bare spin components (labeled by  $m_F$ , with  $|\downarrow\rangle$  in red and  $|\uparrow\rangle$  in blue) are separated along the horizontal axis. The vertical axis shows the atoms' mechanical momentum  $\hbar k$  along the SOC direction ( $\hat{y}$ ). The color scale reflects the measured optical density ( $OD$ , see subsections below). The total condensate atom number of the initial state at  $\Omega_I$  is  $N_c \sim (1-2) \times 10^4$  with trap frequencies  $\omega_z \sim 2\pi \times (37 \pm 5)$  Hz and  $\omega_x \sim \omega_y \sim 2\pi \times (205 \pm 15)$  Hz. The TOF images (and associated analyzed quantities presented later) are typically the average of a few repetitive measurements. . . . . 57
- 3.3 Momentum damping at different  $\Omega_F$ , for SDM and the dipole mode of a single dressed spin component.** (a)-(e) Relative momentum oscillations in SDM,  $\hbar k_{\text{spin}}$ , as a function of  $t_{\text{hold}}$  at various  $\Omega_F$ . The experimental data (scatters) are fitted to a damped sinusoidal function (line) to extract the inverse quality factor  $1/Q$  of the oscillations. (f) Momentum damping (quantified by  $1/Q$ ) versus  $\Omega_F$ . The error bar of  $1/Q$  is the standard error of the fit. The purple circle data correspond to the SDM (illustrated by (g)) and the red square data correspond to the dipole mode of a BEC with a single dressed spin component prepared in  $|\downarrow'\rangle$  (illustrated by (h)). In (g)-(h), the representative band structure is calculated at  $\Omega = 1.0 E_r$ . . . . . 59
- 3.4 Dipole oscillations of a BEC with a single dressed spin component in  $|\downarrow'\rangle$ .** Combined TOF images vs  $t_{\text{hold}}$  for a dressed BEC in  $|\downarrow'\rangle$  ( $\Omega_F = 1.0 E_r$ ,  $\delta_R = \delta'(\Omega_F, \varepsilon)$ , shown in Fig. 3.3h) undergoing dipole oscillations, showing very weak damping ( $1/Q < 0.05$ ) and negligible thermalization. Each slice in the image shown is a TOF image at a given  $t_{\text{hold}}$ , but compressed along the horizontal direction. The vertical axis shows the mechanical momentum  $\hbar k$  of atoms. The time step between successive image slices is 0.5 ms. The figure shows bare spin components  $|\downarrow\rangle$  in red and  $|\uparrow\rangle$  in blue plotted in the lower and upper panels, respectively. 62

**3.5 Common-mode dipole oscillations of two dressed spin components of a SO coupled BEC.** Combined TOF images vs  $t_{\text{hold}}$  for two dressed spin components of a SO coupled BEC with equal populations in  $|\uparrow\rangle$  and  $|\downarrow\rangle$  ( $\Omega_{\text{F}} = 1 E_{\text{r}}$ ,  $\delta_{\text{R}} = \delta'(\Omega_{\text{F}}, \varepsilon)$ ) undergoing in-phase dipole oscillations, showing very little damping ( $1/Q < 0.05$ ) with negligible thermalization. Each slice in the image shown is a TOF image at a given  $t_{\text{hold}}$ , but compressed along the horizontal direction. The time step between successive image slices is 0.5 ms. The figure shows  $|\downarrow\rangle$  in red and  $|\uparrow\rangle$  in blue plotted in the lower and upper panels, respectively. . . . .

63

**3.6 Thermalization and spin current.** (a) The measured condensate fraction  $f_{\text{c}} = N_{\text{c}}/N$  as a function of  $t_{\text{hold}}$  for SDM in the bare case (no SOC,  $\Omega_{\text{F}} = 0$ ) and the dressed cases (with SOC,  $\Omega_{\text{F}} = 1.3 E_{\text{r}}$  and  $\Omega_{\text{F}} = 2.1 E_{\text{r}}$ ). Representative error bars show the average percentage of the standard error of the mean. The solid curves are the shifted exponential fits to the smoothed  $f_{\text{c}}$  (see subsections below). The initial condensate fraction (not shown) at  $\Omega_{\text{I}}$  (measured at  $t_{\text{hold}} = -1$  ms) is  $\sim 0.6 - 0.7$  for all the cases. (b) The saturation time constant  $\tau_{\text{therm}}$  of the decreasing  $f_{\text{c}}$  and the saturation condensate fraction  $f_{\text{s}}$  versus  $\Omega_{\text{F}}$ , where the vertical error bar is the standard error of the fit. (c) Spin current  $I_{\text{s}}$  (normalized by  $v_{\text{r}}/\lambda = 7.4 \times 10^3$  /s, where  $v_{\text{r}} \sim 6$  mm/s is the recoil velocity) as a function of  $t_{\text{hold}}$  for  $\Omega_{\text{F}} = 0$  and  $1.3 E_{\text{r}}$ . The solid curves are fits (see text).

65

**3.7 Observation of deformed atomic clouds and BEC shape oscillations.** (a-d) Observation of deformed atomic clouds at early stages of the SDM. (a-b) TOF images for  $\Omega_F = 0$  and  $\Omega_F = 2.1 E_r$  at  $t_{\text{hold}} = 0.5$  ms are shown for comparison. The corresponding integrated optical density ( $OD_y$ ) versus the momentum in the SOC direction ( $\hat{y}$ ) for the spin down and up components is shown respectively in (c) and (d). (e-f) Observation of BEC shape oscillations. The data showing the aspect ratio  $W_y/W_{z'}$  (see subsections below) of the condensate measured at various  $t_{\text{hold}}$  are extracted from the SDM measurements in Fig. 3.3, except for the additional measurements #2 and #3 in (e). (e) For the three independent measurements in the bare case, the observed oscillations possess a complicated behavior without having a well-defined frequency given the error bars and the fluctuation in the data. Select TOF images for measurement #1 are shown in Fig. 3.2a. (f) In the dressed cases, aspect ratio oscillations with a well-defined frequency are observed in measurements at three different  $\Omega_F$ . The average frequency of the three aspect ratio oscillations obtained from the damped sinusoidal fit is around 58 Hz, consistent with the expected frequency for the  $m = 0$  quadrupole mode  $f_{m=0} = \sqrt{2.5}\omega_z/(2\pi) \sim 59$  Hz for a cigar-shape BEC in the limit of  $\omega_z/\omega_{x,y} \ll 1$  [97]. Note that  $\omega_z$  is not modified by Raman lasers and thus does not depend on  $\Omega_F$ . Select TOF images for  $\Omega_F = 1.3 E_r$  are shown in Fig. 3.2b. The representative error bars in (e-f) are standard deviation of at least three measurements. The dashed lines indicate  $t_{\text{hold}} \sim 2\tau_{\text{damp}}$  after which the SDM is fully damped out. . . . .

69

**3.8 Observation of the quadrupole mode of a dressed BEC with another set of trap frequencies.** (a) For  $\Omega_F = 1.3 E_r$  with trap frequencies  $\omega_z \sim 2\pi \times (21 \pm 3)$  Hz and  $\omega_x \sim \omega_y \sim 2\pi \times (144 \pm 10)$  Hz used in this measurement, the observed aspect ratio oscillation frequency is around 34 Hz, consistent with the expected  $m = 0$  quadrupole mode frequency  $f_{m=0} = \sqrt{2.5}\omega_z/(2\pi) \sim 33$  Hz. This further verifies the excitation of the  $m = 0$  quadrupole mode. The oscillation frequency is obtained using a damped sinusoidal function to fit the data following the SDM is damped out (when  $t_{\text{hold}} \sim 2\tau_{\text{damp}}$  as indicated by the dashed line). The representative error bars are standard deviation of at least three measurements. (b) Select TOF images are typically the average of a few repetitive measurements. . . . .

73

**3.9 GPE simulated SDM at various  $\Omega_F$  and the extracted SDM damping compared with experiment.** (a-b) GPE simulations of the 1D momentum-space density distributions of the two bare spin components as a function of  $t_{\text{hold}}$  for the SDM at  $\Omega_F = 0$  and  $\Omega_F = 1.3 E_r$ , respectively. The 1D momentum density  $\rho_\sigma(k_y)$  is obtained by integrating the 3D momentum density along  $k_x$  and  $k_z$ , i.e.  $\rho_\sigma(k_y) = \int \rho_\sigma(k_x, k_y, k_z) dk_x dk_z$ . Then, these integrated 1D atomic momentum densities for sequential hold times ( $t_{\text{hold}}$ ) are combined to show the atomic density in momentum space along the SOC direction versus  $t_{\text{hold}}$ . (c) GPE simulations of the SDM damping versus  $t_{\text{hold}}$  at various  $\Omega_F$ . The violet lines are the  $\hbar k_{\text{spin}}$  (defined as the difference between the CoM momenta of the two spin components) as a function of  $t_{\text{hold}}$  for various  $\Omega_F$ . The CoM momentum ( $\hbar k_{\uparrow, \downarrow}$ ) of each bare spin component (at a given  $t_{\text{hold}}$ ) is calculated by taking a density-weighted average of the corresponding 1D momentum density distributions such as those shown in (a-b). The black lines are damped sinusoidal fits for the calculated  $\hbar k_{\text{spin}}$  to extract the corresponding SDM damping ( $1/Q$ ) which is shown in (d) along with the experimental data reproduced from Fig. 3.3f. (e) Replotting of (d) with  $1/Q$  shown in logarithmic scale. (f-j) *In situ* (real space) atomic densities calculated from GPE simulations. (f) Initial *in situ* 2D density at  $\Omega = \Omega_I$  (right before applying spin-dependent electric fields  $E_\sigma$ ). (g-j) *In situ* 2D density at  $t_{\text{hold}} = 1.5$  ms (after the application of  $E_\sigma$ ) for  $\Omega_F = 0, 0.4 E_r, 0.9 E_r,$  and  $1.3 E_r$ , respectively. For (f-j), the density is designated by brightness and the bare spin polarization by colors (red:  $\downarrow$ , blue:  $\uparrow$ , white: equal spin populations). The 2D densities  $\rho_\sigma(x, y)$  in (f-j) are obtained by integrating the 3D atomic density along  $z$ , i.e.,  $\rho_\sigma(x, y) = \int \rho_\sigma(x, y, z) dz$ . In this figure, the simulations used the following parameters representative of our experiment:  $\Omega_I = 5.2 E_r$ ,  $\delta_R = 0$ ,  $N_c = 1.6 \times 10^4$ ,  $\omega_z = 2\pi \times 37$  Hz,  $\omega_x = \omega_y = 2\pi \times 205$  Hz,  $t_E = 1.0$  ms. GPE simulations are performed by Chunlei Qu and Chuanwei Zhang. . . . .

**3.10 Calculated nonorthogonality, effective interaction parameters, and immiscibility for two dressed spin states.** In (a-f), the calculations consider  $|\uparrow'\rangle$  and  $|\downarrow'\rangle$  located respectively at  $\hbar q_y$  and  $-\hbar q_y$ . (a) When  $\Omega = 0$ , the nonorthogonality is zero because the two bare spin components are orthogonal. When  $\Omega \neq 0$ , either increasing  $\Omega$  or decreasing  $q_y$  would increase  $\langle \uparrow' | \downarrow' \rangle$ , giving rise to stronger interference and more significant density modulations in the spatially overlapped region of the two dressed spin components. (b-c) Effective interspecies ( $g_{\uparrow'\downarrow'}$ ) and intraspecies ( $g_{\uparrow'\uparrow'}$ ,  $g_{\downarrow'\downarrow'}$ ) interaction parameters versus quasimomentum at  $\Omega = 0.1 E_r$  and  $1.26 E_r$ , respectively. When  $\Omega$  increases or  $q_y$  decreases,  $g_{\uparrow'\downarrow'}$  increases while  $g_{\uparrow'\uparrow'}$  and  $g_{\downarrow'\downarrow'}$  almost remain at the bare values. As  $q_y \rightarrow 0$  at any finite  $\Omega$ ,  $g_{\uparrow'\downarrow'} \rightarrow 2g_{\uparrow'\uparrow'}$  or  $2g_{\downarrow'\downarrow'}$ , which is the upper bound of  $g_{\uparrow'\downarrow'}$  (see subsections below). The inset of (b-c) zooms out to show the maximum. (d) shows the immiscibility metric  $\eta = (g_{\uparrow'\downarrow'}^2 - g_{\uparrow'\uparrow'}g_{\downarrow'\downarrow'})/g_{\uparrow'\uparrow'}^2$  in Eq. (3.29) (see subsections below) versus  $\hbar q_y$  corresponding to (b).  $\eta < 0$  means miscible, and  $\eta > 0$  means immiscible. Over the range of plotted  $\hbar q_y$ , (d) can be miscible or immiscible depending on  $\hbar q_y$ . The inset of (d) zooms in to focus on the sign change of  $\eta$ . The vertical dotted line in (b-d) indicates  $\hbar q_{\sigma \min}$  corresponding to the  $\Omega$  in each case. The calculations are performed in the two-state picture described by Eq. (3.1) with  $\delta_R = 0$ . (e-f) Immiscibility metric  $\eta$  versus  $\Omega$  for various  $q_y$ . In (e), as  $\Omega$  becomes larger or  $q_y$  becomes smaller, the two dressed spin components can become more immiscible until  $\eta$  reaches the maximum value set by the upper bound of  $g_{\uparrow'\downarrow'}$  (see also (b-c)). (f) Zoom-in of (e) showing the miscible to immiscible transition (indicated by the gray dashed line at  $\eta = 0$ ) as a function of  $\Omega$  for various  $q_y$ . The red dot-dashed line corresponds to two dressed spin components located respectively at the band minima  $q_{\sigma \min}$ , showing the well-known miscible to immiscible transition around  $0.2 E_r$  for a stationary SO-coupled BEC. In the dynamical case studied here, BECs can be located away from the band minima and approach  $q_y = 0$ , becoming immiscible even when  $\Omega < 0.2 E_r$  for small enough  $q_y$ . The calculations here are performed by Mingyuan He and Qi Zhou. . .

78

**3.11 Time ( $t_{\text{hold}}$ ) evolution of different forms of energies per particle at different  $\Omega_F$  as calculated by GPE.** (a) The total energy is the sum of the total Raman energy, total potential energy, total interaction energy, and the total KE. The result in (a) confirms that the total energy is conserved during  $t_{\text{hold}}$ . (b) Total Raman energy. (c) Total potential energy. (d) Total interaction energy, sum of the bare interaction energies in (i-k). (e) Total KE, sum of different types of kinetic energies in (f-h). (f) Total CoM KE. (g) Total QP. (h) Total LC KE. (i)  $g_{\uparrow\uparrow}$  interaction energy. (j)  $g_{\downarrow\downarrow}$  interaction energy. (k)  $g_{\uparrow\downarrow}$  interaction energy. The GPE calculations here are performed by Chunlei Qu and Chuanwei Zhang. . .

80

Figure	Page
3.12 <b>Effect of modified bare interactions and interspecies immiscibility on SDM damping.</b> In GPE simulations for the bare case SDM, we can change the original interaction parameters $g_{ii}$ and $g_{ij}$ to new values $\tilde{g}_{ii}$ and $\tilde{g}_{ij}$ respectively, where $i, j = \uparrow$ or $\downarrow$ and $i \neq j$ . The relative momentum $\hbar k_{\text{spin}}$ versus $t_{\text{hold}}$ are shown for five different cases with the corresponding modified interaction parameters and immiscibility metric $\eta = (g_{\uparrow\downarrow}^2 - \tilde{g}_{\uparrow\uparrow}\tilde{g}_{\downarrow\downarrow})/\tilde{g}_{\uparrow\uparrow}^2$ listed in Table 3.1 below. The GPE calculations here are performed by Chunlei Qu and Chuanwei Zhang. . . . .	89
3.13 <b>Effect of interference on the relative motion between two colliding BECs</b> (a) The effective width of the two BECs oscillating against each other in the $y$ direction versus $t_{\text{hold}}$ in the single spin case. (b) The relative momentum between the two orthogonal spin components versus $t_{\text{hold}}$ in the two spin case. For (a, b), the two BECs are initially separated by the same potential barrier in the same double well structure. The barrier is then suddenly removed at $t_{\text{hold}} = 0$ to initiate the dynamics. Note that the oscillation frequency in (a) is twice the frequency in (b) due to the definition of $W_{\text{eff},y}$ . The GPE calculations here are performed by Chunlei Qu and Chuanwei Zhang. . . . .	91
3.14 <b>The bare case SDM with interactions in (a) and without interactions in (b).</b> The case (a) is the same simulation as the case of $\Omega_{\text{F}} = 0$ in Fig. 3.3c but shown up to a longer time of 100 ms. The GPE calculations here are performed by Chunlei Qu and Chuanwei Zhang. . . . .	92
3.15 <b>The two colliding bare BECs without interactions in the single spin case (a) and in the two spin case (b).</b> These simulations used the same parameters as in Fig. 3.13 except the interaction $g$ -parameters have been set to zero. The GPE calculations here are performed by Chunlei Qu and Chuanwei Zhang. . . . .	93
3.16 <b>The dressed case SDM at <math>\Omega_{\text{F}} = 1.3E_{\text{r}}</math> with interactions in (a) and without interactions in (b).</b> The case (a) is the same simulation as the case of $\Omega_{\text{F}} = 1.3 E_{\text{r}}$ in Fig. 3.9c but shown up to a longer time of 100 ms. The GPE calculations here are performed by Chunlei Qu and Chuanwei Zhang. . . . .	93
3.17 <b>Spatial modulation in the phase of BEC wavefunctions.</b> The phase of the bare spin up and down components at $t_{\text{hold}} = 7.2$ ms in SDM is plotted in the $x$ - $y$ plane for (a) bare case, and (b) dressed case at $\Omega_{\text{F}} = 1.3 E_{\text{r}}$ . Here, $x$ and $y$ are spatial coordinates. The GPE calculations here are performed by Chunlei Qu and Chuanwei Zhang. . . . .	94

**4.1 Set-up for realizing a synthetic Hall cylinder.** (a) We apply Raman lasers (at wavelength  $\lambda \sim 790$  nm) with orthogonal linear polarizations (double-headed arrows) counter-propagating along  $\hat{y}$  and microwaves (frequency  $\approx 6.8$  GHz, from a microwave horn) propagating in the  $x - y$  plane to a BEC (typical atom number  $\sim (1 - 2) \times 10^4$ ). Gravity “ $g$ ” is towards  $-\hat{y}$ . (b) Hyperfine spin states (indicated by different colors)  $|1\rangle$ ,  $|2\rangle$ ,  $|3\rangle$ , and  $|4\rangle$  as discrete sites in the synthetic dimension  $\hat{w}$  are cyclically-coupled by Raman coupling  $\Omega$  and microwave couplings  $\Omega_{1,2}$  to form a closed circle, as drawn in (c). Linear Zeeman splitting  $\hbar\omega_Z \approx \hbar\Delta\omega_R \approx h \times (3.5$  MHz) is generated by a bias magnetic field, where  $\Delta\omega_R$  is the Raman lasers’ angular frequency difference. The quadratic Zeeman shift is  $\varepsilon_0 \approx 2.4 E_r$ . (c) Connecting the two edges along  $\hat{w}$  of a 2D planar Hall strip (left) gives rise to a cylindrical surface (right) subject to a net radial synthetic magnetic flux (thick yellow arrows) with a non-uniform distribution of the magnetic field (indicated by shaded regions). The half magnetic flux quantum per unit plaquette (highlighted area in shaded regions) formed by four maxima of the density modulation corresponds to an Aharonov-Bohm phase of  $\pi$ . For a BEC at  $q_y = 0$  in the ground band of Fig. 4.2b, the emergent BEC density modulation along  $\hat{y}$  has a periodicity of  $d/2$ , half the period (d) of the Hamiltonian  $H$ . The phase (with  $+$  and  $-$  representing respectively a phase 0 and  $\pi$  at positions of maximum density) of each spin component’s wavefunction has a periodicity of either  $d$  or  $d/2$ . . . . .

101

**4.2 Band structure with a nonsymmorphic symmetry and observed Bloch oscillations.** (a) Laser and microwave induced couplings between a series of spin and mechanical momentum states form two independent branches (marked by solid/dashed circles) offset from each other by  $\hbar K = 2\hbar k_r$ , manifesting the underlying nonsymmorphic symmetry. (b) Calculated band structure using  $\Omega = 2.3$ ,  $\Omega_1 = 2.5$ ,  $\Omega_2 = 3.4$ ,  $\delta_R = 0$ , and  $\varepsilon_0 = 2.4$ , all in units of  $E_r$ . The spin texture is revealed by colors determined by the population-weighted colors of the four spin states (see subsections below). The first Brillouin zone is between the dashed lines. The BEC initially prepared at  $\hbar q_y = 0$  (dashed circles) in either band 1 or band 2 undergoes gravity-induced transport (indicated by arrows) and Bloch oscillations for various  $t_{\text{hold}}$ . (c-d) TOF images showing spin and mechanical momentum compositions of the BEC taken at various  $t_{\text{hold}}$  and the corresponding  $q_y$ , respectively for the initial preparation in band 1 and band 2. The quasimomentum of the BEC at  $t_{\text{hold}}$  can be measured by the displacement of the mechanical momentum components of, say  $|1\rangle$  and  $|4\rangle$ , at  $t_{\text{hold}}$  relative to those at  $t_{\text{hold}} = 0$  ( $q_y = 0$ ). Each TOF image (and the associated analyzed quantities presented later) is typically an average of a few repetitive measurements. (e-f) Total mechanical momentum of the BEC versus  $t_{\text{hold}}$  and quasimomentum, respectively. The  $q_y$  in (f) is plotted modulo  $2K$  (i.e.,  $q_y$  is equivalent to  $q_y \pm n \times 2K$ ), only between  $-K$  and  $K$  for both band 1 and band 2 due to their  $2K$  periodicity in  $q_y$ . This  $2\hbar K$  periodicity is also reflected by the observed  $2\hbar K$  separation between different mechanical momentum components for each spin state in (c, d). (g-h) Fractional spin populations versus  $t_{\text{hold}}$ . In (e-h), solid lines are single-particle calculations using the same parameters as used in (b) and the average of the measured  $d(\hbar q_y)/d(t_{\text{hold}})$  (see subsections below). . . . .

112

Figure	Page
4.3 <b>Density and phase versus <math>y</math> for each spin state, corresponding to the Hamiltonian <math>H</math>.</b> Calculations are performed for a BEC at $q_y = 0$ in Fig. 4.2b, (a) for the ground band, and (b) for the first excited band. The red line, green dashed line, blue circles, and black squares correspond to the spin states $ 1\rangle$ , $ 2\rangle$ , $ 3\rangle$ , and $ 4\rangle$ , respectively. The plotted density of the spin component $i$ , $\rho_i$ , is normalized by the condition $\sum_i \int_0^1 \rho_i d(y/d) = 1$ (also used for Fig. 4.4). The calculation is performed by Yangqian Yan.	115
4.4 <b>Density and phase versus <math>y</math> for each spin state, corresponding to the Hamiltonian <math>H'</math>.</b> Calculations are performed for a BEC at $q_y = 0$ in Fig. 4.5c, (a) for the ground band, and (b) for the first excited band. The red line, green dashed line, blue circles, and black squares correspond to the spin states $ 1\rangle$ , $ 2\rangle$ , $ 3\rangle$ , and $ 4\rangle$ , respectively. The calculation is performed by Yangqian Yan.	117
4.5 <b>Breaking the nonsymmorphic symmetry and effects on observed Bloch oscillations.</b> (a) RF coupling (wiggling lines) merges the two independent branches in Fig. 4.2b, breaking the nonsymmorphic symmetry. (b) A cylinder with a broken nonsymmorphic symmetry, described by the Hamiltonian $H'$ . For a BEC prepared at $q_y = 0$ in the ground band in (c), both the wavefunction's phase (indicated by + and -) and the density modulation have a periodicity of $d$ , identical to the period of the Hamiltonian $H'$ . (c) Calculated band structure using the same parameters as used in Fig. 4.2b with the addition of an RF coupling $\Omega_{\text{RF}} = 1.6 E_r$ , leading to gaps opened at the band crossings in Fig. 4.2b. (d) TOF images at various $t_{\text{hold}}$ for Bloch oscillations of a BEC starting from $q_y = 0$ (dashed circle in (c)). (e-f) Total mechanical momentum of the BEC versus $t_{\text{hold}}$ and quasimomentum, respectively. The measured Bloch oscillations exhibit a periodicity of $\hbar K$ rather than the $2\hbar K$ observed in Fig. 4.2. $q_y$ becomes equivalent to $q_y \pm nK$ . This $\hbar K$ periodicity is also reflected by the observed $\hbar K$ separation between different mechanical momentum components for each spin state in (d). Data in (f) correspond to the data in the first 1.5 ms in (e) before the Bloch oscillations exhibit notable damping. Solid lines in (e, f) are single-particle calculations using the same parameters as used in (c).	119
4.6 <b>Unzipping the cylinder by breaking the cyclic coupling.</b> (a) In the synthetic space, the unzipped Hall cylinder becomes a 2D planar Hall strip. (b) Dispersion relation calculated for $\Omega_2 = 0$ , while keeping the other parameters the same as used in Fig. 4.2b. The BEC is initially prepared at $q_y \approx K$ , marked by the dashed circle. (c) TOF images at various $t_{\text{hold}}$ and the corresponding quasimomentum for a BEC traveling towards negative $q_y$ in the lowest band. (d) Total mechanical momentum of the BEC versus $t_{\text{hold}}$ . (e) Fractional spin populations versus $t_{\text{hold}}$ . Solid lines in (d, e) are single-particle calculations using the same parameters as used in (b).	121

Figure	Page
4.7 <b>Representative measurement of quasimomentum versus <math>t_{\text{hold}}</math>.</b> (a) and (b) are obtained respectively from the atomic clouds of $ 1\rangle$ and $ 4\rangle$ in the experiment corresponding to Fig. 4.2c. Dots are experimental data and lines are linear fits. . . . .	126
5.1 The frequency shift of the scissors mode of an atomic gas at finite temperatures. The open circles refer to the thermal component whose frequency does not depend on the temperature and is in agreement with the collisionless prediction. The solid circles refer to the condensate component, and are in agreement with the hydrodynamic prediction at the low temperature limit. Reproduced from ref. [153]. . . . .	131
5.2 The moment of inertia normalized to the rigid-body value at various temperatures. The open circles refer to the thermal component. The solid circles refer to the condensate component. The solid squares and line refer to the whole atomic gas. The dashed line refers to the hydrodynamic prediction in the low-temperature limit. The dotted line refers to the finite atom number correction. The moment of inertia is obtained by the measured frequency of the scissors mode (see details in ref. [144]: here, the scissors mode is in the $x - y$ plane, i.e. the atomic cloud rotates around the $z$ axis and thus the associated moment of inertia presented here is with respect to the $z$ axis). The reduced moment of inertia indicates the transition from a normal fluid to a superfluid. Reproduced from ref. [144].	132
5.3 Calculated moment of inertia versus atom number. In the small atom number limit it approaches the prediction based on the non-interacting gas at zero temperature (dotted line). In the large atom number limit it approaches the Thomas-Fermi prediction (dashed line). Reproduced from ref. [144]. . . . .	133
5.4 Scissors mode of an atomic gas. (a) For a thermal gas, its scissors mode oscillates as a beat wave with two frequencies determined by the trap frequencies (see texts). (b) For a BEC exhibiting superfluidity, its scissors mode oscillates at a single frequency (see texts). Reproduced from [156].	134

- 5.5 **Experimental set-up and timing diagram.** (a) Counter-propagating Raman lasers with an angular frequency difference of  $\Delta\omega_R = 2\pi(3.5\text{MHz})$  couple the Zeeman sublevels  $|\downarrow\rangle$  and  $|\uparrow\rangle$  separated by  $\hbar\omega_Z \sim \hbar\Delta\omega_R$  in the  $F = 1$  hyperfine state of  $^{87}\text{Rb}$  to create synthetic SOC along  $\hat{y}$ . The Raman detuning  $\delta$  is controlled by the bias magnetic field  $\mathbf{B}$ . (b) A BEC is prepared in the gray region of the Gaussian distribution of the Raman coupling, experiencing a spatially-varying Raman coupling and a synthetic magnetic field  $\mathbf{B}^*$  (see texts). The Raman coupling at the BEC's center (located around 65-75% of the peak) is  $\Omega$ . (c) Experimental timing diagram. After preparing the BEC at  $\Omega = \Omega_i$  and  $\delta = \delta_i$ ,  $\Omega_i$  and  $\delta_i$  are quickly changed to  $\Omega_f$  and  $\delta_f$  in  $t_E = 1$  ms.  $\Omega_f$  and  $\delta_f$  are then held for  $t_{\text{hold}}$  before a 15-ms TOF and the following absorption imaging. (d) A shear force ( $F_{\text{shear}}(z)$  along  $\hat{y}$ , indicated by gray arrows) induced by the quench process is applied to the BEC, pushing (along  $\hat{y}$ ) and tilting the BEC to induce dipole and scissors (oscillations of the tilt angle  $\theta$ ) modes. Here, the tilt angle is defined as the angle between the  $y$  axis and the major axis of the BEC. . . . . 135
- 5.6 **Exemplary scissors and dipole modes of a regular BEC and of a SO-coupled BEC in  $\mathbf{B}^*$ .** (a) and (b) respectively show scissors and dipole oscillations of a regular BEC ( $\Omega_f = 0$ ) with the corresponding select TOF images (dashed lines indicating the tilt angle) shown in (c). We fit the first 2-3 periods of experimental data (scatters) in (a) and (b) to a single sinusoidal function (solid lines) to obtain the frequency of scissors ( $f_{s, \text{exp}} = 194 \pm 3$  Hz) and dipole ( $f_{d, \text{exp}} = 175 \pm 2$  Hz) modes. (d) and (e) respectively show scissors and dipole oscillations of a SO-coupled BEC in the presence of  $\mathbf{B}^*$  (at  $\Omega_f = 3.5 E_r$  and  $\delta_f = 1.6 E_r$ ) with the corresponding select TOF images shown in (f). The measured scissors and dipole modes' frequencies are  $f_{s, \text{exp}} = 138 \pm 2$  Hz and  $f_{d, \text{exp}} = 138 \pm 5$  Hz, respectively. The error bar in the measured frequency is the standard error of the fit. . . . . 138

5.7	<b>Experiment and GPE simulation for scissors and dipole modes at various <math>\Omega_f</math> and <math>\delta_f</math>.</b> (a-c) show results at various $\delta_f$ with a fixed $\Omega_f = 3.0 E_r$ . (d-f) show results at various $\Omega_f$ with a fixed $\delta_f = 1.6 E_r$ . (a) and (d) show the relevant dispersion relations calculated at the BEC's center. (b) and (e) show the calculated cyclotron frequency $\Omega_{\text{cyc}} = \mathbf{B}^*/(2\pi m^*)$ which reflects the strength of $\mathbf{B}^*$ at various $\Omega_f$ and $\delta_f$ . The dots refer to the value at the BEC's center. The vertical bars indicate the range of $\Omega_{\text{cyc}}$ experienced by the rest part of the BEC. (c) and (f) show frequency of the scissors and dipole modes at various $\Omega_f$ and $\delta_f$ . Scatters are experimental data, where vertical and horizontal error bars are respectively the standard error of measurements and the statistical uncertainties of $\delta_f$ or $\Omega_f$ . $f_s$ and $f_d$ respectively refer to the frequency of the scissors and dipole modes, where the subscript "exp" means experiment, "eff" means the effective mass prediction, "GP" means GPE simulation, and "weighted" means the weighted average (see texts). The GPE simulations are performed by Chunlei Qu. The calculation of the cyclotron frequency at various Raman couplings is performed by Su-Ju Wang. . . . .	140
5.8	<b>Beat waves of the scissors mode, revealed in GPE simulation.</b> (a), (c), and (e) show the tilt angle versus $t_{\text{hold}}$ respectively at $\delta_f = 7.0, 4.0,$ and $2.3 E_r$ (all at a fixed $\Omega_f = 3.0 E_r$ ). (b), (d), and (f) are the corresponding FFT analysis, disclosing the constituent frequency components. In each case, the two main frequency components $f_1$ and $f_2$ ( $f_1 > f_2$ ) are respectively close to the effective mass predicted frequency of the scissors and dipole modes, i.e. $f_1 \sim f_{s, \text{eff}}$ and $f_2 \sim f_{d, \text{eff}}$ . The relative amplitude of $f_2$ increases with decreasing $\delta_f$ . The GPE simulations are performed by Chunlei Qu . . . . .	143
6.1	Preliminary results for the charge pumping of a BEC on a synthetic Hall cylinder. Transport of a BEC in the real space by creating a moving emergent lattice at a constant speed. . . . .	149
6.2	Preliminary results for exploring interaction effects on the transport of a BEC in the momentum-space regular strip. The GPE simulations are performed by Yangqian Yan. . . . .	150
6.3	Ideas to generate an accelerating lattice for exploring interaction effects on the transport of a BEC in the momentum-space regular strip. Such an accelerating lattice may allow us to induce transport of the BEC in the band structure while keeping the trap on as well as the strong interaction. . . . .	151

## ABSTRACT

Li, Chuan-Hsun Ph.D., Purdue University, August 2019. Bose-Einstein Condensates in Synthetic Gauge Fields and Spaces: Quantum Transport, Dynamics, and Topological States. Major Professor: Yong P. Chen.

Bose-Einstein condensates (BECs) in light-induced synthetic gauge fields and spaces can provide a highly-tunable platform for quantum simulations.

Chapter 1 presents a short introduction to the concepts of BECs and our BEC machine. Chapter 2 introduces some basic ideas of how to use light-matter interactions to create synthetic gauge fields and spaces for neutral atoms. Three main research topics of the thesis are summarized below.

Chapter 3: Recently, using bosonic quasiparticles (including their condensates) as spin carriers in spintronics has become promising for coherent spin transport over macroscopic distances. However, understanding the effects of spin-orbit (SO) coupling and many-body interactions on such a spin transport is barely explored. We study the effects of synthetic SO coupling (which can be turned on and off, not allowed in usual materials) and atomic interactions on the spin transport in an atomic BEC.

Chapter 4: Interplay between matter and fields in physical spaces with nontrivial geometries can lead to phenomena unattainable in planar spaces. However, realizing such spaces is often impeded by experimental challenges. We synthesize real and curved synthetic dimensions into a Hall cylinder for a BEC, which develops symmetry-protected topological states absent in the planar counterpart. Our work opens the door to engineering synthetic gauge fields in spaces with a wide range of geometries and observing novel phenomena inherent to such spaces.

Chapter 5: Rotational properties of a BEC are important to study its superfluidity. Recent studies have found that SO coupling can change a BEC's rotational and

superfluid properties, but this topic is barely explored experimentally. We study rotational dynamics of a SO-coupled BEC in an effective rotating frame induced by a synthetic magnetic field. Our work may allow for studying how SO coupling modify a BEC's rotational and superfluid properties.

Chapter 6 presents some possible future directions.

# 1. INTRODUCTION

In this chapter, we will give a short introduction to Bose-Einstein condensates (BECs) and our BEC machine.

## 1.1 Introduction to Bose-Einstein condensates

The behavior of a weakly-interacting bosonic gas at different temperatures is illustrated in Fig. 1.1. At high temperatures, each particle can be regarded as a billiard ball and behaves classically.

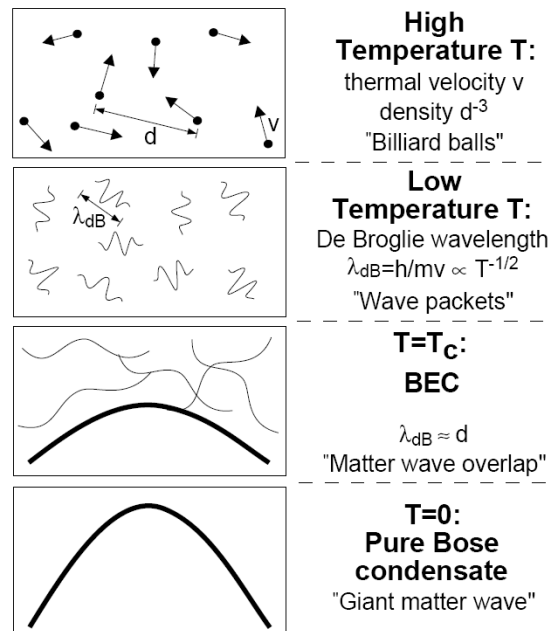


Fig. 1.1. Behavior of a weakly-interacting bosonic gas at different temperatures. When the temperature of the gas is below the critical temperature  $T_c$ , a BEC is formed. Reproduced from ref. [1].

When the temperature of the gas is lowered, the De Broglie wavelength  $\lambda_{\text{dB}} = (2\pi\hbar^2/(mk_{\text{B}}T))^{1/2}$  of each particle becomes larger, where  $\hbar$  is the reduced Plank constant,  $k_{\text{B}}$  is the Boltzmann constant,  $m$  is the mass of an atom, and  $T$  is the temperature of the gas. These atoms can be regarded as quantum mechanical wave packets with a characteristic width of  $\lambda_{\text{dB}}$ . If the gas is further cooled down such that the associated  $\lambda_{\text{dB}}$  becomes comparable to the average inter-particle distance, the majority of the atoms occupies the quantum-mechanical ground state and a macroscopic matter wave forms (a BEC along with thermal atoms). At this point, the corresponding temperature is the critical temperature for the BEC phase transition and can be estimated by the relation  $n_0\lambda_{\text{dB}} \approx 2.612$  [1], where  $n_0$  is the peak atomic density and  $\lambda_{\text{dB}} = (2\pi\hbar^2/(mk_{\text{B}}T))^{1/2}$  is as given above. In the limit of zero temperature, a giant matter wave forms and an almost pure BEC is achieved.

For a dilute gas of atoms at zero temperature, the inter-particle interactions are short-ranged and dominated by the s-wave scattering, thus can be described by a contact pseudo potential. If we further assume that most atoms form a BEC and that the condensate depletion can be neglected, then the many-body wavefunction of the BEC can be described by a single wavefunction, which is simply the product of single-particle wavefunctions  $\psi(r)$  (a complex order parameter), where  $\psi(r)$  satisfies the time-dependent Gross-Pitaevskii (GP) equation [1, 2]:

$$i\hbar\frac{d\psi}{dt} = -\frac{\hbar^2}{2m}\nabla^2\psi + V(r)\psi + U|\psi|^2\psi, \quad (1.1)$$

where  $V(r)$  is the external potential,  $U = 4\pi\hbar^2a/m$  is the parameter characterizing the contact interaction due to two-body collisions,  $a$  is the s-wave scattering length, and  $|\psi|^2$  is the density. Note that the above GP equation is valid when the system is dilute enough such that the average inter-particle distance is much larger than the scattering length  $a$ , i.e.  $n|a|^3 \ll 1$ , where  $n$  is the density of atoms. In many cases including the projects presented in this thesis, the dynamics of a BEC can be properly described by Eq. (1.1).

At the room temperature, the average velocity of atoms is hundreds of meters per second. For ultracold atoms at 100 nK, the average velocity of atoms is millimeters

per second. Therefore, compared to atoms at the room temperature, it is much easier to control (e.g. by light) and measure (e.g. through time-of-flight process and absorption imaging) ultracold atoms. In addition, ultracold atoms can be used to realize novel quantum systems (such as atoms in lattice potentials), where almost every parameter (including particle-particle interactions!) in the system can be well-controlled. Thus, cold atom systems are promising for quantum simulations. In particular, the capability of tuning particle-particle interactions is one of the most attractive features of cold atom systems. One may achieve strong and/or long-range interactions using optical lattices, Feshbach resonances [3], Rydberg atoms [4–7], or atomic/molecular species that have e.g. dipolar interactions, and so on. We will introduce more details about quantum simulations in Chapter 2.

Ultracold atoms also allow for precision measurement (such as atomic clocks), quantum chemistry (such as formation of molecules), and quantum information and computation (e.g. through light-atom interactions), just to name a few. Recently, hybrid quantum systems composed of cold atoms (or cold molecules, ions, and so on), light, and mechanical and solid-state systems have attracted great interest because of their potential for future quantum science and technology such as quantum simulations, information, and computation.

## 1.2 Overview of the $^{87}\text{Rb}$ BEC machine at Purdue

Details about our BEC machine can be found in Abraham J. Olson’s thesis [8] and ref. [9]. Only an overview is given here. Our BEC machine includes optics (lasers, optical elements, and acousto-optical modulators, and so on), electronics, vacuum systems, and computers (Labview is used for experimental control). This machine occupies one optical table. There is another optical table for a Ti-sapphire laser that can be used for several purposes such as optical lattices. One side of the table for the BEC machine is occupied by laser systems and optics for the generation of different colors of light, such as cooling, push, detection, repump, and Raman lasers.

The other side of the table contains ion pumps and vacuum chambers, in which we create magneto-optical traps (MOT, for laser cooling and trapping) and dipole traps (for evaporation cooling). We have MOT-A and MOT-B, which are connected by a differential pump that maintains a higher vacuum in MOT-B and a lower vacuum in MOT-A. Dipole traps are produced by a high power 1550-nm fiber laser. BECs are created in MOT-B.

### 1.2.1 The laser systems for laser cooling and trapping

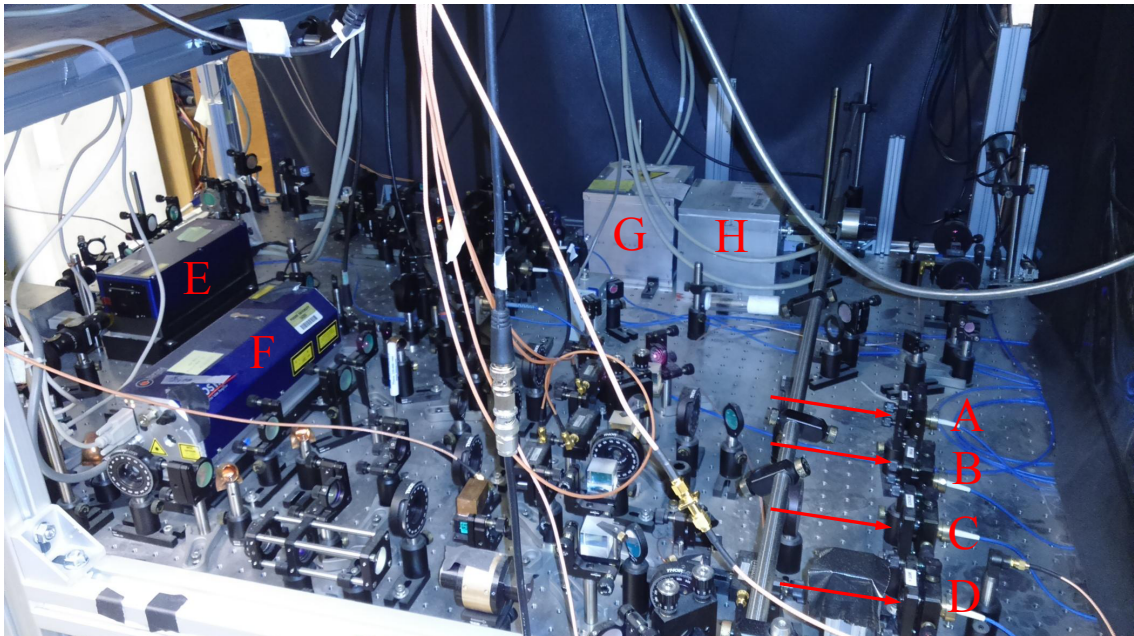


Fig. 1.2. The laser side of the optical table for the BEC machine.

---

Fig. 1.2 shows the laser side of the optical table for the BEC machine. A is the MOT-B cooling laser. B is the push laser, which pushes atoms trapped in MOT-A to MOT-B. C is the detection laser. D is the MOT-A laser. A, B, C, and D are fiber-coupled to the side of the vacuum chamber. E is the master laser (DL-pro), which seeds a home-built tapered amplifier (not shown) to produce B, C, and D. E

also seeds a commercial Boos-TA labeled by F to generate A. G is the home-built Raman laser for creating synthetic gauge fields for BECs. H is the home-built repump laser.

### 1.2.2 The Raman laser system for creating synthetic gauge fields and synthetic spaces

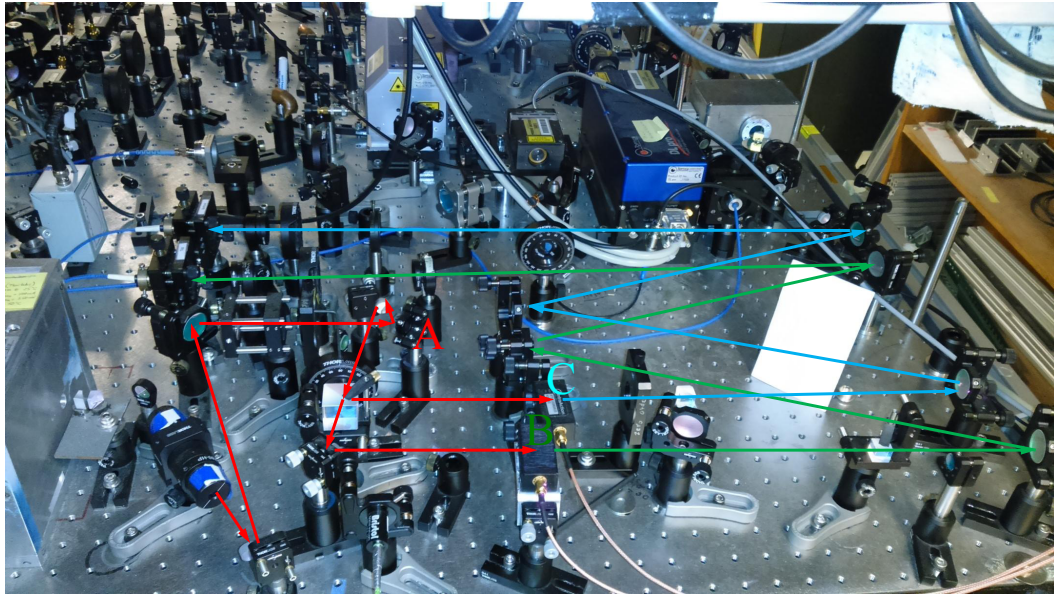


Fig. 1.3. The Raman laser system for creating synthetic gauge fields and synthetic spaces for atoms.

---

As will be introduced in Chapter 2, we will use the “Raman coupling scheme” to realize synthetic gauge fields and synthetic spaces for a BEC. The Raman coupling scheme requires two counter-propagating lasers with a frequency difference around 3.5 MHz to couple atoms’ internal spin states separated by around 3.5 MHz. Please see Chapter 2 for details about the physics. Here, we simply introduce the set-up of our Raman laser system and show measurements of the lifetime of atoms in the presence of Raman lasers. Our Raman laser system is shown in Fig. 1.3. A critical optical

element is a grating (labeled by A) with high diffraction efficiency and reflectivity at the wavelength of the Raman laser. This grating can do a spectral cleaning, which greatly enhances the lifetime of atoms in the presence of Raman lasers by reducing the heating effect from e.g. the residual 780 nm component resonant with the  $D_1$  transition of  $^{87}\text{Rb}$ . Measurements of the lifetime of atoms in the presence of Raman lasers are shown in Figs. 1.5, 1.6, 1.7. The lifetime of atoms in the presence of Raman lasers depends on the Raman coupling  $\Omega$  and is typically hundreds of ms with the grating. The lifetime is only tens of ms without the grating. B and C label the two acousto-optic modulators (AOMs) used for generating two Raman laser beams which have a frequency difference of 3.5 MHz.

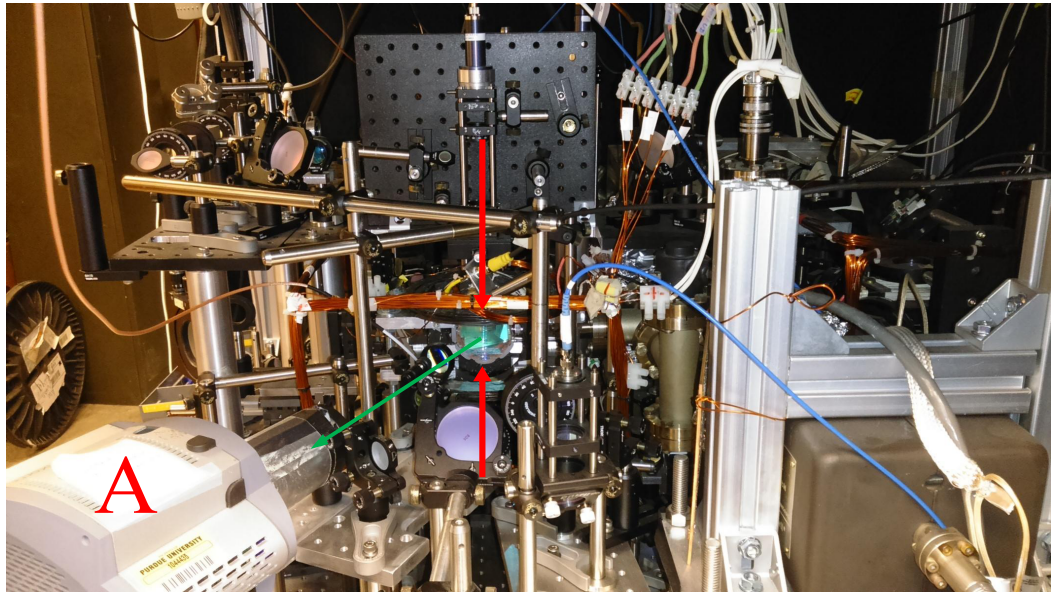


Fig. 1.4. Counter-propagating Raman lasers, detection laser, CCD camera, and MOT-B.

---

In Fig. 1.4, the red arrows indicate the optical paths of the counter-propagating Raman lasers on the vacuum side of the optical table. The green arrow indicates the beam path of the detection laser to the CCD camera, labeled by A. The glass cell is MOT-B, the place we create BECs.

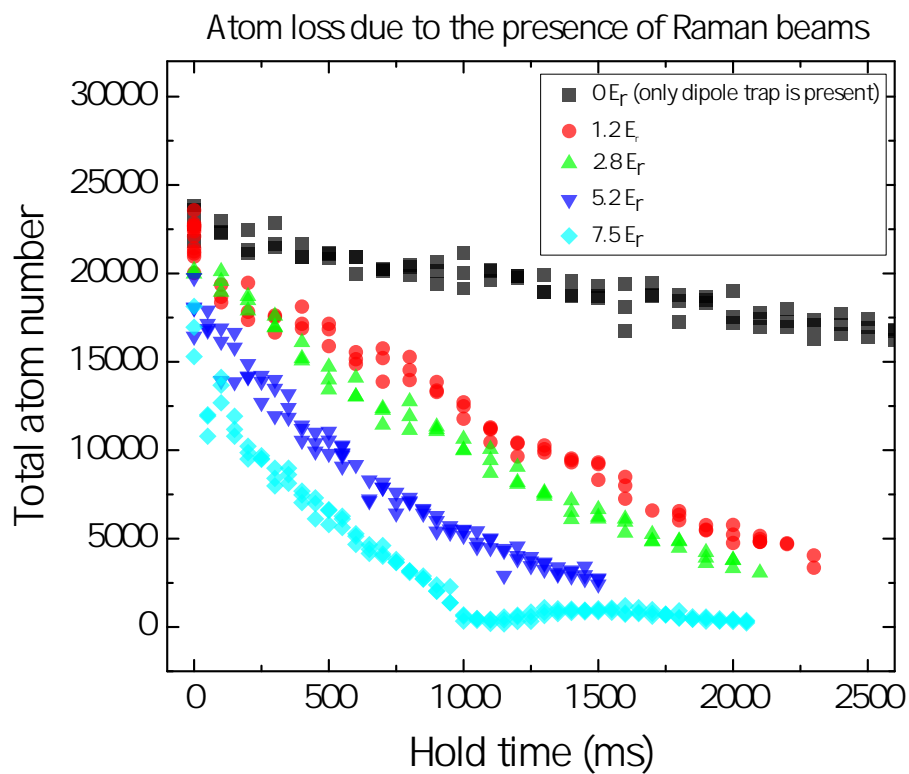


Fig. 1.5. Measurement of the total atom number of a BEC versus hold time at various Raman couplings.

---

Fig. 1.5 shows the measurement of the total atom number of a BEC versus hold time at various Raman couplings. Zoom-in of Fig. 1.5 is shown in Fig. 1.6, which provides useful heating information for the projects in the following chapters.

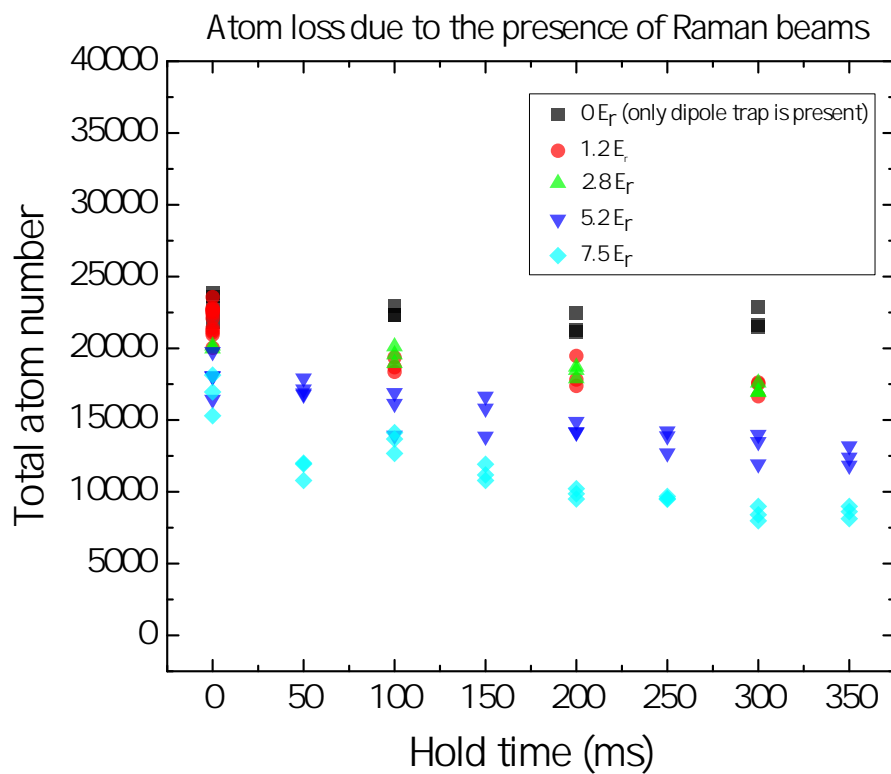


Fig. 1.6. Measurement of the total atom number of a BEC versus hold time at various Raman couplings. This figure is the zoom-in of Fig. 1.5.

---

In addition to the measurement of atom number of a BEC in the presence of Raman lasers, we also measure the condensate fraction of a BEC versus hold time at various Raman couplings, as shown in Fig. 1.7.

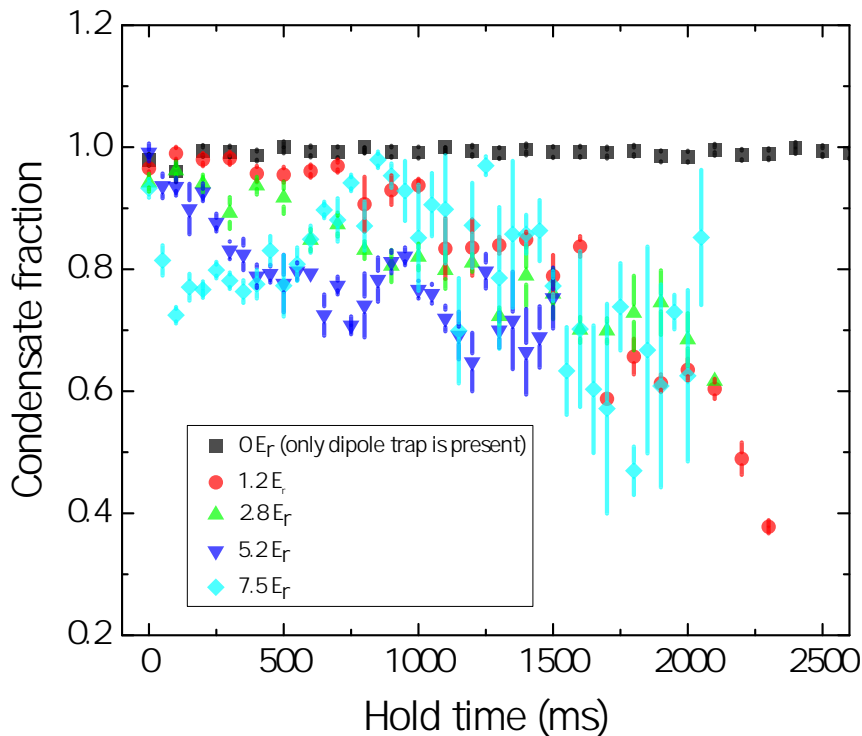


Fig. 1.7. Measurement of the condensate fraction of a BEC versus hold time at various Raman couplings. Note that it can be challenging to extract the condensate fraction when the atom number is small (see Fig. 1.5), for example, when the hold time  $> 700$  ms in the case of  $7.5 E_r$ . Error bar is the standard error of the mean.

### 1.2.3 Microwave and radio frequency (RF) systems

In addition to the Raman lasers, microwaves ( $\sim$  GHz) and RF waves ( $\sim$  MHz) are also important tools to manipulate light-matter interactions. For example, we will apply microwaves and RF waves along with the Raman lasers to realize a cyclic coupling of internal states of atoms to create a synthetic Hall cylinder (Chapter 4). Here we only introduce the set-up of our microwave and RF systems. Fig. 1.8 shows the circuit diagram of our microwave and RF systems.

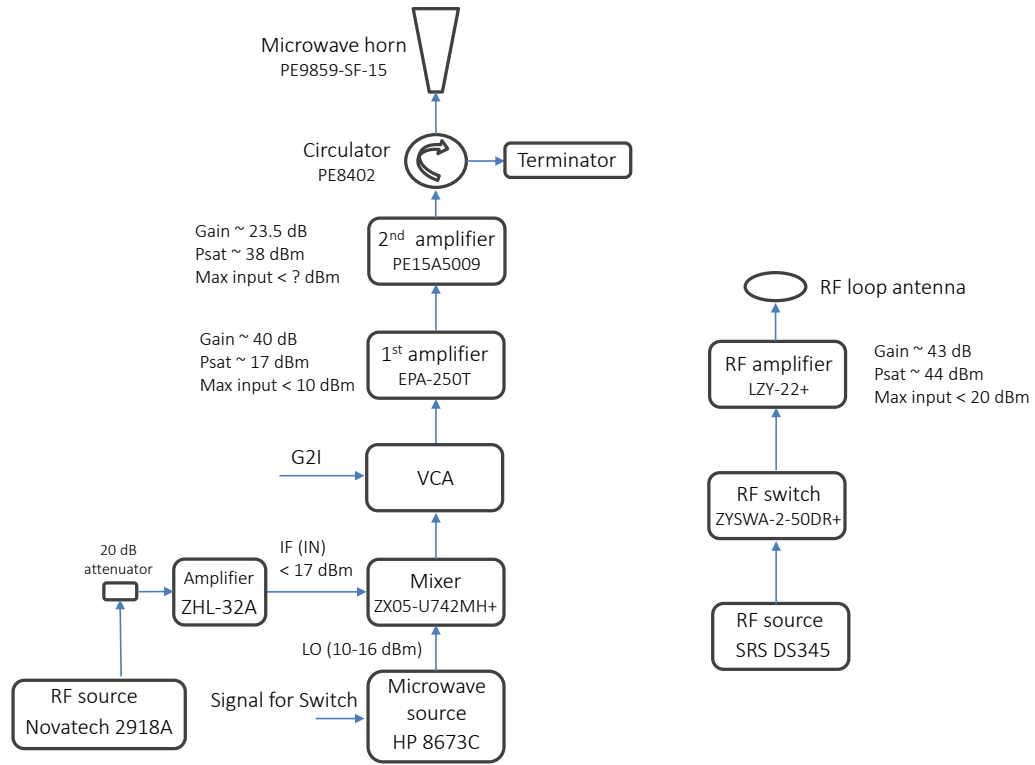


Fig. 1.8. Circuit diagram of our microwave and RF systems.

As shown in Fig. 1.9, we place a microwave horn and an RF loop antenna near the vacuum chamber where we create BECs.

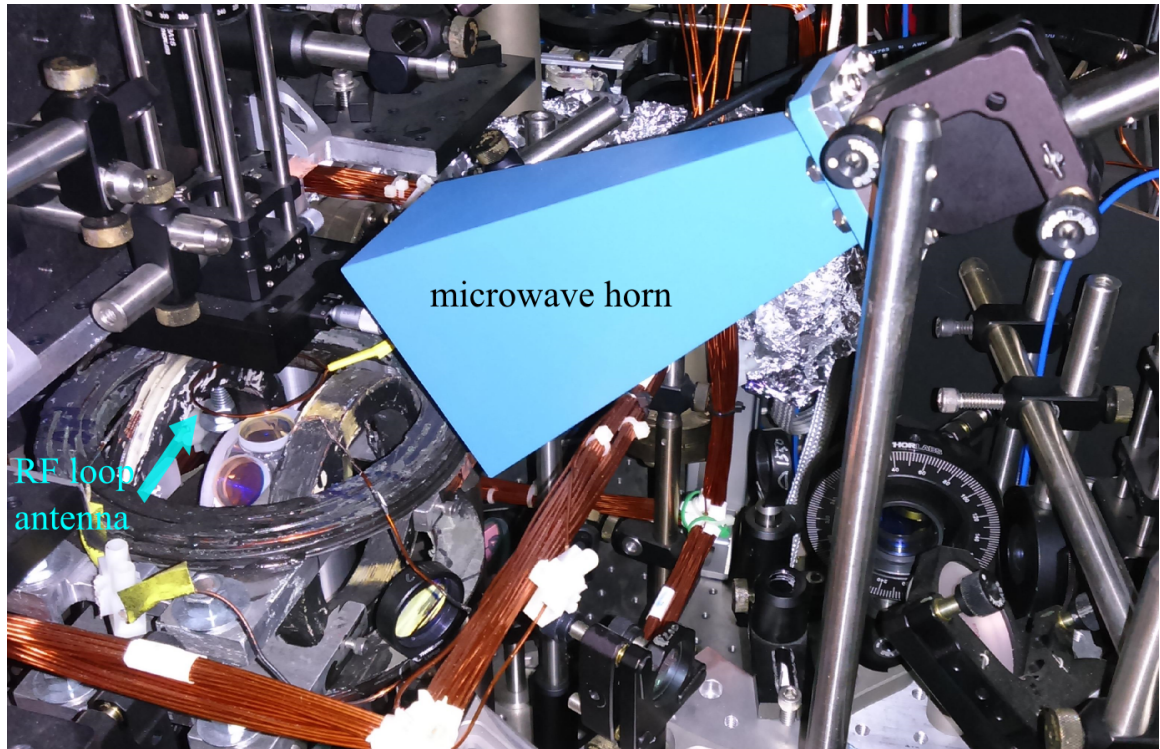


Fig. 1.9. A microwave horn and an RF loop antenna are placed near the vacuum chamber where we create BECs.

---

### 1.2.4 The vacuum side of the optical table

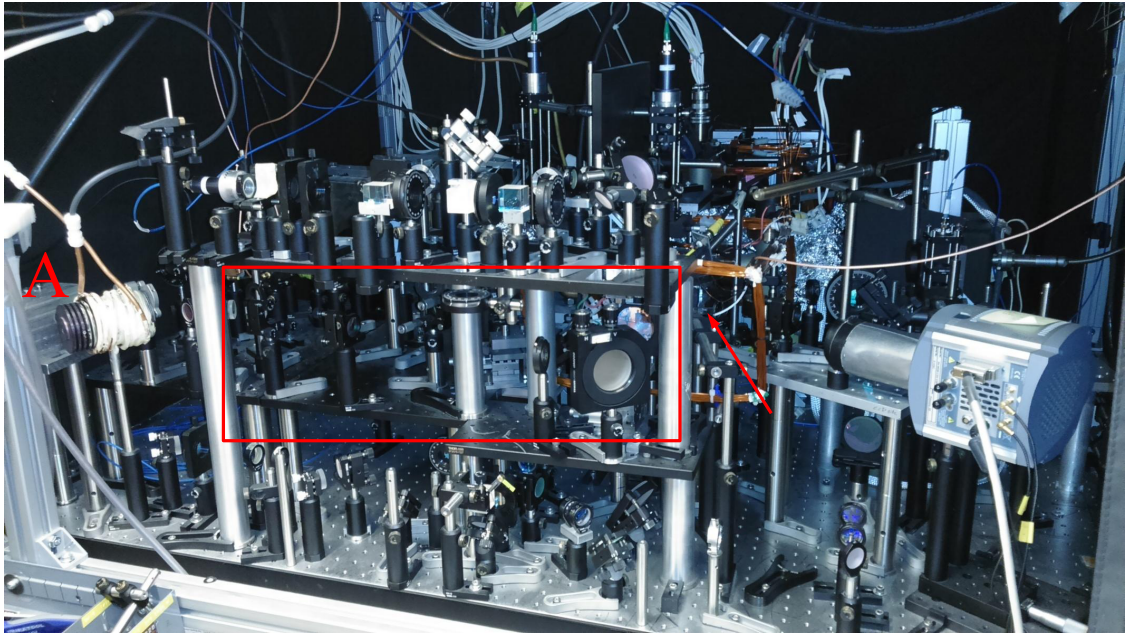


Fig. 1.10. The vacuum side of the optical table for the BEC machine.

---

Fig. 1.10 is the vacuum side of the optical table. The glass cell indicated by the red arrow is MOT-B, where we create BECs. The red box indicates the region occupied by the optics of the lasers for dipole traps. The regions above and below the red box are occupied by several optical paths for MOT-B cooling lasers. A is the laser head of the 40-W 1550-nm fiber laser.

## 2. ENGINEERING LIGHT-MATTER INTERACTIONS TO CREATE SYNTHETIC GAUGE FIELDS AND SPACES FOR NEUTRAL ATOMS

In 1982, Richard Feynman proposed the concept of “quantum simulations” [10]: using a highly-tunable and well-controlled quantum system as a “quantum simulator” to simulate phenomena in another quantum system which is hard to explore. Atomic systems are highly-tunable and allow for very precise measurements, thus are promising candidates for quantum simulations. For example, many fascinating phenomena in solids can be described by the Hubbard model, such as the conducting to Mott-insulating phase transition. Such a model can be exactly realized by applying optical lattice potentials to cold atoms. The quantum phase transition from a superfluid to a Mott insulator has been observed in ultracold bosonic [11] and fermionic [12] gases. In addition, even disordered or quasiperiodic potentials can be engineered for cold atoms. For example, the disordered Bose-Hubbard model can be implemented in cold atom experiment, allowing for dynamically probing the Bose glass-superfluid transition using quantum quenches of disorder [13]. Recently, engineering light-matter interactions to create synthetic gauge fields for neutral atoms (could be bosons or fermions) has attracted great interest, because it further allows for simulating and studying diverse phenomena in other systems. For example, realizing synthetic spin-orbit (SO) coupling for neutral atoms has paved the way to exploring novel topological states of matter, especially those states that may be difficult to access in solids. Moreover, creating synthetic gauge fields may even enable us to explore phenomena that has been predicted in theory but has never been observed in experiment, for example, quantum simulation of a Yang monopole [14].

This chapter only introduces some basic and important ideas about how to engineer light-matter interactions to create synthetic gauge fields and spaces for atoms.

For more information about quantum simulations, synthetic gauge fields, and optical lattices and so on, one can refer to many useful review articles such as refs. [15–28].

## 2.1 Creating synthetic gauge fields using the Raman coupling scheme

Among many proposals for creating synthetic gauge fields for atoms, one of the most popular scheme implemented in experiment is using counter-propagating Raman lasers to couple the internal (pseudo) spin states of atoms [15]. This is the approach we use to generate synthetic SO coupling and synthetic electric and magnetic fields in our lab. The main purpose of using this Raman coupling scheme is to modify the kinetic energy term in the Gross-Pitaevskii equation (GPE) (Eq. (1.1)) to create a new energy-momentum dispersion relation of atoms. To see how this works, see Fig. 2.1 for the experimental setup and the energy level diagram of a (bosonic)  $^{87}\text{Rb}$  atom. This is just an example to demonstrate the ideas. Such a Raman coupling scheme can be applied to other species of atoms and to fermions as well. Applying a bias magnetic field would Zeeman split the sublevels (i.e. Zeeman spin states labeled by  $|m_F = -1\rangle$ ,  $|m_F = 0\rangle$ , and  $|m_F = +1\rangle$ , which are degenerate without the bias magnetic field) of the  $F = 1$  hyperfine state, such that the linear Zeeman splitting is  $\hbar\omega_Z \approx \hbar\Delta\omega_R$  and the quadratic Zeeman shift is  $\hbar\epsilon$ , as shown in Fig. 2.1b. Here,  $\Delta\omega_R$  is the angular frequency difference between the two Raman beams: one Raman laser beam has an angular frequency  $\omega_R$ , and the other Raman laser beam has an angular frequency  $\omega_R + \Delta\omega_R$ .

Via a Raman transition, an atom in a spin state  $|m_F\rangle$  can jump to an adjacent available spin state with  $\Delta m_F = \pm 1$ . The key point is that since Raman lasers are counter-propagating, when an atom change the spin state via a Raman transition by absorbing one photon from one laser and emitting one photon into another laser, the atom would acquire a net momentum change. In other words, when an atom changes the spin via a Raman transition, its mechanical momentum must also change by  $2\hbar k_r$ , where  $\hbar k_r$  is the one photon recoil momentum,  $k_r = 2\pi/\lambda$ , and  $\lambda$  is the wavelength of

the Raman laser (note that  $\Delta\omega_R \ll \omega_R$ , so the two Raman beams essentially have almost the same wavelength).

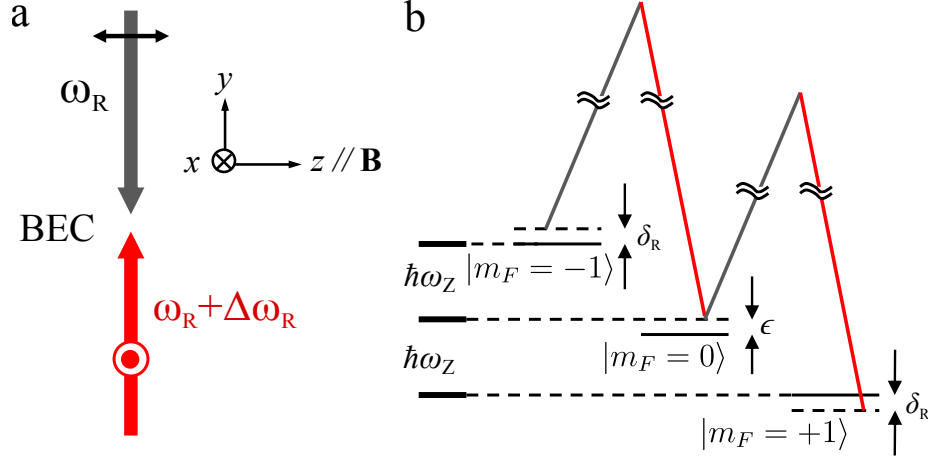


Fig. 2.1. **Raman coupling scheme for generation of synthetic gauge fields.** (a) Counter-propagating Raman lasers with orthogonal linear polarizations couple the internal spin states of atoms. One polarization is parallel to and the other is perpendicular to the bias magnetic field  $\mathbf{B}$  to satisfy the selection rules for such a Raman transition. The angular frequency difference between the Raman lasers is  $\Delta\omega_R$  such that  $\hbar\Delta\omega_R \sim \hbar\omega_Z$ . (b) Energy level diagram of a  $^{87}\text{Rb}$  atom shows the Zeeman sublevels of the  $F = 1$  hyperfine state.

---

This is the underlying mechanism for creating SO coupling (i.e. momentum and spin are coupled). Therefore, if an atom at  $|m_F = 0\rangle$  state has a mechanical momentum  $\hbar q_y$ , then its mechanical momentum would change to  $\hbar(q_y + 2k_x)$  when such an atom jumps to  $|m_F = -1\rangle$  via a Raman transition, and its mechanical momentum would change to  $\hbar(q_y - 2k_x)$  when such an atom jumps to  $|m_F = +1\rangle$  via a Raman transition, where  $q_y$  is an arbitrary real number and  $\hbar q_y$  is called the *quasi-momentum* or *canonical momentum*. Note that for the  $|m_F = 0\rangle$  state, its quasimomentum and mechanical momentum are identical. It is this quasimomentum (canonical momentum) whose commutator with the associated position operator

is equal to  $-i\hbar$ . In summary, a family of spin and mechanical momentum states,  $\{|m_F = -1, \hbar(q_y + 2k_r)\rangle, |m_F = -1, \hbar q_y\rangle, |m_F = +1, \hbar(q_y - 2k_r)\rangle\}$ , are Raman coupled.

Since the Raman lasers are propagating along the  $y$ -direction in this case, thus the dispersion relation of an atom is only modified along  $\hat{y}$ . After using the rotating wave approximation and transforming to a rotating frame at  $\Delta\omega_R$ , the Hamiltonian associated with such a Raman coupling scheme can be written in the basis of  $\{|m_F = -1, \hbar(q_y + 2k_r)\rangle, |m_F = -1, \hbar q_y\rangle, |m_F = +1, \hbar(q_y - 2k_r)\rangle\}$  as [29]:

$$H_3 = \begin{pmatrix} \frac{\hbar^2}{2m}(q_y + 2k_r)^2 - \delta_R & \frac{\Omega}{2} & 0 \\ \frac{\Omega}{2} & \frac{\hbar^2}{2m}(q_y)^2 - \epsilon & \frac{\Omega}{2} \\ 0 & \frac{\Omega}{2} & \frac{\hbar^2}{2m}(q_y - 2k_r)^2 + \delta_R \end{pmatrix} \quad (2.1)$$

Here,  $\delta_R = \Delta\omega_R - \omega_Z$  is the Raman detuning and can be controlled by the bias magnetic field, which adjusts the Zeeman splitting between the spin states (the frequency of the lasers is fixed).  $\Omega$  is the Raman coupling strength and can be calibrated by doing Raman-Rabi oscillations [29] (see the subsection below for details).

In our lab, the Raman laser is set to the magic wavelength ( $\lambda \sim 790$  nm) detuned from both the  $D_1$  ( $\sim 780$  nm) and  $D_2$  ( $\sim 795$  nm) transitions such that the resulting scalar light shift is negligible (see Fig. 2.2 and the section below). The wavelength ( $\lambda \sim 790$  nm) sets some units convenient to use in this system, such as the photon recoil momentum  $\hbar k_r = 2\pi\hbar/\lambda \hat{y}$ , recoil velocity  $v_r \sim 6$  mm/s, and recoil energy  $E_r = \hbar^2 k_r^2 / 2m \sim h \times 3.7$  kHz, where  $m$  is the mass of an  $^{87}\text{Rb}$  atom and  $\hbar$  is the reduced Planck constant.

### 2.1.1 Calculation of the scalar and vector light shifts

When an atom interacting with a monochromatic light, the atom-light interaction Hamiltonian considering dipole-allowed transitions can be written in the form of  $H_{\text{shift}} = \sum_n H_{\text{shift},n}$ , where

$$H_{\text{shift},n} = \underbrace{-\frac{E_0^2}{4}\alpha_{0,n}C_{s,n}(\hat{\epsilon}^* \cdot \hat{\epsilon})}_{\text{scalar light shift}} - \underbrace{\frac{E_0^2}{4}\alpha_{0,n}C_{v,n}(i\hat{\epsilon}^* \times \hat{\epsilon}) \cdot \hat{F}}_{\text{vector light shift}}. \quad (2.2)$$

Here,  $H_{\text{shift}}$  is the total ‘‘light shift’’, and  $H_{\text{shift},n}$  is the light shift associated with a two-level transition labeled by  $n$  in the atomic energy levels and comprises two parts (the *scalar light shift* and the *vector light shift*). Note that there is a tensor light shift term not shown in Eq. (2.2) because it is negligible in our parameter regime. More details about this section can be found in refs. [15, 30–33].  $E_0$  is the amplitude of the electric field of the light,  $\hat{\epsilon}$  is the unit vector of the polarization and  $\hat{\epsilon}^* \cdot \hat{\epsilon} = 1$ , and  $\hbar\hat{F}$  is the total angular momentum operator.  $C_{s,n}$  and  $C_{v,n}$  are coefficients respectively corresponding to the scalar and vector light shifts associated with the two-level transition  $n$ .  $\alpha_0$  is the characteristic polarizability:

$$\alpha_{0,n} = -\frac{3}{32\pi^3} \left(\frac{c}{f_n}\right)^3 \frac{\Gamma_n}{f_L - f_n}, \quad (2.3)$$

where  $c$  is the speed of light,  $f_n$  is the frequency of the two-level transition labeled by  $n$ ,  $f_L$  is the laser frequency (thus  $f_L - f_n$  is the laser detuning from the two-level resonance), and  $\Gamma_n$  is the associated spontaneous emission rate.

If counter-propagating lasers which have parallel linear polarizations and the same frequency are applied to atoms, the vector light shift vanishes because  $\hat{\epsilon}^* \times \hat{\epsilon} = 0$ , but the scalar light shift can be finite and can lead to a conventional optical lattice. On the other hand, for the Raman coupling considered in this chapter (see Fig. 2.1), one Raman laser has a linear polarization parallel to the quantization axis  $\hat{z}$  set by the bias magnetic field while the other Raman laser has a linear polarization in the  $x - y$  plane. Consequently, the polarization of the total electric field can lead to a nonzero  $\hat{\epsilon}^* \times \hat{\epsilon}$  and thus give rise to a *vector light shift* which is responsible for the *Raman coupling* between different spin states in the same  $F$  hyperfine manifold.

In our case, if we consider the  $D_1$  ( $\sim 780$  nm) and  $D_2$  ( $\sim 795$  nm) transitions and a laser detuning much larger than the hyperfine splittings, then in the CGS units

$$C_{s,D_1} = \frac{1}{3}, C_{s,D_2} = \frac{2}{3}, C_{v,D_1} = \frac{g_F}{3}, C_{v,D_2} = -\frac{g_F}{3}, \quad (2.4)$$

where  $g_F$  is the Landé  $g$ -factor,  $g_F = -1/2$  for the  $F = 1$  ground state, and  $g_F = 1/2$  for the  $F = 2$  ground state. Note that the coefficients in Eq. (2.4) above are in CGS units  $\frac{\text{erg}}{(\text{cm})(\text{statVolt})^2}$ , where the conversion to SI units is  $\frac{\text{erg}}{(\text{cm})(\text{statVolt})^2} \approx 1.113 \times 10^{-10} \frac{\text{Joule}}{(\text{m})(\text{Volt})^2}$ .

In the following, we consider Raman lasers having a wavelength  $\lambda_L = c/f_L$  and a total power  $P$ , with a Gaussian intensity profile that has a radius of  $w_0 = 50$  um. By calculating the peak intensity  $I_0 = 2P/(\pi(w_0)^2)$  as would be experienced by the atoms, we obtain  $E_0^2 = 2I_0/(c\varepsilon_0)$ , where  $\varepsilon_0$  is the vacuum permittivity. Using Eqs. (2.2-2.4), the scalar and vector light shifts for atoms in the  $F = 1$  ground state as a function of the laser wavelength  $\lambda_L$  are calculated in Fig. 2.2, which shows that the scalar light shift vanishes around  $\lambda_L \approx 790$  nm (the magic wavelength). In addition, the vector light shift for atoms in the  $F = 1$  or  $F = 2$  ground states is calculated in Fig. 2.3. In general, the vector light shift (responsible for the Raman coupling) for atoms in the  $F = 1$  or  $F = 2$  ground states may be different at a given laser wavelength  $\lambda_L$ , because the corresponding laser detunings from the same excited state are different by  $\approx 6.8$  GHz (the hyperfine splitting between the  $F = 1$  and  $F = 2$  ground states). However, when the laser detuning is much larger than the hyperfine splittings, the difference in the resulting vector light shift between  $F = 1$  and  $F = 2$  is negligible.

When calculating Figs. 2.2-2.3, the following parameters are used:  $\Gamma_{D_1} = 5.746 \times 10^6$  Hz (spontaneous decay rate in frequency, not angular frequency, associated with the  $D_1$  transition),  $\Gamma_{D_2} = 6.065 \times 10^6$  Hz (spontaneous decay rate associated with the  $D_2$  transition),  $f_{F=1,D_1} = (377.1074635 \times 10^{12} - 2.56300597908911 \times 10^9)$  Hz ( $D_1$  transition frequency, not angular frequency, from the  $F = 1$  ground state),  $f_{F=2,D_1} = (377.1074635 \times 10^{12} + 4.27167663181519 \times 10^9)$  Hz ( $D_1$  transition frequency from the  $F = 2$  ground state),  $f_{F=1,D_2} = (384.2304844685 \times 10^{12} - 2.56300597908911 \times$

$10^9$ ) Hz (D<sub>2</sub> transition frequency from the  $F = 1$  ground state), and  $f_{F=2,D_2} = (384.2304844685 \times 10^{12} + 4.27167663181519 \times 10^9)$  Hz (D<sub>2</sub> transition frequency from the  $F = 2$  ground state).

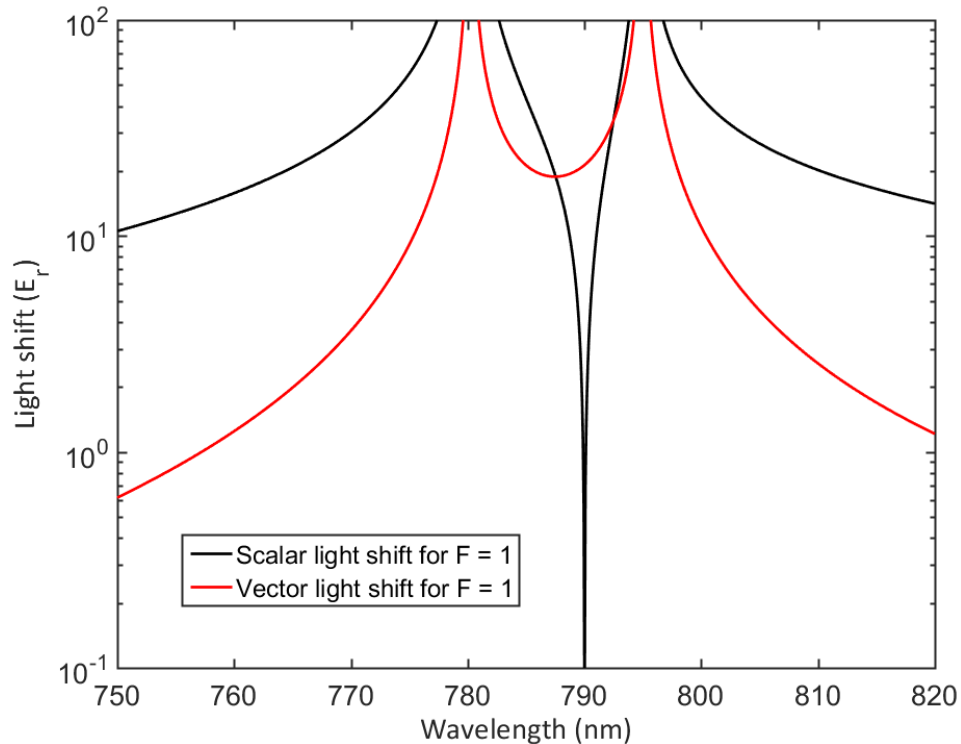


Fig. 2.2. Calculated magnitude of the scalar and vector light shifts for atoms in the  $F = 1$  ground state as a function of the laser wavelength  $\lambda_L$ . The calculation is performed using Eqs. (2.2-2.4). The scalar light shift vanishes around 790 nm, which is the magic wavelength. Note that for different wavelength  $\lambda_L$ ,  $E_r = \hbar^2 k_r^2 / (2m)$  has different values because  $k_r = 2\pi / \lambda_L$ .

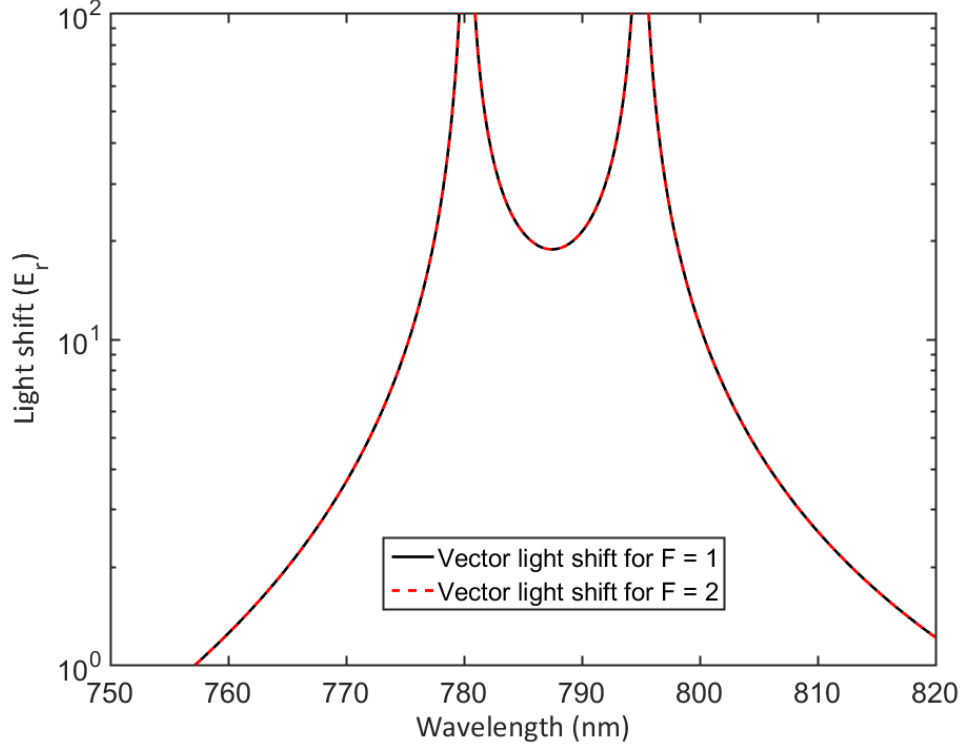


Fig. 2.3. Calculated magnitude of the vector light shift for atoms in the  $F = 1$  or  $F = 2$  ground states. The calculation is performed using Eqs. (2.2-2.4). In general, the vector light shift (responsible for the Raman coupling between different spin states in the same  $F$  hyperfine manifold) for atoms in the  $F = 1$  or  $F = 2$  ground states may be different at a given laser wavelength  $\lambda_L$ , because the corresponding laser detunings from the same excited state are different by  $\approx 6.8$  GHz (the hyperfine splitting between the  $F = 1$  or  $F = 2$  ground states). However, when the laser detuning is much larger than the hyperfine splittings, the difference in the resulting vector light shift between  $F = 1$  and  $F = 2$  is negligible.

---

### 2.1.2 Calibrating the Raman coupling strength with resonant Raman-Rabi oscillations

Resonant Raman-Rabi oscillations between spin and mechanical momentum states  $|m_F = 0, 0\hbar k_r\rangle$  and  $|m_F = +1, -2\hbar k_r\rangle$  can be achieved when the elements (2,2) and (3,3) of the matrix  $H_3$  in Eq. (2.1) become equal. That is, when the Raman detun-

ing  $\delta_R$  is equal to  $\delta_{\text{res},0 \rightarrow +1} = -\epsilon - 4E_r$ . Similarly, resonant Raman-Rabi oscillations between spin and momentum states  $|m_F = 0, 0\hbar k_r\rangle$  and  $|m_F = -1, +2\hbar k_r\rangle$  can be achieved when the elements (2,2) and (1,1) of the matrix  $H_3$  in Eq. (2.1) become equal. That is, when the Raman detuning  $\delta_R$  is equal to  $\delta_{\text{res},0 \rightarrow -1} = \epsilon + 4E_r$ . The  $4E_r$  in  $\delta_{\text{res},0 \rightarrow -1}$  or  $\delta_{\text{res},0 \rightarrow +1}$  comes from the kinetic energy difference between the two Raman-coupled states, reflecting the nature of spin-momentum locking. Experimentally, we adjust the bias magnetic field (controlled by a voltage “SE” applied to the circuit for the magnetic coil) to change the Zeeman splitting such that  $\delta_R = \delta_{\text{res},0 \rightarrow +1}$  or  $\delta_R = \delta_{\text{res},0 \rightarrow -1}$  can be achieved. Fig. 2.4 shows the relative population of  $|m_F = +1, -2\hbar k_r\rangle$  (red scatters),  $|m_F = 0, 0\hbar k_r\rangle$  (blue scatters), and  $|m_F = -1, +2\hbar k_r\rangle$  (green scatters) versus the applied voltage SE. The peak population transfer from  $|m_F = 0\rangle$  to  $|m_F = +1\rangle$  reveals the SE corresponding to  $\delta_{\text{res},0 \rightarrow +1}$ , and the peak population transfer from  $|m_F = 0\rangle$  to  $|m_F = -1\rangle$  reveals the SE corresponding to  $\delta_{\text{res},0 \rightarrow -1}$ .

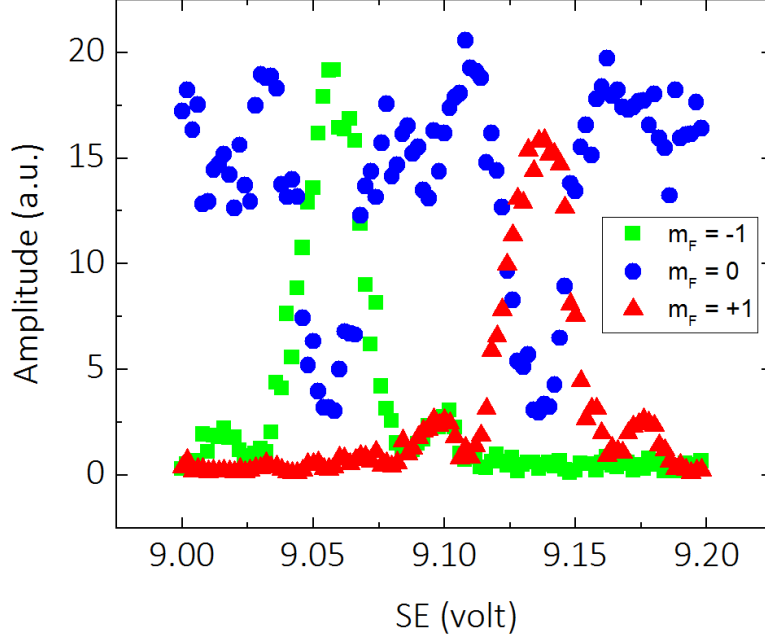


Fig. 2.4. Measurement of the Raman detunings  $\delta_{\text{res},0 \rightarrow -1}$  and  $\delta_{\text{res},0 \rightarrow +1}$  for resonant Raman-Rabi oscillations. The peak population transfer from  $|m_F = 0, 0\hbar k_r\rangle$  to  $|m_F = +1, -2\hbar k_r\rangle$  reveals the SE corresponding to  $\delta_{\text{res},0 \rightarrow +1}$ , and the peak population transfer from  $|m_F = 0, 0\hbar k_r\rangle$  to  $|m_F = -1, +2\hbar k_r\rangle$  reveals the SE corresponding to  $\delta_{\text{res},0 \rightarrow -1}$ . SE is the voltage applied to the circuit for the magnetic coil to control the Zeeman splitting and thus the Raman detuning. See texts for details.

Once we obtain the Raman detuning for resonant Raman-Rabi oscillations, we can suddenly apply Raman lasers with different pulse widths to a BEC to drive resonant Raman-Rabi oscillations between the BEC's different spin and mechanical momentum states. For example, Fig. 2.5 shows a typical resonant Raman-Rabi oscillations between  $|m_F = 0, 0\hbar k_r\rangle$  and  $|m_F = +1, -2\hbar k_r\rangle$  states. Fig. 2.5a shows select time-of-flight (TOF, introduced later) images (where the labeled time is the pulse width) revealing the bare spin and mechanical momentum compositions of the BEC. Fig. 2.5b shows the analyzed relative population of  $|m_F = +1, -2\hbar k_r\rangle$  (red scatters),  $|m_F = 0, 0\hbar k_r\rangle$  (blue scatters), and  $|m_F = -1, +2\hbar k_r\rangle$  (green scatters) versus

the applied pulse width. Solid lines are fits from solving the following time-dependent Schrödinger equation to extract the Raman coupling strength  $\Omega$  ( $\sim 5E_r$  in this case):

$$i\hbar \frac{d\psi}{dt} = H_3\psi, \quad (2.5)$$

where  $H_3$  is given by Eq. (2.1) with  $\Omega$  the only free parameter and the initial condition is  $\psi = (0; 1; 0)$  (a  $3 \times 1$  column vector; all the atoms are in  $|m_F = 0, 0\hbar k_r\rangle$ ).

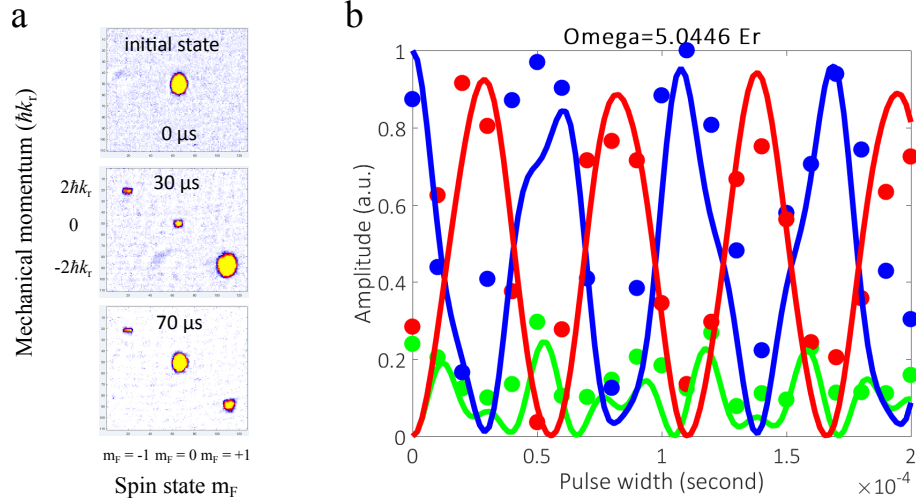


Fig. 2.5. An example for resonant Raman-Rabi oscillations. (a) Select TOF images (where the labeled time is the pulse width) revealing the bare spin and mechanical momentum compositions of the BEC. (b) shows the analyzed relative population of  $|m_F = +1, -2\hbar k_r\rangle$  (red scatters),  $|m_F = 0, 0\hbar k_r\rangle$  (blue scatters), and  $|m_F = +1, +2\hbar k_r\rangle$  (green scatters) versus the applied pulse width. Solid lines are fits to extract the Raman coupling strength. See texts for details.

## 2.2 Synthetic vector potentials and synthetic electric and magnetic fields

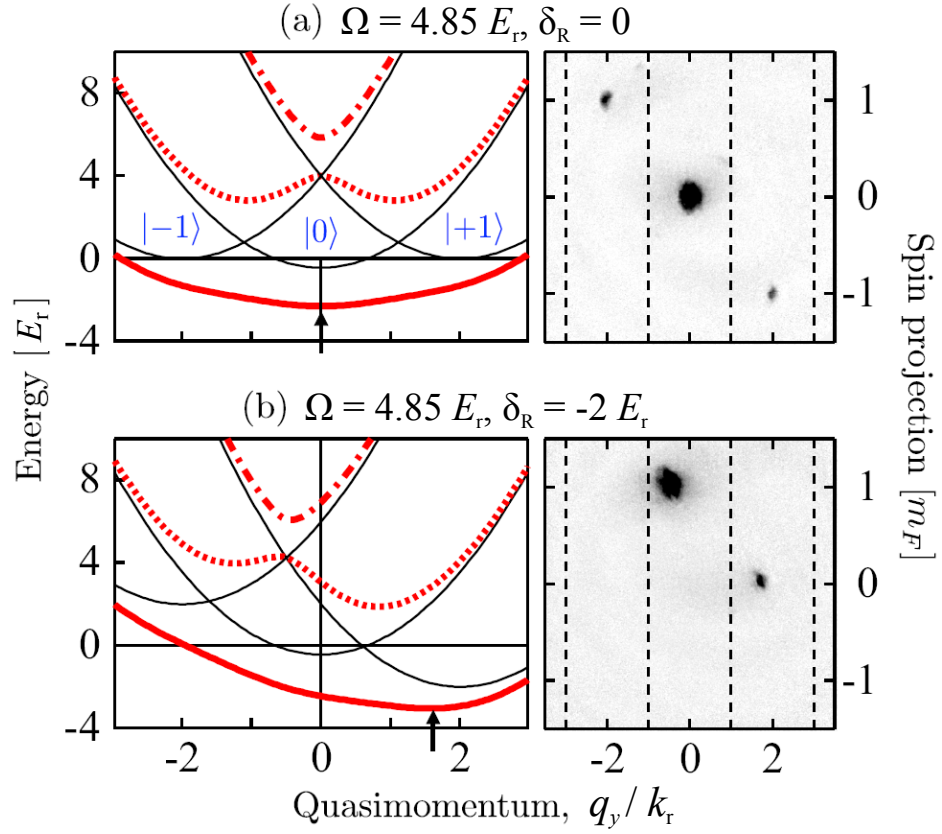


Fig. 2.6. An example of synthetic vector potentials. See texts for details. Reproduced from ref. [29].

When the Raman coupling  $\Omega$  is zero in Eq. (2.1), the diagonal elements are the eigenvalues of the matrix and correspond to a quadratic dispersion relation of a free particle. When  $\Omega \neq 0$ , one then need to diagonalize the matrix to find the new eigenvalues (called the eigenenergies or the “dressed” energies) and eigenstates (called the “dressed” states) of Eq. (2.1). A dressed state at the quasimomentum  $\hbar q_y$  is a superposition of the bare spin and momentum states  $|m_F = -1, q_y + 2k_r\rangle$ ,  $|m_F = 0, q_y\rangle$ , and  $|m_F = +1, q_y - 2k_r\rangle$ .

As an example shown in Fig. 2.6, when  $\Omega \neq 0$ , there are three dressed energy bands (red curves, dressed energy versus the quasimomentum) which are different from the original “bare” bands (black curves). When the Raman detuning  $\delta_R$  is changed from 0 to  $-2 E_r$ , the energy minimum (indicated by the black arrows) of the ground dressed band is shifted. That is, the quasimomentum (labeled by “ $\hbar q_{\min}$ ”) associated with the energy minimum is changed. If a BEC is prepared at the minimum of the ground dressed band in Fig. 2.6a or Fig. 2.6b, the corresponding dressed states of the BEC are different. As shown in Fig. 2.6, performing a time-of-flight (TOF) measurement (including a Stern-Gerlach process for separating different spin states) is equivalent to projecting the dressed state of the BEC onto the basis of bare spin and momentum states, directly revealing the corresponding bare spin and momentum compositions of the dressed BEC in Fig. 2.6a or Fig. 2.6b.

The quasimomentum associated with the energy minimum,  $\hbar q_{\min}$ , is of great importance. The energy spectrum around  $\hbar q_{\min}$  can be expanded as  $E = \frac{\hbar^2}{2m^*} (q_y - q_{\min})^2$ , which is analogous to the Hamiltonian describing a charged particle with a charge  $Q$  in a magnetic vector potential  $A$ ,  $\hat{H} = (\hat{p}_y - QA)^2 / (2m_Q)$  [29, 34], where  $m^*$  is the effective mass of a dressed atom and  $m_Q$  is the mass of the charged particle. Therefore, we can identify the quasimomentum ( $\hbar q_y$ ) with the canonical momentum ( $\hat{p}_y = -i\hbar \frac{\partial}{\partial y}$ ), and  $\hbar q_{\min}$  with the light-induced vector potentials ( $A$ , by setting  $Q = 1$  for our case). Thus, the velocity operator corresponding to the mechanical momentum,  $\hat{v}_y = -[\hat{H}, y] / (i\hbar) = (\hat{p}_y - QA) / m_Q$ , corresponds to  $\hbar(q_y - q_{\min}) / m^*$ . Therefore, when a BEC is prepared around the energy minimum of a dressed band, the atoms feel a synthetic vector potential ( $A$ , i.e.  $\hbar q_{\min}$ ) like a charged particle feels a magnetic vector potential.

It is important to note that the synthetic vector potential  $A$  (or equivalently  $\hbar q_{\min}$ ) can be tuned by changing the Raman coupling  $\Omega$  or Raman detuning  $\delta_R$ , because  $\hbar q_{\min}$  changes as a function of  $\Omega$  and  $\delta_R$  (e.g. see Fig. 2.6). Thus, if  $\Omega$  or  $\delta_R$

is quickly changed in time, then  $A$  is quickly changed in time and the atoms would feel a synthetic electric field  $\mathbf{E}$  [35] according to

$$\mathbf{E} = -\frac{\partial \mathbf{A}}{\partial t}. \quad (2.6)$$

On the other hand, if  $\Omega$  or  $\delta_R$  is made spatially varying (say along  $\hat{z}$ ), then  $\mathbf{A} = A(z)\hat{y}$  becomes spatially varying in  $z$  and the atoms would feel a synthetic magnetic field  $\mathbf{B}^*$  [36] according to

$$\mathbf{B}^* = \nabla \times \mathbf{A}(z) = -\frac{\partial A(z)}{\partial z} \hat{x}. \quad (2.7)$$

More precisely, the Raman coupling scheme here leads to the Hamiltonian in Eq. (2.1) for the light-atom interactions, such that an atom would behave (as described by this equation) like a charged particle in a magnetic vector potential. Further, once the associated synthetic  $A$  for atoms is made time-varying or spatially-varying, an atom would behave like a charged particle in an electric field or a magnetic field, respectively.

### 2.3 Synthetic spin-orbit coupling: spin-dependent vector potentials

One can utilize the quadratic Zeeman shift  $\hbar\epsilon$  (Fig. 2.1b) such that the frequency difference between the Raman lasers is resonant with the energy difference between  $|m_F = -1\rangle$  and  $|m_F = 0\rangle$  but nonresonant with the energy difference between  $|m_F = 0\rangle$  and  $|m_F = +1\rangle$ . In such a case, the  $|m_F = +1\rangle$  state could be excluded in the first-order approximation such that Eq. (2.1) can be rewritten into a  $2 \times 2$  matrix in the basis of  $|m_F = -1, q + k_r\rangle$  and  $|m_F = 0, q - k_r\rangle$  [37]:

$$H_{\text{SOC}} = \begin{pmatrix} \frac{\hbar^2}{2m}(q + k_r)^2 - \frac{\delta_R}{2} & \frac{\Omega}{2} \\ \frac{\Omega}{2} & \frac{\hbar^2}{2m}(q - k_r)^2 + \frac{\delta_R}{2} \end{pmatrix} \quad (2.8)$$

This is the Hamiltonian for the synthetic SO coupling of a spin-1/2 system. When  $\delta_R = 0$  in Eq. (2.8), the dispersion relations at various  $\Omega$  are plotted in Fig. 2.7.

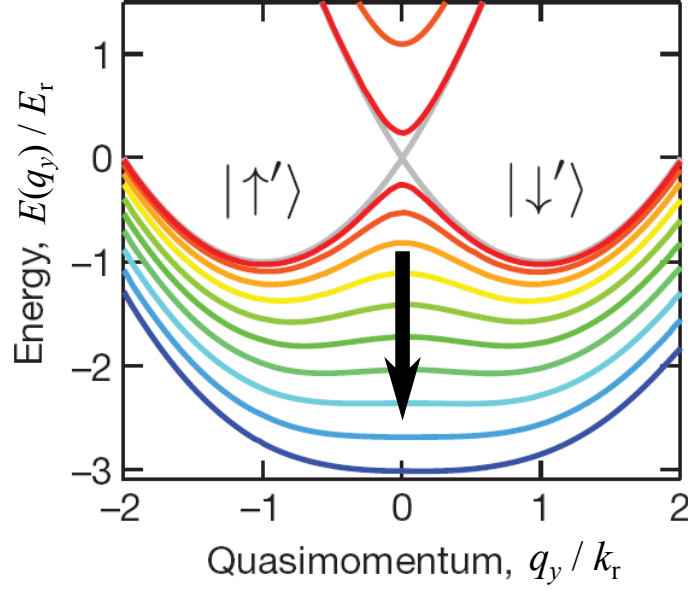


Fig. 2.7. SO-coupled dispersion relations at various Raman coupling  $\Omega$  at  $\delta_R = 0$  in Eq. (2.8). The black arrow indicates increasing  $\Omega$ , showing the evolution of double-minima structures to single-minimum structures. Reproduced from ref. [37].

As shown in Fig. 2.7, SO-coupled dispersion relations can have double-minima or single-minimum structures, depending on  $\Omega$ . A transition from a double-minima structure to a single-minimum structure occurs at a critical Raman coupling  $\Omega_c$ . For a double-minima structure, we may associate atoms occupying the left well with the dressed spin up ( $|\uparrow'\rangle$ ) and atoms occupying the right well with the dressed spin down ( $|\downarrow'\rangle$ ). Different dressed spin states would experience different vector potentials, that is, the vector potential becomes spin-dependent. These spin-dependent vector potentials  $A_\sigma$ , represented by  $\hbar q_{\sigma \min}$ , depend on  $\Omega$ , where  $\sigma = \uparrow', \downarrow'$ . For example, as shown in Fig. 2.7 in the quasimomentum space, we can decrease  $\Omega$  to separate the two  $\hbar q_{\sigma \min}$  (double-minima structure) or increase  $\Omega$  such that they merge into a single minimum. In other words, the spin-dependent vector potentials  $A_\sigma$  can be controlled by the Raman coupling  $\Omega$ .

### 2.3.1 Phase transition diagrams at zero or finite temperatures

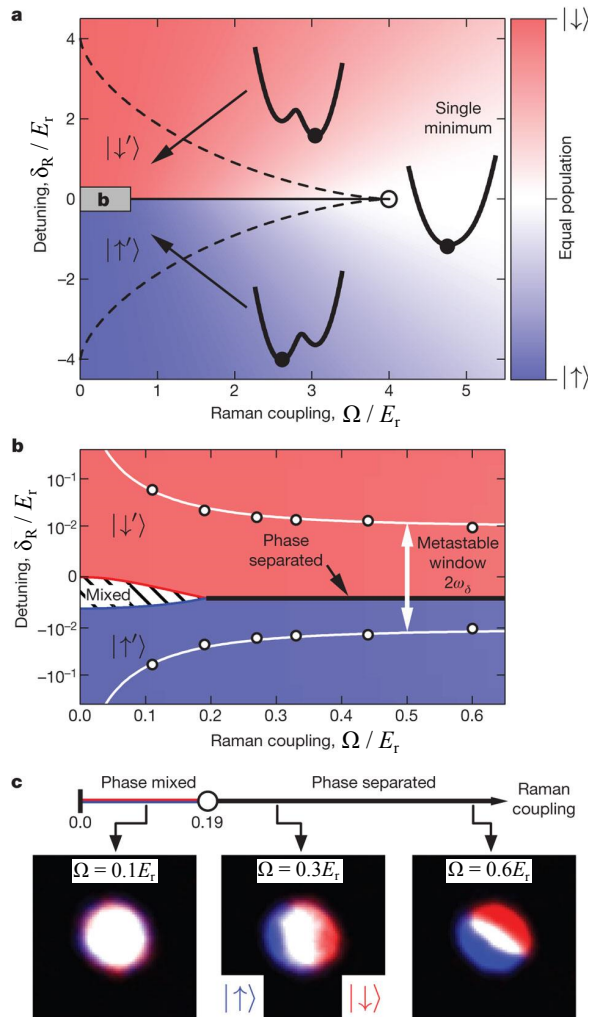


Fig. 2.8. Phase transition diagram of a stationary SO-coupled BEC at zero temperature. (a) The dispersion exhibits a double-minima structure within the region of dashed lines and otherwise a single-minimum structure. The gray area labeled as “b” is shown in (b) for details. (b) shows the metastable window within which both the energy minima of the dispersion may be simultaneously occupied by atoms. A miscible (phase mixed) to immiscible (phase separated) phase transition occurs around  $0.2 E_r$ . (c) shows the phase mixed to phase separated transition with representative images revealing miscible or immiscible atomic clouds of different spin states. Reproduced from ref. [37].

As described in the previous section, the spin-dependent vector potentials  $A_\sigma$  can be controlled by the Raman coupling  $\Omega$  such that the dispersion relation can be a balanced double-minima structure or a balanced single-minimum structure. Furthermore, the dispersion relation becomes tilted when the Raman detuning  $\delta_R$  (controlled by the bias magnetic field) in Eq. (2.8) is nonzero.

Fig. 2.8a shows the phase transition diagram of a SO-coupled BEC at zero temperature. When the Raman detuning (vertical axis)  $\delta_R$  is zero, the double-minima to single-minimum transition occurs at  $\Omega = 4.0 E_r$ . When  $\delta_R$  is nonzero, whether the dispersion has single minimum or double minima depends on both  $\Omega$  and  $\delta_R$ . The dispersion exhibits a double-minima structure within the region of dashed lines and otherwise a single-minimum structure. Fig. 2.8b shows the details of the metastable window represented by the gray region (labeled by “b”) in Fig. 2.8a. Within the metastable window, atoms may stay in a metastable state in which both the left and right wells of the dispersion are occupied by the atoms at the same time. Fig. 2.8b further shows a miscible (phase mixed) to immiscible (phase separated) phase transition occurring at  $\Omega \sim 0.2 E_r$ . Such a phase transition is due to the SOC-modified interaction between different dressed spin states ( $|\uparrow'\rangle$  and  $|\downarrow'\rangle$ ). More details about the SOC-modified interaction and whether the two dressed spin states are miscible or immiscible will be discussed and studied in Chapter 3. As shown in Fig. 2.8c, when  $\Omega < 0.2 E_r$ , the two spin components are spatially overlapped (phase mixed) in real space. In this miscible phase, since the wavefunctions of the two dressed spin states overlap with each other in space and are not orthogonal, the interference of the wavefunctions leads to density modulations. Thus, this miscible phase is also called the stripe phase. When  $\Omega > 0.2 E_r$ , the SOC-modified interaction between different dressed spin states becomes more repulsive as  $\Omega$  is larger, thus the two dressed spin states tend to phase separate in space (the immiscible phase) to save the increased effective interaction energy. The phase transitions illustrated in Fig. 2.8 are also shown in Fig. 2.9a with the corresponding dressed spin wavefunctions.

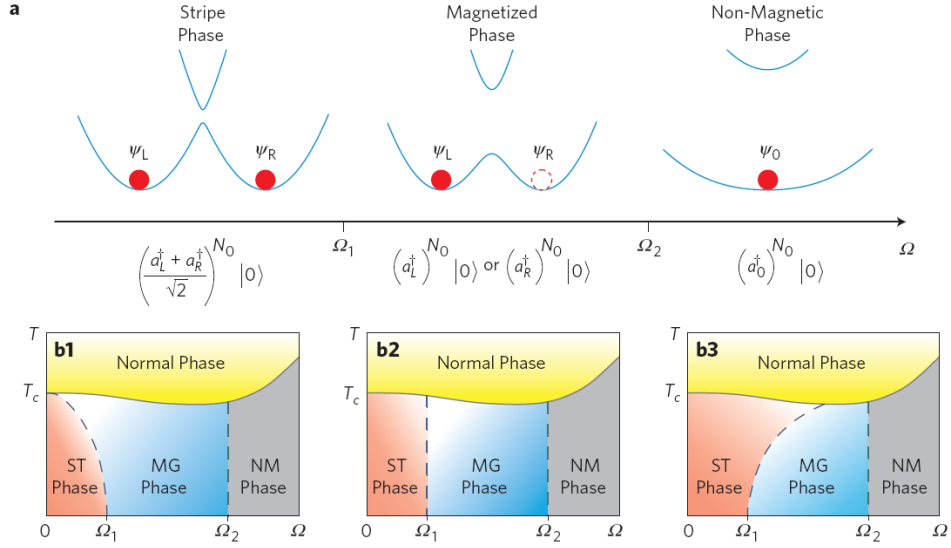


Fig. 2.9. Phase transition diagram of a SO-coupled BEC at finite temperatures. There may be three possible scenarios for the finite-temperature phase transition diagram of a SO-coupled BEC. Experiment can determine (b1) to be the correct diagram based on the measurements of magnetic properties in ST and MG phases. ST: stripe, MG: magnetized, NM: non-magnetic. At zero temperature,  $\Omega_1 \approx 0.2 E_r$  and  $\Omega_2 \approx 4 E_r$  are respectively the Raman coupling for the ST-MG and MG-NM phase transitions. Reproduced from ref. [38].

As shown in Fig. 2.9a, at zero temperature and when  $0.2E_r < \Omega < 4.0E_r$ , the ground state of a SO-coupled BEC is the occupation of either the left or the right well of a double-minima dispersion. Such a phase is called the magnetized phase. Note that occupation of both the minima at the same time is a metastable state described above, not the ground state. As demonstrated in ref. [37], the ground state preparation may only be achieved when the state preparation time is long enough. When the state preparation time is not long enough, metastable states would be achieved. Usually, the state preparation includes a slow ramping process for both  $\Omega$  and  $\delta_R$  followed by a holding time to dissipate the excitations generated during the preparation and to let the system equilibrate. More details about different procedures for state preparation can be found in, for example, ref. [39]. At zero temperature and

when  $\Omega < 0.2 E_r$ , the ground state of a SO-coupled BEC is a superposition of the two dressed spin states (the stripe phase). Thus, the ground states of the stripe and magnetized phases have different magnetic properties.

For a SO-coupled BEC at finite temperatures, there are three possible scenarios for the phase transition diagrams, as shown in Fig. 2.9b1-b3. As demonstrated in ref. [38], the correct phase transition diagram can be experimentally determined to be Fig. 2.9b1 by measuring the distinct magnetic properties of the stripe and magnetic phases.

### 2.3.2 Effects of the excluded $|m_F = +1\rangle$ state

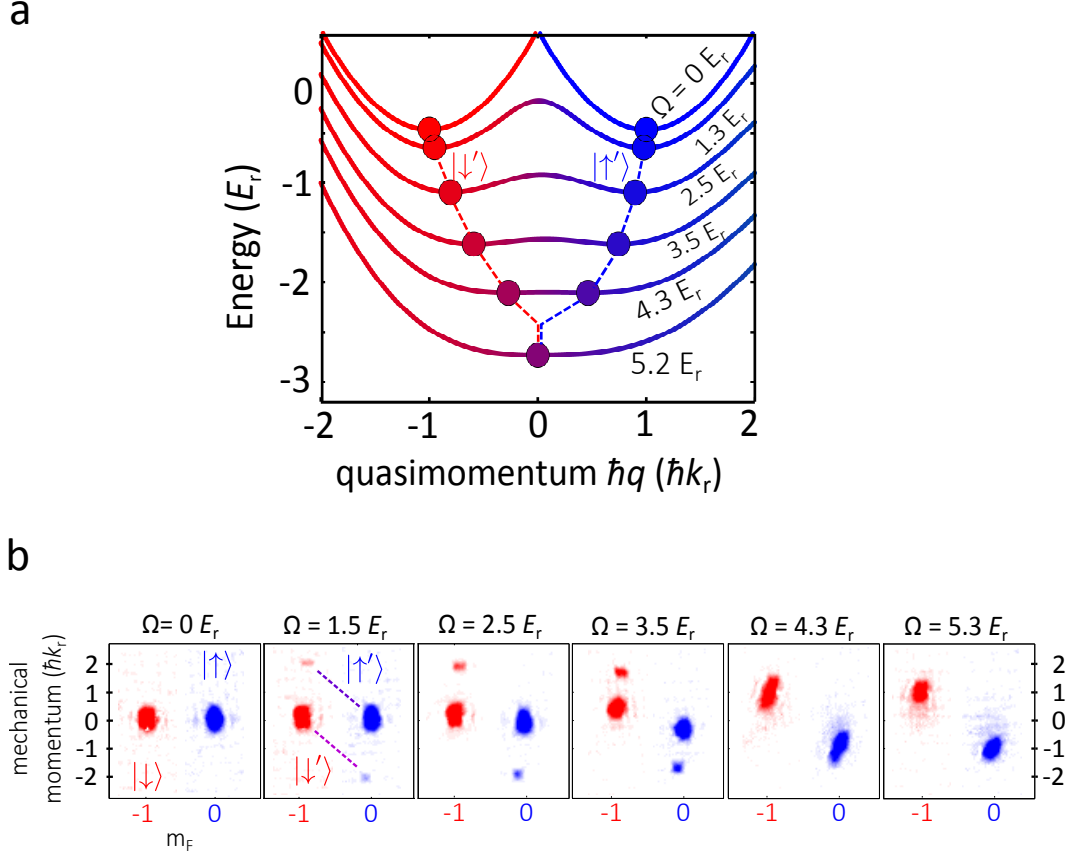


Fig. 2.10. TOF images revealing bare spin and momentum compositions of a dressed BEC at various Raman coupling  $\Omega$  with the corresponding dispersion relations. The double-minima to single-minimum transition observed in our lab occurs around  $\sim 4.7 E_r$  when the quadratic Zeeman shift is  $\hbar\epsilon \sim 0.45 E_r$  (the applied bias magnetic field is  $\sim 5$  gauss).

In our lab, the bias magnetic field is  $\sim 5$  gauss and the corresponding quadratic Zeeman shift is  $\hbar\epsilon \sim 0.45 E_r$ , which is not large enough to completely ignore the effects from the excluded  $|m_F = +1\rangle$  state. Using the full 3-state matrix in Eq. (2.1), we can understand the effects from the excluded state on, e.g. the double-minima to single-minimum transition, which would occur around  $4.7 E_r$  in our case as shown in Fig. 2.10.

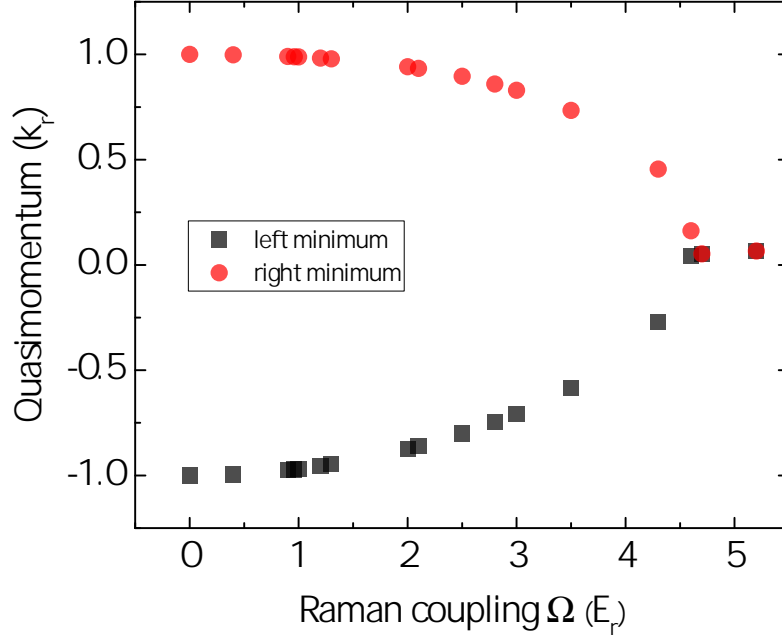


Fig. 2.11. The calculated quasimomentum of the energy minimum/minima (i.e.  $\hbar q_{\sigma \min}$ ) of the SO-coupled dispersion relations at various Raman couplings. The calculated double-minima to single-minimum transition occurs around  $4.7 E_r$  when the quadratic Zeeman shift  $\hbar \epsilon \sim 0.45 E_r$ .

---

The calculated quasimomentum of the energy minimum/minima (i.e.  $\hbar q_{\sigma \min}$ ) of the SO-coupled dispersion relations at various Raman couplings using Eq. (2.1) is shown in Fig. 2.11. The calculated double-minima to single-minimum transition in our case would occur around  $4.7 E_r$ , consistent with our experimental observation in Fig. 2.10.

For a balanced double-minima dispersion, the effects of the excluded state can cause the spin composition of the dressed state in the left well slightly different from that of the dressed state in the right well. The calculated fractional population of the dominant bare spin component of the dressed state in the left or right minimum is shown in Fig. 2.12.

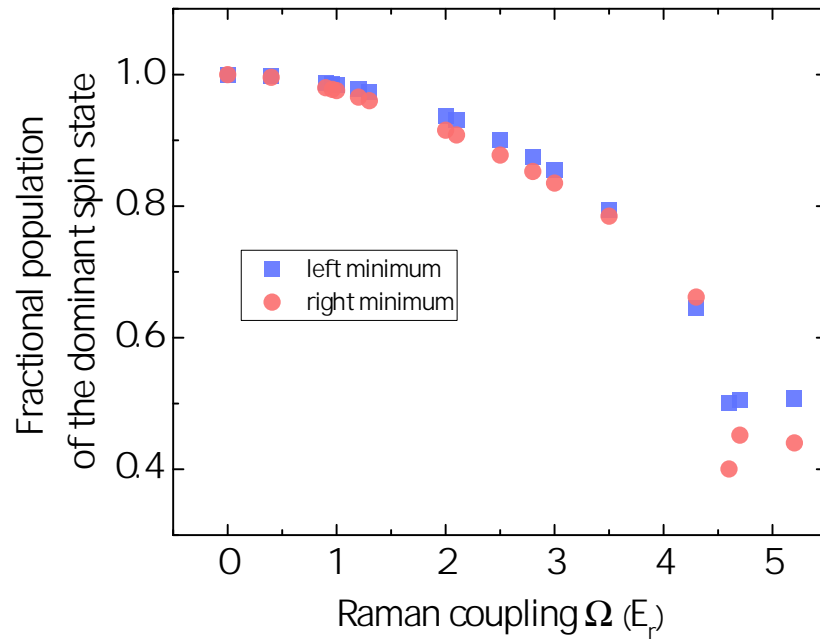


Fig. 2.12. The calculated fractional population of the dominant bare spin component of the dressed state in the left or right minimum.

---

For the 3-state matrix in Eq. (2.8), the calculated Raman detuning  $\delta_R$  that can achieve the balanced double-minima dispersion at the Raman coupling  $\Omega$  is shown in Fig. 2.13.

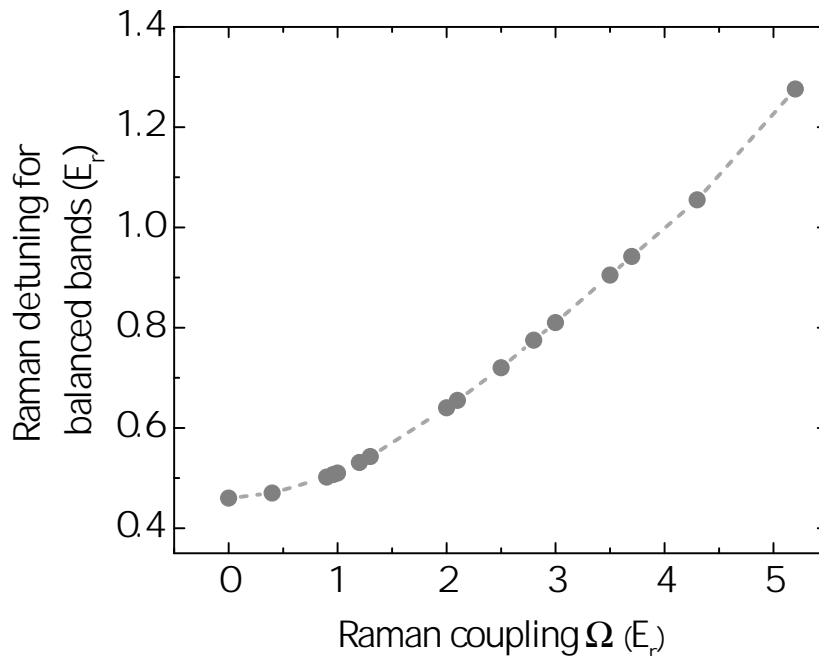


Fig. 2.13. The calculated Raman detuning  $\delta_R$  that can achieve the balanced double-minima dispersion at Raman coupling  $\Omega$  when using the 3-state matrix in Eq. (2.8).

---

## 2.4 Spin-dependent synthetic electric and magnetic fields

Once we can create spin-dependent vector potentials  $A_\sigma$ , we are capable of generating spin-dependent synthetic electric and magnetic fields according to Eqs. (2.6) and (2.7). The spin Hall effect (spin-dependent synthetic magnetic fields) of a quantum gas has been experimentally demonstrated [40]. This is achieved by preparing a BEC at the side of the Gaussian intensity distribution of the Raman lasers such that the Raman coupling  $\Omega$  is spatially varying. Such a technique of generating synthetic magnetic fields is also used in a project that will be introduced in Chapter 5. On the other hand, generation of spin-dependent electric fields is used in a project that will be described in Chapter 3.

In the following, we show our experiment on the generation of spin-dependent synthetic magnetic fields (spin Hall effect) for a BEC, similar to the work in ref. [40]. Fig. 2.14 shows the spin Hall effect of a BEC, which is prepared at the side (gray areas indicated by A and C in the figure) of the Gaussian intensity distribution of the Raman lasers.

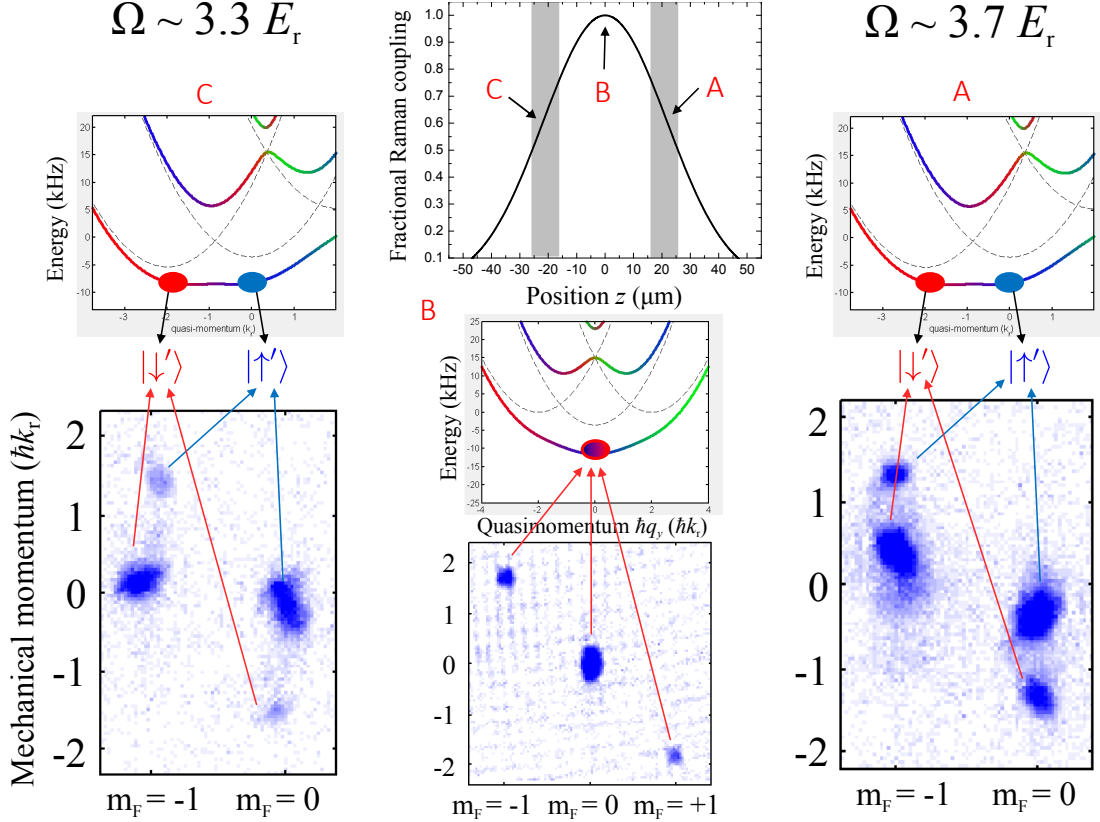


Fig. 2.14. **Spin Hall effect of a BEC.** At the same side of Gaussian intensity distribution, the atomic cloud components of different dressed spin states have opposite tilt angles, reflecting the spin-dependent magnetic fields  $\mathbf{B}_\sigma^*$ . At different sides of the Gaussian intensity distribution, atomic cloud components of the same dressed spin state have opposite tilt angles. The Raman coupling shown in each case refers to the coupling strength at the BEC's center.

In this case, the BEC experiences a  $z$ -dependent Raman coupling  $\Omega(z)$ . The Raman lasers are propagating along  $\hat{y}$ , so the synthetic vector potentials are also along  $\hat{y}$ . Consequently, the synthetic spin-dependent vector potential is a function of  $\Omega(z)$  and  $\delta_R$ ,  $\mathbf{A}_\sigma(\Omega(z), \delta_R) = A_\sigma(z, \delta_R)\hat{y}$ . The synthetic spin-dependent synthetic magnetic field is then  $\mathbf{B}_\sigma^* = \nabla \times \mathbf{A}_\sigma(z) = -(\frac{\partial A_\sigma(z)}{\partial z})\hat{x}$ . In our experiment, a BEC is prepared in a metastable state such that both minima of the dispersions are occupied. As shown in Fig. 2.14, at the same side of the Gaussian intensity distribution, the atomic cloud components of different dressed spin states have opposite tilt angles, reflecting the opposite sign of the spatial dependence of the spin-dependent vector potentials ( $\frac{\partial A_\sigma(z)}{\partial z}$ ) and thus the spin-dependent magnetic fields  $\mathbf{B}_\sigma^*$ . On another hand, at different sides of the Gaussian distribution, the atomic cloud components of the same dressed spin states have opposite tilt angles, reflecting that  $\frac{\partial A_\sigma(z)}{\partial z}$  has an opposite sign for the same dressed spin state  $\sigma$  prepared at opposite sides of the Gaussian intensity distribution.

We can also prepare a dressed spin polarized BEC, that is, either the left minimum or the right minimum of the dispersion is occupied. Fig. 2.15 shows the spin Hall effect of such a dressed spin polarized BEC, similar to Fig. 2.14 except that only one minimum of a double well dispersion is occupied in this case.

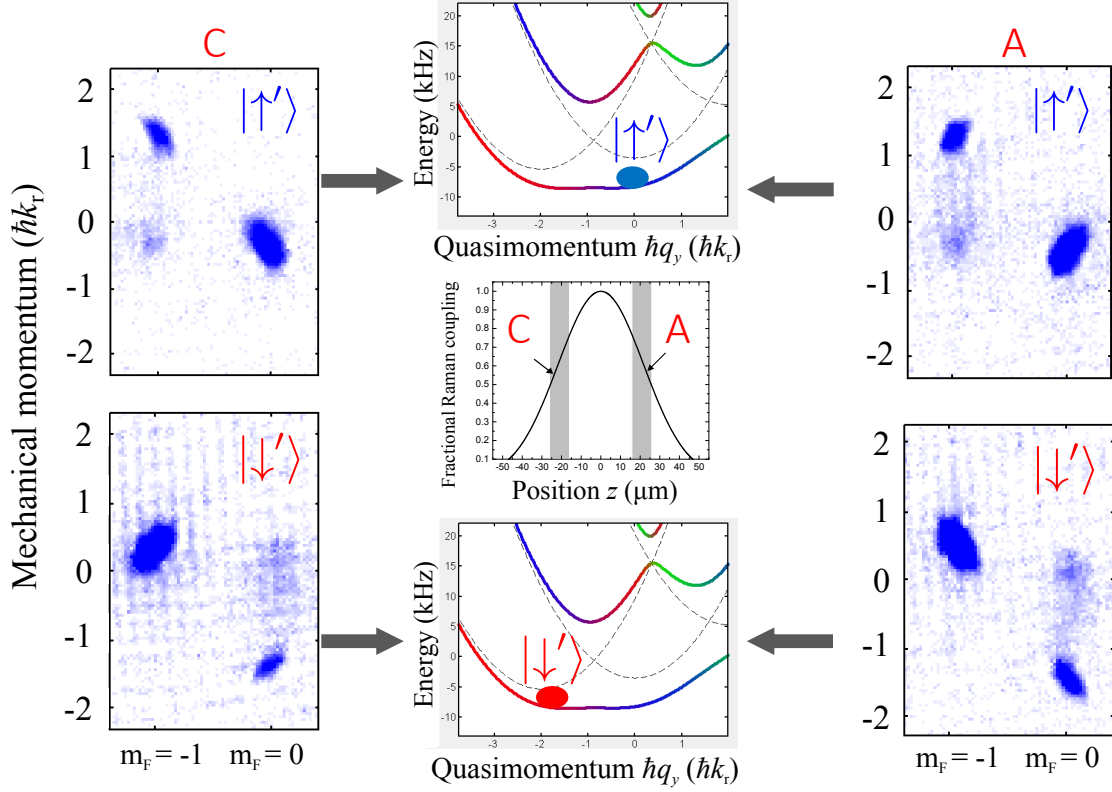


Fig. 2.15. **Spin Hall effect of a BEC.** Similar to Fig. 2.14 except that a dressed spin polarized BEC is used in this case.

In the case of dressed spin polarized BECs, we measure the tilt angle of the BEC whose center position is prepared at various  $z$ . We characterize the spin Hall effect by defining the spin Hall shear coefficient as:

$$S_{yz} = (r - 1/r) \sin(2\theta), \quad (2.9)$$

where  $r = b/a$  is the aspect ratio of the atomic cloud ( $a$  and  $b$  are the lengths along the principal axes) and  $\theta$  is the tilt angle. Both  $r$  and  $\theta$  can be obtained by fitting the TOF images to a rotated ellipse of the form:  $Ay^2 + S_{yz} \frac{yz}{ab} + Bz^2 = 1$ . The measured spin Hall shear coefficient is shown in Fig. 2.16 and is consistent with the observed phenomena shown in Figs. 2.14 and 2.15. In summary, Figs. 2.14, 2.15, 2.16 have demonstrated the spin Hall effect of a BEC.

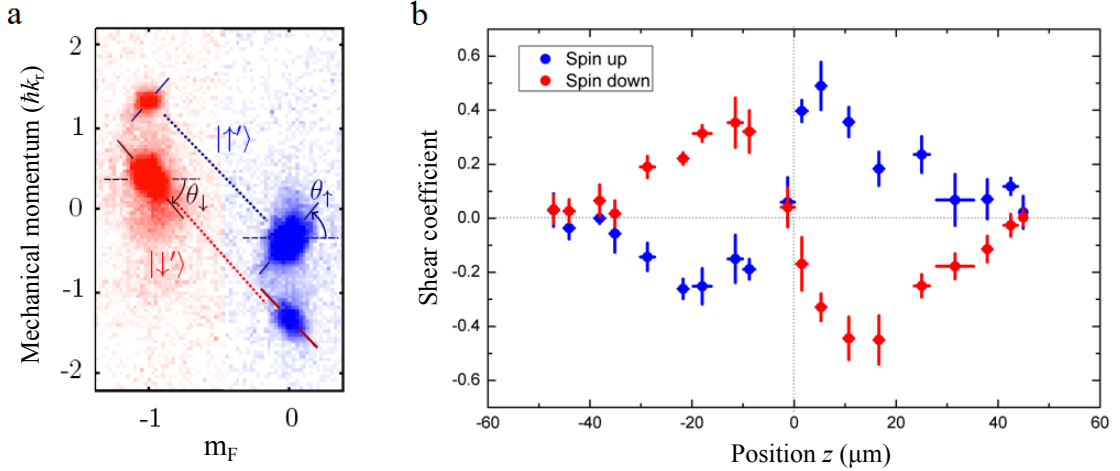


Fig. 2.16. (a) Spin Hall effect of a BEC. At the same side of the Gaussian intensity distribution of the Raman lasers, atomic cloud components from different dressed spin states have opposite tilt angles. (b) Measurement of the spin Hall shear coefficient (see texts) demonstrates the generation of spin-dependent synthetic magnetic fields and the spin Hall effect.

## 2.5 Synthetic spaces and synthetic gauge fields

Previous sections focus on creating synthetic gauge fields in the real space. On the other hand, synthetic gauge fields can also be generated in synthetic spaces, which are capable of lifting many experimental constraints/difficulties (such as manipulating boundary conditions) and thus are flexible and powerful for quantum simulations. The concept of synthetic dimensions and spaces (details can be found in e.g. refs. [41–46] and in recent reviews such as ref. [28]) may be quite general. For instance, multi-dimensional parameter spaces may be regarded as synthetic spaces. A quantum simulated Yang monopole in a high-dimensional parameter space is one example [14]. As another example shown in Fig. 2.17, we use internal spin states (say  $|1\rangle$  and  $|2\rangle$ ) of atoms as discrete sites to construct a “synthetic dimension” (say  $\hat{w}$ ) [41], which along with one real spatial dimension (say  $\hat{y}$ ) comprise a synthetic two-dimensional (2D)

plane ( $w - y$  plane) of a strip geometry. Here, there are no edges in the  $y$  direction, and there are only two sites in the  $w$  direction with a hard-wall potential at the edges (an open boundary condition). Utilizing counter-propagating Raman lasers to Raman couple  $|1\rangle$  and  $|2\rangle$ , an atom at position  $y$  jumping from  $|2\rangle$  to  $|1\rangle$  via a Raman transition would acquire a phase factor  $e^{iKy}$  imprinted by the Raman lasers, where  $\hbar K = 2\hbar k_r$  is the two-photon momentum kick from the Raman transition. Similarly, an atom at position  $y + \Delta y$  jumping from  $|1\rangle$  to  $|2\rangle$  via a Raman transition would acquire a phase factor  $e^{-iK(y+\Delta y)}$ . Therefore, if an atom travels a closed trajectory in the  $w - y$  plane as shown in Fig. 2.17, it acquires a net phase factor  $e^{-iK(\Delta y)}$ , analogous to the Aharonov-Bohm (AB) phase that would be obtained by a charged particle in the presence of a magnetic field. Consequently, there is a corresponding synthetic magnetic flux  $\Phi$  penetrating an area of  $\Delta y$  times one unit length along  $\hat{w}$ .  $\Phi$  is determined by the accumulated phase after the atom completes the closed trajectory, that is,  $\Phi = \frac{\hbar}{q}\Sigma(\text{phase})$ , where  $q$  is the synthetic charge.

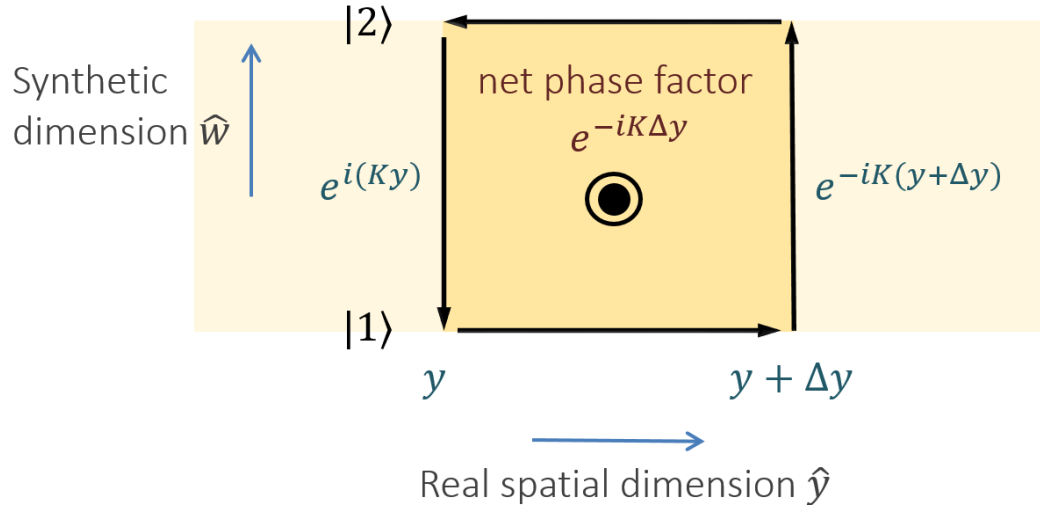


Fig. 2.17. A synthetic 2D plane of a strip geometry subjected to a synthetic magnetic flux. Utilizing counter-propagating Raman lasers to Raman couple internal states ( $|1\rangle$  and  $|2\rangle$ ) of atoms allows for creating synthetic magnetic flux in a synthetic two-dimensional plane composed of a synthetic dimension  $\hat{w}$  and a real spatial dimension  $\hat{y}$ . There are no edges in the  $y$  direction, and there are only two sites in the  $w$  direction with a hard-wall potential at the edges (an open boundary condition). See texts for details.

Fig. 2.17 has illustrated the generation of synthetic magnetic fields in a 2D synthetic plane, composed of a synthetic dimension  $\hat{w}$  and a real spatial dimension  $\hat{y}$ . If an optical lattice is added in the real spatial dimension  $\hat{y}$ , then a Hall strip of lattice (a lattice with a strip geometry penetrated by a synthetic magnetic flux) can be realized as shown in Fig. 2.18. Such a Hall strip of lattice with a hard-wall potential at the edges is an important model to understand the quantum Hall effect and has been implemented experimentally in refs. [47, 48], which report the observation of chiral edge states.

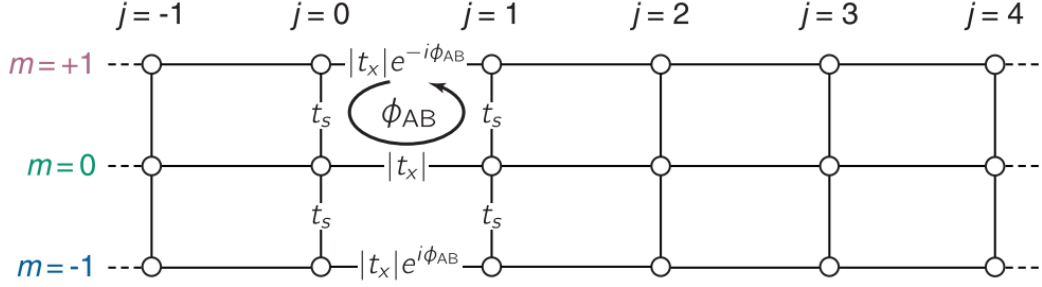


Fig. 2.18. A Hall strip of lattice. A lattice with a strip geometry penetrated by a synthetic magnetic flux is realized using internal spin states ( $m = -1, 0, +1$ ) of atoms as a synthetic dimension and an optical lattice along a real spatial dimension. “ $j$ ” labels different lattice sites in the real spatial dimension.  $t_s$  and  $t_x$  are hopping amplitudes determined by the light couplings. Counter-propagating Raman lasers coupling  $m = -1$  and  $m = 0$ , and  $m = 0$  and  $m = +1$ , allow for generating an Aharonov-Bohm (AB) phase  $\phi_{AB}$  corresponding to a synthetic magnetic flux for atoms. Reproduced from ref. [47].

We can further use synthetic dimensions to realize a “curved” geometry, such as a synthetic circle as shown in Fig. 2.19, by fulfilling a periodic boundary condition in the synthetic dimension. Here, the synthetic circle can be constructed by an atom’s internal spin states (say  $|1\rangle$ ,  $|2\rangle$ ,  $|3\rangle$ ,  $|4\rangle$ , and  $|5\rangle$ ), which can be regarded as discrete sites in a curved synthetic dimension  $\hat{w}$ . Hopping of atoms between different sites is induced by light (e.g. Raman, microwave, or RF couplings). Thus, engineering synthetic spaces offers a flexible approach to explore spaces beyond planar geometries, such as the synthetic circle here and a synthetic cylindrical surface that will be introduced in Chapter 4. We will discuss more details about synthetic spaces and the project of realizing a synthetic Hall cylinder (a synthetic cylindrical surface penetrated by a net synthetic magnetic flux) for a BEC in Chapter 4.

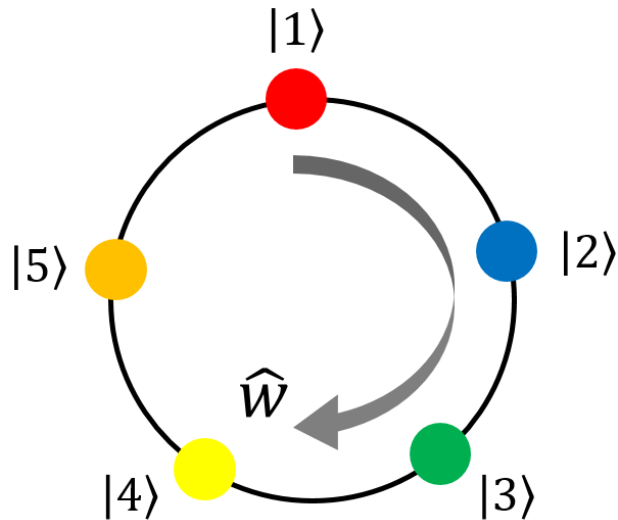


Fig. 2.19. Using internal spin states (labeled as  $|1\rangle$ ,  $|2\rangle$ ,  $|3\rangle$ ,  $|4\rangle$ , and  $|5\rangle$ ) of atoms as discrete sites allows for creating a synthetic circle in a curved synthetic dimension  $\hat{w}$ . Hopping of atoms between different sites is induced by light (e.g. Raman, microwave, or RF couplings).

---

Alternatively, one can use discrete momentum states of an atom as discrete sites to construct a synthetic dimension [43–46] as shown in Fig. 2.20. Here, different mechanical momentum states ( $p$ ) of atoms are coupled by unique pairs of Bragg lasers (far-detuned from excited states  $|e\rangle$ , Fig. 2.20ab) to realize a 1D synthetic lattice (Fig. 2.20c). Since the coupling strength of each pair of Bragg lasers can be individually controlled, hopping amplitudes ( $t_{-2,-1,0,1,2}$  in Fig. 2.20c) between different sites can be individually controlled. In addition, since the phase acquired by an atom from each pair of Bragg lasers can be individually controlled, the acquired phase ( $\varphi_{-2,-1,0,1,2}$  in Fig. 2.20c) associated with each hopping can also be individually controlled.

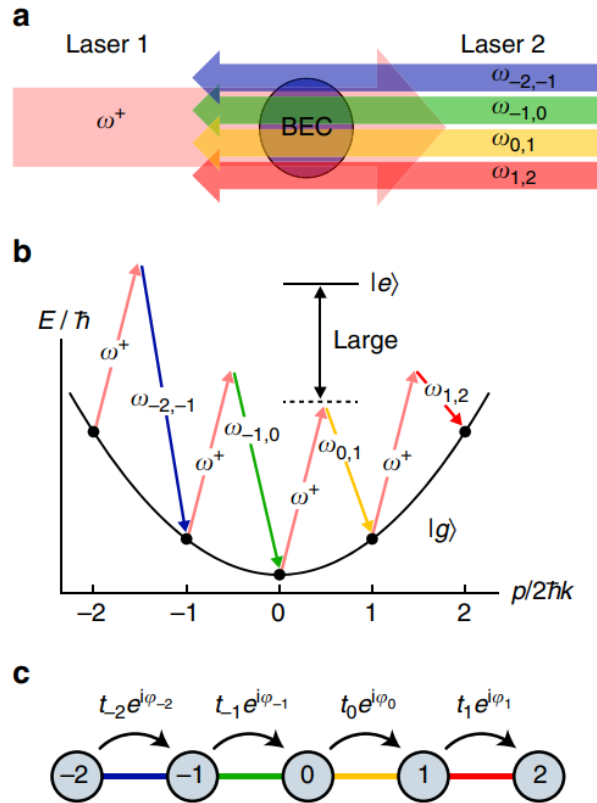


Fig. 2.20. A 1D synthetic lattice is constructed using an atom's different mechanical momentum states coupled by unique pairs of Bragg lasers. (a) Counter-propagating Bragg lasers are used to couple unique pairs of mechanical momentum states ( $p$ ) of atoms as shown in (b) to realize a 1D synthetic lattice shown in (c). Each hopping amplitude ( $t_{-2,-1,0,1}$ ) and the associated phase ( $\varphi_{-2,-1,0,1}$ ) can be individually controlled. See texts for details. Reproduced from ref. [45].

Besides, periodically modulating parameters in a system's Hamiltonian also allows for generating synthetic dimensions and has been used to build a 4D quantum Hall system [49]. Many other approaches are proposed or used for constructing synthetic spaces but are beyond the scope of this section.

### 3. SPIN CURRENT GENERATION AND RELAXATION IN A QUENCHED SPIN-ORBIT-COUPLED BOSE-EINSTEIN CONDENSATE

The work presented in this chapter has been published in Nature Communications 10, 375 (2019) [50].

In the following sections, the main results of each section will be presented first to help the reader grasp the main messages. Then, the relevant details will be introduced in subsections of each section.

#### 3.1 Introduction and motivation

Understanding the effects of spin-orbit coupling (SOC) and many-body interactions on spin transport is important in condensed matter physics and spintronics. This topic has been intensively studied for spin carriers such as electrons but barely explored for charge-neutral bosonic quasiparticles (including their condensates), which hold promises for coherent spin transport over macroscopic distances. Here, we explore the effects of synthetic SOC (induced by optical Raman coupling) and atomic interactions on the spin transport in an atomic Bose-Einstein condensate (BEC), where the spin-dipole mode (SDM, actuated by quenching the Raman coupling) of two interacting spin components constitutes an alternating spin current. We experimentally observe that SOC significantly enhances the SDM damping while reducing the thermalization (the reduction of the condensate fraction). We also observe generation of BEC collective excitations such as shape oscillations. Our theory reveals that the SOC-modified interference, immiscibility, and interaction between the spin components can play crucial roles in spin transport.

Spin, an internal quantum degree of freedom of particles, is central to many condensed matter phenomena such as topological insulators and superconductors [51, 52] and technological applications such as spintronics [53] and spin-based quantum computation [54].

In spintronics, electrons are usually the carriers for spin currents. Recently, using charge-neutral bosonic quasiparticles (such as exciton-polaritons and magnons) or their condensates [55–57] as spin carriers for spin transport in solids have attracted great interest because of several promising features. For example, spin (current) relaxation (which causes loss of spin information) can be reduced because charge neutrality avoids the Coulomb interaction and bosons can in principle possess a small momentum distribution. Amplifying a bosonic spin current is even possible thanks to the bosonic nature. Using neutral bosonic quasiparticles or their condensates (quantum fluids) thus opens a door to propagate and manipulate spin information over macroscopic distances with the potential of utilizing quantum coherent effects. Such bosonic spin currents have been generated experimentally, for example, using exciton-polaritons [58] and excitons [59] in semiconductors and magnons [60, 61] in a magnetic insulator.

Precise control of spin currents is crucial to information transfer and storage in spin-based devices, in which spin-orbit coupling (SOC) and many-body interactions are key factors for spin current manipulations. SOC, the interaction between a particle’s spin and its momentum, can play a particularly crucial role. On one hand, SOC may provide a mechanism (such as spin Hall effect) to control the spin. On the other hand, SOC can also cause spin current relaxation, leading to loss of spin information. Understanding the effects of SOC and many-body interactions on spin relaxation is thus of great interest and importance but also challenging due to the complications from the disorder/impurity and the lack of experimental tunability in solid state systems. This topic has been intensively studied for electrons, but barely explored in bosonic quasiparticles or their quantum fluids.

Cold atomic gases provide a clean and highly-controllable [16] platform for simulating and exploring many condensed matter phenomena [15, 16, 26, 62, 63]. For example, the generation of synthetic electric [35] and magnetic [36] fields allows neutral atoms to behave like charged particles. The synthetic magnetic and spin-dependent magnetic fields have been realized to demonstrate respectively the superfluid Hall [64] and spin Hall effects [40] in BECs. The creation of synthetic SOC in bosonic [37, 65–70] and fermionic [71–74] atoms further paves the way to explore diverse phenomena such as topological states [27] and exotic condensates and superfluids [63, 75–79]. Here, we study the effects of one-dimensional (1D) synthetic SOC on the spin relaxation in a disorder-free atomic BEC using a condensate collider, in which the spin-dipole mode (SDM) [80] of two BECs of different (pseudo) spin states constitute an alternating (AC) spin current. The SDM is initiated by applying a spin-dependent synthetic electric field to the BEC via quenching the Raman coupling that generates the spin-orbit-coupled (SO-coupled) band structure. Similar quantum gas collider systems (without SOC [81–85]) have been used to study physics that are difficult to access in other systems.

Charge or mass currents are typically unaffected by interactions between particles because the currents are associated with the total momentum that is unaffected by interactions. In contrast, spin currents can be intrinsically damped due to the friction resulting from the interactions between different spin components. In electronic systems, such a friction has been referred to as the spin Coulomb drag [86, 87]. In atomic systems, previous studies have shown that a similar spin drag [88, 89] also exists. Even in the absence of SOC, the relaxation of spin currents can be nontrivial due to, for example, interactions [80, 83, 90–93] and quantum statistical effects [89, 94]. In one previous experiment [40], bosonic spin currents have been generated in a SO-coupled BEC using the spin Hall effect. However, how the spin currents may relax in the presence of SOC and interactions has not been explored. Here, we observe that SOC can significantly enhance the relaxation of a coherent spin current in a BEC while reducing the thermalization during our experiment. Moreover, our theory, consistent

with the observations, discloses that the interference, immiscibility, and interaction between the two colliding spin components can be notably modified by SOC and play an important role in spin transport. Our study may contribute to the fundamental understanding of spin transport as well as quenched many-body dynamics in SO-coupled bosonic quantum fluids.

### 3.2 Experimental setup and timing diagram

In our experiments, we create 3D  $^{87}\text{Rb}$  BECs in the  $F = 1$  hyperfine state in an optical dipole trap with condensate fraction  $f_c > 0.6$  containing condensate atom number  $N_c \sim 1 - 2 \times 10^4$ . As shown in Fig. 3.1a, counter-propagating Raman lasers with an angular frequency difference  $\Delta\omega_R$  couple bare spin and momentum states  $|\downarrow, \hbar(q_y + k_r)\rangle$  and  $|\uparrow, \hbar(q_y - k_r)\rangle$  to create synthetic 1D SOC (so called equal Rashba-Dresselhaus SOC) along  $\hat{y}$  [67], where the bare spin states  $|\downarrow\rangle = |m_F = -1\rangle$  and  $|\uparrow\rangle = |m_F = 0\rangle$  are Zeeman split by  $\hbar\omega_Z \approx \hbar\Delta\omega_R$  using a bias magnetic field  $\mathbf{B} = B\hat{z}$ . Here,  $\hbar k_\downarrow = \hbar(q_y + k_r)$  ( $\hbar k_\uparrow = \hbar(q_y - k_r)$ ) is the mechanical momentum in the  $y$  direction of the bare spin component  $|\downarrow\rangle$  ( $|\uparrow\rangle$ ), where  $\hbar q_y$  is the quasimomentum. The photon recoil momentum  $\hbar k_r = 2\pi\hbar/\lambda$  and recoil energy  $E_r = \hbar^2 k_r^2 / (2m)$  are set by the Raman laser at the magic wavelength  $\lambda \sim 790$  nm [95], where  $\hbar$  is the reduced Planck constant and  $m$  is the atomic mass of  $^{87}\text{Rb}$ . The  $|m_F = +1\rangle$  state can be neglected in a first-order approximation due to the quadratic Zeeman shift (see subsections below). The single-particle SOC Hamiltonian,  $H_{\text{SOC}}$ , can be written in the basis of bare spin and momentum states  $\{|\downarrow, \hbar(q_y + k_r)\rangle, |\uparrow, \hbar(q_y - k_r)\rangle\}$  as [37]:

$$H_{\text{SOC}} = \begin{pmatrix} \frac{\hbar^2}{2m}(q_y + k_r)^2 - \delta_R & \frac{\Omega}{2} \\ \frac{\Omega}{2} & \frac{\hbar^2}{2m}(q_y - k_r)^2 \end{pmatrix} \quad (3.1)$$

where  $\Omega$  is the Raman coupling (tunable by the Raman laser intensity),  $\delta_R = \hbar(\Delta\omega_R - \omega_Z)$  is the Raman detuning (tunable by  $B$ ) and is zero in our main measurements (see subsections below). A dressed state is an eigenstate of Eq. (3.1), labeled by  $q_y$ , and is a superposition of bare spin and momentum states. The  $q_y$ -dependent eigenvalues of

(3.1) define the ground and excited energy bands. When  $\Omega$  is below a critical  $\Omega_c$ , the ground band exhibits double wells, which we associate with the dressed spin up  $|\uparrow\rangle$  and down  $|\downarrow\rangle$  states. The double minima at quasimomentum  $\hbar q_{\sigma \min}$  can be identified with the light-induced spin-dependent vector potentials  $\mathbf{A}_\sigma = A_\sigma \hat{y}$  (controllable by  $\Omega$ ), where  $\sigma$  labels  $|\uparrow\rangle$  or  $|\downarrow\rangle$  [40] (see subsections below). The double minima merge into a single minimum as  $\Omega$  increases beyond  $\Omega_c$ , as shown in the dashed line trajectories in Fig. 3.1c.

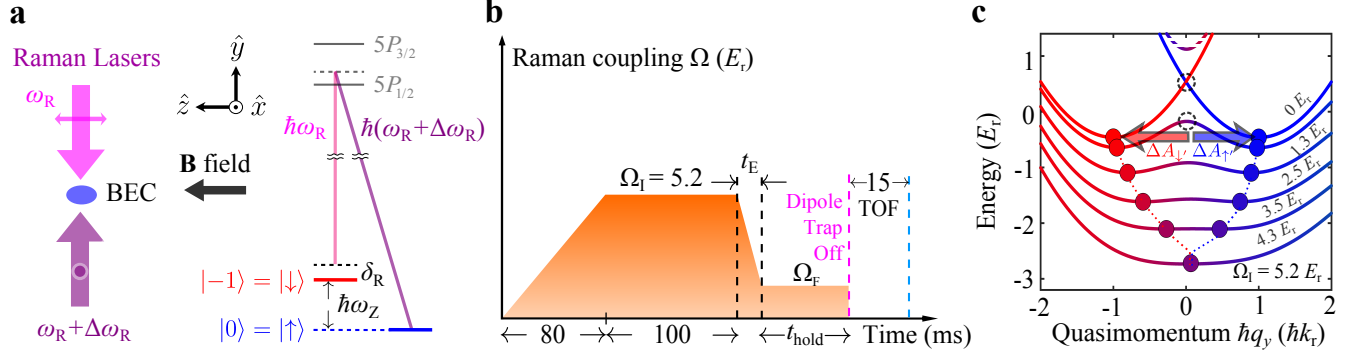


**Fig. 3.1. Experimental setup and timing diagram used for the spin-dipole mode (SDM) experiments.** (a) Linearly-polarized Raman beams with orthogonal polarizations (indicated by the double-headed arrows along  $\hat{z}$  and  $\hat{x}$ ) counter-propagating along  $\hat{y}$  couple  $m_F$  hyperfine sublevels (bare spin states) of  $^{87}\text{Rb}$  atoms. The sublevels are Zeeman split by  $\hbar\omega_Z \approx \hbar\Delta\omega_R = h \times (3.5 \text{ MHz})$  using a bias magnetic field  $\mathbf{B} = B\hat{z}$ , which controls the Raman detuning  $\delta_R = \hbar(\Delta\omega_R - \omega_Z)$ . (b) Experimental timing diagram: Raman coupling  $\Omega$  (with an experimental uncertainty of  $< 10\%$ ) is slowly ramped up in 80 ms to an initial value  $\Omega_I$  and held for 100 ms to prepare the BEC around the single minimum of the ground band at  $\Omega_I$  as shown in (c). Then,  $\Omega$  is quickly lowered to a final coupling  $\Omega_F$  in time  $t_E$  and held for some time  $t_{\text{hold}}$ , during which we study the dynamics of the BEC in the dipole trap. Subsequently, the atoms are released for absorption imaging after a 15 ms time of flight (TOF), at the beginning of which a Stern-Gerlach process is performed for 9 ms to separate atoms of different bare spin states. (c) The ground band (solid lines) of synthetic SOC is calculated for a few representative  $\Omega$  at  $\delta_R = 0$ . A higher band calculated for  $\Omega = 1.3 E_r$  is shown as dashed lines. The colors indicate the spin compositions, with red for  $|\downarrow\rangle$  and blue for  $|\uparrow\rangle$ . The ground band minima in quasimomentum marked by dots are identified with spin-dependent vector potentials ( $A_\sigma$ ), which shift in opposite directions as  $\Omega$  is lowered into the double minima regime during  $t_E$ . This generates spin-dependent synthetic electric fields  $E_\sigma$  and thus excites the SDM and an AC spin current along the SOC direction in a trapped BEC. The upper (lower) dashed circle represents the region around  $q_y = 0$  in the double minima band at an exemplary  $\Omega_F = 0$  ( $\Omega_F = 1.3 E_r$ ), from which the two (dressed) spin components of the BEC roll down towards the corresponding band minima in response to the application of  $E_\sigma$ .

We prepare a BEC around the single minimum of the ground dressed band at  $\Omega_I$  ( $= 5.2 E_r$  for this work) and  $\delta_R = 0$  by ramping on  $\Omega$  slowly in 80 ms and holding it for

100 ms (Fig. 3.1b, c, see subsections below for details). Then, we quickly lower  $\Omega$  from  $\Omega_I$  to a final value  $\Omega_F$  into the double minima regime in time  $t_E$ . The  $t_E = 1$  ms used in this work is slow enough to avoid higher band excitations but is fast compared to the trap frequencies. The dotted lines in Fig. 3.1c trace the opposite trajectories of  $A_{\uparrow'}$  and  $A_{\downarrow'}$  during  $t_E$ . This quench process drives the system across the single minimum to double minima phase transition and generates spin-dependent synthetic electric fields  $\mathbf{E}_\sigma = E_\sigma \hat{y} = -(\partial A_\sigma / \partial t) \hat{y} \approx -(\Delta A_\sigma / t_E) \hat{y}$ . Consequently, atoms in different dressed spin components move off in opposite directions from the trap center (or from the region around  $q_y = 0$  in the quasimomentum space as shown in Fig. 3.1c as dashed circles for two representative  $\Omega_F = 0, 1.3 E_r$ ) and then undergo out-of-phase oscillations, thus exciting the SDM and an AC spin current. Approximately equal populations in the two dressed (or bare) spin components are maintained by keeping  $\delta_R = 0$  as  $\Omega$  is changed from  $\Omega_I$  to  $\Omega_F$  (see subsections below). After the application of  $E_\sigma$ , the Raman coupling is maintained at  $\Omega_F$  during the hold time ( $t_{\text{hold}}$ ). We then abruptly turn off both the Raman lasers and the dipole trap for time of flight (TOF) absorption imaging, measuring the bare spin and momentum composition of the atoms (Fig. 3.1b). Experiments are performed at various  $t_{\text{hold}}$  to map out the time evolution in the trap.

### 3.2.1 Theoretical and experimental backgrounds

Before the experimental results are presented, relevant theoretical and experimental backgrounds are introduced in detail as follows.

#### Spin vector potentials

In Eq. (3.1), the eigenenergies at  $\delta_R = 0$  are given by:

$$E_\pm(q_y) = \frac{\hbar^2 q_y^2}{2m} + E_r \pm \sqrt{\left(\frac{\Omega}{2}\right)^2 + \left(\frac{\hbar^2 k_r q_y}{m}\right)^2} \quad (3.2)$$

For  $\Omega < \Omega_c$ , the ground band of the energy-quasimomentum dispersion has two minima at:

$$q_{\sigma \min}(\Omega) = \pm k_r \sqrt{1 - (\Omega/\Omega_c)^2} \quad (3.3)$$

The state of the atoms associated with each minimum at  $q_{\sigma \min}$  can be regarded as a dressed spin state. For a double minima band structure, we thus have two dressed spin components  $\sigma = |\downarrow'\rangle$  and  $|\uparrow'\rangle$  that constitute a pseudo spin-1/2 system (when  $\Omega = 0$ ,  $|\uparrow'\rangle$  and  $|\downarrow'\rangle$  become the bare spin  $|\uparrow\rangle$  and  $|\downarrow\rangle$ , respectively). The energy spectrum expanded around each  $q_{\sigma \min}$  as  $E(q_y) = \hbar^2(q_y - q_{\sigma \min})^2/(2m^*)$  is analogous to the Hamiltonian describing a charged particle with charge  $Q$  in a magnetic vector potential  $A$ ,  $\hat{H} = (\hat{p}_y - QA)^2/(2m_Q)$ , where  $m^*$  is the effective mass of a dressed atom and  $m_Q$  is the mass of the charged particle. Therefore, we can identify the quasimomentum ( $\hbar q_y$ ) with the canonical momentum ( $\hat{p}_y = -i\hbar \frac{\partial}{\partial y}$ ), and  $\hbar q_{\sigma \min}$  with the light-induced spin-dependent vector potentials ( $A_\sigma$ , by setting  $Q = 1$  for our case [40]). The velocity operator corresponding to the mechanical momentum,  $\hat{v}_y = -[\hat{H}, y]/(i\hbar) = (\hat{p}_y - QA)/m_Q$ , thus corresponds to  $\hbar(q_y - q_{\sigma \min})/m^*$ . These spin-dependent vector potentials  $A_\sigma$  (represented by  $\hbar q_{\sigma \min}$ ) are tunable by  $\Omega$ . For example, as seen in Fig. 3.1c, we can decrease  $\Omega$  to separate the two  $\hbar q_{\sigma \min}$  or increase  $\Omega$  to combine them in the quasimomentum space.

### Effects of the neglected $|m_F = +1\rangle$ state

We apply an external bias magnetic field  $\mathbf{B} = B\hat{z}$  ( $\sim 5$  gauss) to Zeeman split the energies  $E_{-1}$ ,  $E_0$ , and  $E_{+1}$  of the  $|m_F = -1\rangle$ ,  $|m_F = 0\rangle$ , and  $|m_F = +1\rangle$  sublevels respectively (in the  $F = 1$  hyperfine state of  $^{87}\text{Rb}$  atoms), where  $E_{-1} - E_0 = \hbar\omega_Z$ ,  $E_0 - E_{+1} = \hbar\omega_Z - 2\varepsilon$ ,  $\hbar$  is the reduced Planck constant and  $\varepsilon = (E_{-1} + E_{+1})/2 - E_0$  is the quadratic Zeeman shift. The frequency difference between the two Raman lasers is  $\Delta\omega_R/(2\pi) = 3.5$  MHz. The Raman detuning  $\delta_R = \hbar(\Delta\omega_R - \omega_Z)$  is controlled by  $B$  that controls  $\hbar\omega_Z$ . In a first-order approximation, the third state  $|m_F = +1, \hbar k = \hbar(q_y - 3k_r)\rangle$  can be excluded in Eq. (3.1) due to the quadratic Zee-

man shift ( $2\varepsilon \sim 0.9 E_r$ ) from  $B$  but can be included in the following three-state Hamiltonian:

$$H_3 = \begin{pmatrix} \frac{\hbar^2}{2m}(q_y + k_r)^2 - \delta_R & \frac{\Omega}{2} & 0 \\ \frac{\Omega}{2} & \frac{\hbar^2}{2m}(q_y - k_r)^2 & \frac{\Omega}{2} \\ 0 & \frac{\Omega}{2} & \frac{\hbar^2}{2m}(q_y - 3k_r)^2 + \delta_R + 2\varepsilon \end{pmatrix} \quad (3.4)$$

In our SDM experiments, we always maintain approximately equal spin populations in the  $|\downarrow\rangle = |m_F = -1\rangle$  and  $|\uparrow\rangle = |m_F = 0\rangle$  states both in the initial dressed state prepared at  $\Omega_I$  and in the final dressed state at  $\Omega_F$  (with approximately equal populations also achieved in  $|\downarrow'\rangle$  and  $|\uparrow'\rangle$  at  $\Omega_F$ ). In Eq. (3.1) based on the two-state picture,  $\delta_R = 0$  can give rise to such balanced (dressed/bare) spin populations at any given  $\Omega$ . However, in Eq. (3.4) with  $\delta_R = 0$ , a finite  $\Omega$  can lead to unbalanced (dressed/bare) spin populations. Therefore, in our experiment  $\delta_R$  at a given  $\Omega$  has to be changed to  $\delta'(\Omega, \varepsilon)$  to achieve the balanced spin populations (note that in the double minima regime of Eq. (3.4), this requirement is in a good approximation equivalent to the so-called balanced band condition where the two minima in the ground dressed band have equal energy). Such an effect is addressed in details in ref. [37]. In our case, also note that including the third state in Eq. (3.4) would cause the actual transition from the double minima to single minimum to occur at  $\Omega_c \sim 4.7 E_r$  rather than at  $\Omega_c = 4.0 E_r$  as would be predicted by Eq. (3.1). Additionally, Eq. (3.4) is used for plotting Fig. 3.1c and Fig. 3.3g, h, which more precisely means  $\delta_R = \delta'(\Omega, \varepsilon)$  to achieve the balanced spin populations for the corresponding  $\Omega$ . In the following, we use Eq. (3.4) to describe the initial state preparation process.

### Initial state preparation, spin population balance, and imaging process

We create spin-polarized  $^{87}\text{Rb}$  BECs in  $|m_F = 0\rangle$  in an optical dipole trap consisting of three cross laser beams (with a third beam added to the double beam dipole trap described in ref. [9]). To prepare the initial state of the BEC at the single

minimum of the ground dressed band at  $\Omega_I = 5.2 E_r$  (at  $\delta_R = \delta'(\Omega_I, \varepsilon)$ , shown in Fig. 3.1c), first the Raman coupling  $\Omega$  is ramped on slowly from 0 to  $\Omega_I$  in 80 ms (slow enough compared to the trap period and any inter-band excitation process) with  $\delta_R \sim -\varepsilon$  in Eq. (3.4), such that the dominant bare spin component of the dressed BEC at any finite  $\Omega$  during the ramping process remains in  $|m_F = 0\rangle$ . Subsequently, while holding  $\Omega$  at  $\Omega_I$ , we adjust  $B$  to change the Raman detuning from  $\delta_R \sim -\varepsilon$  to  $\delta_R = \delta'(\Omega_I, \varepsilon)$  in 80 ms, and then we hold both  $\Omega$  and  $\delta_R$  for another 20 ms to let the system equilibrate. Note that adjusting  $\delta_R$  to  $\delta'(\Omega_I, \varepsilon)$  has to be empirically achieved by realizing the balanced spin populations, with the reasons addressed in the next paragraph. When the BEC is successfully prepared in the initial state at  $\Omega_I$ , equal populations in the  $|m_F = -1, +\hbar k_r\rangle$  and  $|m_F = 0, -\hbar k_r\rangle$  states can be achieved and seen in TOF images measured at  $t_{\text{hold}} = -1$  ms.

In addition to the change in the band structure when going from the two-state picture to the three-state picture as discussed in the previous section, there are several other experimental factors that can lead to unbalanced spin populations. First, the slow drift in  $\Omega$  can tilt (therefore unbalance) the band at a fixed  $\delta_R$ . Second, a slow drift in  $B$  would give rise to a drift in  $\delta_R$ . Third, sometimes there may still be excitations (for example, small-amplitude collective dipole oscillations of a dressed BEC) at the end of the initial state preparation [39], making the quasimomentum of the dressed BEC deviate slightly from the quasimomentum of the band minimum. As a result, the dressed BEC can have a nonzero group velocity and unbalanced spin populations at  $\Omega_I$  (before applying the spin-dependent electric fields  $E_\sigma$ ). Hence, this can lead to unbalanced spin populations after the application of  $E_\sigma$ , and the spin polarization  $P$  of atoms is not maintained around zero during  $t_{\text{hold}}$ . Here, we define  $P = (N^\uparrow - N^\downarrow)/(N^\uparrow + N^\downarrow)$ , where  $N^{\uparrow(\downarrow)}$  is the total atom number of the atomic cloud (measured in the TOF images) for the bare spin component  $\uparrow(\downarrow)$ . Fourth, the quench process from the single minimum to double minima bands during  $t_E$  (Fig. 3.1c) may also give rise to unbalanced spin populations, presumably because of the access to the magnetic phase in the double minima regime where the ground state is the occupation

of a single dressed spin state (the two occupied dressed spin states are metastable states).

The above effects are avoided in our experiments by making sure that the balanced spin populations are empirically achieved throughout our experiment (with occasional adjustment of  $\delta_R$ , and discarding runs with notably unbalanced spin populations). More specifically, we first make sure that balanced spin populations can be achieved at  $\Omega_I$ , assuring  $\delta_R = \delta'(\Omega_I, \varepsilon)$  after the initial preparation described above. Then, we linearly ramp  $\delta_R$  from  $\delta'(\Omega_I, \varepsilon)$  to  $\delta'(\Omega_F, \varepsilon)$  as we change  $\Omega$  from  $\Omega_I$  to  $\Omega_F$  in  $t_E$ , and subsequently hold  $\delta_R$  at  $\delta'(\Omega_F, \varepsilon)$  for various  $t_{\text{hold}}$ . Here,  $\delta_R = \delta'(\Omega_F, \varepsilon)$  is empirically achieved by realizing balanced spin populations at  $\Omega = \Omega_F$  for various  $t_{\text{hold}}$ . Therefore, when we state  $\delta_R = 0$  at a given  $\Omega$ , it more precisely means that we realize balanced spin populations (as would be achieved at  $\delta_R = 0$  in the 2-state picture described by Eq. (3.1)).

The above-mentioned procedure of realizing  $\delta_R = \delta'(\Omega_F, \varepsilon)$  is further experimentally verified by observing balanced spin populations using the same bias magnetic fields but with  $t_E = 15$  ms and  $t_{\text{hold}} = 30$  ms (slow enough to not to excite notable SDM). This suggests that such a choice of  $\delta_R = \delta'(\Omega_F, \varepsilon)$  approximates a balanced double minima band (with two equal-energy minima) at  $\Omega_F$ .

For the SDM measurements (e.g., Fig. 3.3), we make sure that the typical spin polarization is close to zero, with  $|P| = 0.05 \pm 0.04$ , where 0.05 is the mean and 0.04 is the standard deviation of the data. Note that we used the total atom numbers  $N^{\uparrow(\downarrow)}$  instead of condensate atom numbers  $N_c^{\uparrow(\downarrow)}$  to obtain  $P$  due to the less fluctuation in the fitted  $N^{\uparrow(\downarrow)}$ . Typically images with such small  $P$ , indicating good spin population balance for the whole atomic cloud, also do not exhibit notable spin population imbalance in their condensate parts.

After holding the atoms in the trap at  $\Omega_F$  for various  $t_{\text{hold}}$ , we turn off all lasers abruptly and do a 15-ms TOF, which includes a 9-ms Stern-Gerlach process in the beginning to separate the atoms of different bare spin states. Then, the absorption imaging is performed at the end of TOF to obtain the bare spin and momentum

compositions of atoms. We then extract the physical quantities such as the mechanical momentum, condensate and thermal atom numbers of the atomic cloud in each spin state from such TOF images.

### 3.3 Measurements of the spin-dipole mode (SDM) and its damping

Fig. 3.2 presents SDM measurements for a bare BEC (at  $\Omega_F = 0$ ) and a dressed (or SO-coupled) BEC (at  $\Omega_F = 1.3 E_r$ ), with select TOF images taken after representative  $t_{\text{hold}}$  in the trap. Two TOF images labeled by  $t_{\text{hold}} = -1$  ms are taken right before the application of  $E_\sigma$ . In the bare case (Fig. 3.2a), the images taken at increasing  $t_{\text{hold}}$  show several cycles of relative oscillations (SDM) between the two spin components in the momentum space, accompanied by a notable reduction in the BEC fraction.

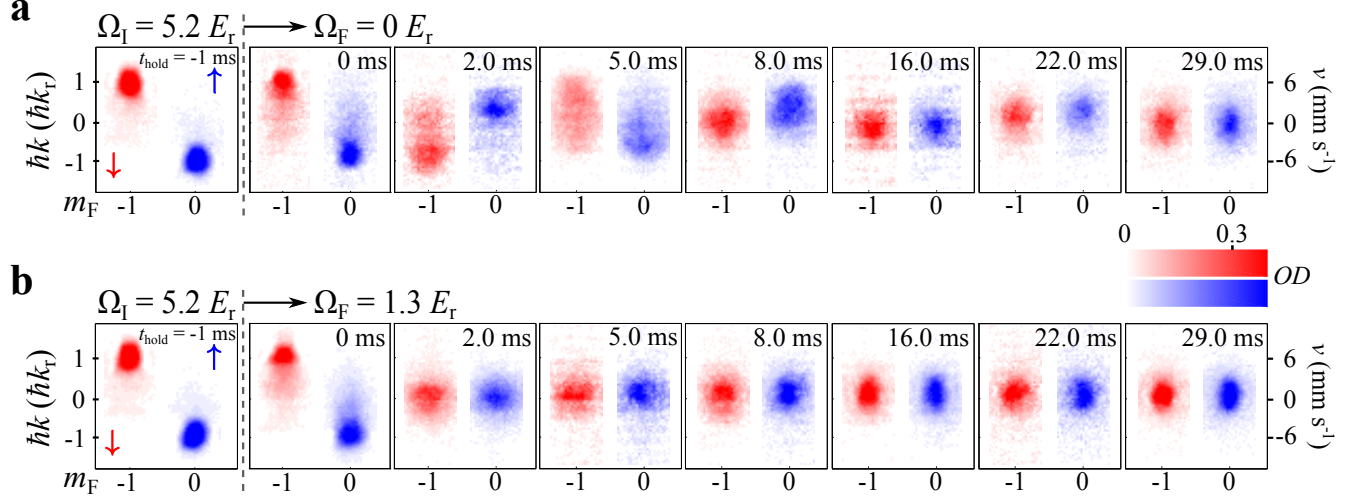


Fig. 3.2. **SDM of a bare or a dressed BEC.** Select TOF images showing the bare spin and momentum compositions of atoms taken after applying spin-dependent synthetic electric fields  $E_\sigma$  with  $\Omega_F = 0$  (bare BEC) in (a) and  $\Omega_F = 1.3 E_r$  (SO-coupled BEC) in (b), followed by various hold times ( $t_{\text{hold}}$ ) in the dipole trap. The TOF images labeled by  $t_{\text{hold}} = -1$  ms are taken right before the application of  $E_\sigma$ . The bare spin components (labeled by  $m_F$ , with  $|\downarrow\rangle$  in red and  $|\uparrow\rangle$  in blue) are separated along the horizontal axis. The vertical axis shows the atoms' mechanical momentum  $\hbar k$  along the SOC direction ( $\hat{y}$ ). The color scale reflects the measured optical density (OD, see subsections below). The total condensate atom number of the initial state at  $\Omega_I$  is  $N_c \sim (1-2) \times 10^4$  with trap frequencies  $\omega_z \sim 2\pi \times (37 \pm 5)$  Hz and  $\omega_x \sim \omega_y \sim 2\pi \times (205 \pm 15)$  Hz. The TOF images (and associated analyzed quantities presented later) are typically the average of a few repetitive measurements.

We refer to the reduction of condensate fraction in this paper as thermalization. In the dressed case at  $\Omega_F = 1.3 E_r$  (Fig. 3.2b), despite the fact that  $A_\sigma$  are nearly the same as that for the bare case, the SDM is now strongly damped without completing one period. Besides, we observe higher BEC fraction remaining at the end of the measurement compared with the bare case. This can be seen in the narrower momentum distribution of thermal atoms with a more prominent condensate peak in Fig. 3.2b.

From the TOF images, we fit the atomic cloud of each bare spin component (or dominant bare spin component of a dressed spin component) to a 2D bimodal distri-

bution to extract the center-of-mass (CoM) momentum  $\hbar k_{\uparrow(\downarrow)}$  or other (dressed) spin-dependent quantities (see subsections below). The relative mechanical momentum between the two spin components in the SDM is then determined by  $\hbar k_{\text{spin}} = \hbar(k_{\uparrow} - k_{\downarrow})$ .

Fig. 3.3a-e presents measurements of  $\hbar k_{\text{spin}}$  versus  $t_{\text{hold}}$  at various  $\Omega_{\text{F}}$ . We see that the initial amplitude ( $2\hbar k_{\text{r}}$ ) of  $\hbar k_{\text{spin}}$  is larger than the width of the atomic momentum distribution ( $< \hbar k_{\text{r}}$ ), and  $\hbar k_{\text{spin}}$  damps to around zero at later times. The observed  $\hbar k_{\text{spin}}$  as a function of  $t_{\text{hold}}$  is fitted to a damped sinusoid  $A_0 e^{-t_{\text{hold}}/\tau_{\text{damp}}} \cos(\omega t_{\text{hold}} + \theta_0) + B_0$  (see subsections below) to extract the decay time constant  $\tau_{\text{damp}}$ . The SDM damping is then quantified by the inverse quality factor  $1/Q = t_{\text{trap}}/(\pi\tau_{\text{damp}})$ , where  $1/t_{\text{trap}}$  is the trap frequency along  $\hat{y}$  taking into account of the effective mass for the dressed case (see subsections below). We observe that the damping ( $1/Q$ ) is higher for larger  $\Omega_{\text{F}}$ , summarized by the purple data in Fig. 3.3f. Additionally, we have performed two control experiments, which suggest that SOC alone cannot cause momentum damping and thermalization if there are no collisions between the two dressed spin components. Only when there is SDM would notable thermalization be observed within the time of measurement. First, we measure the dipole oscillations [35, 65] of a SO-coupled BEC with a single dressed spin component prepared in  $|\downarrow'\rangle$  at various  $\Omega_{\text{F}}$ . This gives a spin current as well as a net mass current. We observe (e.g. Fig. 3.4 in subsection 3.3.2) that these single-component cases exhibit very small damping ( $1/Q < 0.05$ , summarized by the red square data in Fig. 3.3f) and negligible thermalization. In another control experiment, we generate only an AC mass current without a spin current by exciting in-phase dipole oscillations of two dressed spin components of a SO-coupled BEC without relative collisions (SDM). This experiment also reveals very small damping and negligible thermalization (see Fig. 3.5 in subsection 3.3.2).

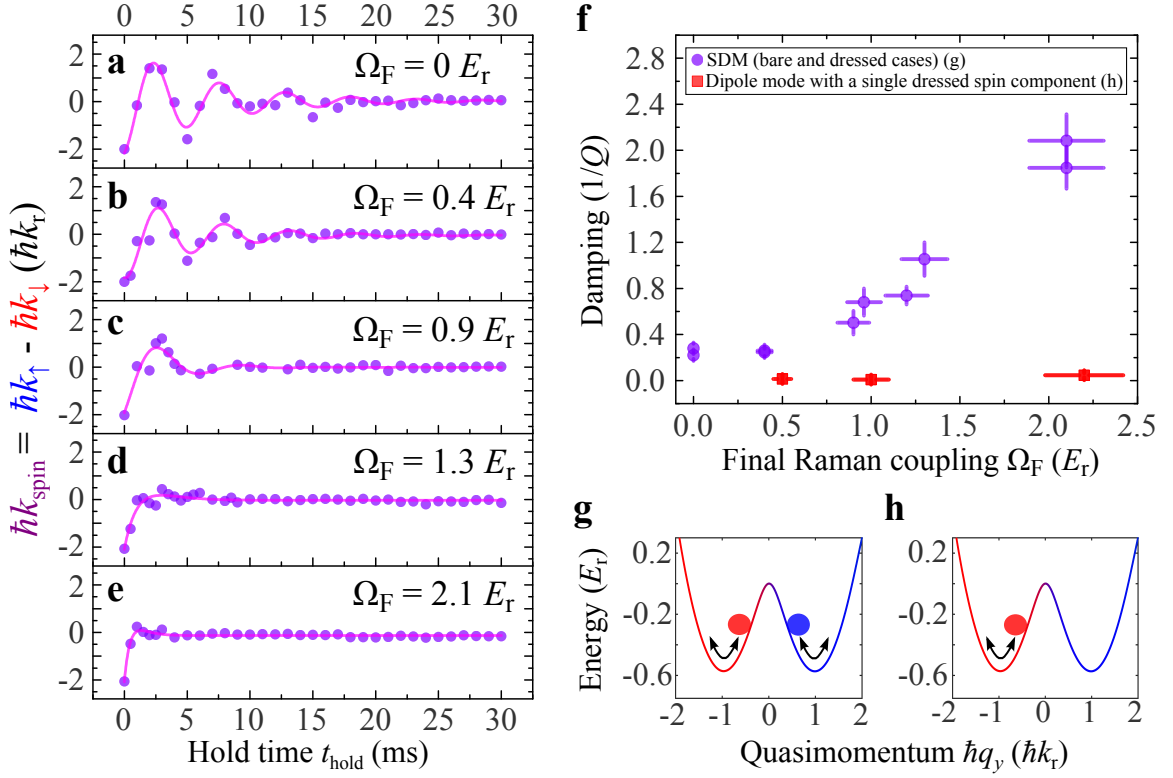


Fig. 3.3. **Momentum damping at different  $\Omega_F$ , for SDM and the dipole mode of a single dressed spin component.** (a)-(e) Relative momentum oscillations in SDM,  $\hbar k_{\text{spin}}$ , as a function of  $t_{\text{hold}}$  at various  $\Omega_F$ . The experimental data (scatters) are fitted to a damped sinusoidal function (line) to extract the inverse quality factor  $1/Q$  of the oscillations. (f) Momentum damping (quantified by  $1/Q$ ) versus  $\Omega_F$ . The error bar of  $1/Q$  is the standard error of the fit. The purple circle data correspond to the SDM (illustrated by (g)) and the red square data correspond to the dipole mode of a BEC with a single dressed spin component prepared in  $|\downarrow'\rangle$  (illustrated by (h)). In (g)-(h), the representative band structure is calculated at  $\Omega = 1.0 E_r$ .

### 3.3.1 Analysis of momentum damping

Since the propagation direction ( $\hat{x}'$ ) of our imaging laser is  $\sim 27^\circ$  with respect to the  $x$ -axis in the  $x-z$  plane (see Fig. 3.1a), the TOF images are in the  $y-z'$  plane (where  $\hat{z}'$  is perpendicular to  $\hat{x}'$  in the  $x-z$  plane). The atomic cloud of

each (dominant) bare spin component in the TOF images is fitted to a 2D bimodal distribution:

$$\begin{aligned}
& A \max \left( 1 - \left( \frac{y - y_c}{R_y} \right)^2 - \left( \frac{z' - z_c}{R_{z'}} \right)^2, 0 \right)^{3/2} \\
& + B \exp \left( -\frac{1}{2} \left( \left( \frac{y - y_{cT}}{\sigma_y} \right)^2 + \left( \frac{z' - z_c}{\sigma_{z'}} \right)^2 \right) \right)
\end{aligned} \tag{3.5}$$

where the first term corresponds to the condensate part according to the Thomas-Fermi approximation and the second term corresponds to the thermal part. Note that we only fit the majority bare spin cloud component when there is a distinguishable minority bare spin cloud component (which belongs to the same dressed spin state, but has a population  $< 9\%$  of the majority component in our experiments). This convention also applies to the analysis of the spin polarization defined above, condensate fraction, and the coherent spin current (see below). In the spin current or SOC directions ( $\hat{y}$ ), we obtain the relative mechanical momentum between the two bare spin components  $\hbar k_{\text{spin}} = \hbar(k_{\uparrow} - k_{\downarrow})$  from the difference between the center-of-mass positions of their condensate parts ( $y_c^{\uparrow} - y_c^{\downarrow}$ ) and the calibration of  $2\hbar k_r$  in TOF images (for example,  $2\hbar k_r$  can be calibrated from the distance between different bare spin components  $\uparrow$  and  $\downarrow$  that are in the same dressed spin state  $\uparrow'$ ). To obtain the damping ( $1/Q$ ) of the relative momentum oscillations in SDM (Fig. 3.3),  $\hbar k_{\text{spin}}$  as a function of  $t_{\text{hold}}$  is fitted to a damped sinusoidal function  $A_0 e^{-t_{\text{hold}}/\tau_{\text{damp}}} \cos(\omega t_{\text{hold}} + \theta_0) + B_0$ , where  $\tau_{\text{damp}}$  is the momentum decay time constant. The data have a small offset  $B_0$  because we only use the majority bare spin component in each dressed spin component when extracting  $\hbar k_{\uparrow, \downarrow}$ . We extract  $\tau_{\text{damp}}$  to obtain the inverse quality factor  $1/Q = t_{\text{trap}}/(\pi\tau_{\text{damp}})$ , where  $t_{\text{trap}} = (2\pi/\omega_y)\sqrt{m_{\text{eff}}/m}$  is the trap period along the  $y$  direction taking into account of the effective mass  $m_{\text{eff}}$  for the dressed band around  $q_{\sigma \text{ min}}$ ,  $m$  is the bare atomic mass, and  $\omega_y/(2\pi)$  is the trap frequency along the  $y$  direction in the absence of Raman lasers. Note that the effective masses around the two minima in the dressed ground band are nearly the same so we take their average

as the  $m_{\text{eff}}$ . The standard error of the fit (95% confidence intervals) is obtained for determining the uncertainty of  $1/Q$  shown in Fig. 3.3.

For the dipole oscillations of a BEC with a single dressed spin component prepared in the  $|\downarrow'\rangle$  state (see subsection 3.3.2), we fit  $\hbar k_{\downarrow}$  (mechanical momentum of the dominant bare spin component  $|\downarrow\rangle$ ) as a function of  $t_{\text{hold}}$  to a damped sinusoidal function to extract  $\tau_{\text{damp}}$  and thus to obtain  $1/Q$ . The minority bare spin  $|\uparrow\rangle$  component oscillates in phase with the dominant  $|\downarrow\rangle$  component with similar damping, and thus is not taken into account for determining  $1/Q$ .

### 3.3.2 Control experiment 1: dipole oscillations of a SO-coupled BEC with a single dressed spin component in the $|\downarrow'\rangle$ state

By quickly changing the Raman coupling/detuning as in [65], we can apply a synthetic electric field to a BEC with a single dressed spin component to excite its dipole oscillations in the optical trap. The experimental timing diagram is similar to Fig. 3.1b. First, an 80 ms ramp is used to achieve an initial Raman coupling  $\Omega_{\text{I}} = 3.7 E_{\text{r}}$ , where the initial detuning in this case is chosen such that the band is tilted and only  $|\downarrow'\rangle$  is present. Subsequently, both  $\Omega_{\text{I}}$  and the initial detuning are held for another 100 ms. Then,  $\Omega_{\text{I}}$  is changed to  $\Omega_{\text{F}}$  while the initial detuning is changed to  $\delta_{\text{R}} = \delta'(\Omega_{\text{F}}, \varepsilon)$  (which realizes a balanced band at  $\Omega_{\text{F}}$ ) in 1 ms. This gives a spin current with a net mass current generated from a single dressed spin component. For example, Fig. 3.4 shows the dipole oscillations of a dressed BEC in the  $|\downarrow'\rangle$  state at  $\Omega_{\text{F}} = 1.0 E_{\text{r}}$  and  $\delta_{\text{R}} = \delta'(\Omega_{\text{F}}, \varepsilon)$  (such that the double minima in the ground dressed band are balanced, although only the one corresponding to  $|\downarrow'\rangle$  is occupied). Such single-component dipole oscillations are observed to possess very little damping ( $1/Q < 0.05$ ) and without noticeable thermalization within the time scale of the experiment (30 ms), similar to the work in [65]. Similar results are obtained for the measurements performed at different  $\Omega_{\text{F}}$ , as shown in the red square data in Fig. 3.3f. Note that in the TOF images, the dominant bare spin component is

$|\downarrow\rangle$  (red). There is a minority component in  $|\uparrow\rangle$  oscillating in phase with but is  $2\hbar k_r$  away from  $|\downarrow\rangle$ , and thus is not shown in Fig. 3.4. The control experiment shows that without a collision partner (i.e. the other dressed spin component in the  $|\uparrow\rangle$  state), the dipole oscillations of a single dressed spin component is very weakly damped without noticeable thermalization within the time scale of the experiment.

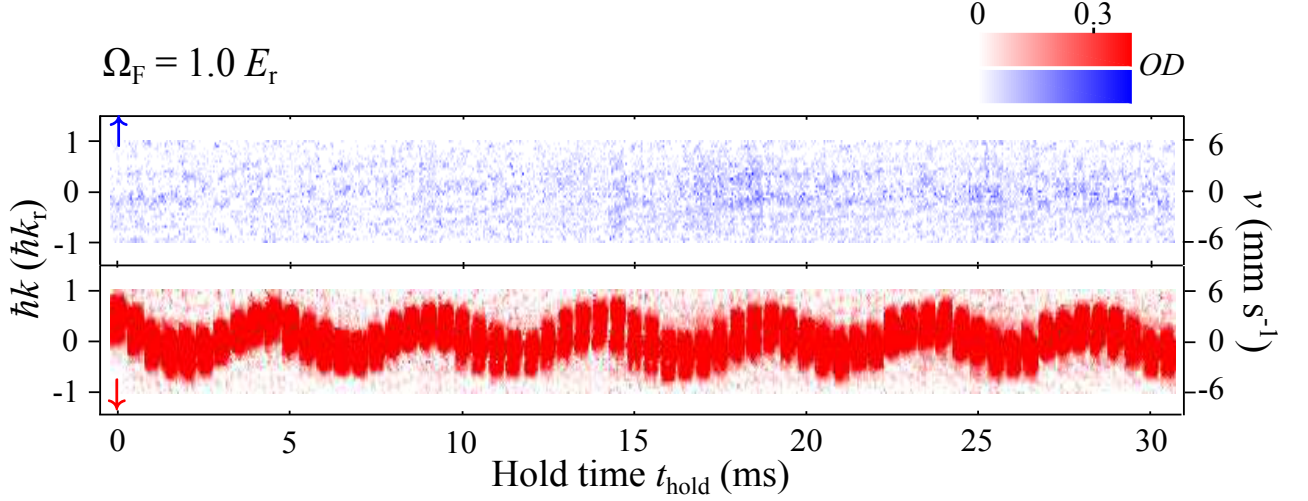
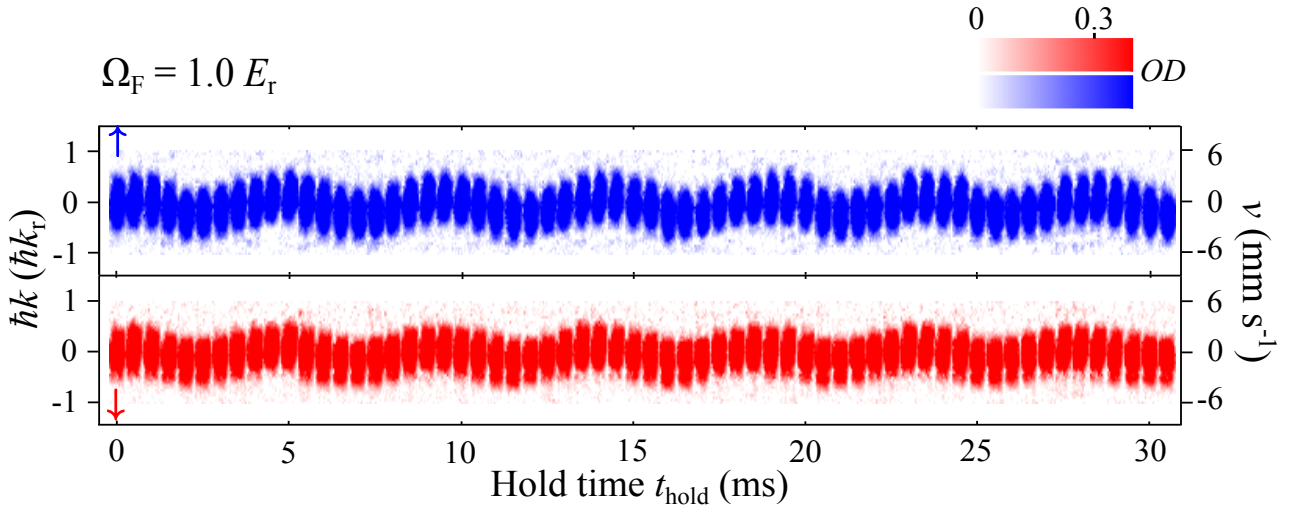


Fig. 3.4. **Dipole oscillations of a BEC with a single dressed spin component in  $|\downarrow'\rangle$ .** Combined TOF images vs  $t_{\text{hold}}$  for a dressed BEC in  $|\downarrow'\rangle$  ( $\Omega_F = 1.0 E_r$ ,  $\delta_R = \delta'(\Omega_F, \varepsilon)$ , shown in Fig. 3.3h) undergoing dipole oscillations, showing very weak damping ( $1/Q < 0.05$ ) and negligible thermalization. Each slice in the image shown is a TOF image at a given  $t_{\text{hold}}$ , but compressed along the horizontal direction. The vertical axis shows the mechanical momentum  $\hbar k$  of atoms. The time step between successive image slices is 0.5 ms. The figure shows bare spin components  $|\downarrow\rangle$  in red and  $|\uparrow\rangle$  in blue plotted in the lower and upper panels, respectively.

### 3.3.3 Control experiment 2: common-mode dipole oscillations of two dressed spin components of a SO-coupled BEC

We also excite common-mode dipole oscillations of two dressed spin components of a SO coupled BEC with equal populations in  $|\uparrow\rangle$  and  $|\downarrow\rangle$  (Fig. 3.5) by ramping

the optical trap power up and back down in 1 ms. This applies the same force to both dressed spin components and actuates their in-phase dipole oscillations in the trap, creating a mass current without a spin current, therefore also no collisions between the two dressed spin components. To analyze the momentum damping of the individual atomic cloud,  $\hbar k_{\uparrow}$  or  $\hbar k_{\downarrow}$  is fitted to a damped sinusoidal function to obtain the corresponding  $1/Q$ . We find that such common-mode dipole oscillations in the trap are very weakly damped ( $1/Q < 0.05$ ) without noticeable thermalization within the time scale of the experiment (30 ms). This shows that SOC alone would not cause momentum damping of the individual atomic cloud if there is no relative collision between the two spin components.



**Fig. 3.5. Common-mode dipole oscillations of two dressed spin components of a SO coupled BEC.** Combined TOF images vs  $t_{\text{hold}}$  for two dressed spin components of a SO coupled BEC with equal populations in  $|\uparrow\rangle$  and  $|\downarrow\rangle$  ( $\Omega_F = 1 E_T$ ,  $\delta_R = \delta'(\Omega_F, \varepsilon)$ ) undergoing in-phase dipole oscillations, showing very little damping ( $1/Q < 0.05$ ) with negligible thermalization. Each slice in the image shown is a TOF image at a given  $t_{\text{hold}}$ , but compressed along the horizontal direction. The time step between successive image slices is 0.5 ms. The figure shows  $|\downarrow\rangle$  in red and  $|\uparrow\rangle$  in blue plotted in the lower and upper panels, respectively.

### 3.4 Thermalization and spin current

We now turn our attention to the thermalization, i.e. the reduction of condensate fraction due to collisions between the two spin components. To quantitatively describe the observed thermalization, the integrated optical density of the atomic cloud in each spin component is fitted to a 1D bimodal distribution to extract the total condensate fraction  $f_c = N_c/N$  (see subsections below) with  $N$  being the total atom number and  $N_c$  the total condensate atom number (including both spin states). The time ( $t_{\text{hold}}$ ) evolution of the measured  $f_c$  is plotted for the bare ( $\Omega_F = 0$ ) and dressed ( $\Omega_F = 1.3 E_r$  and  $2.1 E_r$ ) cases in Fig. 3.6a. In all the cases, we observe that  $f_c$  first decreases with time before it no longer changes substantially (within the experimental uncertainty) after some characteristic thermalization time ( $\tau_{\text{therm}}$ ). To capture the overall behavior of the thermalization, we fit the smoothed  $t_{\text{hold}}$ -dependent data of  $f_c$  to a shifted exponential decay  $f_c(t_{\text{hold}}) = f_s + (f_i - f_s) \exp(-t_{\text{hold}}/\tau_{\text{therm}})$ , where  $\tau_{\text{therm}}$  represents the time constant for the saturation of the decreasing condensate fraction and  $f_s$  the saturation condensate fraction (see subsections below). We obtain  $\tau_{\text{therm}} = 3.8(4)$  ms,  $2.4(3)$  ms, and  $0.4(1)$  ms for  $\Omega_F = 0$ ,  $1.3 E_r$ , and  $2.1 E_r$ , respectively. Besides, a notably larger condensate fraction ( $f_s$ ) is left for a larger  $\Omega_F$ , where  $f_s \sim 0.2$ ,  $0.3$ , and  $0.4$  for  $\Omega_F = 0$ ,  $1.3 E_r$ , and  $2.1 E_r$ , respectively. Since thermalization during our measurement time is induced by the SDM, the observation that a larger  $\Omega_F$  gives rise to a smaller  $\tau_{\text{therm}}$  and a larger  $f_s$  (Fig. 3.6b) thus less thermalization is understood as due to the stronger SDM damping (smaller  $\tau_{\text{damp}}$ ) at larger  $\Omega_F$ , stopping the relative collision between the two spin components thus the collision-induced thermalization earlier.

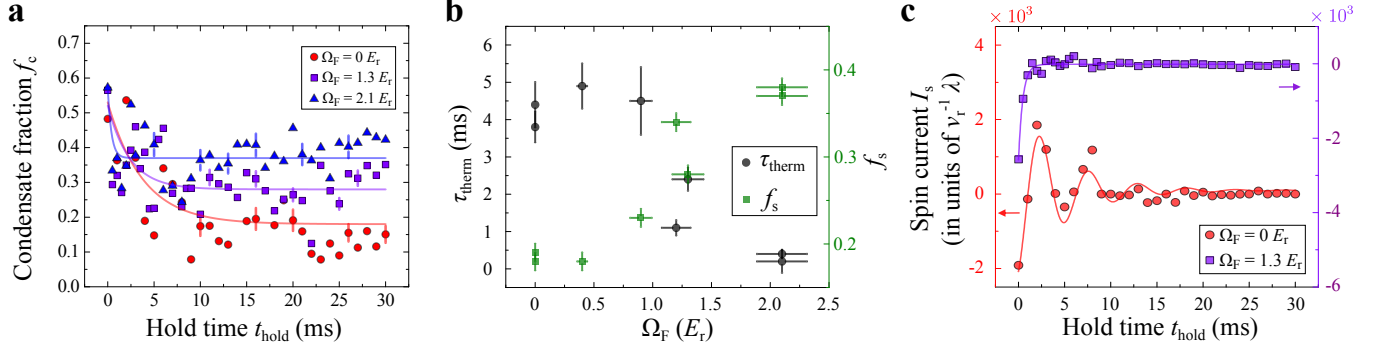


Fig. 3.6. **Thermalization and spin current.** (a) The measured condensate fraction  $f_c = N_c/N$  as a function of  $t_{\text{hold}}$  for SDM in the bare case (no SOC,  $\Omega_F = 0$ ) and the dressed cases (with SOC,  $\Omega_F = 1.3 E_r$  and  $\Omega_F = 2.1 E_r$ ). Representative error bars show the average percentage of the standard error of the mean. The solid curves are the shifted exponential fits to the smoothed  $f_c$  (see subsections below). The initial condensate fraction (not shown) at  $\Omega_I$  (measured at  $t_{\text{hold}} = -1$  ms) is  $\sim 0.6 - 0.7$  for all the cases. (b) The saturation time constant  $\tau_{\text{therm}}$  of the decreasing  $f_c$  and the saturation condensate fraction  $f_s$  versus  $\Omega_F$ , where the vertical error bar is the standard error of the fit. (c) Spin current  $I_s$  (normalized by  $v_r/\lambda = 7.4 \times 10^3$  /s, where  $v_r \sim 6$  mm/s is the recoil velocity) as a function of  $t_{\text{hold}}$  for  $\Omega_F = 0$  and  $1.3 E_r$ . The solid curves are fits (see text).

The coherent spin current is phenomenologically defined as  $I_s = I_{\uparrow} - I_{\downarrow}$  (see subsections below), where  $I_{\sigma=\uparrow,\downarrow}$  is given by:

$$I_{\sigma} = \frac{N_c^{\sigma}}{L^{\sigma}} v^{\sigma} = f_c^{\sigma} v^{\sigma} \frac{N^{\sigma}}{L^{\sigma}} \quad (3.6)$$

Here,  $\sigma$  labels the physical quantities associated with the spin component  $\sigma$ ,  $L^{\sigma}$  is the *in situ* BEC size along the current direction, and  $v^{\sigma} = \hbar k_{\sigma}/m$ . We exclude the contribution from the thermal atoms as only the condensate atoms participate in the coherent spin transport. In our experiments,  $N^{\uparrow}/L^{\uparrow} \approx N^{\downarrow}/L^{\downarrow}$  is not observed to decrease significantly with  $t_{\text{hold}}$ , and  $f_c^{\uparrow} \approx f_c^{\downarrow} \approx f_c$ , thus the relaxation of  $I_s$  is mainly controlled by that of  $f_c^{\uparrow} v^{\uparrow} - f_c^{\downarrow} v^{\downarrow} \approx f_c (v^{\uparrow} - v^{\downarrow})$ . Therefore, the SDM damping (reduction of  $v^{\uparrow} - v^{\downarrow}$ ) and thermalization (reduction of  $f_c$ ) provide the two main mechanisms for the relaxation of coherent spin current.

Fig. 3.6c shows the normalized  $I_s$  as a function of  $t_{\text{hold}}$  extracted (see subsections below) for  $\Omega_F = 0$  and  $1.3 E_r$ . In the bare case, the spin current oscillates around and decays to zero. In the dressed case, the spin current relaxes much faster to zero without completing one oscillation. Fitting  $I_s$  versus  $t_{\text{hold}}$  to a damped sinusoidal function for  $\Omega_F = 0$  or to an exponential decay for  $\Omega_F = 1.3 E_r$  (with no observable  $I_s$  oscillations) allows us to extract the spin current decay time constant  $\tau_{\text{spin}}$ , which is 5.1(8) ms and 0.5(0) ms, respectively. In the dressed case  $I_s$  decays much faster compared to the bare case because both  $\tau_{\text{damp}}$  and  $\tau_{\text{therm}}$  are much smaller due to stronger SDM damping. In the bare case, the thermalization plays a more important role in the relaxation of  $I_s$  due to the larger reduction of condensate fraction ( $f_i - f_s$ ) compared to the dressed case.

### 3.4.1 Analysis of condensate fraction

During the SDM, the atomic cloud can be significantly deformed along  $\hat{y}$  due to the interference between the two dressed spin components (see e.g. Fig. 3.7). Therefore, in order to extract the total condensate fraction ( $f_c = N_c/N$ ) of atoms to study the thermalization behavior as shown in Fig. 3.6a, b, the measured optical density ( $OD$ ) of each bare spin component  $\sigma$  in the  $y - z'$  plane is integrated along the  $y$  direction (the direction of SOC and the spin current as well as the direction along which the cloud can be significantly distorted) to obtain an integrated optical density versus  $z'$  (denoted by  $OD_{z'}$ ). We fit  $OD_{z'}$  of each bare spin component  $\sigma$  to a 1D bimodal distribution  $A \max\left(1 - \left(\frac{z' - z_c}{R_{z'}}\right)^2, 0\right)^2 + B \exp\left(-\frac{1}{2}\left(\frac{z' - z_c}{\sigma_{z'}}\right)^2\right)$ , where the first term corresponds to the condensate part according to the Thomas-Fermi approximation and the second term corresponds to the thermal part, to get the corresponding condensate and thermal atom numbers,  $N_c^\sigma$  and  $N_{\text{therm}}^\sigma$ , respectively. The total condensate fraction is calculated as  $f_c = N_c/N = (N_c^\uparrow + N_c^\downarrow) / (N_c^\uparrow + N_{\text{therm}}^\uparrow + N_c^\downarrow + N_{\text{therm}}^\downarrow)$ , shown as the scatters (unsmoothed raw data) in Fig. 3.6a.

To quantitatively describe the thermalization, we fit the smoothed total condensate fraction versus  $t_{\text{hold}}$  to a shifted exponential decay  $f_c(t) = f_s + (f_i - f_s) \exp(-t/\tau_{\text{therm}})$ , where  $\tau_{\text{therm}}$  represents the time constant for the thermalization to stop and for the decreasing condensate fraction to saturate, with  $f_s$  being the saturation condensate fraction. Because the large fluctuations in the unsmoothed data can give erroneous fitting results, each fitted curve shown as a solid line in Fig. 3.6a is the average of the three fits performed on the smoothed data, obtained using different levels ( $M = 1, 2, 3$ ) of smoothing, where the smoothing is done by taking the average of the raw data within the nearest  $M$  time intervals.

Notice that the heating effect due to our Raman lasers (such as from spontaneous emission) is negligible within the time scale of the experiments (30 ms), because the lifetime of our BEC in the presence of the Raman lasers (with the Raman coupling considered in this work) is measured to be hundreds of ms. For example, the control experiment in Fig. 3.4 shows no observable thermalization within 30 ms for dipole oscillations of a BEC with a single dressed spin component in the presence of the Raman lasers.

### 3.4.2 Coherent spin current

The  $I_\sigma$  in Eq. (3.6) reflects the number of BEC atoms of a specific spin state passing through a cross section per unit time, and can be related to  $JA$ , where  $J = n_c v$  is the current density along the SOC direction ( $\hat{y}$ ) with the effective number density  $n_c = N_c/(LA)$ ,  $v$  is the corresponding velocity, and  $A$  is an effective cross sectional area (the spin index  $\sigma$  is dropped in this discussion for simplicity in notations). The *in situ* length in the  $y$  direction,  $L$ , of each bare spin component can be estimated from the measured length of the BEC after TOF by  $L_y(t_{\text{TOF}}) = \sqrt{1 + (\omega_y t_{\text{TOF}})^2} L_y(t_{\text{TOF}} = 0)$  for a cigar-shape interacting BEC with  $\omega_{x,y} \gg \omega_z$  and in the Thomas-Fermi approximation [96], where  $L_y(t_{\text{TOF}})$  is defined as  $2R_y$  in Eq. (3.5) and  $L_y(t_{\text{TOF}} = 0) = L$ . For example, for a typical  $L_y(t_{\text{TOF}} = 15$

ms) = 88  $\mu\text{m}$  measured for one bare spin component of a dressed BEC prepared at  $\Omega_{\text{I}}$ , we get  $L = 4.5 \mu\text{m}$  for  $\omega_y = 2\pi \times 205 \text{ Hz}$ . The two spin components have similar  $L$  when the spin populations are balanced. The *in situ* length  $L$  is  $t_{\text{hold}}$ -dependent during the dynamics and calculated from the  $t_{\text{hold}}$ -dependent TOF size, and is then used to obtain the  $t_{\text{hold}}$ -dependent spin current in Fig. 3.6b.

In the Thomas-Fermi approximation, we can also calculate  $L$  for the initial state at  $\Omega_{\text{I}}$  from the condensate atom number and trap frequencies. For example, we obtain  $L = 4.7 \mu\text{m}$  using  $N_c = 1.6 \times 10^4$  and  $\omega_y = 2\pi \times 205 \text{ Hz}$  by  $\mu = \frac{1}{2}m\omega_y^2 L^2$ , where  $\mu = \frac{15^{\frac{2}{5}}}{2}(N_c a / \bar{a})^{\frac{2}{5}} \hbar \bar{\omega}$ ,  $\bar{\omega} = (\omega_x \omega_y \omega_z)^{1/3}$ ,  $a$  is the  $s$ -wave scattering length, and  $\bar{a} = \sqrt{\hbar / (m\bar{\omega})}$ . In addition, the GPE-simulated  $L$  is 4.7  $\mu\text{m}$ . These results of  $L$  are consistent with the value calculated from the TOF width.

### 3.5 Observation of deformed atomic clouds and BEC shape oscillations

In addition to the SDM damping and thermalization, the atomic clouds can exhibit other rich dynamics after the application of  $E_\sigma$ . We observe deformation of atomic clouds at early stages of the SDM, as shown in Fig. 3.7a-d. Fig. 3.7b, d shows the observation of an elongated atomic cloud at  $t_{\text{hold}} = 0.5 \text{ ms}$  in the dressed case at  $\Omega_{\text{F}} = 2.1 E_{\text{r}}$ , in comparison with the atomic cloud at  $t_{\text{hold}} = 0.5 \text{ ms}$  in the bare case shown in Fig. 3.7a, c. Fig. 3.7c, d shows the integrated optical density (denoted by  $OD_y$ ) of the atomic cloud versus the  $y$  direction, obtained by integrating the measured optical density over the horizontal direction in TOF images.

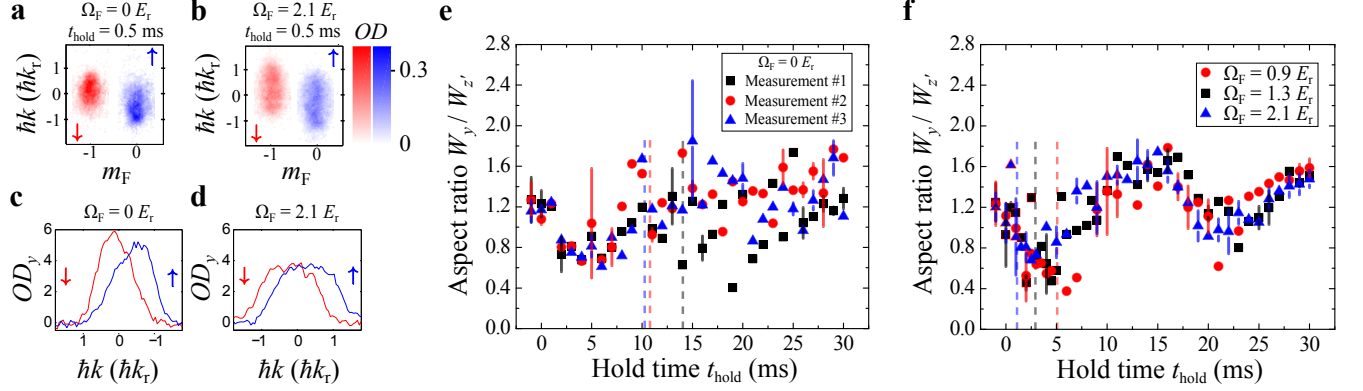


**Fig. 3.7. Observation of deformed atomic clouds and BEC shape oscillations.**

(a-d) Observation of deformed atomic clouds at early stages of the SDM. (a-b) TOF images for  $\Omega_F = 0$  and  $\Omega_F = 2.1 E_r$  at  $t_{\text{hold}} = 0.5$  ms are shown for comparison. The corresponding integrated optical density ( $OD_y$ ) versus the momentum in the SOC direction ( $\hat{y}$ ) for the spin down and up components is shown respectively in (c) and (d). (e-f) Observation of BEC shape oscillations. The data showing the aspect ratio  $W_y/W_z$  (see subsections below) of the condensate measured at various  $t_{\text{hold}}$  are extracted from the SDM measurements in Fig. 3.3, except for the additional measurements #2 and #3 in (e). (e) For the three independent measurements in the bare case, the observed oscillations possess a complicated behavior without having a well-defined frequency given the error bars and the fluctuation in the data. Select TOF images for measurement #1 are shown in Fig. 3.2a. (f) In the dressed cases, aspect ratio oscillations with a well-defined frequency are observed in measurements at three different  $\Omega_F$ . The average frequency of the three aspect ratio oscillations obtained from the damped sinusoidal fit is around 58 Hz, consistent with the expected frequency for the  $m = 0$  quadrupole mode  $f_{m=0} = \sqrt{2.5}\omega_z/(2\pi) \sim 59$  Hz for a cigar-shape BEC in the limit of  $\omega_z/\omega_{x,y} \ll 1$  [97]. Note that  $\omega_z$  is not modified by Raman lasers and thus does not depend on  $\Omega_F$ . Select TOF images for  $\Omega_F = 1.3 E_r$  are shown in Fig. 3.2b. The representative error bars in (e-f) are standard deviation of at least three measurements. The dashed lines indicate  $t_{\text{hold}} \sim 2\tau_{\text{damp}}$  after which the SDM is fully damped out.

The momentum distribution of the atoms at  $\Omega_F = 2.1 E_r$  has lower  $OD_y$  and is more elongated without a sharp peak along the SOC direction, in comparison with the bare case that has higher  $OD_y$  and a more prominent peak momentum. Furthermore, we observe that the relaxation of the spin current is accompanied by

BEC shape oscillations [97–99] (Fig. 3.7e, f), which remain even after the spin current is fully damped. These additional experimental observations are closely related to the spin current relaxation, as discussed below.

### 3.5.1 Analysis of BEC shape oscillations

We characterize a condensate’s shape oscillations (in the  $y - z'$  plane) of the bare spin component  $\sigma$  by its aspect ratio  $W_y^\sigma/W_{z'}^\sigma$ , where the condensate widths  $W_y^\sigma = 2R_y^\sigma$  and  $W_{z'}^\sigma = 2R_{z'}^\sigma$  (respectively along the  $y$  and  $z'$  directions) are obtained from Eq. (3.5). We take the average of the aspect ratios of the two spin components ( $W_y/W_{z'} = (W_y^\uparrow/W_{z'}^\uparrow + W_y^\downarrow/W_{z'}^\downarrow)/2$ ), and plot  $W_y/W_{z'}$  as a function of  $t_{\text{hold}}$  in Fig. 3.7. In Fig. 3.7e, caution has to be paid because the prominent thermalization in the bare case can make it challenging to fit the 2D cloud and extract the aspect ratio. The notable distortion of the cloud at the early stages of SDM can also make it difficult to perform the 2D Thomas-Fermi fit. Therefore, in Fig. 3.7f, we choose the  $t_{\text{hold}}$ -dependent  $W_y/W_{z'}$  data after the corresponding dashed line (indicating  $t_{\text{hold}} \sim 2\tau_{\text{damp}}$  after which the SDM is fully damped) to fit to a damped sinusoidal function to extract the frequency of the aspect ratio oscillations.

In our experiments, there is no external modulation of the trapping potentials or shapes of the BECs to intentionally excite the shape oscillations. However, it is worth noting that shape oscillations can be induced via a non-adiabatic change in the internal energy of atomic clouds [100, 101], which can take place when  $\Omega$  is quickly changed or when the two spin components collide within the trap. On the other hand, we notice that in the dressed case the formation of density modulations can significantly deform the shape of a BEC (Fig. 3.7b, d; Movies 2, 4, 5 in section 3.7) and may thus also induce energetically-allowed BEC shape oscillations, because the modified shape of the atomic cloud is no longer in equilibrium with the trap. Note that such a shape deformation can also change the internal energy. The  $m = 0$  quadrupole mode excitation observed in our experiments has the lowest mode frequency among all pos-

sible quadrupole modes given our trap geometry and thus is the most energetically favorable (its mode frequency is also lower than the SDM frequency  $\sim \omega_y/(2\pi)$  for our trap parameters). Such nonresonant mode excitation is quite different from most previous studies, in which a collective mode of an atomic cloud is efficiently excited when it matches with the external modulation or perturbation of the trap [98, 102] spatially and also spectrally (resonant with the modulation frequency). Compared to the dressed case, the bare case has less damped SDM and more significant thermalization, thus may complicate the shape oscillations due to more repeated SDM collisions and more atom loss [100, 101]. We expect that the energy of the shape oscillations may eventually be converted to the energy of thermal atoms, leading to decay of the collective modes.

To further verify the excitation of the  $m = 0$  quadrupole mode in the dressed case, we used another set of trap frequencies (see Fig. 3.8 in subsection 3.5.2), and measured the condensate's aspect ratio as a function of  $t_{\text{hold}}$ . The extracted frequency for the aspect ratio oscillations is again consistent with the predicted frequency for the  $m = 0$  quadrupole mode.

### 3.5.2 Observation of the $m = 0$ quadrupole mode of a dressed BEC with another set of trap frequencies

To further verify the excitation of the  $m = 0$  quadrupole mode in the dressed case, we intentionally changed the trap frequencies to  $\omega_z \sim 2\pi \times (21 \pm 3)$  Hz and  $\omega_x \sim \omega_y \sim 2\pi \times (144 \pm 10)$  Hz, and measured the aspect ratio of the condensate as a function of  $t_{\text{hold}}$  at  $\Omega_F = 1.3 E_r$  (Fig. 3.8a, with select TOF images shown in Fig. 3.8b) with all the other experimental parameters similar to Fig. 3.9f. The data after the dashed line ( $t_{\text{hold}} \sim 2\tau_{\text{damp}}$ ) is fitted to a damped sinusoidal function. The extracted aspect ratio oscillation frequency is around 34 Hz, again consistent with the prediction  $f_m = \sqrt{2.5}\omega_z/(2\pi) \sim 33$  Hz for the  $m = 0$  quadrupole mode. This

confirms the excitation of the  $m = 0$  quadrupole mode after the SDM is damped out in the dressed case.

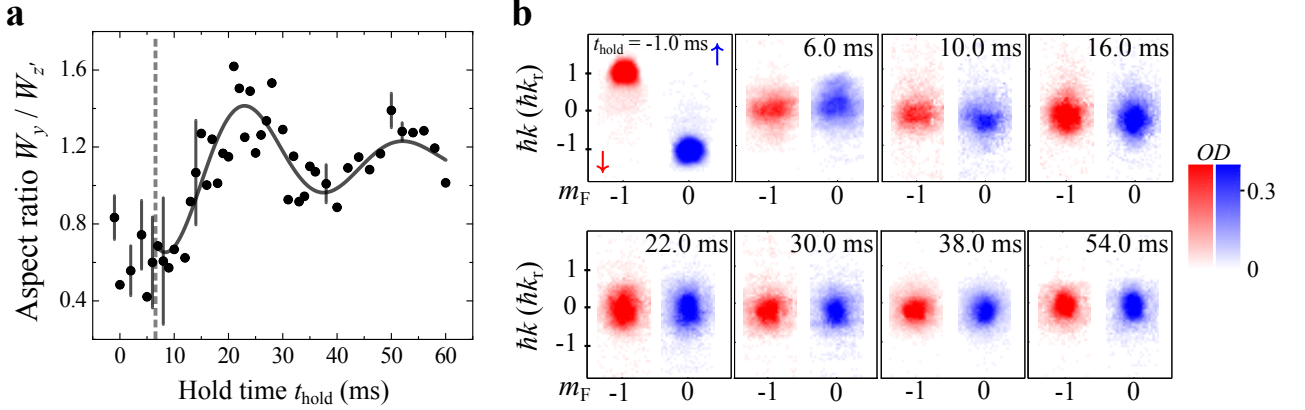
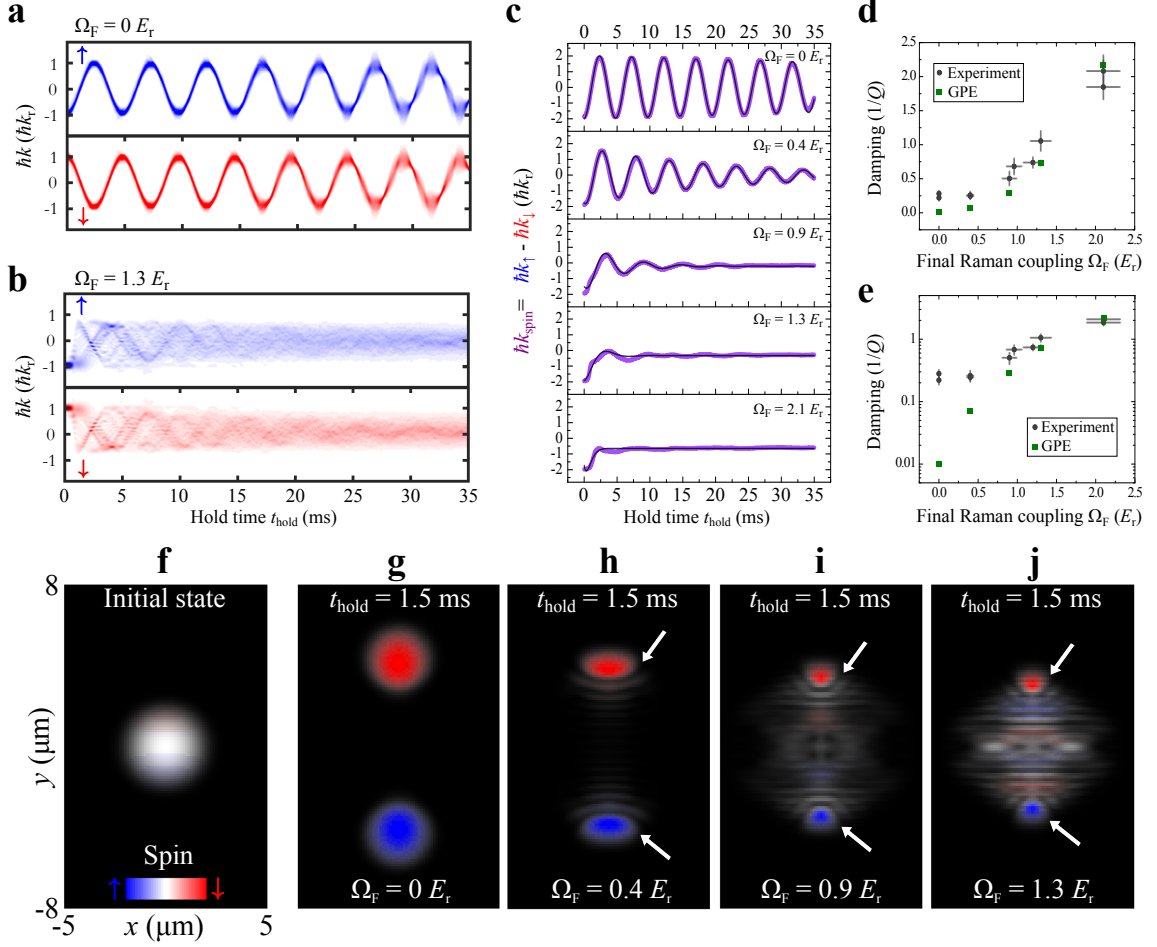


Fig. 3.8. **Observation of the quadrupole mode of a dressed BEC with another set of trap frequencies.** (a) For  $\Omega_F = 1.3 E_r$  with trap frequencies  $\omega_z \sim 2\pi \times (21 \pm 3)$  Hz and  $\omega_x \sim \omega_y \sim 2\pi \times (144 \pm 10)$  Hz used in this measurement, the observed aspect ratio oscillation frequency is around 34 Hz, consistent with the expected  $m = 0$  quadrupole mode frequency  $f_{m=0} = \sqrt{2.5}\omega_z/(2\pi) \sim 33$  Hz. This further verifies the excitation of the  $m = 0$  quadrupole mode. The oscillation frequency is obtained using a damped sinusoidal function to fit the data following the SDM is damped out (when  $t_{\text{hold}} \sim 2\tau_{\text{damp}}$  as indicated by the dashed line). The representative error bars are standard deviation of at least three measurements. (b) Select TOF images are typically the average of a few repetitive measurements.

### 3.6 GPE simulations and interpretations

We have performed numerical simulations for the SDM based on the 3D time-dependent Gross-Pitaevskii equation (GPE), using similar parameters as in the experiments. The  $\Omega_F$ -dependent  $1/Q$  extracted from the GPE-simulated SDM (Fig. 3.9a-c) shows qualitative agreement with the experimental measurements (Fig. 3.9d, e). Quantitatively, we notice that the GPE simulation generally underestimates the momentum damping compared to the experimental observation (Fig. 3.9e), especially at low  $\Omega_F$  (including the bare case). This is possibly related to the fact that our GPE simulation cannot treat thermalization (which is more prominent at low  $\Omega_F$ ) and effects of thermal atoms. Nonetheless, the *in situ* (real space) spin-dependent

density profiles (Fig. 3.9f-j) of the BECs calculated from the GPE simulations have provided important insights to understand why SOC can significantly enhance the SDM damping.



**Fig. 3.9. GPE simulated SDM at various  $\Omega_F$  and the extracted SDM damping compared with experiment.** (a-b) GPE simulations of the 1D momentum-space density distributions of the two bare spin components as a function of  $t_{\text{hold}}$  for the SDM at  $\Omega_F = 0$  and  $\Omega_F = 1.3 E_r$ , respectively. The 1D momentum density  $\rho_\sigma(k_y)$  is obtained by integrating the 3D momentum density along  $k_x$  and  $k_z$ , i.e.  $\rho_\sigma(k_y) = \int \rho_\sigma(k_x, k_y, k_z) dk_x dk_z$ . Then, these integrated 1D atomic momentum densities for sequential hold times ( $t_{\text{hold}}$ ) are combined to show the atomic density in momentum space along the SOC direction versus  $t_{\text{hold}}$ . (c) GPE simulations of the SDM damping versus  $t_{\text{hold}}$  at various  $\Omega_F$ . The violet lines are the  $\hbar k_{\text{spin}}$  (defined as the difference between the CoM momenta of the two spin components) as a function of  $t_{\text{hold}}$  for various  $\Omega_F$ . The CoM momentum ( $\hbar k_{\uparrow, \downarrow}$ ) of each bare spin component (at a given  $t_{\text{hold}}$ ) is calculated by taking a density-weighted average of the corresponding 1D momentum density distributions such as those shown in (a-b). The black lines are damped sinusoidal fits for the calculated  $\hbar k_{\text{spin}}$  to extract the corresponding SDM damping ( $1/Q$ ) which is shown in (d) along with the experimental data reproduced from Fig. 3.3f. (e) Replotting of (d) with  $1/Q$  shown in logarithmic scale. (f-j) *In situ* (real space) atomic densities calculated from GPE simulations. (f) Initial *in situ* 2D density at  $\Omega = \Omega_I$  (right before applying spin-dependent electric fields  $E_\sigma$ ). (g-j) *In situ* 2D density at  $t_{\text{hold}} = 1.5$  ms (after the application of  $E_\sigma$ ) for  $\Omega_F = 0, 0.4 E_r, 0.9 E_r$ , and  $1.3 E_r$ , respectively. For (f-j), the density is designated by brightness and the bare spin polarization by colors (red:  $\downarrow$ , blue:  $\uparrow$ , white: equal spin populations). The 2D densities  $\rho_\sigma(x, y)$  in (f-j) are obtained by integrating the 3D atomic density along  $z$ , i.e.,  $\rho_\sigma(x, y) = \int \rho_\sigma(x, y, z) dz$ . In this figure, the simulations used the following parameters representative of our experiment:  $\Omega_I = 5.2 E_r$ ,  $\delta_R = 0$ ,  $N_C = 1.6 \times 10^4$ ,  $\omega_z = 2\pi \times 37$  Hz,  $\omega_x = \omega_y = 2\pi \times 205$  Hz,  $t_E = 1.0$  ms. GPE simulations are performed by Chunlei Qu and Chuanwei Zhang.

Fig. 3.9f shows that the initial BEC (just before applying  $E_\sigma$ ) in the trap is in an equal superposition of bare spin up and down states. Fig. 3.9g-j shows the density profiles of the BECs at  $t_{\text{hold}} = 1.5$  ms (after applying  $E_\sigma$ ) in the trap with four different  $\Omega_F$  (see Movies 2, 4, 5 in section 3.7). For the bare case, the two spin components fully separate in the real space within the trap. As  $\Omega_F$  becomes larger, we observe that only a smaller portion of atoms in each spin component is well separated, as marked by the white arrows. Concomitantly, a larger portion of atoms appears to get stuck around the trap center and form a prominent standing wave pattern, which we interpret as density modulations arising from the interference between the BEC wavefunctions of the two dressed spin components when  $|\uparrow'\rangle$  and  $|\downarrow'\rangle$  are no longer orthogonal in the presence of SOC (see Fig. 3.10a) [37, 103–106].

Compared to the bare case, the formation of density modulations in the dressed case can lead to more deformed clouds in both the real and momentum spaces at early stages in the SDM, as revealed by the GPE simulations (Fig. 3.9a, b, f-j; Movies 2, 4, 5 in section 3.7). This is consistent with our experimental observation of a highly elongated momentum distribution of the atomic cloud along the SOC direction ( $\hat{y}$ ) at early instants in the SDM of a SO-coupled BEC (Fig. 3.7b, d). In addition to density modulations, our GPE simulation also reveals complex spatial modulation in the phase of the BEC wavefunctions (see Fig. 3.17 and Movies 3, 6 in section 3.7). Such distortions of BEC wavefunctions in the amplitude (which determines the density) and the phase contribute to quantum pressure [2] and local current kinetic energy (see subsections below) respectively, two forms of the kinetic energy that do not contribute to the global translational motion (or CoM kinetic energy) of each spin component. The sum of the CoM kinetic energy, quantum pressure, and local current kinetic energy is the total kinetic energy (see subsections below). We have used GPE to calculate the time evolution of these different parts of kinetic energy for the dressed case, showing that the damping of the CoM kinetic energy (which decays to zero at later times) is accompanied by (thus likely related to) prominent increase

of the quantum pressure and the local current kinetic energy (both remain at some notable finite values at later times) (see Fig. 3.11e-h).

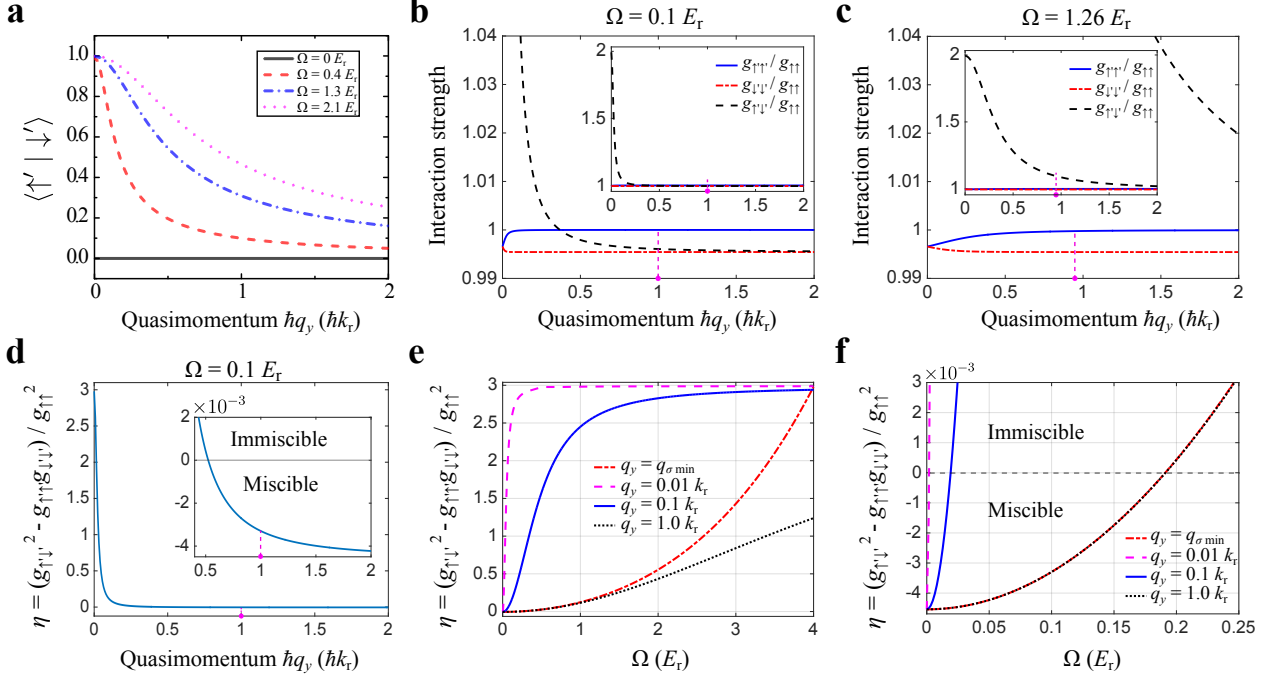


**Fig. 3.10. Calculated nonorthogonality, effective interaction parameters, and immiscibility for two dressed spin states.**

In (a-f), the calculations consider  $|\uparrow'\rangle$  and  $|\downarrow'\rangle$  located respectively at  $\hbar q_y$  and  $-\hbar q_y$ . (a) When  $\Omega = 0$ , the nonorthogonality is zero because the two bare spin components are orthogonal. When  $\Omega \neq 0$ , either increasing  $\Omega$  or decreasing  $q_y$  would increase  $\langle \uparrow' | \downarrow' \rangle$ , giving rise to stronger interference and more significant density modulations in the spatially overlapped region of the two dressed spin components. (b-c) Effective interspecies ( $g_{\uparrow'\downarrow'}$ ) and intraspecies ( $g_{\uparrow'\uparrow'}$ ,  $g_{\downarrow'\downarrow'}$ ) interaction parameters versus quasimomentum at  $\Omega = 0.1 E_r$  and  $1.26 E_r$ , respectively. When  $\Omega$  increases or  $q_y$  decreases,  $g_{\uparrow'\downarrow'}$  increases while  $g_{\uparrow'\uparrow'}$  and  $g_{\downarrow'\downarrow'}$  almost remain at the bare values. As  $q_y \rightarrow 0$  at any finite  $\Omega$ ,  $g_{\uparrow'\downarrow'} \rightarrow 2g_{\uparrow'\uparrow'}$  or  $2g_{\downarrow'\downarrow'}$ , which is the upper bound of  $g_{\uparrow'\downarrow'}$  (see subsections below). The inset of (b-c) zooms out to show the maximum. (d) shows the immiscibility metric  $\eta = (g_{\uparrow'\downarrow'}^2 - g_{\uparrow'\uparrow'}g_{\downarrow'\downarrow'})/g_{\uparrow'\uparrow'}^2$  in Eq. (3.29) (see subsections below) versus  $\hbar q_y$  corresponding to (b).  $\eta < 0$  means miscible, and  $\eta > 0$  means immiscible. Over the range of plotted  $\hbar q_y$ , (d) can be miscible or immiscible depending on  $\hbar q_y$ . The inset of (d) zooms in to focus on the sign change of  $\eta$ . The vertical dotted line in (b-d) indicates  $\hbar q_{\sigma \min}$  corresponding to the  $\Omega$  in each case. The calculations are performed in the two-state picture described by Eq. (3.1) with  $\delta_R = 0$ . (e-f) Immiscibility metric  $\eta$  versus  $\Omega$  for various  $q_y$ . In (e), as  $\Omega$  becomes larger or  $q_y$  becomes smaller, the two dressed spin components can become more immiscible until  $\eta$  reaches the maximum value set by the upper bound of  $g_{\uparrow'\downarrow'}$  (see also (b-c)). (f) Zoom-in of (e) showing the miscible to immiscible transition (indicated by the gray dashed line at  $\eta = 0$ ) as a function of  $\Omega$  for various  $q_y$ . The red dot-dashed line corresponds to two dressed spin components located respectively at the band minima  $q_{\sigma \min}$ , showing the well-known miscible to immiscible transition around  $0.2 E_r$  for a stationary SO-coupled BEC. In the dynamical case studied here, BECs can be located away from the band minima and approach  $q_y = 0$ , becoming immiscible even when  $\Omega < 0.2 E_r$  for small enough  $q_y$ . The calculations here are performed by Mingyuan He and Qi Zhou.

---

The increasing quantum pressure and local current kinetic energy may reflect the emergence of excitations that do not have the CoM kinetic energy. This is consistent with the experimentally observed generation of BEC shape oscillations (Fig. 3.7e, f), whose kinetic energy can be accounted for by the quantum pressure and the local current kinetic energy. Note that the excitation of BEC shape oscillations may also be understood by the observation of deformed clouds at early stages of the SDM (Fig. 3.7a-d), because the deformed shape of the BEC is no longer in equilibrium with the trap and thus initiates the shape oscillations. The observed BEC shape oscillations remain even after the SDM is completely damped in both bare and dressed cases. This indicates that the BECs are still excited even after the CoM relaxes to the single-particle band minima within the time of measurement.

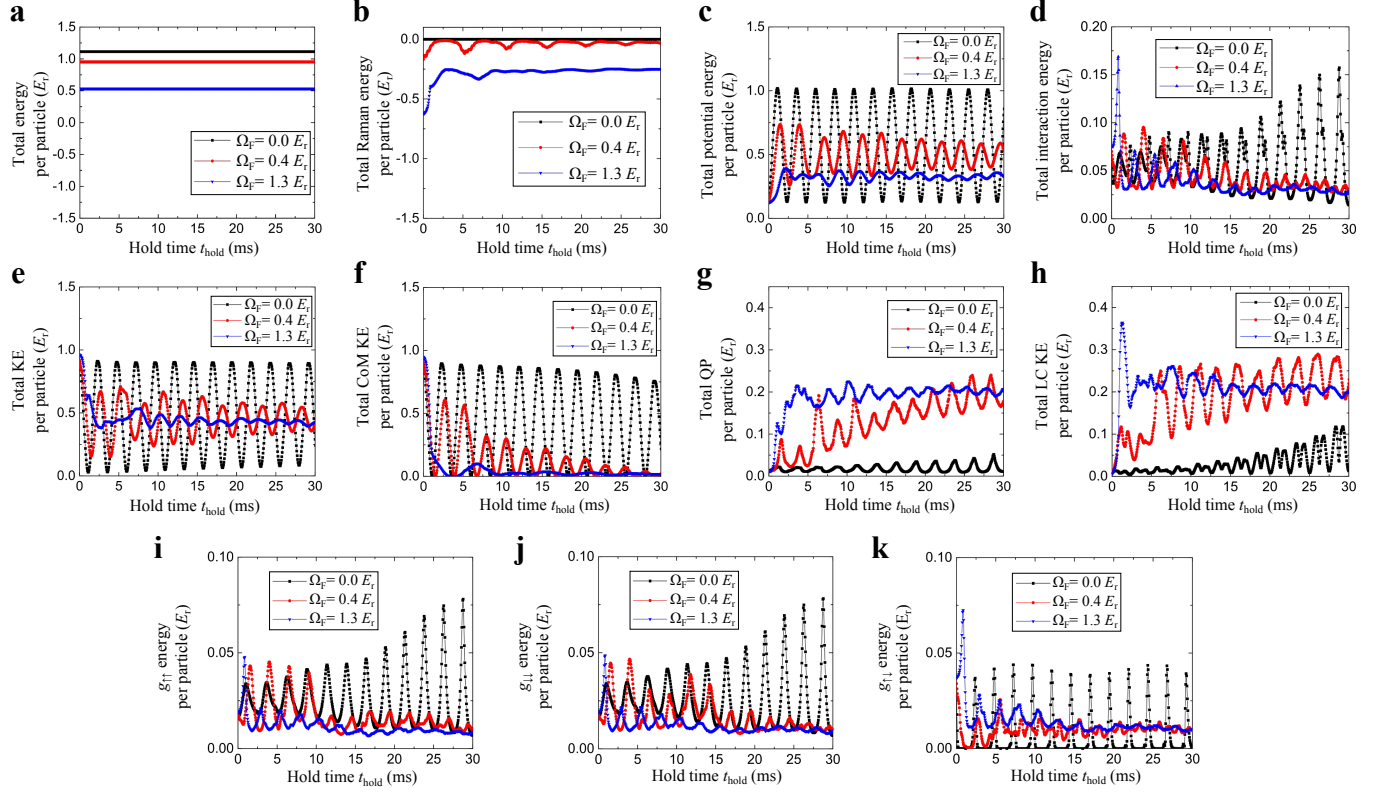


Fig. 3.11. **Time ( $t_{\text{hold}}$ ) evolution of different forms of energies per particle at different  $\Omega_F$  as calculated by GPE.** (a) The total energy is the sum of the total Raman energy, total potential energy, total interaction energy, and the total KE. The result in (a) confirms that the total energy is conserved during  $t_{\text{hold}}$ . (b) Total Raman energy. (c) Total potential energy. (d) Total interaction energy, sum of the bare interaction energies in (i-k). (e) Total KE, sum of different types of kinetic energies in (f-h). (f) Total CoM KE. (g) Total QP. (h) Total LC KE. (i)  $g_{\uparrow\uparrow}$  interaction energy. (j)  $g_{\downarrow\downarrow}$  interaction energy. (k)  $g_{\uparrow\downarrow}$  interaction energy. The GPE calculations here are performed by Chunlei Qu and Chuanwei Zhang.

### 3.6.1 Details in GPE simulations

The dynamical evolution of a BEC is simulated by the 3D time-dependent GPE [107]. To compare with the experimental data, we conduct simulations with similar

parameters as those used in our experiment. The GPE of a SO-coupled BEC can be written in the following form:

$$i\hbar \frac{\partial}{\partial t} \Psi(\mathbf{r}, t) = H_{\text{tot}} \Psi(\mathbf{r}, t) = \left( \frac{\hat{p}_x^2}{2m} + \frac{\hat{p}_z^2}{2m} + H_{\text{SOC}} + V_{\text{trap}} + V_{\text{int}} \right) \Psi(\mathbf{r}, t) \quad (3.7)$$

where  $\hat{p}_x = -i\hbar \frac{\partial}{\partial x}$  ( $\hat{p}_z = -i\hbar \frac{\partial}{\partial z}$ ) is the momentum operator along  $\hat{x}$  ( $\hat{z}$ ), and  $H_{\text{SOC}}$  is the (two-state) single-particle Hamiltonian Eq. (3.1), with  $q_y$  replaced by  $\hat{q}_y = \hat{p}_y/\hbar = -i\frac{\partial}{\partial y}$ .  $V_{\text{trap}}$  is the external trapping potential:

$$V_{\text{trap}} = \frac{1}{2}m\omega_x^2 x^2 + \frac{1}{2}m\omega_y^2 y^2 + \frac{1}{2}m\omega_z^2 z^2 \quad (3.8)$$

where  $\omega_{x(y,z)}$  is the angular trap frequency along the spatial coordinate  $x(y, z)$ . The wavefunction (order parameter) of a spinor BEC can be written in the form

$$\Psi = \begin{pmatrix} \psi_{\downarrow} \\ \psi_{\uparrow} \end{pmatrix} = \begin{pmatrix} \sqrt{n_{\downarrow}(\mathbf{r}, t)} e^{i\phi_{\downarrow}(\mathbf{r}, t)} \\ \sqrt{n_{\uparrow}(\mathbf{r}, t)} e^{i\phi_{\uparrow}(\mathbf{r}, t)} \end{pmatrix} \quad (3.9)$$

where  $\psi_{\downarrow}$  and  $\psi_{\uparrow}$  are the respective condensate wavefunctions of the two components,  $n_{\downarrow}(n_{\uparrow})$  is the condensate density,  $\phi_{\downarrow}(\phi_{\uparrow})$  is the phase of the wavefunction,  $\mathbf{r}$  is the position, and  $t$  is time. The spatial integration of  $(n_{\downarrow} + n_{\uparrow})$  gives the total atom number  $N$ . The two-body interactions between atoms are described by the nonlinear interaction term  $V_{\text{int}}$ , which can be written in the basis of  $\{\psi_{\downarrow}, \psi_{\uparrow}\}$ :

$$V_{\text{int}} = \begin{pmatrix} g_{\downarrow\downarrow}|\psi_{\downarrow}|^2 + g_{\downarrow\uparrow}|\psi_{\uparrow}|^2 & 0 \\ 0 & g_{\uparrow\uparrow}|\psi_{\uparrow}|^2 + g_{\uparrow\downarrow}|\psi_{\downarrow}|^2 \end{pmatrix} \quad (3.10)$$

The interaction parameters are given by

$$g_{\downarrow\downarrow} = g_{\uparrow\uparrow} = g_{\uparrow\downarrow} = \frac{4\pi\hbar^2(c_0 + c_2)}{m} \quad (3.11)$$

and

$$g_{\uparrow\uparrow} = \frac{4\pi\hbar^2 c_0}{m} \quad (3.12)$$

The spin-dependent  $s$ -wave scattering lengths for  $^{87}\text{Rb}$  atoms are  $c_0$  and  $c_0 + c_2$ , where  $c_2 = -0.46a_0$  and  $c_0 = 100.86a_0$  ( $a_0$  is the Bohr radius). The initial state of the SO-coupled BEC is obtained by using the imaginary time propagation method. Next we

change  $\Omega_I$  to a final value  $\Omega_F$  in  $t_E = 1.0$  ms to simulate the spin-dependent synthetic electric fields. Eq. (3.7) is used to simulate the dynamics of the BECs. The momentum space wavefunctions are calculated from the Fourier transformation of the real space wave functions. The squared amplitude of the momentum space wavefunctions is used to obtain the time-dependent momentum space density distributions shown in e.g. Fig. 3.9a, b.

For the GPE simulations in Fig. 3.9, we have checked that moderate variations in these parameters (as in our experimental data) do not affect our conclusions (while they can slightly change the  $1/Q$  values, for example, larger  $1/Q$  found for higher  $N_c$ ). The simulations also reveal additional interesting features, such as the appearance of the opposite momentum (back-scattering) peak for each spin component in Fig. 3.9a, b, which are not well resolved in our experimental data.

### 3.6.2 Different forms of energies in GPE simulations

Using Eq. (3.9), the total energy density  $\varepsilon$  (the spatial integration of which gives the total energy of the system) can be expressed as the sum of several terms [2, 79]:

$$\varepsilon = \varepsilon_1 + \varepsilon_2 + \varepsilon_3 + \varepsilon_4 + \varepsilon_5 \quad (3.13)$$

$$\varepsilon_1 = \frac{\hbar^2}{8mn_\downarrow}(\nabla n_\downarrow)^2 + \frac{\hbar^2}{8mn_\uparrow}(\nabla n_\uparrow)^2 \quad (3.14)$$

$$\varepsilon_2 = \frac{\hbar^2 n_\downarrow}{2m}(\nabla \phi_\downarrow)^2 + \frac{\hbar^2 n_\uparrow}{2m}(\nabla \phi_\uparrow)^2 + \frac{\hbar^2 k_r}{m}(n_\downarrow \nabla_y \phi_\downarrow - n_\uparrow \nabla_y \phi_\uparrow) + \frac{\hbar^2 k_r^2}{2m}(n_\downarrow + n_\uparrow) \quad (3.15)$$

$$\varepsilon_3 = \Omega \sqrt{n_\downarrow n_\uparrow} \cos(\phi_\downarrow - \phi_\uparrow) \quad (3.16)$$

$$\varepsilon_4 = \frac{g_{\downarrow\downarrow}}{2}(n_\downarrow)^2 + \frac{g_{\uparrow\uparrow}}{2}(n_\uparrow)^2 + g_{\downarrow\uparrow} n_\downarrow n_\uparrow \quad (3.17)$$

$$\varepsilon_5 = V_{\text{trap}}(n_\downarrow + n_\uparrow) \quad (3.18)$$

In the above equations,  $\nabla = \frac{\partial}{\partial x} \hat{x} + \frac{\partial}{\partial y} \hat{y} + \frac{\partial}{\partial z} \hat{z}$  and  $\nabla_y = \frac{\partial}{\partial y}$ . We will introduce  $\varepsilon_1$  to  $\varepsilon_5$  one by one in the following. The expression of  $\varepsilon_1$  in Eq. (3.14) is the density of the total (including two spin components) quantum pressure (QP), which is a type of kinetic energy (KE) associated with the spatial variation of the condensate density.

An imaginary term  $-\frac{i\hbar^2 k_r}{m} \nabla_y (n_\downarrow - n_\uparrow)$  appearing in the derivation of  $\varepsilon_1$  is not shown in Eq. (3.14) as its spatial integration (for a confined system) is zero and thus has no contribution to the energy. The expression of  $\varepsilon_2$  in Eq. (3.15) is the density of the sum of two types of KE, the total CoM KE (sum of the CoM KE of both bare spin components) and the total local current kinetic energy (LC KE). Both the CoM KE and LC KE are associated with the spatial variation of the phase of wavefunctions. The sum of the three types of kinetic energy (total QP, total CoM KE, and total LC KE) gives the total KE. That is, the sum of  $\varepsilon_1$  and  $\varepsilon_2$  is the density of the total KE. In the following, we derive explicit expressions for the CoM KE and LC KE. For CoM KE, it is nonzero only in the  $y$  direction because the SDM is along the  $y$  direction. Thus, the expression of CoM KE is:

$$\text{CoM KE} = \frac{1}{2m} (\langle \psi_\downarrow | \hbar \hat{k}_\downarrow | \psi_\downarrow \rangle^2 + \langle \psi_\uparrow | \hbar \hat{k}_\uparrow | \psi_\uparrow \rangle^2) \quad (3.19)$$

$$\begin{aligned} &= \frac{\hbar^2}{2m} (\langle \psi_\downarrow | \nabla_y \phi_\downarrow | \psi_\downarrow \rangle^2 + \langle \psi_\uparrow | \nabla_y \phi_\uparrow | \psi_\uparrow \rangle^2) \quad (3.20) \\ &+ \frac{\hbar^2 k_r}{m} (\langle \psi_\downarrow | \nabla_y \phi_\downarrow | \psi_\downarrow \rangle - \langle \psi_\uparrow | \nabla_y \phi_\uparrow | \psi_\uparrow \rangle) \\ &+ \langle \Psi | \frac{\hbar^2 k_r^2}{2m} | \Psi \rangle, \end{aligned}$$

where  $\hbar \hat{k}_\downarrow = \hbar(\hat{q}_y + k_r) = \hbar(-i\frac{\partial}{\partial y} + k_r)$  ( $\hbar \hat{k}_\uparrow = \hbar(\hat{q}_y - k_r) = \hbar(-i\frac{\partial}{\partial y} - k_r)$ ) is the momentum operator along  $\hat{y}$  for the spin down (up) component, and the last term in Eq. (3.20) is simply  $N \frac{\hbar^2 k_r^2}{2m}$ . Recall that  $\varepsilon_2$  in Eq. (3.15) is the density of the sum of CoM KE and LC KE. Thus, the expression of LC KE can be obtained by subtracting the expression of CoM KE in Eq. (3.20) from the spatial integration of  $\varepsilon_2$  (Eq. (3.15)):

$$\text{LC KE} = \frac{\hbar^2}{2m} (\langle \psi_\downarrow | (\nabla \phi_\downarrow)^2 | \psi_\downarrow \rangle + \langle \psi_\uparrow | (\nabla \phi_\uparrow)^2 | \psi_\uparrow \rangle) \quad (3.21)$$

$$\begin{aligned} &- \frac{\hbar^2}{2m} (\langle \psi_\downarrow | \nabla_y \phi_\downarrow | \psi_\downarrow \rangle^2 + \langle \psi_\uparrow | \nabla_y \phi_\uparrow | \psi_\uparrow \rangle^2) \\ &= \frac{\hbar^2}{2m} (\Delta(\nabla_x \phi_\downarrow) + \Delta(\nabla_x \phi_\uparrow) + \Delta(\nabla_z \phi_\downarrow) \quad (3.22) \\ &+ \Delta(\nabla_z \phi_\uparrow) + \Delta(\nabla_y \phi_\downarrow) + \Delta(\nabla_y \phi_\uparrow)), \end{aligned}$$

where  $\Delta(\nabla_{x,y,z}\phi_{\downarrow,\uparrow})$  is the standard deviation of  $\nabla_{x,y,z}\phi_{\downarrow,\uparrow}$ , and note  $\langle \nabla_{x,z}\phi_{\downarrow,\uparrow} \rangle = 0$ . Thus, if the wavefunction is a plane wave with a phase  $\phi = q_y y$ , its LC KE is zero. For collective modes that do not have the CoM KE (for example, the quadrupole modes), the associated motional (kinetic) energy can be accounted for by LC KE and QP. The expression of  $\varepsilon_3$  in Eq. (3.16) is the density of the Raman energy, associated with the Raman coupling  $\Omega$ . The expression of  $\varepsilon_4$  in Eq. (3.17) is the density of the sum of the bare intraspecies and interspecies interaction energies. The expression of  $\varepsilon_5$  in Eq. (3.18) is the density of the total potential energy.

To calculate the time ( $t_{\text{hold}}$ ) evolution of the various forms of energies, we can in principle integrate the corresponding time-dependent energy densities over the real space. In practice, for the kinetic energy part we only perform spatial integration of  $\varepsilon_2$  (given by Eq. (3.15)). For convenience of computation, the total KE, total CoM KE, total LC KE, and total QP are calculated using a different approach taking advantages of the (quasi)momentum space representation of the quantum mechanical wavefunctions and operators. Specifically, the total KE is calculated by  $\langle \psi_{\downarrow}(\mathbf{q}, t) | \frac{(\hbar\hat{k}_{\downarrow})^2 + \hat{p}_x^2 + \hat{p}_z^2}{2m} | \psi_{\downarrow}(\mathbf{q}, t) \rangle + \langle \psi_{\uparrow}(\mathbf{q}, t) | \frac{(\hbar\hat{k}_{\uparrow})^2 + \hat{p}_x^2 + \hat{p}_z^2}{2m} | \psi_{\uparrow}(\mathbf{q}, t) \rangle$  in the quasimomentum space, where  $\hbar\hat{k}_{\downarrow} = \hbar(\hat{q}_y + k_r)$  ( $\hbar\hat{k}_{\uparrow} = \hbar(\hat{q}_y - k_r)$ ) is the momentum operator along  $\hat{y}$  for the spin down (up) component, and  $\psi_{\downarrow,\uparrow}(\mathbf{q}, t)$  is the momentum-space representation of the wavefunctions (in the two directions not affected by SOC,  $x$  and  $z$ , we simply have  $\hbar q_x = p_x$  and  $\hbar q_z = p_z$ ). Similarly, the total CoM KE is calculated in the quasimomentum space using Eq. (3.19). The total LC KE is calculated by subtracting the calculated total CoM KE from the spatial integration of  $\varepsilon_2$  (Eq. (3.15)). The total QP is calculated indirectly by subtracting the spatial integration of  $\varepsilon_2$  from the total KE.

The total Raman energy is calculated by the spatial integration of  $\varepsilon_3$  (Eq. (3.16)). The total bare intraspecies ( $g_{\uparrow\uparrow}$  and  $g_{\downarrow\downarrow}$ ) and interspecies ( $g_{\uparrow\downarrow}$ ) interaction energies are calculated by the spatial integration of the corresponding terms in  $\varepsilon_4$  (Eq. (3.17)). The total interaction energy is calculated as the sum of the bare intraspecies and interspecies interaction energies. The total potential energy is calculated by the spatial

integration of  $\varepsilon_5$  (Eq. (3.18)). Lastly, the total energy of the system is calculated as the sum of the total Raman energy, total potential energy, total interaction energy, and total KE.

We note that even though our GPE simulations do not treat thermalization and thermal energies, the calculated different forms of condensate energies and their time evolution still provide valuable insights to understand the dynamical processes involved in the SDM. The GPE calculated different forms of energies shown in Fig. 3.11 and discussed in the associated texts below refer to the energies per particle (i.e. the calculated energies divided by the total atom number  $N$ ).

In Fig. 3.11a, the total energy is a constant during  $t_{\text{hold}}$ , confirming the conservation of the total energy. In Fig. 3.11b, the total Raman energy has relatively small variations during  $t_{\text{hold}}$ . In Fig. 3.11c, the total potential energy in dressed cases has smaller variations during  $t_{\text{hold}}$  compared with that in the bare case. In Fig. 3.11d, the time evolution of the total interaction energy at different  $\Omega_F$  possesses a complicated behavior, mainly due to the complicated dynamics of the densities of the two spin components as well as their spatial overlap (see Movies 2, 4, 5 in section 3.7).

Fig. 3.11e-h shows the time evolution of the calculated total KE, total CoM KE, total QP, and total LC KE at different  $\Omega_F$ , respectively. When  $\Omega_F$  is larger, the total CoM KE (Fig. 3.11f) exhibits a faster damping while QP as well as LC KE exhibit a faster increase (Fig. 3.11g, h, focusing on the relatively early stage of SDM) presumably due to the enhancement of the interference, immiscibility, and effective interaction between the two dressed spin components.

Fig. 3.11i-k shows the time evolution of the calculated intraspecies and interspecies interaction energies at different  $\Omega_F$ . Note that the interaction energies are relatively small compared to other forms of energies, but are essential for the damping mechanisms as discussed in Sections 3.6 and 3.8.

### 3.6.3 Calculation of nonorthogonality, effective interaction parameters, and immiscibility

The interactions between atoms in bare spinor BECs are characterized by the interspecies ( $g_{\uparrow\downarrow}, g_{\downarrow\uparrow}$ ) and intraspecies ( $g_{\uparrow\uparrow}, g_{\downarrow\downarrow}$ ) interaction parameters, where  $g_{\downarrow\downarrow} = g_{\downarrow\uparrow} = g_{\uparrow\downarrow} = \frac{4\pi\hbar^2(c_0+c_2)}{m}$ ,  $g_{\uparrow\uparrow} = \frac{4\pi\hbar^2c_0}{m}$ ,  $c_2 = -0.46a_0$ , and  $c_0 = 100.86a_0$  ( $a_0$  is the Bohr radius) for  $^{87}\text{Rb}$  atoms in our case. For a dressed BEC, in which  $|\uparrow'\rangle$  is at some quasimomentum  $\hbar q_y$  ( $> 0$ ) and  $|\downarrow'\rangle$  is at  $-\hbar q_y$  in the ground dressed band at  $\Omega$  (in the two-state picture described by Eq. (3.1) with  $\delta_R = 0$ ), the effective interspecies ( $g_{\uparrow'\downarrow'} = g_{\downarrow'\uparrow'}$ ) and intraspecies ( $g_{\uparrow'\uparrow'}, g_{\downarrow'\downarrow'}$ ) interaction parameters can be expressed in terms of the bare interaction  $g$ -parameters:

$$g_{\uparrow'\uparrow'} = \frac{g_{\uparrow\uparrow}}{4}(1 + \cos \theta_{q_y})^2 + \frac{g_{\downarrow\downarrow}}{4}(1 - \cos \theta_{q_y})^2 + \frac{g_{\uparrow\downarrow}}{2}(1 - \cos^2 \theta_{q_y}) \quad (3.23)$$

$$g_{\downarrow'\downarrow'} = \frac{g_{\uparrow\uparrow}}{4}(1 - \cos \theta_{q_y})^2 + \frac{g_{\downarrow\downarrow}}{4}(1 + \cos \theta_{q_y})^2 + \frac{g_{\uparrow\downarrow}}{2}(1 - \cos^2 \theta_{q_y}) \quad (3.24)$$

$$g_{\uparrow'\downarrow'} = \frac{g_{\uparrow\uparrow} + g_{\downarrow\downarrow}}{2}(1 - \cos^2 \theta_{q_y}) + g_{\uparrow\downarrow} \quad (3.25)$$

where  $\cos \theta_{q_y} = (\hbar^2 q_y k_r / m) / \sqrt{\hbar^4 q_y^2 k_r^2 / m^2 + (\Omega/2)^2}$ . The dressed spin states  $|\downarrow'\rangle$  at  $-\hbar q_y$  and  $|\uparrow'\rangle$  at  $\hbar q_y$  in the ground dressed band can be expressed as

$$|\downarrow'\rangle = \begin{pmatrix} \cos(\frac{\theta_{q_y}}{2}) \\ -\sin(\frac{\theta_{q_y}}{2}) \end{pmatrix} \quad (3.26)$$

$$|\uparrow'\rangle = \begin{pmatrix} \sin(\frac{\theta_{q_y}}{2}) \\ -\cos(\frac{\theta_{q_y}}{2}) \end{pmatrix} \quad (3.27)$$

in the bare spin basis of  $\{|\downarrow\rangle, |\uparrow\rangle\}$ . Using Eqs. (3.26, 3.27), we can further obtain

$$\langle \uparrow' | \downarrow' \rangle = \sin \theta_{q_y} = (\Omega/2) / \sqrt{\hbar^4 q_y^2 k_r^2 / m^2 + (\Omega/2)^2} \quad (3.28)$$

which characterizes the nonorthogonality (and thus the interference) between the two dressed spin states (where  $|\uparrow'\rangle$  is located at  $\hbar q_y$  and  $|\downarrow'\rangle$  is located at  $-\hbar q_y$

in the ground dressed band at  $\Omega$ ). Fig. 3.10a plots such nonorthogonality versus quasimomentum for various  $\Omega$ .

Note that  $\theta_{q_y}$  (which is between 0 and  $\pi/2$  in our case) characterizes the degree of bare spin mixing of a single dressed spin state (Eqs. (3.26, 3.27)) as well as the nonorthogonality (due to the bare spin mixing, see Eq. (3.28)) between the two dressed spin states. As we can see, either decreasing  $\Omega$  or increasing  $q_y$  would decrease  $\theta_{q_y}$  (or increase  $\cos \theta_{q_y}$ ). When  $\theta_{q_y} \rightarrow 0$  (or  $\cos \theta_{q_y} \rightarrow 1$ ), all the dressed spin states would approach the corresponding bare spin states, i.e.,  $|\uparrow'\rangle \rightarrow |\uparrow\rangle$  and  $|\downarrow'\rangle \rightarrow |\downarrow\rangle$ , thus the nonorthogonality  $\langle \uparrow' | \downarrow' \rangle \rightarrow 0$ . In addition, all the effective interaction parameters would approach the corresponding bare values, i.e.,  $g_{\uparrow'\uparrow'} \rightarrow g_{\uparrow\uparrow}$ ,  $g_{\downarrow'\downarrow'} \rightarrow g_{\downarrow\downarrow}$ , and  $g_{\uparrow'\downarrow'} \rightarrow g_{\uparrow\downarrow}$ .

On the other hand, either increasing  $\Omega$  or decreasing  $q_y$  would increase  $\theta_{q_y}$  towards  $\pi/2$  (or decrease  $\cos \theta_{q_y}$ ), thus enhancing the bare spin mixing, nonorthogonality and  $g_{\uparrow'\downarrow'}$ . When  $\theta_{q_y} \rightarrow \pi/2$  (or  $\cos \theta_{q_y} \rightarrow 0$ ),  $g_{\uparrow'\uparrow'} \rightarrow \frac{g_{\uparrow\uparrow}}{4} + \frac{g_{\downarrow\downarrow}}{4} + \frac{g_{\uparrow\downarrow}}{2}$ ,  $g_{\downarrow'\downarrow'} \rightarrow \frac{g_{\uparrow\uparrow}}{4} + \frac{g_{\downarrow\downarrow}}{4} + \frac{g_{\uparrow\downarrow}}{2}$ , and  $g_{\uparrow'\downarrow'} \rightarrow \frac{g_{\uparrow\uparrow}}{2} + \frac{g_{\downarrow\downarrow}}{2} + g_{\uparrow\downarrow}$ . Therefore,  $g_{\uparrow'\downarrow'} \rightarrow 2g_{\uparrow'\uparrow'}$  or  $2g_{\downarrow'\downarrow'}$ , which is the upper bound of the effective interspecies interaction parameter. Fig. 3.10b, c shows the effective interaction parameters normalized by  $g_{\uparrow\uparrow}$  versus quasimomentum  $\hbar q_y$  at  $\Omega = 0.1 E_r$  and  $\Omega = 1.26 E_r$ , respectively. When  $\Omega$  increases or  $q_y$  decreases,  $g_{\uparrow'\downarrow'}$  increases while  $g_{\uparrow'\uparrow'}$  and  $g_{\downarrow'\downarrow'}$  almost remain at the bare values. As  $q_y \rightarrow 0$  at any finite  $\Omega$ ,  $g_{\uparrow'\downarrow'}$  approaches the upper limit  $2g_{\uparrow'\uparrow'}$  or  $2g_{\downarrow'\downarrow'}$ .

In the case of SDM, assume that in the ground dressed band at  $\Omega$ ,  $|\uparrow'\rangle$  is located at  $\hbar q_y$  and  $|\downarrow'\rangle$  is located at  $-\hbar q_y$  at  $t_{\text{hold}}$ , we may use the immiscibility metric [108]

$$\eta = (g_{\uparrow'\downarrow'}^2 - g_{\uparrow'\uparrow'}g_{\downarrow'\downarrow'})/g_{\uparrow\uparrow}^2 \quad (3.29)$$

to understand how  $\Omega$  may modify the miscibility ( $\eta < 0$ ) or immiscibility ( $\eta > 0$ ) between  $|\uparrow'\rangle$  and  $|\downarrow'\rangle$ .

### 3.7 Control simulations, phase of BEC wavefunctions in SDM, and movies

#### 3.7.1 Effect of immiscibility on SDM

We have used GPE simulations for the bare case with intentionally modified interactions to study the effect of immiscibility on the SDM. Fig. 3.12 shows the damping of the relative momentum  $\hbar k_{\text{spin}}$  of the SDM for 5 cases without and with modified interactions. Case 1 is the original bare case without modification of interactions, with the intraspecies and interspecies interaction parameters  $g_{ii}$  and  $g_{ij}$  ( $i, j = \uparrow, \downarrow$  and  $i \neq j$ ) given by Eqs. (3.11, 3.12), respectively. Case 2 corresponds to the same intraspecies interaction parameter  $\tilde{g}_{ii} = g_{ii}$  and a modified interspecies interaction parameter  $\tilde{g}_{ij} = 1.5g_{ij}$ . Case 3 corresponds to  $\tilde{g}_{ii} = 1.5g_{ii}$  and  $\tilde{g}_{ij} = 1.5g_{ij}$ . Case 4 corresponds to  $\tilde{g}_{ii} = 1.5g_{ii}$  and  $\tilde{g}_{ij} = g_{ij}$ . Case 5 corresponds to  $\tilde{g}_{ii} = 1.8g_{ii}$  and  $\tilde{g}_{ij} = g_{ij}$ . Such modification of interactions is done by immediately increasing the interaction  $g$ -parameters to the desired values as soon as  $\Omega$  is changed from  $\Omega_I$  to  $\Omega_F$ . Among all the cases, only case 2 is immiscible and we observe that case 2 possesses the strongest damping, thus suggesting that immiscibility is particularly effective to enhance the damping of the SDM. This is further supported by the observation that case 4 and case 5 have similar damping which is less than the original bare case (case 1), presumably because these two cases are more miscible than case 1. We have also calculated and listed the immiscibility metric  $\eta$  (defined in Eq. (3.29)) in Fig. 3.12 for the various cases. Note that simply increasing all the interaction  $g$ -parameters without notably changing  $\eta$  can also enhance the SDM damping, as suggested by the observation that the damping in case 3 ( $\eta = -0.0045$ , miscible) is stronger than that in case 1 ( $\eta = -0.0045$ , miscible) but is not as prominent as in case 2 ( $\eta = 1.2341$ , immiscible).

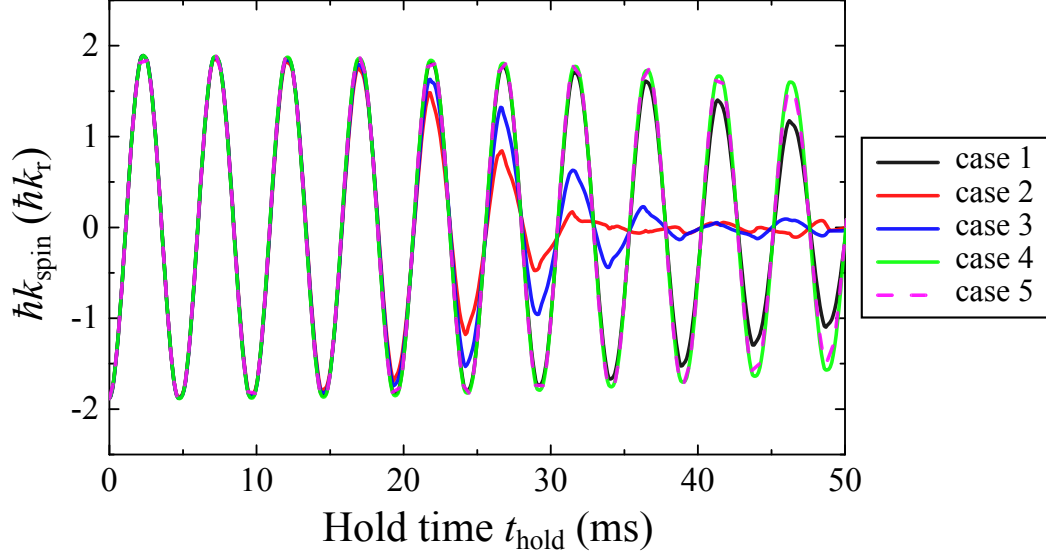


Fig. 3.12. **Effect of modified bare interactions and interspecies immiscibility on SDM damping.** In GPE simulations for the bare case SDM, we can change the original interaction parameters  $g_{ii}$  and  $g_{ij}$  to new values  $\tilde{g}_{ii}$  and  $\tilde{g}_{ij}$  respectively, where  $i, j = \uparrow$  or  $\downarrow$  and  $i \neq j$ . The relative momentum  $\hbar k_{\text{spin}}$  versus  $t_{\text{hold}}$  are shown for five different cases with the corresponding modified interaction parameters and immiscibility metric  $\eta = (\tilde{g}_{\uparrow\downarrow}^2 - \tilde{g}_{\uparrow\uparrow}\tilde{g}_{\downarrow\downarrow})/\tilde{g}_{\uparrow\uparrow}^2$  listed in Table 3.1 below. The GPE calculations here are performed by Chunlei Qu and Chuanwei Zhang.

Table 3.1

**Cases with different modified interaction parameters and the immiscibility metric.** For each case, the corresponding immiscibility metric  $\eta = (\tilde{g}_{\uparrow\downarrow}^2 - \tilde{g}_{\uparrow\uparrow}\tilde{g}_{\downarrow\downarrow})/\tilde{g}_{\uparrow\uparrow}^2$  is calculated. The corresponding simulated SDM for each case is shown in Fig. 3.12 above.

Case number	$\tilde{g}_{ii}/g_{ii}$	$\tilde{g}_{ij}/g_{ij}$	$\eta$
Case 1	1.0	1.0	-0.0045 (miscible)
Case 2	1.0	1.5	1.2341 (immiscible)
Case 3	1.5	1.5	-0.0045 (miscible)
Case 4	1.5	1.0	-0.5550 (miscible)
Case 5	1.8	1.0	-0.6896 (miscible)

---

### 3.7.2 Effect of interference on the relative motion between two colliding BECs

To investigate the effect of interference on the relative motion between two colliding BECs, we have performed another set of control GPE simulations, in which two (bare) BECs are initially in a double well trap such that they are separated in real space by a potential barrier. Then, we change the double well trap to a single harmonic potential by suddenly removing the potential barrier at  $t_{\text{hold}} = 0$ , allowing the two BECs to collide and oscillate against each other in the  $y$  direction. We conduct the following simulations: case 1, the two BECs initially in the double well are in the same spin state (called the single spin case), with only one interaction parameter  $g = \frac{4\pi\hbar^2}{m}100a_0$ . Case 2, two BECs initially in the double well have orthogonal spin states ( $\downarrow$  and  $\uparrow$ ) with  $g_{\uparrow\uparrow} = g_{\downarrow\downarrow} = g_{\uparrow\downarrow} = g$  (called the two spin case; here all the interaction  $g$ -parameters are set to be the same to focus on the effect of interference. The cases where the interaction  $g$ -parameters are varied differently and the effect of immiscibility are also studied separately).

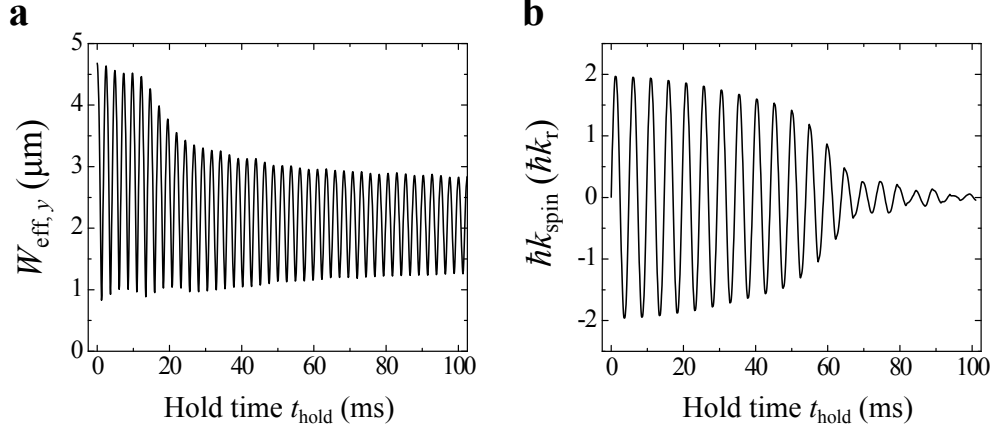


Fig. 3.13. **Effect of interference on the relative motion between two colliding BECs** (a) The effective width of the two BECs oscillating against each other in the  $y$  direction versus  $t_{\text{hold}}$  in the single spin case. (b) The relative momentum between the two orthogonal spin components versus  $t_{\text{hold}}$  in the two spin case. For (a, b), the two BECs are initially separated by the same potential barrier in the same double well structure. The barrier is then suddenly removed at  $t_{\text{hold}} = 0$  to initiate the dynamics. Note that the oscillation frequency in (a) is twice the frequency in (b) due to the definition of  $W_{\text{eff},y}$ . The GPE calculations here are performed by Chunlei Qu and Chuanwei Zhang.

The damping of the relative motion in case 1 is characterized by the  $t_{\text{hold}}$ -dependent effective width ( $W_{\text{eff},y}$ , shown in Fig. 3.13a) of the two BECs oscillating against each other in the  $y$  direction, where  $W_{\text{eff},y} = \sqrt{\langle y^2 \rangle}$  ( $\langle y^2 \rangle$  is the expectation value of  $y^2$  and is calculated using the whole wavefunction of the two BECs). In this case, we find that the relative motion almost damps out after  $t_{\text{hold}} = 30$  ms (when we can no longer observe any relative motion between *two* BECs, which have merged into one BEC; the relatively undamped remnant oscillations in the data after  $\sim 30$  ms reflect the breathing of width of this merged BEC. See [Movie 1](#)). On the other hand, in case 2 we observe prominent damping only after  $t_{\text{hold}} = 60$  ms (Fig. 3.13b). By comparing case 1 with case 2, we avoid the effect of immiscibility and investigate the effect purely due to the interference on damping. This suggests that the interference between the two colliding BECs can enhance the damping of the relative motion. In

addition, in the two spin case we have modified the interaction parameters similar to the cases in Fig. 3.12. These results also suggest that immiscibility is particularly effective to enhance the damping of SDM.

### 3.7.3 Effect of turning off interactions on the relative motion between two colliding BECs

To further investigate the role of interactions on the relative motion between two colliding BECs, we have performed three control GPE simulations where all the interaction parameters are set to zero (i.e.  $g = g_{\uparrow\uparrow} = g_{\downarrow\downarrow} = g_{\uparrow\downarrow} = 0$ ): (1) the bare case SDM. (2) the single spin case and the two spin case with two BECs initially in a double well as described in the previous section. (3) the dressed case SDM at  $\Omega_F = 1.3 E_F$ . The results of these cases are shown respectively in Figs. 3.14, 3.15, and 3.16. In all these non-interacting cases, we find that the relative motion between the two colliding BECs has no noticeable damping within the time of simulation. This suggests that interactions are essential for the damping mechanisms studied in this work.

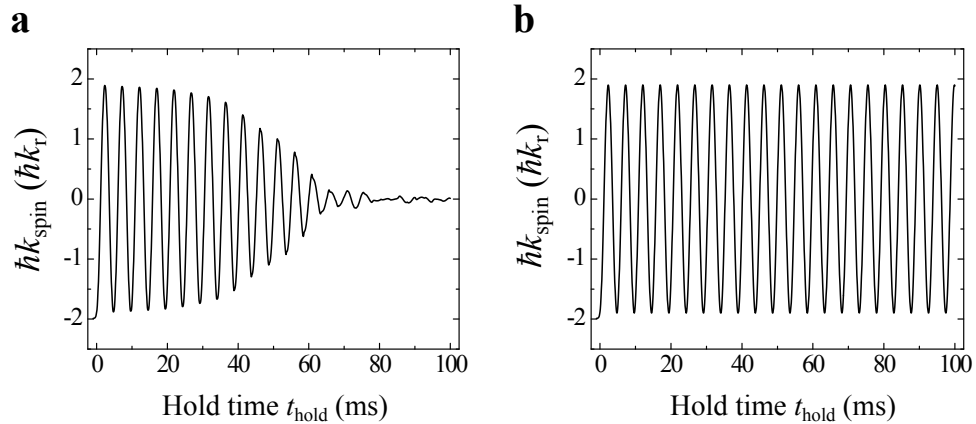


Fig. 3.14. **The bare case SDM with interactions in (a) and without interactions in (b).** The case (a) is the same simulation as the case of  $\Omega_F = 0$  in Fig. 3.3c but shown up to a longer time of 100 ms. The GPE calculations here are performed by Chunlei Qu and Chuanwei Zhang.

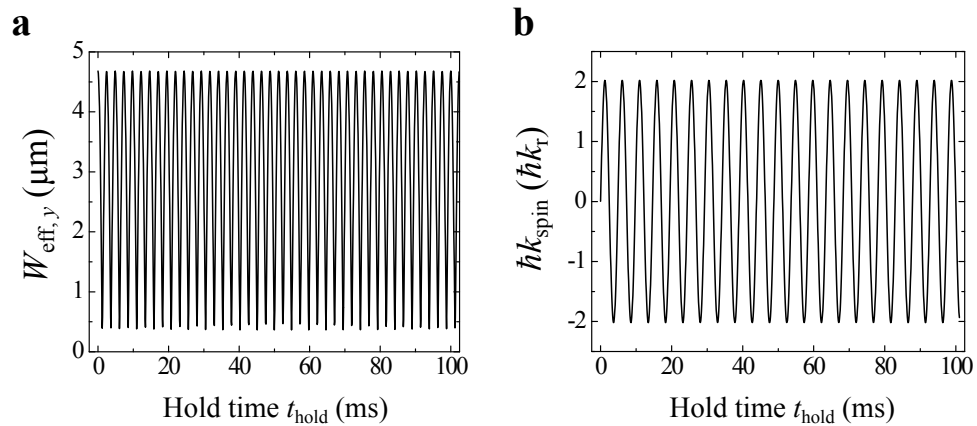


Fig. 3.15. **The two colliding bare BECs without interactions in the single spin case (a) and in the two spin case (b).** These simulations used the same parameters as in Fig. 3.13 except the interaction  $g$ -parameters have been set to zero. The GPE calculations here are performed by Chunlei Qu and Chuanwei Zhang.

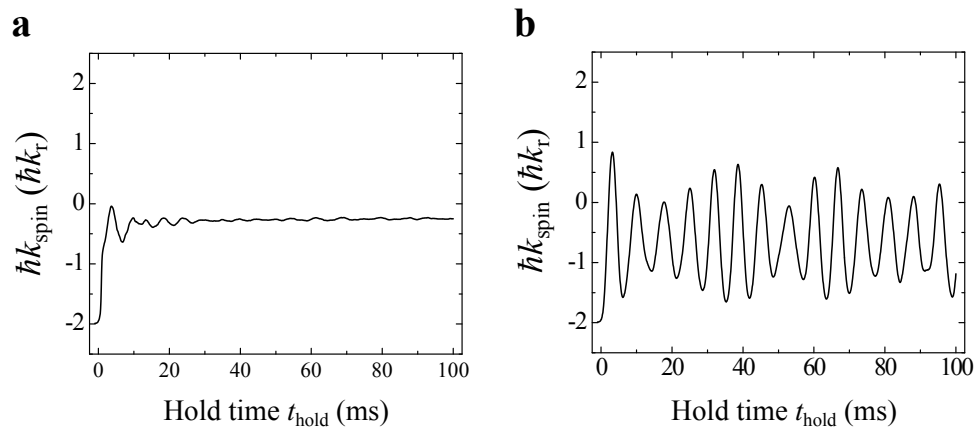
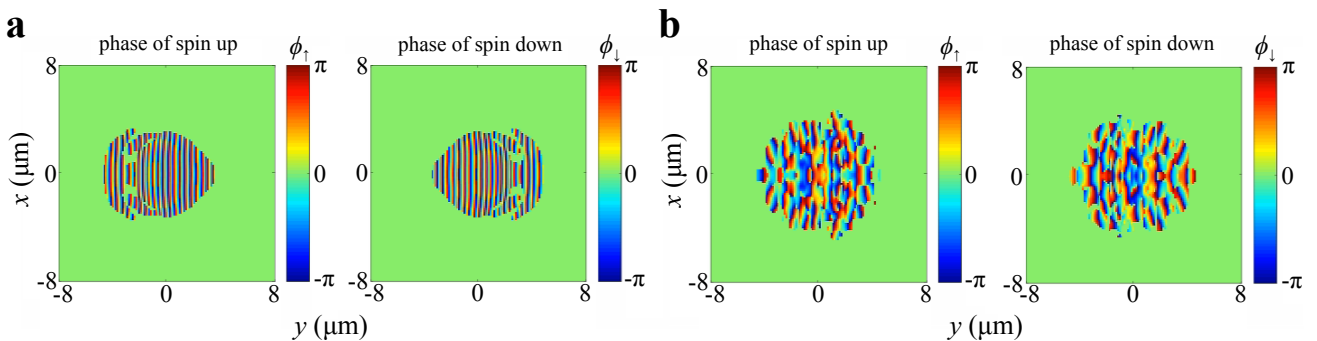


Fig. 3.16. **The dressed case SDM at  $\Omega_F = 1.3E_r$  with interactions in (a) and without interactions in (b).** The case (a) is the same simulation as the case of  $\Omega_F = 1.3 E_r$  in Fig. 3.9c but shown up to a longer time of 100 ms. The GPE calculations here are performed by Chunlei Qu and Chuanwei Zhang.

### 3.7.4 Spatial modulation in the phase of BEC wavefunctions in SDM.

Fig. 3.17 is an example showing the spatial modulation in the phase of BEC wavefunctions (Eq. (3.9)) at  $t_{\text{hold}} = 7.2$  ms during SDM for the bare case and the dressed case at  $\Omega_F = 1.3 E_r$  (snapshots taken from [Movie 3](#) and [Movie 6](#) below). We notice much less spatial variation in the gradient of the phase in the bare case than in the dressed case at  $\Omega_F = 1.3 E_r$ , suggesting that LC KE in the bare case is generally smaller than that in the dressed case at this time (consistent with Fig. 3.11h).



**Fig. 3.17. Spatial modulation in the phase of BEC wavefunctions.** The phase of the bare spin up and down components at  $t_{\text{hold}} = 7.2$  ms in SDM is plotted in the  $x$ - $y$  plane for (a) bare case, and (b) dressed case at  $\Omega_F = 1.3 E_r$ . Here,  $x$  and  $y$  are spatial coordinates. The GPE calculations here are performed by Chunlei Qu and Chuanwei Zhang.

### 3.7.5 Movies of GPE simulations for the SDM

The movies here are created by Chunlei Qu. When linked to the webpage for the following files, choose the web browser to watch it online or download the files. These movies are also downloadable from ref. [50].

[Movie 2](#)

[Movie 3](#)

[Movie 4](#)

[Movie 5](#)

[Movie 6](#)

Here, the momentum-space (in the  $k_x$ - $k_y$  plane) 2D density distributions (obtained by the integration over  $k_z$ , where  $\hbar k_{x(y,z)}$  is the mechanical momentum in the  $x(y,z)$  direction) of different bare spin components (separated vertically from each other for better visualization) are the Fourier transform of the real-space 2D densities (as those shown in Fig. 3.9). The momentum-space and real-space 1D atomic densities in the  $y$  direction (SOC direction) are obtained by integrating the momentum-space and real-space 2D densities over  $k_x$  and  $x$ , respectively. In addition, the snapshot shown in Fig. 3.17 for comparing the phase in the cases of  $\Omega_F = 0$  and  $\Omega_F = 1.3 E_r$  is taken from [Movie 3](#) and [Movie 6](#).

### 3.8 Discussion and conclusion

Previous studies in stationary SO-coupled BECs (located at ground dressed band minima) have found that increasing  $\Omega$  drives a miscible to immiscible phase transition at  $\Omega \sim 0.2 E_r$  due to the increased effective interspecies interaction (characterized by the interaction parameter  $g_{\uparrow\downarrow'}$ ) [37,38,103–105]. In the miscible phase, the two dressed spin components have substantial spatial overlap, where density modulations form. It is important to note that the effective interactions, immiscibility and interference between the two dressed spin components depend on the quasimomentum ( $\hbar q_y$ ) and  $\Omega_F$  (Fig. 3.10, see subsections below for details). Therefore, in the dynamical case studied here, these properties vary with time and can be notably different from those in the stationary case. During the SDM, the two dressed spin components are forced to collide due to  $E_\sigma$ .

This can give rise to interference-induced density modulations in their spatially overlapped region even when they are immiscible. In addition, the BECs during the SDM can be located away from the band minima and approach  $q_y = 0$ . For the two dressed spin components with quasimomenta  $\pm \hbar q_y$ , either increasing  $\Omega_F$  or decreasing  $|q_y|$  (towards 0) would increase  $\langle \uparrow' | \downarrow' \rangle$  (Fig. 3.10a), giving rise to stronger interference and more significant density modulations. Such increased non-orthogonality between the two dressed spin states also notably increases the effective interspecies interaction ( $g_{\uparrow'\downarrow'}$ ) to become even larger than the effective intraspecies interactions ( $g_{\uparrow'\uparrow'} \approx g_{\downarrow'\downarrow'}$ ) (Fig. 3.10b, c), enhancing further the immiscibility (Fig. 3.10d-f). For example, Fig. 3.10d shows the calculated immiscibility metric (see subsections below),  $\eta = (g_{\uparrow'\downarrow'}^2 - g_{\uparrow'\uparrow'}g_{\downarrow'\downarrow'}) / g_{\uparrow'\uparrow'}^2$ , versus  $\hbar q_y$  corresponding to Fig. 3.10b. Notice that when  $\Omega$  is large enough,  $|\uparrow'\rangle$  and  $|\downarrow'\rangle$  can become immiscible in the whole range of quasimomentum that a BEC can access during the SDM. Fig. 3.10e shows  $\eta$  versus  $\Omega$  at various  $\hbar q_y$ . We see that as  $\Omega$  becomes larger or  $q_y$  becomes smaller, the two dressed spin components can become more immiscible (i.e.  $\eta$  becomes more positive) until  $\eta$  reaches the maximum value set by the upper bound of  $g_{\uparrow'\downarrow'}$ . Fig. 3.10f zooms in the region of small  $\Omega$  in Fig. 3.10e to focus on the sign change of  $\eta$  from negative to positive, which indicates the miscible to immiscible transition. Note that the red dot-dashed line (for  $q_y = q_{\sigma \min}$ ) corresponds to two dressed spin components located respectively at the band minima  $q_{\sigma \min}$ , showing the well-known miscible to immiscible transition around  $0.2 E_r$  for a stationary SO-coupled BEC. In the dynamical case studied here, BECs can be located away from the band minima and approach  $q_y = 0$ , becoming immiscible even when  $\Omega < 0.2 E_r$  for small enough  $q_y$ .

We have performed several additional control GPE simulations, showing that the presence or the enhancement of any of these three factors can increase the damping of the relative motion between two colliding BECs: (1) interference (Fig. 3.13 and Movie 1 in section 3.7), (2) immiscibility (Fig. 3.12 and Table 1 in section 3.7), and (3) interactions (Figs. 3.12, 3.14, 3.15, 3.16 and Table 3.1 in section 3.7), presumably by distorting the BEC wavefunctions (see Movies 1-6 in section 3.7) irreversibly in

the presence of interactions to decrease the CoM kinetic energy while increasing the quantum pressure and the local current kinetic energy. Therefore, enhanced immiscibility, interference, and interactions can all increase the damping of the SDM. For simulations in the absence of interactions, we do not observe irreversible damping within the simulation time of 100 ms (Figs. 3.14, 3.15, 3.16 in section 3.7), suggesting that the interactions play an essential role for the damping mechanisms.

The physical mechanisms and processes revealed in our work may provide insights to understand spin transport in interacting SO-coupled systems. Our experiment also provides an exemplary study of the evolution of a quantum many-body system, including the generation and decay of collective excitations, following a non-adiabatic parameter change (quench). Such quench dynamics has been of great interest to study many outstanding questions in many-body quantum systems. For example, how such a system, initially prepared in the ground state but driven out of equilibrium due to a parameter quench that drives the system across a quantum phase transition, would evolve to the new ground state or thermalize has attracted great interests (see, e.g., a recent study where coherent inflationary dynamics has been observed for BECs crossing a ferromagnetic quantum critical point [109]). In our case, the sudden reduction of  $\Omega$  in the Hamiltonian Eq. (3.1) excites the coherent spin current, whose relaxation is strongly affected by SOC and is related to the SDM damping as well as thermalization. Besides, the relaxation may be accompanied by the generation of other collective excitations such as BEC shape oscillations. Furthermore, compared to the bare case, the SOC-enhanced damping of the SDM notably reduces the collision-induced thermalization of the BEC, resulting in a higher condensate fraction left in the BEC. This condensate part exhibits a more rapid localization of its CoM motion, which may be more effectively converted to other types of excitations (associated with the SOC-enhanced distortion of the BEC wavefunctions). These features suggest that SOC opens pathways for our interacting quantum system to evolve that are absent without interactions, in our case providing new mechanisms for the spin current relaxation. Experiments on SO-coupled BECs, where many parameters can be well

controlled in real time and with the potential of adding other types of synthetic gauge fields, may offer rich opportunities to study nonequilibrium quantum dynamics [110], such as Kibble-Zurek physics while quenching through quantum phase transitions [111], and superfluidity [63, 77] in SO-coupled systems.

### 3.9 Note

The SDM measurements in a SO-coupled BEC were first performed by Robert Niffenegger [112], a former graduate student in our lab. However, these earlier measurements have many issues such as atom number calibration, trap frequency calibration, and severe Raman laser induced heating (leading to notable generation of thermal components not related to the SDM), which complicate the interpretations of the results. My labmate David Blasing and I have redesigned and reconstructed the experimental setup of the Raman laser. In particular, we have significantly reduced the Raman laser induced heating by adding an optical grating in the Raman laser system for spectral cleaning, such that the lifetime of a BEC in the presence of the Raman laser is improved from  $\leq 30$  ms (in those earlier measurements) to hundreds of ms (in the work presented in this chapter and ref. [50]). Details and characterization of our Raman laser have been addressed in subsection 1.2.2 in Chapter 1. In addition, I have improved the experimental procedures (e.g. a long initial state preparation to let the system equilibrate), and performed new and systematic measurements (e.g. nearly identical atom number and condensate fraction prepared at the beginning of SDM measurements at various Raman couplings) numerous times along with many control experiments. These new improvements and measurements are presented in this thesis and ref. [50].

## 4. A BOSE-EINSTEIN CONDENSATE WITH EMERGENT TOPOLOGICAL LATTICES ON A SYNTHETIC HALL CYLINDER

Results presented in this chapter have been submitted for publication with a preprint [\[113\]](#).

### 4.1 Introduction and motivation

Interplay between matter and fields in physical spaces with nontrivial geometries is central to various disciplines such as general relativity and cosmology [\[114\]](#), photonics [\[115, 116\]](#), and condensed matter [\[117\]](#). It can give rise to intriguing phenomena unattainable in planar spaces, ranging from superfluids carrying unusual vortices on curved manifolds [\[118, 119\]](#) to degenerate many-body ground states on a quantum Hall torus [\[120\]](#). However, realizing such spaces is often impeded by experimental challenges. For example, generating a net magnetic flux through the cylindrical surface of a nanotube is difficult, even impossible for closed surfaces because magnetic monopoles may not exist in nature. Highly controllable atomic systems [\[42, 62, 121\]](#) hold promises to explore phenomena inaccessible in conventional systems. Here, we realize a Bose-Einstein condensate (BEC) on a synthetic cylindrical surface, composed of a real spatial dimension and a curved synthetic dimension formed by cyclically-coupled atomic spin states, subject to a net radial synthetic magnetic flux. The BEC on such a Hall cylinder develops symmetry-protected topological states absent in the planar-space counterpart. We observe Bloch oscillations of the BEC with doubled periodicity of the band structure, analogous to traveling on a Möbius strip in momentum space, reflecting band crossings protected by a nonsymmorphic symmetry that underlines the emergent crystalline order in the BEC wavefunction. We further

demonstrate such topological operations as gapping the band crossings and unzipping the cylinder. Our work manifests emergence of topological states stemming from manipulating the geometry of space, opening the door to engineering synthetic gauge fields in spaces with a wide range of geometries and observing unprecedented phenomena, such as intriguing topological states of matter, inherent to such spaces.

## 4.2 Experimental set-up for realizing a synthetic Hall cylinder

Engineering synthetic gauge fields [15, 62, 63] in atomic systems has opened the possibility to deliver diverse synthetic quantum matter, such as artificial magnetic monopoles [14, 122], and synthetic spin-orbit-coupled bosonic and fermionic atoms [15, 63]. Utilizing synthetic dimensions [28, 41–46] has further offered a promising route to realizing high-dimensional systems [49] and manipulating boundary conditions. However, most experimental studies have been focusing on spaces with simple geometries, such as one dimensional (1D) atomic wires [46], and atoms subject to synthetic magnetic fields in 2D planar ladders/strips [47, 48, 74, 123, 124].

In our experiments, a  $^{87}\text{Rb}$  BEC is produced in an optical dipole trap [50]. As shown in Fig. 4.1ab, four internal spin states,  $|F, m_F\rangle = |2, 2\rangle, |2, 1\rangle, |1, 0\rangle, |1, 1\rangle$  relabeled as  $|1\rangle, |2\rangle, |3\rangle, |4\rangle$ , form discrete sites in the synthetic dimension (the  $w$  direction), where  $F$  ( $m_F$ ) is the hyperfine spin (the magnetic quantum number). Raman lasers along  $\pm\hat{y}$  couple  $|1\rangle$  and  $|2\rangle$  as well as  $|3\rangle$  and  $|4\rangle$  with a strength  $\Omega$ . Photon recoil momentum  $\hbar k_r = 2\pi\hbar/\lambda$  and recoil energy  $E_r = \hbar^2 k_r^2 / (2m)$  are used respectively for units of momentum and energy, where  $\lambda$  is the Raman lasers' wavelength,  $\hbar$  is the reduced Planck constant, and  $m$  is the mass of  $^{87}\text{Rb}$ . Two microwave fields, with coupling strengths  $\Omega_1$  and  $\Omega_2$ , couple respectively  $|2\rangle$  and  $|3\rangle$ , and  $|1\rangle$  and  $|4\rangle$ . This setup delivers a cyclic coupling (a periodic boundary condition) in the  $w$  direction (Fig. 4.1c). Differently from other cyclic couplings for creating 2D spin-orbit couplings [73, 125] and Yang monopoles [14], our scheme (Fig. 4.1bc) connects two edges of a 2D planar Hall strip and thus synthesizes the  $y$  and the curved

$w$  dimension into a Hall cylinder, a cylindrical surface with a net radial synthetic magnetic flux.

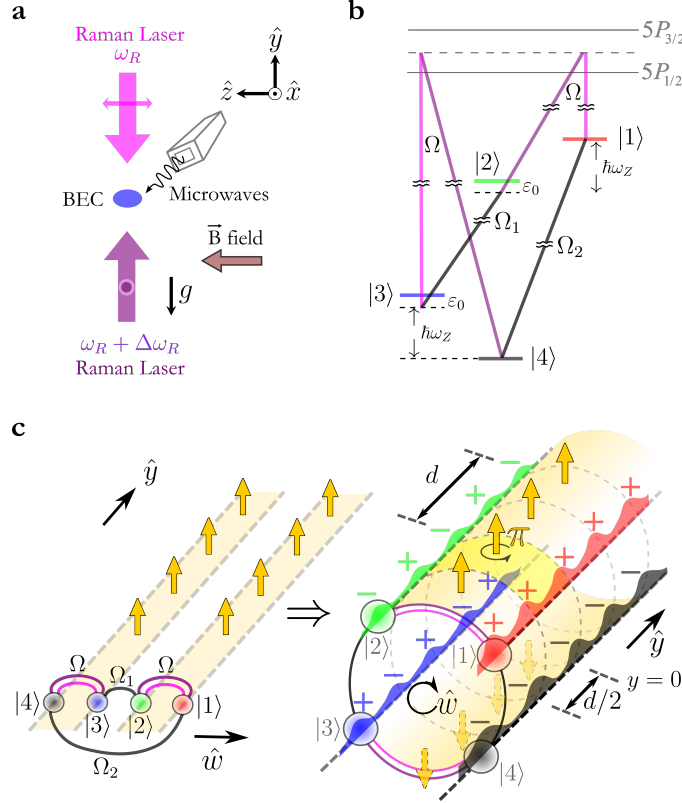


**Fig. 4.1. Set-up for realizing a synthetic Hall cylinder.** (a) We apply Raman lasers (at wavelength  $\lambda \sim 790$  nm) with orthogonal linear polarizations (double-headed arrows) counter-propagating along  $\hat{y}$  and microwaves (frequency  $\approx 6.8$  GHz, from a microwave horn) propagating in the  $x - y$  plane to a BEC (typical atom number  $\sim (1 - 2) \times 10^4$ ). Gravity “ $g$ ” is towards  $-\hat{y}$ . (b) Hyperfine spin states (indicated by different colors)  $|1\rangle$ ,  $|2\rangle$ ,  $|3\rangle$ , and  $|4\rangle$  as discrete sites in the synthetic dimension  $\hat{w}$  are cyclically-coupled by Raman coupling  $\Omega$  and microwave couplings  $\Omega_{1,2}$  to form a closed circle, as drawn in (c). Linear Zeeman splitting  $\hbar\omega_Z \approx \hbar\Delta\omega_R \approx h \times (3.5 \text{ MHz})$  is generated by a bias magnetic field, where  $\Delta\omega_R$  is the Raman lasers’ angular frequency difference. The quadratic Zeeman shift is  $\varepsilon_0 \approx 2.4 E_r$ . (c) Connecting the two edges along  $\hat{w}$  of a 2D planar Hall strip (left) gives rise to a cylindrical surface (right) subject to a net radial synthetic magnetic flux (thick yellow arrows) with a non-uniform distribution of the magnetic field (indicated by shaded regions). The half magnetic flux quantum per unit plaquette (highlighted area in shaded regions) formed by four maxima of the density modulation corresponds to an Aharonov-Bohm phase of  $\pi$ . For a BEC at  $q_y = 0$  in the ground band of Fig. 4.2b, the emergent BEC density modulation along  $\hat{y}$  has a periodicity of  $d/2$ , half the period ( $d$ ) of the Hamiltonian  $H$ . The phase (with + and - representing respectively a phase 0 and  $\pi$  at positions of maximum density) of each spin component’s wavefunction has a periodicity of either  $d$  or  $d/2$ .

### 4.3 The single-particle Hamiltonian $H$ for the synthetic Hall cylinder

An atom at location  $y$  hopping along  $\pm\hat{w}$  obtains a net momentum of  $\hbar K$  along  $\pm\hat{y}$ , acquiring a Raman laser-imprinted  $y$ -dependent phase factor,  $e^{\pm iKy}$  (see subsections below), where  $K = 2k_r$ . For shaded regions in Fig. 4.1c, the phase acquired by an atom after traveling around an area of  $\Delta y$  times one unit length along  $\hat{w}$  is  $\pm K\Delta y$ , analogous to the Aharonov-Bohm (AB) phase acquired by charged particles in a magnetic field, and thus corresponds to an artificial magnetic flux (thick yellow arrows) [41, 47, 48, 126, 127].

Since the transverse  $x$  and  $z$  directions are decoupled from the cylinder, the single-particle Hamiltonian describing the couplings in Fig. 4.1b and the motion along  $\hat{y}$  is written in the basis of  $\{|1\rangle, |2\rangle, |3\rangle, |4\rangle\}$  as (see subsections below)

$$H = \frac{\hat{p}_y^2}{2m} \mathbf{I} + \begin{pmatrix} 0 & \frac{\Omega}{2} e^{iKy} & 0 & \frac{\Omega_2}{2} \\ \frac{\Omega^*}{2} e^{-iKy} & \varepsilon_0 & \frac{\Omega_1}{2} & 0 \\ 0 & \frac{\Omega_1^*}{2} & \varepsilon_0 & \frac{\Omega}{2} e^{iKy} \\ \frac{\Omega_2^*}{2} & 0 & \frac{\Omega^*}{2} e^{-iKy} & 0 \end{pmatrix}, \quad (4.1)$$

where  $\hat{p}_y = -i\hbar \frac{\partial}{\partial y}$ ,  $\mathbf{I}$  is the identity matrix, and  $\varepsilon_0$  is the quadratic Zeeman shift. Here, the Raman-induced  $y$ -dependent phase factor,  $e^{\pm iKy}$ , cannot be gauged away due to our implemented periodic boundary condition, unlike open boundary conditions such as when  $\Omega_2 = 0$  (see subsections below). This makes  $H$  periodic with a period of  $d = 2\pi/K = \pi/k_r$ .  $H$  also has a nonsymmorphic symmetry: a translation of  $d/2$  along  $\hat{y}$  followed by a unitary transformation along  $\hat{w}$ ,  $|1\rangle \rightarrow |1\rangle$ ,  $|2\rangle \rightarrow -|2\rangle$ ,  $|3\rangle \rightarrow -|3\rangle$ ,  $|4\rangle \rightarrow |4\rangle$ . A BEC on this Hall cylinder develops a crystalline order in its wavefunction with an underlying nonsymmorphic symmetry, as sketched in Fig. 4.1c. The density modulation along  $\hat{y}$  has a period of  $d/2$  (half the period of  $H$ ) while the phase of each spin component modulates with a period of either  $d$  or  $d/2$ . Thus, an effective magnetic flux  $\Phi/\Phi_0 = (Kd/2)/(2\pi) = 1/2$  pierces a plaquette formed by four maxima of the density modulation in shaded regions in Fig. 4.1c, where  $\Phi_0 = 2\pi\hbar/e$  is the magnetic flux quantum,  $q \equiv -e$  ( $e$  is the elementary charge) is defined as the effective

charge of a particle. In addition, a periodic band structure emerges, possessing band crossings that are manifestation of and protected by the underlying nonsymmorphic symmetry. Such band crossings play important roles in topological quantum matter such as topological semimetals [121, 128, 129], because their existence is topologically robust against perturbations respecting the symmetry, such as deformations of the cylindrical surface (i.e. variations of parameters in Equation (4.1)) here.

Unlike previous works using external optical lattices [41, 47, 48, 130], here, the emergent crystalline order results from “curving” a 2D planar Hall strip to a Hall cylinder. As shown later, the emergent crystalline order and the corresponding topological band structure vanish on an “unzipped” cylinder (i.e. a planar Hall strip) when imposing an open boundary condition along  $\hat{w}$  by turning off  $\Omega_2$ . The net magnetic flux threading the cylindrical surface is also essential for the phenomena studied here, which would otherwise disappear without a net threaded flux (see subsections below).

#### 4.3.1 Derivation of the single-particle Hamiltonians $H$ and $H_{q_y}$

In the following, we derive the single-particle Hamiltonian for the cylindrical surface with a nonsymmorphic symmetry: the Hamiltonian  $H$  (used for Fig. 4.1c and relevant calculations shown below) and the corresponding momentum-space Hamiltonian  $H_{q_y}$  (used for Fig. 4.2). Both  $H$  and  $H_{q_y}$  take into account  $\Omega$  and  $\Omega_{1,2}$ .

We relabel the spin states  $|2, 2\rangle = |\tilde{1}\rangle$ ,  $|2, 1\rangle = |\tilde{2}\rangle$ ,  $|1, 0\rangle = |\tilde{3}\rangle$ , and  $|1, 1\rangle = |\tilde{4}\rangle$  (where tilde refers to a non-rotating frame, as explained below), with respective energies  $E_1$ ,  $E_2$ ,  $E_3$ , and  $E_4$ . Counter-propagating Raman lasers along  $\pm\hat{y}$  with an angular frequency difference  $\Delta\omega_R$  couple  $|\tilde{1}\rangle$  and  $|\tilde{2}\rangle$ , and  $|\tilde{3}\rangle$  and  $|\tilde{4}\rangle$ , with a coupling strength  $\Omega$ . Two microwaves with angular frequencies  $\omega_1$  and  $\omega_2$  couple  $|\tilde{2}\rangle$  and  $|\tilde{3}\rangle$ , and  $|\tilde{1}\rangle$  and  $|\tilde{4}\rangle$ , with respective coupling strengths  $\Omega_1$  and  $\Omega_2$ . Utilizing  $F = 1$  and  $F = 2$  (hyperfine) manifolds makes a cyclic coupling in the  $w$  direction possible, since doing this within only the  $F = 1$  manifold would be difficult due to the extremely weak two-photon Raman transition of  $\Delta m_F = \pm 2$  in alkali atoms. In Fig. 4.1b, we

define  $E_3 - E_4 = \hbar\omega_Z + \varepsilon_0$  and  $E_1 - E_2 = \hbar\omega_Z - \varepsilon_0$ , where  $\hbar\omega_Z$  is the linear Zeeman splitting and  $\varepsilon_0$  is the quadratic Zeeman shift. In our experiments,  $\varepsilon_0 \sim 2.4 E_r$ , given by the applied bias magnetic field ( $\sim 5$  gauss). We define the Raman laser detuning  $\delta_R = (2\hbar\Delta\omega_R - (E_3 - E_4) - (E_1 - E_2))/2 = \hbar(\Delta\omega_R - \omega_Z)$ , the microwave detunings  $\delta_1 = \hbar\omega_1 - (E_2 - E_3)$  and  $\delta_2 = \hbar\omega_2 - (E_1 - E_4)$ .

In this work, we focus on the atomic motion along  $\hat{y}$  and write the free atomic Hamiltonian as:

$$\tilde{H}_{\text{free}} = \frac{\hat{p}_y^2}{2m} \mathbf{I} + E_1 |\tilde{1}\rangle \langle \tilde{1}| + E_2 |\tilde{2}\rangle \langle \tilde{2}| + E_3 |\tilde{3}\rangle \langle \tilde{3}| + E_4 |\tilde{4}\rangle \langle \tilde{4}|, \quad (4.2)$$

where  $\mathbf{I}$  is the identity matrix and  $\hat{p}_y = -i\hbar \frac{\partial}{\partial y}$  is the momentum operator along  $\hat{y}$ . In the rotating wave approximation, the Hamiltonians describing the Raman and microwave couplings are respectively written as (assuming the initial phases of these coupling fields are zero):

$$\tilde{H}_{\text{Raman}} = \frac{\Omega}{2} e^{i(Ky - \Delta t)} (|\tilde{1}\rangle \langle \tilde{2}| + |\tilde{3}\rangle \langle \tilde{4}|) + h.c. \quad (4.3)$$

$$\tilde{H}_1 = \frac{\Omega_1}{2} e^{-i\omega_1 t} (|\tilde{2}\rangle \langle \tilde{3}|) + h.c. \quad (4.4)$$

$$\tilde{H}_2 = \frac{\Omega_2}{2} e^{-i\omega_2 t} (|\tilde{1}\rangle \langle \tilde{4}|) + h.c. \quad (4.5)$$

where  $K = 2k_r$  and  $h.c.$  stands for Hermitian conjugate. We choose a rotating frame defined by the following unitary transformations to eliminate the time-dependent terms in Eqs. (4.3-4.5):

$$\begin{aligned} |\tilde{1}\rangle &= e^{i\Delta t} |1\rangle e^{i\frac{\omega_1}{2}t}, |\tilde{2}\rangle = e^{i\frac{\omega_1}{2}t} |2\rangle, \\ |\tilde{3}\rangle &= e^{-i\frac{\omega_1}{2}t} |3\rangle, |\tilde{4}\rangle = e^{-i\Delta t} |4\rangle e^{-i\frac{\omega_1}{2}t}. \end{aligned} \quad (4.6)$$

In such a rotating frame (without tilde),

$$\begin{aligned} H_{\text{free}} &= \frac{\hat{p}_y^2}{2m} \mathbf{I} + (E_1 - \hbar\Delta\omega_R - \frac{\hbar\omega_1}{2}) |1\rangle \langle 1| + (E_2 - \frac{\hbar\omega_1}{2}) |2\rangle \langle 2| \\ &\quad + (E_3 + \frac{\hbar\omega_1}{2}) |3\rangle \langle 3| + (E_4 + \hbar\Delta\omega_R + \frac{\hbar\omega_1}{2}) |4\rangle \langle 4| \end{aligned} \quad (4.7)$$

$$H_{\text{Raman}} = \frac{\Omega}{2} e^{i(Ky)} (|1\rangle \langle 2| + |3\rangle \langle 4|) + h.c. \quad (4.8)$$

$$H_1 = \frac{\Omega_1}{2} (|2\rangle \langle 3|) + h.c. \quad (4.9)$$

$$H_2 = \frac{\Omega_2}{2} e^{-i\omega_2 t} e^{i2\Delta\omega_R t} e^{i\omega_1 t} (|1\rangle \langle 4|) + h.c. \quad (4.10)$$

where  $H_{\text{Raman}}$  and  $H_1$  become time-independent. By further requiring

$$\omega_2 = 2\Delta\omega_R + \omega_1, \quad (4.11)$$

Eq. (4.10) becomes  $H_2 = \frac{\Omega_2}{2} (|1\rangle \langle 4|) + h.c.$ , which is also time-independent. Eq. (4.11) is called the resonance condition for the cyclic coupling. This resonance condition, as depicted in Fig. 4.1b, is realized during our whole experiment.

Therefore, in the rotating frame defined by Eq. (4.6) and when the resonance condition in Eq. (4.11) is fulfilled,  $H = H_{\text{free}} + H_{\text{Raman}} + H_1 + H_2$  is time-independent and can be written in the basis of  $\{|1\rangle, |2\rangle, |3\rangle, |4\rangle\}$  as:

$$H = \frac{\hat{p}_y^2}{2m} \mathbf{I} + \begin{pmatrix} E_1 - \hbar\Delta\omega_R - \frac{\hbar\omega_1}{2} & \frac{\Omega}{2} e^{i(Ky)} & 0 & \frac{\Omega_2}{2} \\ \frac{\Omega^*}{2} e^{-i(Ky)} & E_2 - \frac{\hbar\omega_1}{2} & \frac{\Omega_1}{2} & 0 \\ 0 & \frac{\Omega_1^*}{2} & E_3 + \frac{\hbar\omega_1}{2} & \frac{\Omega}{2} e^{i(Ky)} \\ \frac{\Omega_2^*}{2} & 0 & \frac{\Omega^*}{2} e^{-i(Ky)} & E_4 + \hbar\Delta\omega_R + \frac{\hbar\omega_1}{2} \end{pmatrix}. \quad (4.12)$$

From the above equation, we see that the Raman transition corresponds to the  $y$ -dependent phase factor,  $e^{\pm iKy}$ , while a microwave transition does not lead to a position-dependent phase change. Redefining all energies such that  $E_3 + \hbar\omega_1/2 = \varepsilon_0$  and using the definitions of  $\varepsilon_0$ ,  $\delta_R$ ,  $\delta_1$ ,  $\delta_2$ , and the resonance condition in Eq. (4.11), we obtain

$$\delta_1 + 2\delta_R = \delta_2 \quad (4.13)$$

and rewrite Eq. (4.12) as

$$H = \frac{\hat{p}_y^2}{2m} \mathbf{I} + \begin{pmatrix} -\delta_R - \frac{\delta_1}{2} & \frac{\Omega}{2} e^{i(Ky)} & 0 & \frac{\Omega_2}{2} \\ \frac{\Omega^*}{2} e^{-i(Ky)} & \varepsilon_0 - \frac{\delta_1}{2} & \frac{\Omega_1}{2} & 0 \\ 0 & \frac{\Omega_1^*}{2} & \varepsilon_0 + \frac{\delta_1}{2} & \frac{\Omega}{2} e^{i(Ky)} \\ \frac{\Omega_2^*}{2} & 0 & \frac{\Omega^*}{2} e^{-i(Ky)} & \delta_R + \frac{\delta_1}{2} \end{pmatrix}. \quad (4.14)$$

This equation includes Raman and microwave detunings, which can be nonzero during the initial preparation process as discussed below. After the initial preparation, we achieve  $\delta_R = \delta_1 = \delta_2 = 0$  and thus Eq. (1) and Fig. 4.1b do not carry such detunings. To calculate the band structures, we derive the momentum-space Hamiltonian  $H_{q_y}$  by considering the coupling scheme in Fig. 4.2a. The spin and mechanical momentum states comprise a plane wave basis, denoted by

$$\{|\hbar(q_y + nK); m\rangle\} = \{e^{i(q_y + nK)y} |m\rangle\}, \quad (4.15)$$

where  $\hbar(q_y + nK)$  is the mechanical momentum,  $m = 1, 2, 3, 4$  labels the spin,  $\hbar q_y$  is the quasimomentum, and  $n$  is an integer. Then,  $H_{q_y}$  reads

$$H_{q_y} = \begin{pmatrix} \ddots & \vdots & \vdots & \vdots & \vdots & \vdots & \ddots \\ \dots & A_{-2} & B & 0 & 0 & 0 & \dots \\ \dots & B^\dagger & A_{-1} & B & 0 & 0 & \dots \\ \dots & 0 & B^\dagger & A_0 & B & 0 & \dots \\ \dots & 0 & 0 & B^\dagger & A_1 & B & \dots \\ \dots & 0 & 0 & 0 & B^\dagger & A_2 & \dots \\ \ddots & \vdots & \vdots & \vdots & \vdots & \vdots & \ddots \end{pmatrix}, \quad (4.16)$$

where  $A_n$  matrices are on the diagonal of  $H_{q_y}$ . Each  $A_n$  is a 4 by 4 matrix written in the basis of  $\{|\hbar(q_y + nK); m\rangle\}$ , where the four spin states have the same mechanical

momentum (i.e., same  $n$ ). Thus,  $A_n$  only includes microwave couplings. When all the detunings are zero, we obtain

$$A_n = \begin{pmatrix} \frac{\hbar^2}{2m}(q_y + nK)^2 & 0 & 0 & \frac{\Omega_2}{2} \\ 0 & \frac{\hbar^2}{2m}(q_y + nK)^2 + \varepsilon_0 & \frac{\Omega_1}{2} & 0 \\ 0 & \frac{\Omega_1^*}{2} & \frac{\hbar^2}{2m}(q_y + nK)^2 + \varepsilon_0 & 0 \\ \frac{\Omega_2^*}{2} & 0 & 0 & \frac{\hbar^2}{2m}(q_y + nK)^2 \end{pmatrix}. \quad (4.17)$$

$B$  is a 4 by 4 matrix accounting for the Raman coupling between adjacent  $A_n$  matrices:

$$B = \begin{pmatrix} 0 & 0 & 0 & 0 \\ \Omega/2 & 0 & 0 & 0 \\ 0 & 0 & 0 & 0 \\ 0 & 0 & \Omega/2 & 0 \end{pmatrix}. \quad (4.18)$$

### 4.3.2 Symmetries of the Hamiltonian $H$

In this subsection, the calculation is performed by Yangqian Yan. For  $\delta_R = \delta_1 = \delta_2 = 0$ , the Hamiltonian  $H$  in Eq. (4.14) is invariant under a generalized inversion symmetry, i.e., a spatial inversion ( $y \rightarrow -y$ ) followed by the spin inversion ( $|1\rangle, |2\rangle, |3\rangle, |4\rangle \rightarrow |4\rangle, |3\rangle, |2\rangle, |1\rangle$ ). This generalized inversion symmetry guaranties that the energy spectrum  $E(q_y)$  is symmetric with respect to  $q_y$ , i.e.,

$$E(q_y) = E(-q_y). \quad (4.19)$$

The Hamiltonian  $H$  is also invariant under a nonsymmorphic symmetry, which comprises a translational operation  $\hat{G} = e^{-i\hat{p}d/(2\hbar)}$  ( $d = 2\pi/\lambda$ ) followed by a unitary transformation  $\hat{U}$  given by

$$\hat{U} = \begin{pmatrix} 1 & 0 & 0 & 0 \\ 0 & -1 & 0 & 0 \\ 0 & 0 & -1 & 0 \\ 0 & 0 & 0 & 1 \end{pmatrix}. \quad (4.20)$$

That is,  $\hat{U}\hat{G}H\hat{G}^{-1}\hat{U}^{-1} = H$ . Defining the nonsymmorphic symmetry operator  $\hat{S} = \hat{U}\hat{G}$ , we readily obtain  $[\hat{S}, H] = 0$ , which implies that  $\hat{S}$  and  $H$  share the same set

of eigenstates. The physical meanings of  $\hat{U}$  and  $\hat{G}$  are explained below. First, the translational operator  $\hat{G}$  can be understood as shifting the entire  $y$  coordinate to  $y + d/2$  by half the period ( $d$ ) of  $H$ . Applying  $\hat{G}$  to  $H$ , i.e.  $\hat{G}H\hat{G}^{-1}$ , the matrix elements  $\langle 1|H|2\rangle$ ,  $\langle 2|H|1\rangle$ ,  $\langle 3|H|4\rangle$ , and  $\langle 4|H|3\rangle$  flip their sign. Second, the unitary transformation  $\hat{U}$  can be understood as flipping the sign of the second and third spin states. Applying  $\hat{U}$  to  $\hat{G}H\hat{G}^{-1}$ , i.e.  $\hat{U}\hat{G}H\hat{G}^{-1}\hat{U}^{-1}$ , the matrix elements  $\langle 1|\hat{G}H\hat{G}^{-1}|2\rangle$ ,  $\langle 2|\hat{G}H\hat{G}^{-1}|1\rangle$ ,  $\langle 3|\hat{G}H\hat{G}^{-1}|4\rangle$ , and  $\langle 4|\hat{G}H\hat{G}^{-1}|3\rangle$  flip their sign. The Hamiltonian after these two symmetry operations ( $\hat{U}$  and  $\hat{G}$ ) thus returns to the original Hamiltonian  $H$ .

$\hat{S}^2(= \hat{G}^2)$  is a translational operator corresponding to a shift of  $d$  in the  $y$  coordinate, such that  $[\hat{S}^2, H] = 0$ . Therefore, the Hamiltonian  $H$  is invariant after a shift of  $d$  in  $y$ , a discrete translational symmetry. The eigenvalues of  $H$  thus have a periodicity of  $d$  in  $y$ . The eigenwavefunctions of  $H$  can be written in the form of Bloch waves,  $e^{iq_y y} w(y)$ , where  $w(y)$  has a period of  $d$ . Since the nonsymmorphic symmetry operator  $\hat{S}$  and the Hamiltonian  $H$  share the same set of eigenstates, we can construct the eigenstates of  $H$  (and  $\hat{S}$ ) in the following two types (in the form of Bloch waves) by considering the physical meanings of  $\hat{S}$  mentioned above:

$$\psi_p(q_y) = e^{iq_y y} (u_1(y) |1\rangle + u_2(y) |2\rangle + u_3(y) |3\rangle + u_4(y) |4\rangle) \quad (4.21)$$

$$\psi_m(q_y) = e^{iq_y y} (v_1(y) |1\rangle + v_2(y) |2\rangle + v_3(y) |3\rangle + v_4(y) |4\rangle), \quad (4.22)$$

where

$$\begin{aligned} u_1(y + d/2) - u_1(y) &= u_2(y + d/2) + u_2(y) \\ &= u_3(y + d/2) + u_3(y) = u_4(y + d/2) - u_4(y) = 0 \end{aligned} \quad (4.23)$$

$$\begin{aligned} v_1(y + d/2) + v_1(y) &= v_2(y + d/2) - v_2(y) \\ &= v_3(y + d/2) - v_3(y) = v_4(y + d/2) + v_4(y) = 0. \end{aligned} \quad (4.24)$$

Applying  $\hat{S}$  to Eqs. (4.21, 4.22), one can verify that  $\psi_p$  and  $\psi_m$  are eigenfunctions of  $\hat{S}$  with the corresponding eigenvalues  $\pm e^{iq_y d/2}$ . With Eqs. (4.23, 4.24), we also see that  $\psi_p(q_y)$  and  $\psi_m(q_y)$  are still Bloch waves labeled by  $q_y$ .

Consider two sets of eigenfunctions  $\{\psi_p(q_y), \psi_m(q_y)\}$  and  $\{\psi_p(q_y + K), \psi_m(q_y + K)\}$ . Their corresponding eigenvalues of the operator  $\hat{S}$  are  $\{e^{iq_y d/2}, -e^{iq_y d/2}\}$  and  $\{-e^{iq_y d/2}, e^{iq_y d/2}\}$ . Thus, one obtains  $\psi_p(q_y) = \psi_m(q_y + K)$  and  $\psi_m(q_y) = \psi_p(q_y + K)$ . This suggests two properties associated with the nonsymmorphic symmetry: (1) both  $\psi_p(q_y)$  and  $\psi_m(q_y)$  have a periodicity of  $2K$  in  $q_y$ , and (2)  $\psi_p(q_y)$  and  $\psi_m(q_y)$  are offset from each other by  $K$  in  $q_y$ . Denote the corresponding eigenenergies (eigenvalues of  $H$ ) for  $\psi_p(q_y)$  and  $\psi_m(q_y)$  as  $E_p$  and  $E_m$ , the energy spectrum also possesses properties associated with the nonsymmorphic symmetry and corresponding to properties (1) and (2) above. Corresponding to (1), we have

$$E_p(q_y) = E_m(q_y + K). \quad (4.25)$$

This suggests that the band structure has crossing points at some  $q_y$ . Recall that the Hamiltonian  $H$  with  $\delta_R = \delta_1 = \delta_2 = 0$  possesses a generalized inversion symmetry in Eq. (4.19). Given the relations in Eq. (4.19) and Eq. (4.25), we obtain

$$E_p(q_y) = E_m(-q_y + K). \quad (4.26)$$

Consequently, for  $q_y = (2n + 1)K/2$  where  $n$  is an integer,  $E_p$  is equal to  $E_m$ , corresponding to a degenerate point (band crossing) in the band structure. Such a degeneracy at  $q_y = (2n + 1)K/2$  is protected by the nonsymmorphic symmetry and the generalized inversion symmetry. If any of  $\delta_R, \delta_1, \delta_2$  is nonzero, the generalized inversion symmetry is broken while the nonsymmorphic symmetry is retained, the two branches still cross but at  $q_y \neq (2n + 1)K/2$ .

Furthermore, the two independent branches in the spin-mechanical momentum coupling scheme in Fig. 4.2a implies that the plane wave basis  $\{|\hbar(q_y + nK); m\rangle\}$  in Eq. (4.15) can also be decomposed into two subsets based on the nonsymmorphic symmetry. These two branches can be written in the following form:

$$\begin{aligned} \phi_p(q_y) = \sum_n & (c_{1,n} |q_y + 2nK; 1\rangle + c_{2,n} |q_y + 2nK + K; 2\rangle \\ & + c_{3,n} |q_y + 2nK + K; 3\rangle + c_{4,n} |q_y + 2nK; 4\rangle) \end{aligned} \quad (4.27)$$

and

$$\begin{aligned} \phi_m(q_y) = \sum_n (d_{1,n} |q_y + 2nK + K; 1\rangle + d_{2,n} |q_y + 2nK; 2\rangle \\ + d_{3,n} |q_y + 2nK; 3\rangle + d_{4,n} |q_y + 2nK + K; 4\rangle). \end{aligned} \quad (4.28)$$

Equating Eqs. (4.27, 4.28) with Eqs. (4.21, 4.22) respectively, the coefficients in the above equations satisfy

$$\begin{aligned} \sum_n c_{1,n} e^{i2nKy} = u_1(y), \quad \sum_n c_{2,n} e^{i(2nK+K)y} = u_2(y), \\ \sum_n c_{3,n} e^{i(2nK+K)y} = u_3(y), \quad \sum_n c_{4,n} e^{i2nKy} = u_4(y), \end{aligned} \quad (4.29)$$

and

$$\begin{aligned} \sum_n d_{1,n} e^{i(2nK+K)y} = v_1(y), \quad \sum_n d_{2,n} e^{i2nKy} = v_2(y), \\ \sum_n d_{3,n} e^{i2nKy} = v_3(y), \quad \sum_n d_{4,n} e^{i(2nK+K)y} = v_4(y). \end{aligned} \quad (4.30)$$

From Eqs. (4.27, 4.28), we readily see that  $\phi_p(q_y)$  and  $\phi_m(q_y + K)$  are identical if one equates  $d_{1,n}$  with  $c_{1,n+1}$ ,  $d_{4,n}$  with  $c_{4,n+1}$ ,  $d_{2,n}$  with  $c_{2,n}$ , and  $d_{3,n}$  with  $c_{3,n}$ . Thus, Eqs. (4.27, 4.28) respectively correspond to the band 1 and band 2, providing another way to understand band crossings due to the nonsymmorphic symmetry.

#### 4.4 Quantum transport on a symmetry-protected Möbius strip in momentum space

To gain further insights, Fig. 4.2a illustrates the Hamiltonian in the momentum space (see  $H_{q_y}$  in subsections below). Two independent branches,  $H_{i=1,2}(q_y)$  (line-connected solid/dashed circles), satisfy  $H_i(q_y) = H_i(q_y + n \times 2K)$ , thus corresponding to a  $d/2$  periodicity of the real-space density modulation, where  $\hbar q_y$  is the quasi-momentum,  $\hbar k_y = \hbar(q_y \pm nK)$  is the mechanical momentum, and  $n$  is an integer. Besides, these two branches are offset from each other by  $\hbar K$ . Therefore, two sets of Bloch bands  $E_1(q_y)$  and  $E_2(q_y)$  also satisfy  $E_1(q_y) = E_2(q_y + K)$  and intersect at the

boundary of the first Brillouin zone ( $q_y = \pm\pi/d = \pm K/2$ ) when  $E(q_y) = E(-q_y)$  is fulfilled (see subsections below).

To probe the band structure, we perform spin-resolved quantum transport measurements, using Bloch oscillations of a BEC initially prepared (see subsections below) at  $q_y = 0$  in either band 1 or band 2 (Fig. 4.2b). After the initial preparation, the dipole trap is abruptly turned off at  $t_{\text{hold}} = 0$ , allowing atoms to fall under gravity (towards  $-\hat{y}$ , Fig. 4.1a) for various time  $t_{\text{hold}}$ , during which the Raman and microwave couplings remain at the final values. The gravity thus induces transport of the BEC towards negative  $q_y$  (Fig. 4.2b) for various  $t_{\text{hold}}$ . Such a procedure is used for all transport measurement presented later. During Bloch oscillations, BEC's total mechanical momentum along  $\hat{y}$ ,  $\hbar k_{\text{BEC}}$ , and spin compositions respectively probe the slope (group velocity) [131] and spin texture of the Bloch band, unveiling the band structure. After various  $t_{\text{hold}}$ , we immediately turn off all coupling fields to release the atoms for a 15-ms time-of-flight (TOF) including a 9-ms spin-resolved Stern-Gerlach process, and then perform absorption imaging. These TOF images disclose the spin and mechanical momentum compositions of the BEC at various  $t_{\text{hold}}$  and the corresponding  $q_y$ . We obtain  $\hbar k_{\text{BEC}}$  by summing over population-weighted mechanical momentum components along  $\hat{y}$  (see subsections below).

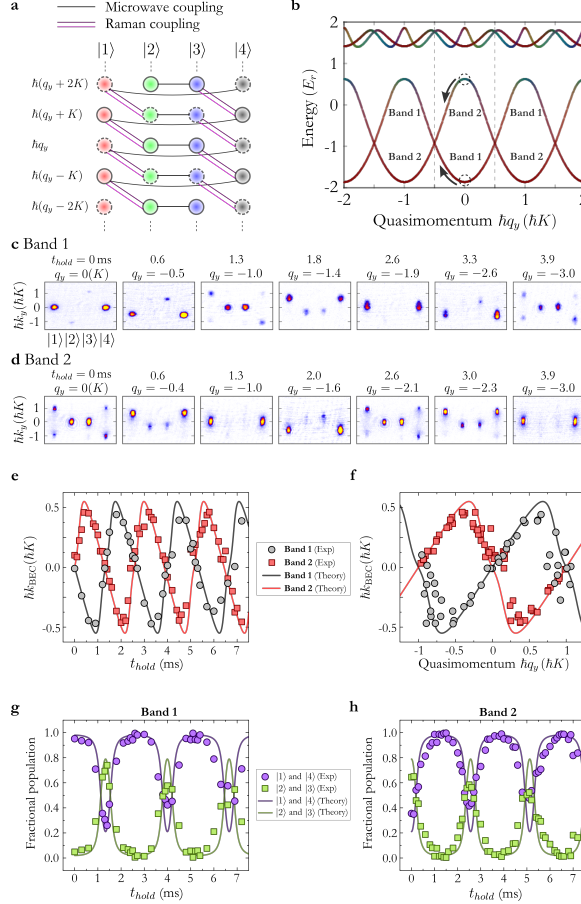


**Fig. 4.2. Band structure with a nonsymmorphic symmetry and observed Bloch oscillations.** (a) Laser and microwave induced couplings between a series of spin and mechanical momentum states form two independent branches (marked by solid/dashed circles) offset from each other by  $\hbar K = 2\hbar k_r$ , manifesting the underlying nonsymmorphic symmetry. (b) Calculated band structure using  $\Omega = 2.3$ ,  $\Omega_1 = 2.5$ ,  $\Omega_2 = 3.4$ ,  $\delta_R = 0$ , and  $\varepsilon_0 = 2.4$ , all in units of  $E_r$ . The spin texture is revealed by colors determined by the population-weighted colors of the four spin states (see subsections below). The first Brillouin zone is between the dashed lines. The BEC initially prepared at  $\hbar q_y = 0$  (dashed circles) in either band 1 or band 2 undergoes gravity-induced transport (indicated by arrows) and Bloch oscillations for various  $t_{\text{hold}}$ . (c-d) TOF images showing spin and mechanical momentum compositions of the BEC taken at various  $t_{\text{hold}}$  and the corresponding  $q_y$ , respectively for the initial preparation in band 1 and band 2. The quasimomentum of the BEC at  $t_{\text{hold}}$  relative to those at  $t_{\text{hold}} = 0$  ( $q_y = 0$ ) can be measured by the displacement of the mechanical momentum components of, say |1> and |4>, at  $t_{\text{hold}}$  relative to those at  $t_{\text{hold}} = 0$  ( $q_y = 0$ ). Each TOF image (and the associated analyzed quantities presented later) is typically an average of a few repetitive measurements. (e-f) Total mechanical momentum of the BEC versus  $t_{\text{hold}}$  and quasimomentum, respectively. The  $q_y$  in (f) is plotted modulo  $2K$  (i.e.,  $q_y$  is equivalent to  $q_y \pm n \times 2K$ ), only between  $-K$  and  $K$  for both band 1 and band 2 due to their  $2K$  periodicity in  $q_y$ . This  $2\hbar K$  periodicity is also reflected by the observed  $2\hbar K$  separation between different mechanical momentum components for each spin state in (c, d). (g-h) Fractional spin populations versus  $t_{\text{hold}}$ . In (e-h), solid lines are single-particle calculations using the same parameters as used in (b) and the average of the measured  $d(\hbar q_y)/d(t_{\text{hold}})$  (see subsections below).

TOF images shown in Fig. 4.2cd and their corresponding analyzed data (dots in Fig. 4.2e-h) are labeled by either band 1 or band 2 (indicating different initial

preparations). Fig. 4.2e and Fig. 4.2f respectively show  $\hbar k_{\text{BEC}}$  versus  $t_{\text{hold}}$  and versus quasimomentum. Spin populations in  $|1\rangle$  and  $|4\rangle$ , and in  $|2\rangle$  and  $|3\rangle$ , versus  $t_{\text{hold}}$  are shown in Fig. 4.2gh. TOF images in Fig. 4.2cd show reoccurrence of spin and momentum compositions of the BEC with a period of  $2\hbar K$  in quasimomentum (or a period of  $\sim 2.6$  ms in time), consistent with the  $2\hbar K$  periodicity demonstrated in Fig. 4.2f. Thus, Bloch oscillations possess twice the  $\hbar K$  periodicity of the band structure (Fig. 4.2b). This is analogous to traveling on a Möbius strip in momentum space: atoms have to travel twice the period of the band structure to reach the same quantum state (up to a phase). Such a  $2\hbar K$  periodicity of Bloch oscillations is consistent with the  $d/2$  periodicity of the density modulation. TOF images in Fig. 4.2c are also consistent with those in Fig. 4.2d with an offset by  $\sim 1.3$  ms or  $\sim K$ . Such offsets are demonstrated as out-of-phase Bloch oscillations shown in Fig. 4.2e-h. These transport phenomena unveil band crossings: atoms traveling to band touching points undergo a diabatic transition from the ground band to the first excited band.

We have solved the time-dependent 3D Gross-Pitaevskii (GP) equation to simulate both the initial preparation and Bloch oscillations using similar experimental parameters including the present inter-particle interactions (see subsections below). The simulated loading process achieves an initial state 96% overlapped with the ground state. The GP numerical results for Fig. 4.2e-h agree well with the non-interacting theoretical results.

#### 4.4.1 Importance of the synthetic magnetic flux threading the cylinder

A net magnetic flux threading the cylinder is key to many phenomena emerging on the Hall cylinder, such as the emergent BEC crystalline order and the corresponding band structure with their underlying nonsymmorphic symmetry. These phenomena would otherwise disappear in the absence of the net threaded flux. To understand this, for example, one can realize a periodic boundary condition by replacing the Raman

coupling in Fig. 4.1b with an RF coupling, which does not change the momentum of an atom. Consequently, such a cyclic coupling gives rise to a cylinder with zero magnetic flux everywhere on the cylindrical surface. The Hamiltonian for this case is similar to  $H$  but without the  $y$ -dependent phase factors, i.e.  $e^{\pm iKy} = 1$ . Thus, one obtains the trivial dispersion relation of a free atom and the two independent branches in Fig. 4.2a disappear. Consequently, those new phenomena mentioned above disappear. Interestingly, one may realize another periodic boundary condition by replacing the two identical Raman couplings (coming from the same pair of Raman laser) in Fig. 4.1b with two independent Raman couplings (from two different pairs of Raman lasers) such that the corresponding phase factor in  $H_{3,4}$  ( $H_{4,3}$ ) that describes the coupling between  $|3\rangle$  and  $|4\rangle$  becomes  $e^{-iKy}$  ( $e^{iKy}$ ) rather than  $e^{iKy}$  ( $e^{-iKy}$ ) as in current Eq. (1). In such a case, a cylinder is penetrated by magnetic fluxes, but the net threaded magnetic flux is zero, and one can show that those new phenomena also disappear because such  $y$ -dependent phase factors in the Hamiltonian can be gauged away. This again emphasizes the importance of the net threaded magnetic flux for those new phenomena.

#### 4.4.2 Calculations of BEC wavefunctions in the real space

**For the cylinder with a nonsymmorphic symmetry in Fig. 4.1c**

We solve the Hamiltonians  $H_{q_y}$  or  $H'_{q_y}$  to obtain the probability amplitude ( $b_{n,m}^{q_y}$ ) of the constituent plane waves of the form,  $b_{n,m}^{q_y} e^{i(q_y + nK)y} |m\rangle$ , whose superposition gives the BEC wavefunction in the real space. From the BEC wavefunction, we obtain the variations of the density and phase in the real space for each spin state. For example, density and phase are illustrated in Fig. 4.1c and Fig. 4.5b for a BEC at  $q_y = 0$  and  $\delta_R = \delta_1 = \delta_2 = 0$  (both are used for all the calculations in this section) in the ground band in Fig. 4.2b and Fig. 4.5c, respectively. In addition to the results for the ground band, here we also perform calculations for a BEC in the first excited band in Fig. 4.2b and Fig. 4.5c.

Regarding Fig. 4.1c, we perform calculations using  $\Omega = 2.3 E_r$ ,  $\Omega_1 = 2.5 E_r$ ,  $\Omega_2 = 3.4 E_r$ , and  $\varepsilon_0 = 2.4 E_r$ , the same parameters as used in Fig. 4.2b. The calculated density and phase in the real space for each spin state are shown in Fig. 4.3a and Fig. 4.3b for a BEC in the ground and the first excited bands, respectively. The red line, green dashed line, blue circles and black squares respectively correspond to spin states  $|1\rangle$ ,  $|2\rangle$ ,  $|3\rangle$ , and  $|4\rangle$ .

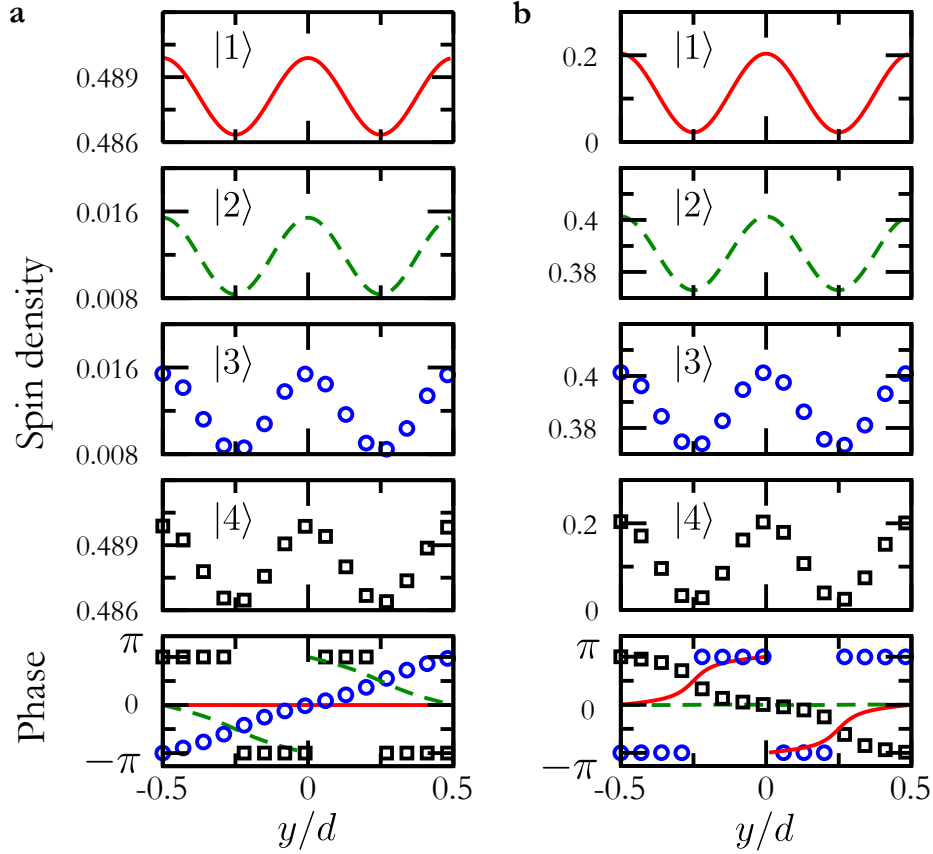


Fig. 4.3. **Density and phase versus  $y$  for each spin state, corresponding to the Hamiltonian  $H$ .** Calculations are performed for a BEC at  $q_y = 0$  in Fig. 4.2b, (a) for the ground band, and (b) for the first excited band. The red line, green dashed line, blue circles, and black squares correspond to the spin states  $|1\rangle$ ,  $|2\rangle$ ,  $|3\rangle$ , and  $|4\rangle$ , respectively. The plotted density of the spin component  $i$ ,  $\rho_i$ , is normalized by the condition  $\sum_i \int_0^1 \rho_i d(y/d) = 1$  (also used for Fig. 4.4). The calculation is performed by Yangqian Yan.

### For the cylinder with a broken nonsymmorphic symmetry in Fig. 4.5b

The following calculations are important to understand the results in Fig. 4.5 as shown later. Here we show the calculated results in order to compare them with the results shown in section 4.4.2 above.

The BEC wavefunction corresponding to Fig. 4.3a(b) can be described by  $\phi_p(q_y = 0)$  ( $\phi_m(q_y = 0)$ ) in Eq. (4.27) (Eq. (4.28)), an eigenfunction of the  $\hat{S}$  operator with an eigenvalue of  $e^{iq_y d/2} = 1$  ( $-e^{iq_y d/2} = -1$ ). Due to the nonsymmorphic symmetry, we find that (1) The calculated density of each spin state has a periodicity of  $d/2$ . (2) For the ground band, the phase of spin states  $|1\rangle$  and  $|4\rangle$  ( $|2\rangle$  and  $|3\rangle$ ) have a period of  $d/2$  ( $d$ ). For the first excited band, the phase of spin states  $|1\rangle$  and  $|4\rangle$  ( $|2\rangle$  and  $|3\rangle$ ) have a period of  $d$  ( $d/2$ ). In general, for  $q_y \neq 0$ , the phase of two spin states would have a periodicity of  $d$  while the phase of the other two would have a periodicity of  $d/2$ , because a nonzero  $q_y$  would only introduce an overall phase factor to the spin states at  $q_y = 0$ .

An additional RF coupling between spin states  $|1\rangle$  and  $|2\rangle$ , and  $|3\rangle$  and  $|4\rangle$  breaks the nonsymmorphic symmetry. In this case, the calculated spin density and phase in the real space are shown in Fig. 4.4ab respectively for a BEC in the ground and the first excited bands in Fig. 4.5c. The periodicity of the density and phase for each spin state is identical to the periodicity of the Hamiltonian  $H'$ . The maximum density of the ground state sits at  $y = \pm nd$ , where  $n$  is an integer, because of the  $s$ -wave nature of the ground state. For the first excited state, the maximum density of the spin states  $|1\rangle$  and  $|4\rangle$  sits at  $y = \pm(2n + 1)d/2$  rather than  $y = \pm nd$ . In addition, there is also local peak density appearing at  $y = \pm nd$ .

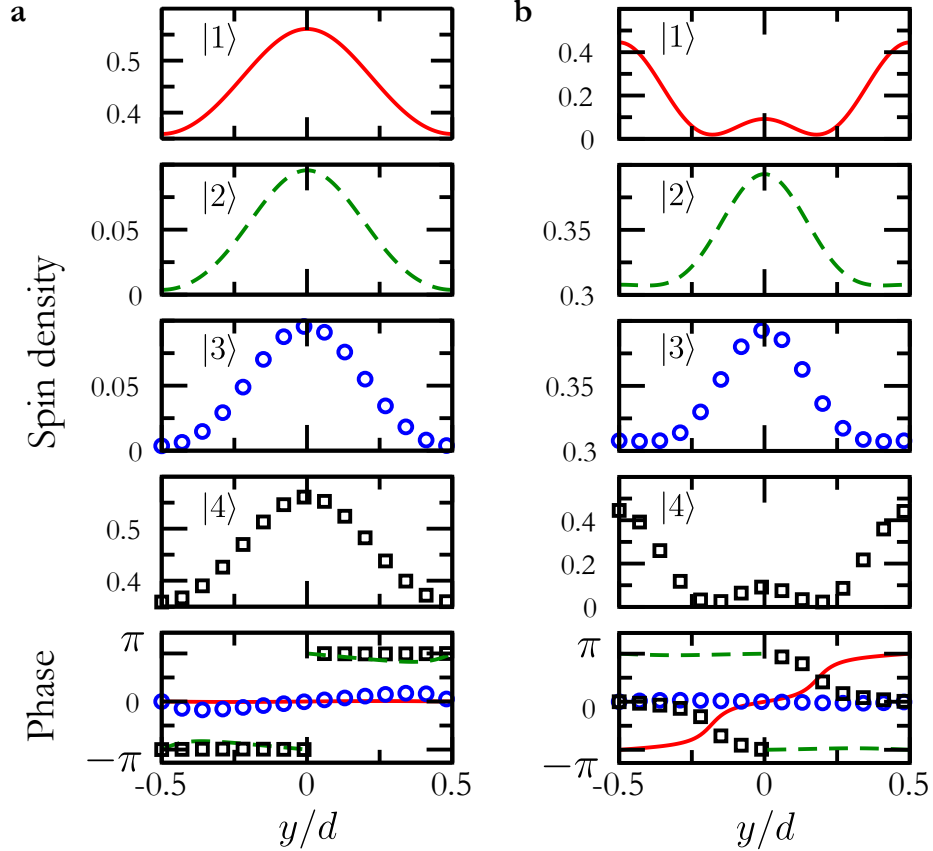
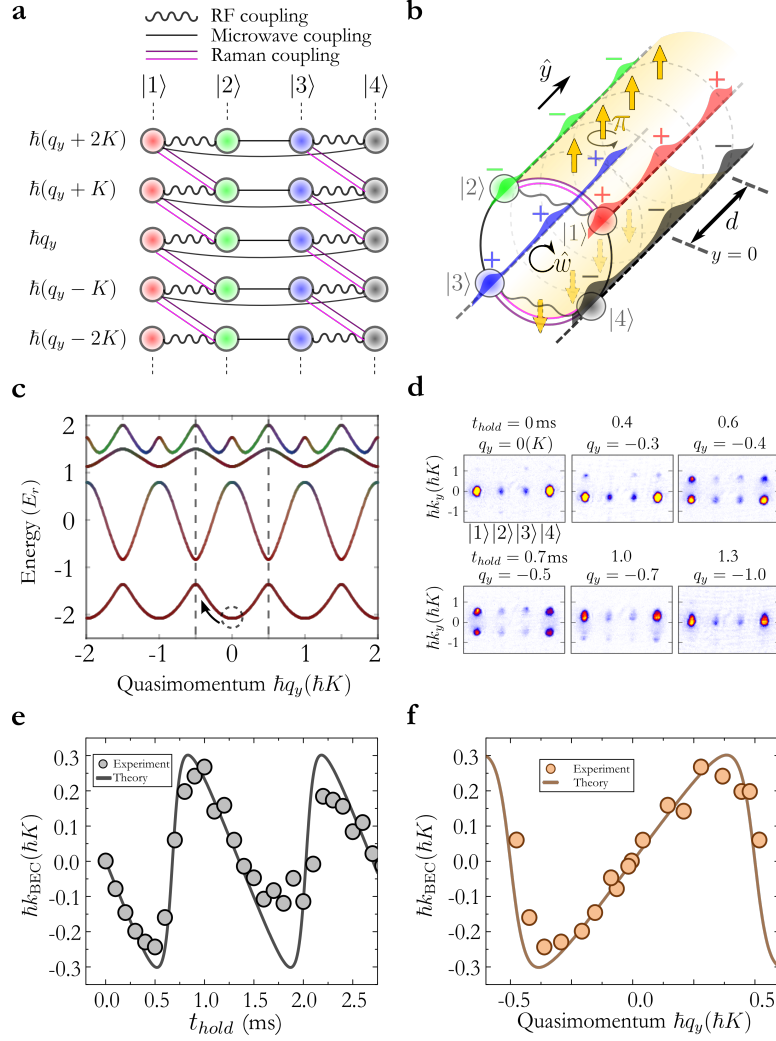


Fig. 4.4. **Density and phase versus  $y$  for each spin state, corresponding to the Hamiltonian  $H'$ .** Calculations are performed for a BEC at  $q_y = 0$  in Fig. 4.5c, (a) for the ground band, and (b) for the first excited band. The red line, green dashed line, blue circles, and black squares correspond to the spin states  $|1\rangle$ ,  $|2\rangle$ ,  $|3\rangle$ , and  $|4\rangle$ , respectively. The calculation is performed by Yangqian Yan.

#### 4.5 Quantum transport on a regular strip in momentum space

The demonstrated “momentum-space Möbius strip” is topologically protected by the nonsymmorphic symmetry, as band crossings remain under perturbations respecting this symmetry. We introduce a symmetry-breaking perturbation, a radio frequency (RF) wave (with an angular frequency identical to  $\Delta\omega_R$ ), to couple  $|1\rangle$  and  $|2\rangle$  as well as  $|3\rangle$  and  $|4\rangle$  (Fig. 4.5ab). The new Hamiltonian,  $H'$  (see subsections be-

low), does not have the nonsymmorphic symmetry but still has identical  $d$  periodicity as  $H$ . The two branches in Fig. 4.2a now merge into one that has a  $\hbar K$  periodicity (Fig. 4.5a) and band gaps open (Fig. 4.5c) at crossing points in Fig. 4.2b. We probe this new band structure using the same transport measurement. Fig. 4.5d presents TOF images at various  $t_{\text{hold}}$  and the corresponding  $q_y$ , with the analyzed data (dots) for  $\hbar k_{\text{BEC}}$  versus  $t_{\text{hold}}$  and versus quasimomentum respectively shown in Fig. 4.5e and Fig. 4.5f. Fig. 4.5d-f shows that Bloch oscillations in this case have a period of  $\sim 1.3$  ms or  $\hbar K$  (identical to the band structure's period), half the period of those observed in Fig. 4.2. Thus, the symmetry-breaking perturbation has effectively performed a topology-change operation of “untwisting” the Möbius strip in momentum space.



**Fig. 4.5. Breaking the nonsymmorphic symmetry and effects on observed Bloch oscillations.** (a) RF coupling (wiggling lines) merges the two independent branches in Fig. 4.2b, breaking the nonsymmorphic symmetry. (b) A cylinder with a broken nonsymmorphic symmetry, described by the Hamiltonian  $H'$ . For a BEC prepared at  $q_y = 0$  in the ground band in (c), both the wavefunction's phase (indicated by + and -) and the density modulation have a periodicity of  $d$ , identical to the period of the Hamiltonian  $H'$ . (c) Calculated band structure using the same parameters as used in Fig. 4.2b with the addition of an RF coupling  $\Omega_{\text{RF}} = 1.6 E_r$ , leading to gaps opened at the band crossings in Fig. 4.2b. (d) TOF images at various  $t_{\text{hold}}$  for Bloch oscillations of a BEC starting from  $q_y = 0$  (dashed circle in (c)). (e-f) Total mechanical momentum of the BEC versus  $t_{\text{hold}}$  and quasimomentum, respectively. The measured Bloch oscillations exhibit a periodicity of  $\hbar K$  rather than the  $2\hbar K$  observed in Fig. 4.2.  $q_y$  becomes equivalent to  $q_y \pm nK$ . This  $\hbar K$  periodicity is also reflected by the observed  $\hbar K$  separation between different mechanical momentum components for each spin state in (d). Data in (f) correspond to the data in the first 1.5 ms in (e) before the Bloch oscillations exhibit notable damping. Solid lines in (e, f) are single-particle calculations using the same parameters as used in (c).

### 4.5.1 Derivation of the Hamiltonians $H'$ and $H'_{q_y}$

In the following, we derive the single-particle Hamiltonian for the cylinder without a nonsymmorphic symmetry: the Hamiltonian  $H'$  and the corresponding momentum-space Hamiltonian  $H'_{q_y}$  (used for Fig. 4.5). Both take into account  $\Omega$ ,  $\Omega_{1,2}$ , and  $\Omega_{\text{RF}}$ .

$H'$  can be obtained by adding the RF coupling  $\Omega_{\text{RF}}$  to  $H$ . Since  $\Omega_{\text{RF}}$  couples  $|1\rangle$  and  $|2\rangle$ , and  $|3\rangle$  and  $|4\rangle$ , we obtain

$$H' = \frac{\hat{p}_y^2}{2m} \mathbf{I} + \begin{pmatrix} -\delta_{\text{R}} & \frac{\Omega_{\text{RF}}}{2} + \frac{\Omega}{2} e^{i(Ky)} & 0 & \frac{\Omega_2}{2} \\ \frac{\Omega_{\text{RF}}^*}{2} + \frac{\Omega^*}{2} e^{-i(Ky)} & \varepsilon_0 & \frac{\Omega_1}{2} & 0 \\ 0 & \frac{\Omega_1^*}{2} & \varepsilon_0 & \frac{\Omega_{\text{RF}}}{2} + \frac{\Omega}{2} e^{i(Ky)} \\ \frac{\Omega_2^*}{2} & 0 & \frac{\Omega_{\text{RF}}^*}{2} + \frac{\Omega^*}{2} e^{-i(Ky)} & \delta_{\text{R}} \end{pmatrix}. \quad (4.31)$$

Since RF waves only couple spin states that have the same mechanical momentum,  $H'_{q_y}$  would have the same form as Eq. (4.16) but with a modified  $A_n$  denoted by  $A'_n$ :

$$A'_n = \begin{pmatrix} \frac{\hbar^2}{2m} (q + nK)^2 & \frac{\Omega_{\text{RF}}}{2} & 0 & \frac{\Omega_2}{2} \\ \frac{\Omega_{\text{RF}}^*}{2} & \frac{\hbar^2}{2m} (q + nK)^2 + \varepsilon_0 & \frac{\Omega_1}{2} & 0 \\ 0 & \frac{\Omega_1^*}{2} & \frac{\hbar^2}{2m} (q + nK)^2 + \varepsilon_0 & \frac{\Omega_{\text{RF}}}{2} \\ \frac{\Omega_2^*}{2} & 0 & \frac{\Omega_{\text{RF}}^*}{2} & \frac{\hbar^2}{2m} (q + nK)^2 \end{pmatrix}. \quad (4.32)$$

## 4.6 Unzipping the Hall cylinder into a planar Hall strip

Lastly, we demonstrate another topological operation by unzipping the Hall cylinder into a 2D planar Hall strip. We keep  $\Omega$  and  $\Omega_1$  and remove  $\Omega_2$  in Fig. 4.1b, effectively imposing an open boundary condition along  $\hat{w}$  (Fig. 4.6a). This leads to a strip pierced by the same magnetic flux as for the cylinder. Nonetheless, the Raman-imprinted phase factor  $e^{\pm iKy}$  can now be gauged away (see subsections below), resulting in a non-periodic single-particle dispersion (Fig. 4.6b) which is then probed by the transport measurement. Fig. 4.6c presents TOF images at various  $t_{\text{hold}}$

and the corresponding  $q_y$ , with analyzed data (dots) for  $\hbar k_{\text{BEC}}$  versus  $t_{\text{hold}}$  shown in Fig. 4.6d and spin populations versus  $t_{\text{hold}}$  shown in Fig. 4.6e. In this case,  $\hbar k_{\text{BEC}}$  keeps increasing due to the gravity. The BEC is initially dominated by  $|4\rangle$  but becomes dominated by  $|1\rangle$  at later times (Fig. 4.6c).

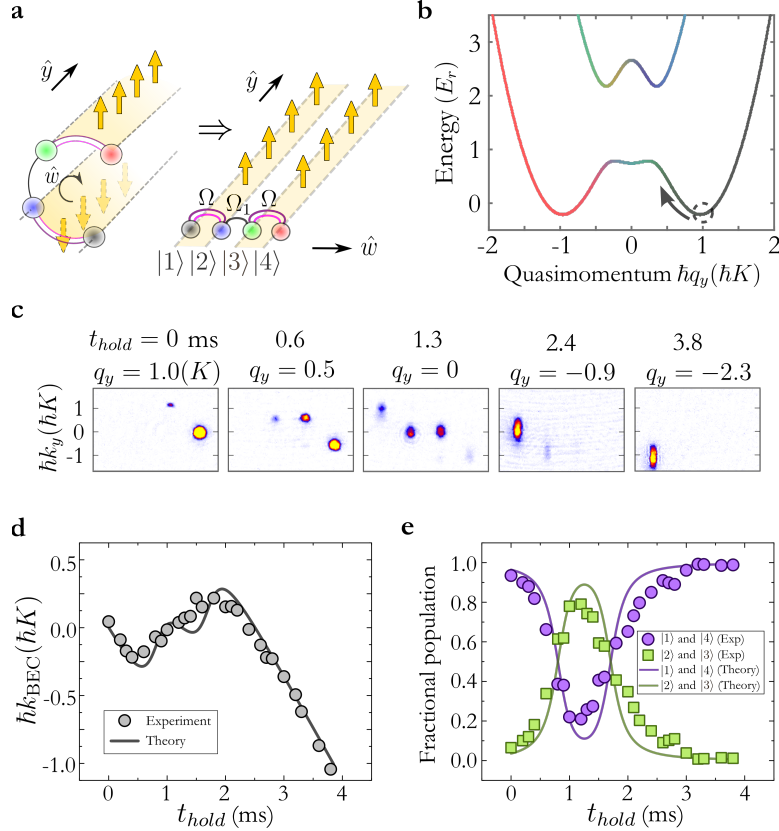


Fig. 4.6. **Unzipping the cylinder by breaking the cyclic coupling.** (a) In the synthetic space, the unzipped Hall cylinder becomes a 2D planar Hall strip. (b) Dispersion relation calculated for  $\Omega_2 = 0$ , while keeping the other parameters the same as used in Fig. 4.2b. The BEC is initially prepared at  $q_y \approx K$ , marked by the dashed circle. (c) TOF images at various  $t_{\text{hold}}$  and the corresponding quasimomentum for a BEC traveling towards negative  $q_y$  in the lowest band. (d) Total mechanical momentum of the BEC versus  $t_{\text{hold}}$ . (e) Fractional spin populations versus  $t_{\text{hold}}$ . Solid lines in (d, e) are single-particle calculations using the same parameters as used in (b).

### 4.6.1 Derivation of the Hamiltonian $H_{\text{unzip}}$

In the following, we derive the single-particle Hamiltonian for the unzipped cylinder: the momentum-space Hamiltonian  $H_{\text{unzip}}$  (used for Fig. 4.6), which takes into account  $\Omega$  and  $\Omega_1$ .

For  $H_{\text{unzip}}$ , only  $\Omega$  and  $\Omega_1$  are present. We apply a unitary transformation

$$\hat{U}_0 = \begin{pmatrix} e^{-iKy} & 0 & 0 & 0 \\ 0 & 1 & 0 & 0 \\ 0 & 0 & 1 & 0 \\ 0 & 0 & 0 & e^{iKy} \end{pmatrix} \quad (4.33)$$

to  $H$  in Eq. (4.14) (noting  $\hat{p}_y^2/(2m)\text{I} = \hbar^2 q_y^2/(2m)\text{I}$  for plane wave basis) with  $\Omega_2 = 0$  and  $\delta_{\text{R}} = \delta_1 = \delta_2 = 0$ , i.e.,  $\hat{U}_0 H \hat{U}_0^{-1}$ , to gauge away the  $y$ -dependent phase factor and obtain  $H_{\text{unzip}}$  written in the basis of  $\{|1\rangle, |2\rangle, |3\rangle, |4\rangle\}$  as:

$$H_{\text{unzip}} = \begin{pmatrix} \frac{\hbar^2}{2m}(q_y + K)^2 & \frac{\Omega}{2} & 0 & 0 \\ \frac{\Omega^*}{2} & \frac{\hbar^2}{2m}(q_y)^2 + \varepsilon_0 & \frac{\Omega_1}{2} & 0 \\ 0 & \frac{\Omega_1^*}{2} & \frac{\hbar^2}{2m}(q_y)^2 + \varepsilon_0 & \frac{\Omega}{2} \\ 0 & 0 & \frac{\Omega^*}{2} & \frac{\hbar^2}{2m}(q_y - K)^2 \end{pmatrix}. \quad (4.34)$$

If  $\Omega_2 \neq 0$ , the  $y$ -dependent phase factor cannot be gauged away because  $\hat{U}_0 H \hat{U}_0^{-1}$  would still have the  $y$ -dependent terms  $\Omega_2 e^{2iKy}$  and  $\Omega_2^* e^{-2iKy}$ .

## 4.7 Details in experiments and calculations

### 4.7.1 Initial state preparations for experiments in the previous sections

We note that the eigenstate of the BEC at  $q_y = 0$  in band 1 (band 2) shown in Fig. 4.2b has dominant populations in  $|4\rangle$  and  $|1\rangle$  ( $|3\rangle$  and  $|2\rangle$ ). Thus, to load a BEC into such an eigenstate, we first prepare a BEC at  $|4\rangle$  ( $|3\rangle$ ) with  $\delta_{\text{R}} < -2.5 E_{\text{r}}$  and  $\delta_1 < -2.5 E_{\text{r}}$ . Note that we do not specify the value of  $\delta_2$ , which is inferred from

$\delta_2 = \delta_1 + 2\delta_R$  (Eq. 4.13) due to fulfillment of the resonance condition in Eq. (4.11). For band 1, we then ramp on the Raman and microwave couplings  $\Omega$  and  $\Omega_{1,2}$  from zero to final values while ramping  $\delta_R$  and  $\delta_1$  to zero in 15 ms. For band 2, we ramp on the microwave couplings  $\Omega_{1,2}$  from zero to final values while ramping both  $\delta_R$  and  $\delta_1$  to around  $-0.6 E_r$  in 15 ms. Subsequently, while keeping  $\Omega_{1,2}$  at the final values, we ramp on the Raman coupling  $\Omega$  from zero to final values in 5 ms during which we ramp  $\delta_R$  and  $\delta_1$  to zero in 3 ms and then hold  $\delta_R$  and  $\delta_1$  at zero for the rest 2 ms.

For the initial state preparation in the lowest band in Fig. 4.5b, we first prepare a BEC at  $|4\rangle$  with  $\delta_R < -5 E_r$  and  $\delta_1 < -5 E_r$ . Then, we ramp on the Raman and microwave couplings  $\Omega$  and  $\Omega_{1,2}$  from zero to final values while ramping  $\delta_R$  and  $\delta_1$  to zero in 15 ms. At the very beginning (at which  $\delta_R < -5 E_r$  and  $\delta_1 < -5 E_r$ , so the RF wave is off-resonant) of this 15-ms ramp, the RF coupling  $\Omega_{\text{RF}}$  is abruptly turned on to the final value. Then,  $\Omega_{\text{RF}}$  is held at the same final value while  $\delta_R$  and  $\delta_1$  are ramped to zero in 15 ms.

For the initial state preparation at the minimum of the right well in Fig. 4.6b, we first prepare a BEC at  $|4\rangle$  with  $\delta_R < -2.5 E_r$  and  $\delta_1 < -2.5 E_r$ . Then, we ramp on the Raman and microwave couplings  $\Omega$  and  $\Omega_1$  from zero to final values while ramping  $\delta_R$  and  $\delta_1$  to zero in 15 ms. In this case,  $\Omega_2$  is zero throughout the experiment.

### 4.7.2 Imaging analysis

The propagation direction ( $\hat{x}'$ ) of our imaging laser is  $\sim 27^\circ$  with respect to the  $x$ -axis in the  $x-z$  plane (Fig. 4.1a). Thus, the TOF images are in the  $y-z'$  plane (where  $\hat{z}'$  is perpendicular to  $\hat{x}'$  in the  $x-z$  plane). In each TOF image, we individually fit

the atomic cloud of each spin and mechanical momentum component to a 2D bimodal distribution of the form:

$$\begin{aligned}
 & A \max \left( 1 - \left( \frac{y - y_c}{R_y} \right)^2 - \left( \frac{z' - z_c}{R_{z'}} \right)^2, 0 \right)^{3/2} \\
 & + B \exp \left( -\frac{1}{2} \left( \left( \frac{y - y_{cT}}{\sigma_y} \right)^2 + \left( \frac{z' - z_c}{\sigma_{z'}} \right)^2 \right) \right),
 \end{aligned} \tag{4.35}$$

where the first term corresponds to the condensate part according to the Thomas-Fermi approximation and the second term corresponds to the thermal part. In our experiments, a nearly pure BEC with a typical condensate fraction  $> 90\%$  is prepared at the end of the evaporation cooling (before turning on the coupling fields). After the initial state preparation and right before the transport measurement, the typical condensate fraction is  $> 50\%$ . After  $\sim 10$  ms of transport in the band, the typical condensate fraction is  $> 30\%$ . The measured quantities such as mechanical momentum and spin populations are referred to the condensate part. For each atomic cloud component  $i$ , its condensate atom number  $N_i$  and mechanical momentum  $p_i$  are extracted from the fitting to obtain the total mechanical momentum of the BEC,  $\hbar k_{\text{BEC}} = N_i p_i / (\sum_i N_i)$ . Each cloud component's mechanical momentum  $p_i$  is determined by the difference between its center-of-mass position ( $y_c$ ) and the center-of-mass position of a BEC that has zero mechanical momentum, based on the calibrated conversion between  $\hbar K$  and image pixels.

### 4.7.3 Calculated curves shown in figures in the previous sections

When using the Hamiltonians  $H_{q_y}$  and  $H'_{q_y}$  (see Eq. (4.16)) to calculate the band structures, we use  $n$  ranging from  $-13$  to  $13$ , i.e., each Hamiltonian is a  $108$  by  $108$  matrix. On the other hand,  $H_{\text{unzip}}$  in Eq. (4.34) is a  $4$  by  $4$  matrix. We solve the eigenstates of  $H_{q_y}$ ,  $H'_{q_y}$ , and  $H_{\text{unzip}}$ , as a function of quasimomentum to obtain the corresponding mechanical momentum and spin compositions of the BEC traveling in bands. In general, the eigenstate is a normalized vector of the form  $(\dots, b_{n,m}^{q_y}, \dots)^T$ , where the coefficient  $b_{n,m}^{q_y}$  is the probability amplitude ( $|b_{n,m}^{q_y}|^2$  is the fractional popu-

lation) corresponding to the state  $|\hbar(q_y + nK); m\rangle$ . The total mechanical momentum of the BEC at  $q_y$  is determined as  $\hbar k_{\text{BEC}}(q_y) = \hbar \sum_{n,m} |b_{n,m}^{q_y}|^2 (q_y + nK)$ . The fractional population of the spin state  $|m\rangle$  at  $q_y$  is  $\sum_n |b_{n,m}^{q_y}|^2$ . The spin texture of band structures such as Fig. 4.2b is revealed by the  $q_y$ -dependent color, determined by the population-weighted colors of the constituent spin states. That is, the color of an eigenstate at  $q_y$  is determined by  $\sum_m (\sum_n |b_{n,m}^{q_y}|^2) (\text{color})_m$ , where  $(\text{color})_m$  is a 1 by 3 vector representing the color of the spin state  $|m\rangle$ , with  $(\text{color})_1 = (1, 0, 0)$  for red,  $(\text{color})_2 = (0, 1, 0)$  for green,  $(\text{color})_3 = (0, 0, 1)$  for blue, and  $(\text{color})_4 = (0, 0, 0)$  for black. Note that the theoretical  $\hbar k_{\text{BEC}}$  is calculated as  $\hbar k_{\text{BEC}}(q_y) = m v_p(q_y) = \frac{m}{\hbar} \frac{dE(q_y)}{dq_y}$  [131], where  $v_p$  is the group velocity,  $E$  is the band (eigen)energy, and  $\frac{dE(q_y)}{dq_y}$  is the slope of the band. Both  $v_p$  and  $E$  are functions of  $q_y$ , where  $q_y = q_0 + F_g t_{\text{hold}}/\hbar$  is a function of  $t_{\text{hold}}$ ,  $F_g = d(\hbar q_y)/dt_{\text{hold}}$  is the total force acting on the atoms during the transport, and here the initial quasimomentum  $\hbar q_0 = 0$ .

The above calculated physical quantities are functions of  $q_y$ . They can be converted to functions of  $t_{\text{hold}}$  based on the measurement of quasimomentum versus  $t_{\text{hold}}$  in each set of experiment. Fig. 4.7 is a representative measurement obtained from the experiment corresponding to Fig. 4.2c, showing the measured quasimomentum versus  $t_{\text{hold}}$  obtained from the atomic clouds of  $|1\rangle$  and  $|4\rangle$ . The corresponding slope,  $d(\hbar q_y)/d(t_{\text{hold}}) = F_g$ , is obtained by a linear fit to the data. The average of the slope,  $0.751 \hbar K/ms$  in this case, is then used to calculate various physical quantities versus  $t_{\text{hold}}$ . Note this total force is primarily due to the gravity (which would give a slope of  $0.843 \hbar K/ms$  with  $g = 9.81 m/s^2$ ) but also contains a small contribution (with the opposite sign) from other background (e.g. magnetic) fields present during the experiment.

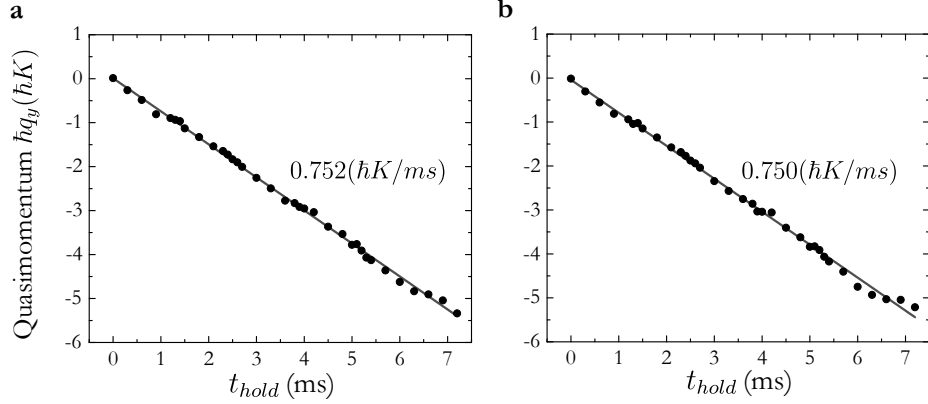


Fig. 4.7. **Representative measurement of quasimomentum versus  $t_{\text{hold}}$ .** (a) and (b) are obtained respectively from the atomic clouds of  $|1\rangle$  and  $|4\rangle$  in the experiment corresponding to Fig. 4.2c. Dots are experimental data and lines are linear fits.

#### 4.8 Discussion and conclusion

Differently from the realization of a Hall tube with fermions [130], we do not use an external optical lattice. Instead, topological lattices emerge due to curving a Hall strip into a Hall cylinder. In addition, differently from the generalized inversion symmetry-protected gapped topological band in ref. [130], we observe a nonsymmetric symmetry-protected gapless topological band which allows for observing the quantum transport in the resulting momentum-space Möbius strip. Moreover, we apply a controllable symmetry-breaking perturbation to open a band gap and explore the quantum transport in the resulting momentum-space regular strip, which may allow for studying interaction effects on such a transport as will be discussed in Chapter 6.

In summary, we have observed topological states absent in planar space but emerging due to manipulating the geometry of space. Direct extensions of this work include studying superfluidity on curved surfaces [118,119], implementing a Laughlin's charge pump [132] (e.g. by making Equation (4.1) time-dependent), and exploring the frac-

tal energy spectrum of Hofstadter butterfly as suggested in ref. [41]. Our work also paves the way to creating synthetic gauge fields in diverse geometries of spaces [42]. For example, using Laguerre-Gaussian beams as the Raman lasers in Fig. 4.1a may create a Hall torus [133]. Furthermore, increasing inter-particle interactions (e.g. by imposing strong confining potentials in  $x$  and  $z$  directions in our case or enhancing the scattering length by Feshbach resonance) in spaces with curved geometries, for instance a Hall cylinder or torus, may allow exploring intriguing quantum many-body phases such as fractional quantum Hall states as suggested in refs. [134–136].

## 5. SCISSORS MODE AND ROTATIONAL PROPERTIES OF A SPIN-ORBIT-COUPLED BOSE-EINSTEIN CONDENSATE

### 5.1 Introduction and motivation

The rotational properties of a Bose-Einstein condensate (BEC) are important to study its superfluidity. For example, the scissors mode of a trapped BEC (rotational oscillations of a BEC with respect to trap axes) has proven to be important for probing rotational properties and superfluidity. Recent studies have found that spin-orbit coupling (SOC) can change a BEC's superfluid properties, such as the superfluid critical velocity, superfluid fraction, and the quenching of the moment of inertia. Here, we study the scissors mode of a Raman-induced spin-orbit-coupled (SO-coupled) BEC of  $^{87}\text{Rb}$  in an effective rotating frame induced by a synthetic magnetic field  $\mathbf{B}^*$ . A SO-coupled BEC is first prepared in the presence of  $\mathbf{B}^*$  generated by a spatially-varying Raman coupling. We then quench the Raman coupling or detuning to generate a synthetic shear force, which pushes and tilts the BEC. After such a quench, both the dipole and scissors modes are excited, and their dynamics is studied in the presence (or absence) of SOC and  $\mathbf{B}^*$ . We experimentally find that the measured scissors frequency does not agree with the prediction based on effective masses. Our simulations reveal that the scissors mode can contain two frequency components, which are important to understand the experimental results. Our work may allow us to study how SOC modify a BEC's rotational and superfluid properties.

Superfluids are interesting in their own right, and could be a platform to study closely-related phenomena such as superconductivity. Atomic quantum gases can possess rich superfluid properties and are highly controllable. Thus, novel superfluids difficult to explore in conventional systems may be studied in such atomic systems.

Recently, SO-coupled quantum gases have attracted a lot of attention because of their potential for quantum simulation of diverse phenomena [15]. On the other hand, SO-coupled BECs have been theoretically predicted to be an intriguing superfluid. For instances, SOC can change several superfluid properties of an atomic BEC, such as the superfluid critical velocity [20, 77] and superfluid fraction [137, 138]. In addition, irrotationality, a fundamental feature of superfluids and characterized by  $\nabla \times \mathbf{v} = 0$  ( $\mathbf{v}$  is the velocity), is broken for a SO-coupled BEC [79]. Consequently, a rotating SO-coupled BEC could exhibit diffused vorticity [79] and unusual moment of inertia (as exhibited by a rigid body rather than a quenched value that would be exhibited by a superfluid) [79] and angular momentum [139]. In contrast, a regular BEC possessing irrotationality manifests rotational superfluid phenomena such as quantized vortices [140–142] and quenching of the moment of inertia [143, 144]. In other words, a SO-coupled BEC can have rotational properties distinct from that of a regular BEC, because irrotationality is violated in the former due to SOC but conserved in the latter. Besides, rotational and superfluid properties are closely related, and thus studying rotational properties of a SO-coupled BEC may provide us insights to understand how SOC change a BEC’s superfluid properties .

So far, rotational and superfluid properties of a SO-coupled BEC are barely explored experimentally. Only the sound velocity [145] (which along with the calculated compressibility [137, 138] can reveal the superfluid fraction) and roton-maxon excitation spectrum [145, 146] of a SO-coupled BEC have been measured. To explore rotational properties of a SO-coupled BEC, instead of a physical rotation, we put the BEC into an effective rotation by generating a synthetic magnetic field  $\mathbf{B}^*$  for the BEC. In this work, we first prepare a SO-coupled BEC in the presence of such a  $\mathbf{B}^*$  field with an initial value  $\mathbf{B}_i^*$ . Then, we suddenly change  $\mathbf{B}_i^*$  to a final value  $\mathbf{B}_f^*$ , inducing the scissors mode (an important rotational probe for superfluidity and will be introduced below) of a SO-coupled BEC in the presence of various  $\mathbf{B}_f^*$  (including  $\mathbf{B}_f^* = 0$ ). The behavior of such a scissors mode is the focus of this work.

### 5.1.1 BECs versus superfluids

BECs and superfluids are closely related but different. BEC density ( $n_c$ ) and superfluid density ( $n_s$ ) of a quantum fluid can be different because their definitions are physically different [147]. The BEC density is defined as the particle density in the zero momentum state. The superfluid density is defined as the particle density participating in the superflow based on the two-fluid model. For a regular BEC of weakly-interacting Bose gases at absolute zero temperature,  $n_c \approx n$  and  $n_s = n$ , where  $n$  is the total particle density. However, for a superfluid of  $^4\text{He}$  at absolute zero temperature,  $n_c \approx 0.1n$  and  $n_s = n$  (i.e. all particles participate in the superflow even though the BEC fraction is only around 10%), where the notable difference between  $n_c$  and  $n_s$  is due to the strong inter-particle interactions that play important roles in determining the many-body wave function of the system [147].

### 5.1.2 Introduction to the scissors mode

The scissors mode is a type of collective excitations. Studying collective excitations has been an important tool to unveil properties of a quantum gas. For instances, breathing and scissors modes are used to probe the BEC-BCS crossover of a degenerate fermionic gas [148]. Spin-momentum locking and quantum phase transitions of a SO-coupled BEC are disclosed by dipole oscillations [149]. Dipole oscillations of a SO-coupled BEC may be used to probe its anomalous Hall conductivity [150]. Spin transport is studied in strongly-interacting fermionic gases [151] and in SO-coupled BECs [50] using the spin-dipole mode. Superfluid Hall effect is demonstrated by the coupling between quadrupole and scissors modes of a BEC in synthetic magnetic fields [152].

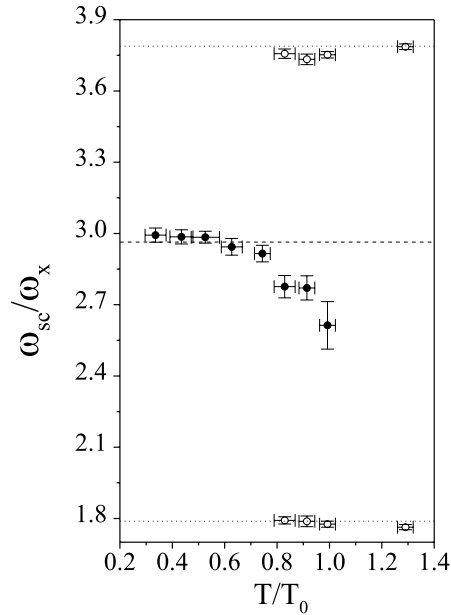


Fig. 5.1. The frequency shift of the scissors mode of an atomic gas at finite temperatures. The open circles refer to the thermal component whose frequency does not depend on the temperature and is in agreement with the collisionless prediction. The solid circles refer to the condensate component, and are in agreement with the hydrodynamic prediction at the low temperature limit. Reproduced from ref. [153].

---

Among various collective excitations, only the scissors mode has proven to be able to probe superfluidity. Such a mode is first studied in atomic nuclei. The out-of-phase rotation of neutron and proton clouds unveils the emergence of superfluidity of deformed atomic nuclei [154]. For trapped atomic gases, the scissors mode has been shown theoretically [155] and experimentally [156] as an important rotational probe for superfluidity. Its frequency shift and damping at different temperatures can probe the BEC phase transition [153], as shown in Fig. 5.1.

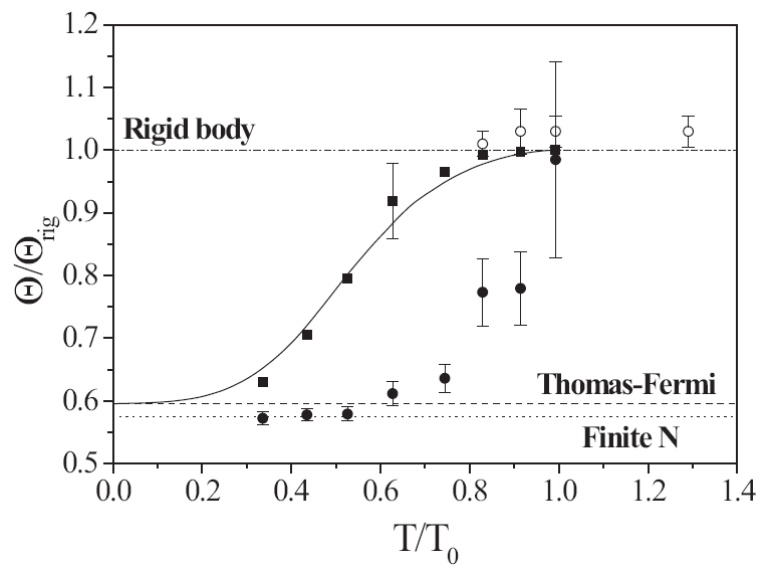


Fig. 5.2. The moment of inertia normalized to the rigid-body value at various temperatures. The open circles refer to the thermal component. The solid circles refer to the condensate component. The solid squares and line refer to the whole atomic gas. The dashed line refers to the hydrodynamic prediction in the low-temperature limit. The dotted line refers to the finite atom number correction. The moment of inertia is obtained by the measured frequency of the scissors mode (see details in ref. [144]: here, the scissors mode is in the  $x - y$  plane, i.e. the atomic cloud rotates around the  $z$  axis and thus the associated moment of inertia presented here is with respect to the  $z$  axis). The reduced moment of inertia indicates the transition from a normal fluid to a superfluid. Reproduced from ref. [144].

---

Besides, its frequency can be used to measure a quantum gas's moment of inertia, whose quenching behavior with decreasing temperature discloses the normal fluid to superfluid transition [144, 153], as shown in Fig. 5.2. For a regular BEC, the scissors mode of an expanding BEC [157] or of a rotating BEC [158] further manifests a regular BEC's intriguing superfluid behaviors and demonstrates the important role of the associated irrotational flow. Recently, the scissors mode is used to probe the anisotropic dipole-dipole interaction in dipolar quantum droplets of  $^{164}\text{Dy}$  [159].

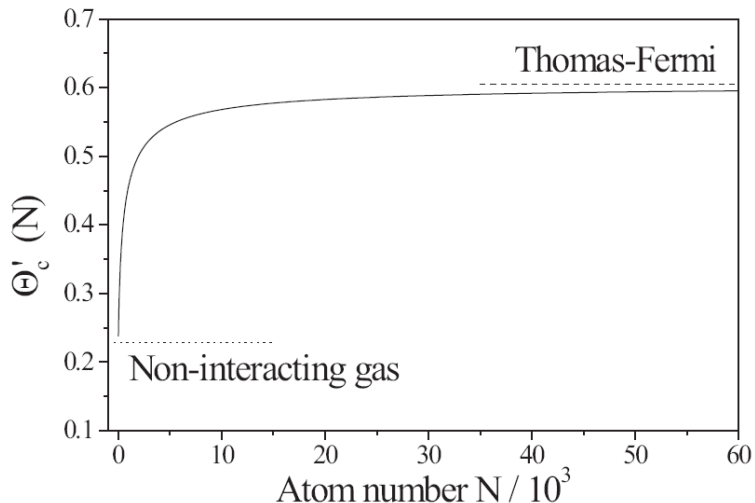


Fig. 5.3. Calculated moment of inertia versus atom number. In the small atom number limit it approaches the prediction based on the non-interacting gas at zero temperature (dotted line). In the large atom number limit it approaches the Thomas-Fermi prediction (dashed line). Reproduced from ref. [144].

Notice that the moment of inertia or the frequency of the scissors mode do not strongly depend on the atom number (or interaction) as long as the atom number is large enough. Fig. 5.3 shows the calculated moment of inertia versus atom number. In the small atom number limit it approaches the prediction based on the non-interacting gas at zero temperature (dotted line). In the large atom number limit it approaches the Thomas-Fermi prediction (dashed line).

At absolute zero temperature, a regular BEC exhibits superfluidity. Its scissors mode in the  $y - z$  plane in either the hydrodynamic or collisionless regime is a sinusoidal oscillation at a single frequency  $f_s = \sqrt{f_y^2 + f_z^2}$  [144, 153, 155, 156], where  $f_y$  and  $f_z$  are trap frequencies, as shown in Fig. 5.4b. For a thermal gas, its scissors mode is a beat wave (as shown in Fig. 5.4a) comprising two equal-amplitude frequency components (manifesting both the rotational and irrotational characteristics of a normal fluid) at  $|f_y - f_z|$  and  $|f_y + f_z|$  in the collisionless regime, or becomes a damped sinusoidal oscillation in the hydrodynamic regime [144, 153, 155].

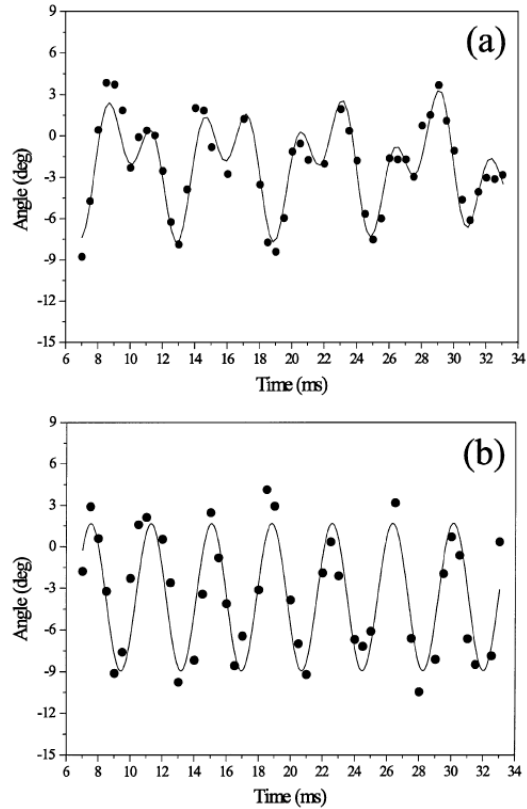


Fig. 5.4. Scissors mode of an atomic gas. (a) For a thermal gas, its scissors mode oscillates as a beat wave with two frequencies determined by the trap frequencies (see texts). (b) For a BEC exhibiting superfluidity, its scissors mode oscillates at a single frequency (see texts). Reproduced from [156].

---

## 5.2 Experimental set-up and timing diagram

In our experiment, a  $^{87}\text{Rb}$  BEC in the  $F = 1$  hyperfine state with condensate atom number  $N_c \sim 1 - 2 \times 10^4$  is produced in an optical dipole trap [50]. Trap frequencies are  $f_z \sim (75 \pm 5)$  Hz and  $f_x \sim f_y \sim (175 \pm 5)$  Hz.

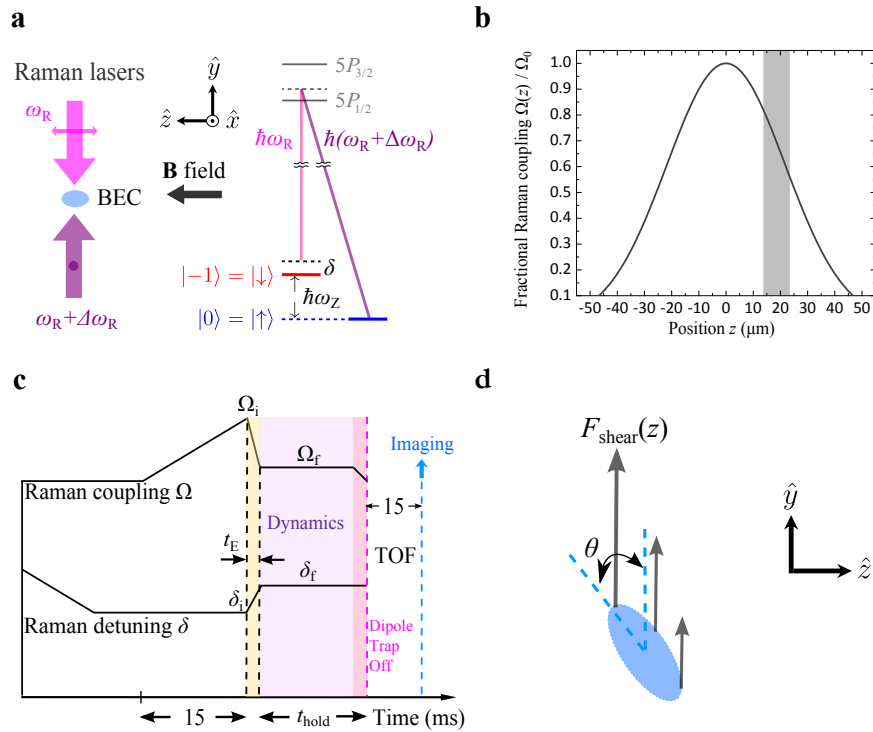


Fig. 5.5. **Experimental set-up and timing diagram.** (a) Counter-propagating Raman lasers with an angular frequency difference of  $\Delta\omega_R = 2\pi(3.5\text{MHz})$  couple the Zeeman sublevels  $|\downarrow\rangle$  and  $|\uparrow\rangle$  separated by  $\hbar\omega_Z \sim \hbar\Delta\omega_R$  in the  $F = 1$  hyperfine state of  $^{87}\text{Rb}$  to create synthetic SOC along  $\hat{y}$ . The Raman detuning  $\delta$  is controlled by the bias magnetic field  $\mathbf{B}$ . (b) A BEC is prepared in the gray region of the Gaussian distribution of the Raman coupling, experiencing a spatially-varying Raman coupling and a synthetic magnetic field  $\mathbf{B}^*$  (see texts). The Raman coupling at the BEC's center (located around 65-75% of the peak) is  $\Omega$ . (c) Experimental timing diagram. After preparing the BEC at  $\Omega = \Omega_i$  and  $\delta = \delta_i$ ,  $\Omega_i$  and  $\delta_i$  are quickly changed to  $\Omega_f$  and  $\delta_f$  in  $t_E = 1$  ms.  $\Omega_f$  and  $\delta_f$  are then held for  $t_{\text{hold}}$  before a 15-ms TOF and the following absorption imaging. (d) A shear force ( $F_{\text{shear}}(z)$  along  $\hat{y}$ , indicated by gray arrows) induced by the quench process is applied to the BEC, pushing (along  $\hat{y}$ ) and tilting the BEC to induce dipole and scissors (oscillations of the tilt angle  $\theta$ ) modes. Here, the tilt angle is defined as the angle between the  $y$  axis and the major axis of the BEC.

As shown in Fig. 5.5a, hyperfine spin states  $|m_F = -1\rangle = |\downarrow\rangle$  and  $|m_F = 0\rangle = |\uparrow\rangle$  (Zeeman split by  $\hbar\omega_Z \approx \hbar\Delta\omega_R$  using a bias magnetic field  $\mathbf{B} = B\hat{z}$ ) are coupled by counter-propagating Raman laser beams (whose angular frequency difference is

$\Delta\omega_{\text{R}}$ ) along  $\pm\hat{y}$ . The Raman laser's wavelength ( $\lambda \sim 790$  nm) sets the photon recoil momentum  $\hbar k_{\text{r}} = 2\pi\hbar/\lambda$  and energy  $E_{\text{r}} = \hbar^2 k_{\text{r}}^2/2m$ , where  $m$  is the mass of a  $^{87}\text{Rb}$  atom and  $\hbar$  is the reduced Planck constant. Such a Raman coupling scheme creates synthetic one-dimensional (1D) SOC (so-called equal Rashba-Dresselhaus SOC) [37, 50, 65–68, 71–74, 160] along  $\hat{y}$ . The single-particle SO-coupled Hamiltonian,  $H_{\text{SOC}}$ , written in the basis of bare spin and momentum states  $\{|\downarrow, \hbar(q_y + k_{\text{r}})\rangle, |\uparrow, \hbar(q_y - k_{\text{r}})\rangle\}$  is [37]:

$$H_{\text{SOC}} = \begin{pmatrix} \frac{\hbar^2}{2m}(q_y + k_{\text{r}})^2 - \delta & \frac{\Omega}{2} \\ \frac{\Omega}{2} & \frac{\hbar^2}{2m}(q_y - k_{\text{r}})^2 \end{pmatrix}, \quad (5.1)$$

where  $\Omega$  is the Raman coupling (tunable by the intensity of the Raman laser),  $\delta = \hbar(\Delta\omega_{\text{R}} - \omega_{\text{z}})$  is the Raman detuning (tunable by  $B$ ). Here,  $\hbar k_{\downarrow} = \hbar(q_y + k_{\text{r}})$  ( $\hbar k_{\uparrow} = \hbar(q_y - k_{\text{r}})$ ) is the mechanical momentum in the  $y$  direction of the bare spin component  $|\downarrow\rangle$  ( $|\uparrow\rangle$ ), where  $\hbar q_y$  is the quasimomentum. The eigenvalues of (5.1) versus  $\hbar q_y$  define the ground and excited energy bands. In this work,  $\delta > 0$  and the ground dressed band is tilted such that there exists only one energy minimum (e.g. see Fig. 5.7ad), which can be identified with a synthetic vector potential  $\mathbf{A}$  [29]. Note that  $\mathbf{A}$  is tunable by  $\Omega$  and  $\delta$  [29, 37].

By making  $\Omega$  spatially-dependent,  $\mathbf{A}$  becomes spatially-dependent and thus corresponds to a synthetic magnetic field  $\mathbf{B}^*$ , which creates an effective rotation for a SO-coupled BEC. We prepare the BEC at the side of the Gaussian intensity distribution of the Raman laser (gray region in Fig. 5.5b, similar to ref. [40]), such that the BEC experiences a  $z$ -dependent  $\Omega(z)$  (while  $\delta$  is spatially uniform). This leads to a  $z$ -dependent  $\mathbf{A}(\Omega(z), \delta) = A(z, \delta)\hat{y}$  and a corresponding  $\mathbf{B}^* = \nabla \times \mathbf{A}(z, \delta) = -\frac{\partial A(z, \delta)}{\partial z}\hat{x}$  for the BEC. In our setup, the fractional Raman coupling  $\Omega(z)/\Omega_0 = \exp(-z^2/(2\sigma^2))$  shown in Fig. 5.5b is empirically determined by the average of several measurements, where  $\Omega_0$  is the Raman coupling at  $z = 0$ ,  $z$  is in  $\mu\text{m}$ , and  $\sigma = 21.785 \pm 2.059 \mu\text{m}$ . The BEC's center  $z_0$  is chosen such that  $\Omega(z_0)/\Omega_0 \sim 0.7 \pm 0.05$  and is used for all the experiments in this work. For simplicity,  $\Omega$ ,  $\Omega_{\text{i}}$ , and  $\Omega_{\text{f}}$  below refer to the Raman coupling at the BEC's center, i.e.  $\Omega(z_0)$ ,  $\Omega_{\text{i}}(z_0)$ , and  $\Omega_{\text{f}}(z_0)$ .

We first prepare a SO-coupled BEC in the presence of an initial synthetic magnetic field  $\mathbf{B}_i^*$ . Starting with a bare BEC (centered at  $z_0$ ) at  $|m_F = -1\rangle$  state,  $\Omega$  is slowly ramped from 0 to an initial value  $\Omega_i$  in 15 ms at some initial detuning  $\delta_i$  (see the timing diagram in Fig. 5.5c), such that the center of the BEC would be prepared around the energy minimum of a tilted ground dressed band at  $\Omega_i$  and  $\delta_i$ . After preparing such an initial state, we quickly change  $\Omega_i$  and  $\delta_i$  to respective final values  $\Omega_f$  and  $\delta_f$  in  $t_E = 1$  ms. Such a quench process is slow enough to keep the BEC staying in the ground dressed band but fast enough to apply a spatially-varying synthetic electric field [35]  $\mathbf{E}(z) = -\frac{\partial \mathbf{A}(z)}{\partial t} \approx -\frac{\Delta A(z)}{t_E} \hat{y}$  to the static BEC, where  $\Delta A(z) = (A(\Omega_f, \delta_f) - A(\Omega_i, \delta_i))|_z$ . This leads to a shear force (along  $\hat{y}$ , Fig. 5.5d) that kicks and tilts the BEC such that the center of mass and tilt angle (defined in Fig. 5.5d) of the BEC are no longer in equilibrium with the trap center and axes, respectively. Therefore, a dipole mode (along  $\hat{y}$ ) and a scissors mode (angle oscillations in the  $y - z$  plane) are induced. Both  $\Omega_f$  and  $\delta_f$  are maintained for various time  $t_{\text{hold}}$ , during which the dynamics of the dipole and scissors modes is studied. Subsequently, the Raman laser and dipole trap are turned off in 1 ms and the atoms are released for a 15 ms time of flight (TOF), at the beginning of which a Stern-Gerlach process is performed for 9 ms to separate atoms of different bare spin states. We then perform absorption imaging to obtain TOF images, which reveal spin and momentum compositions of atoms at various  $t_{\text{hold}}$ . During  $t_{\text{hold}}$ , the spin composition of a dressed BEC is dominated by the  $|m_F = -1\rangle$  state. Thus, we focus on the dynamics of this dominant spin component, which is fitted to a rotated 2D Gaussian distribution to extract its center-of-mass and angle oscillations. Note that the tilt angle of the BEC after TOF could be different from the in-situ tilt angle [144, 156]. Nevertheless, when the duration of TOF is fixed, the scissors mode's frequency in these two cases would be identical.

### 5.3 Experimental and simulation results

#### 5.3.1 Experimental results

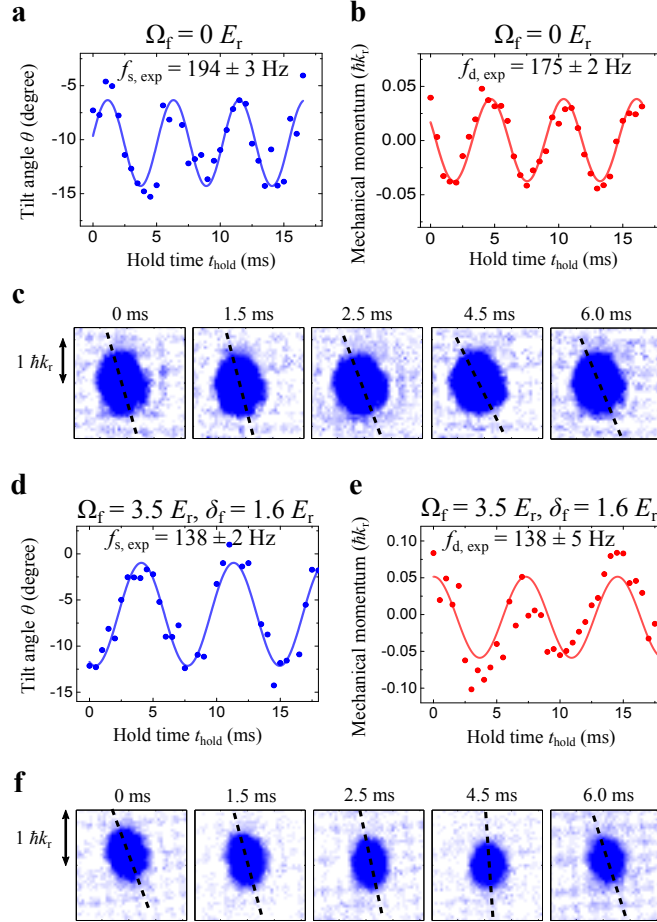


Fig. 5.6. **Exemplary scissors and dipole modes of a regular BEC and of a SO-coupled BEC in  $\mathbf{B}^*$ .** (a) and (b) respectively show scissors and dipole oscillations of a regular BEC ( $\Omega_f = 0$ ) with the corresponding select TOF images (dashed lines indicating the tilt angle) shown in (c). We fit the first 2-3 periods of experimental data (scatters) in (a) and (b) to a single sinusoidal function (solid lines) to obtain the frequency of scissors ( $f_{s, \text{exp}} = 194 \pm 3$  Hz) and dipole ( $f_{d, \text{exp}} = 175 \pm 2$  Hz) modes. (d) and (e) respectively show scissors and dipole oscillations of a SO-coupled BEC in the presence of  $\mathbf{B}^*$  (at  $\Omega_f = 3.5 E_r$  and  $\delta_f = 1.6 E_r$ ) with the corresponding select TOF images shown in (f). The measured scissors and dipole modes' frequencies are  $f_{s, \text{exp}} = 138 \pm 2$  Hz and  $f_{d, \text{exp}} = 138 \pm 5$  Hz, respectively. The error bar in the measured frequency is the standard error of the fit.

---

As shown in Fig. 5.6ab, when  $\Omega_f = 0$ , the measured frequencies of dipole (along  $\hat{y}$ ) and scissors (in  $y - z$  plane) modes are respectively  $f_{d, \text{exp}} = 175 \pm 2$  Hz and  $f_{s, \text{exp}} = 194 \pm 3$  Hz, in agreement with the corresponding predicted frequencies  $f_{d, \text{eff}} = f_y = 175$  Hz and  $f_{s, \text{eff}} = \sqrt{f_y^2 + f_z^2} \sim 192$  Hz for a bare BEC (in this measurement,  $f_y = 175$  Hz and  $f_z = 80$  Hz). Select TOF images for this case are shown in Fig. 5.6c. When  $\Omega_f \neq 0$ , taking into account the effective mass  $m^*$  resulting from the ground dressed band, the predicted dipole mode's frequency along  $\hat{y}$  is

$$f_{d, \text{eff}} = f_y \sqrt{m/m^*}, \quad (5.2)$$

and the scissors mode's frequency is

$$f_{s, \text{eff}} = \sqrt{f_d^2 + f_z^2}. \quad (5.3)$$

As shown in Fig. 5.6de for  $\Omega_f = 3.5 E_r$  and  $\delta_f = 1.6 E_r$ , the measured dipole mode's frequency  $f_{d, \text{exp}} = 138 \pm 3$  Hz is approximately in agreement with the effective mass prediction of 149 Hz (given the uncertainties in Raman coupling and trap frequencies), however, the measured scissors mode's frequency  $f_{s, \text{exp}} = 138 \pm 7$  Hz is notably different from the effective mass prediction of 167 Hz. Select TOF images for this case are shown in Fig. 5.6f.

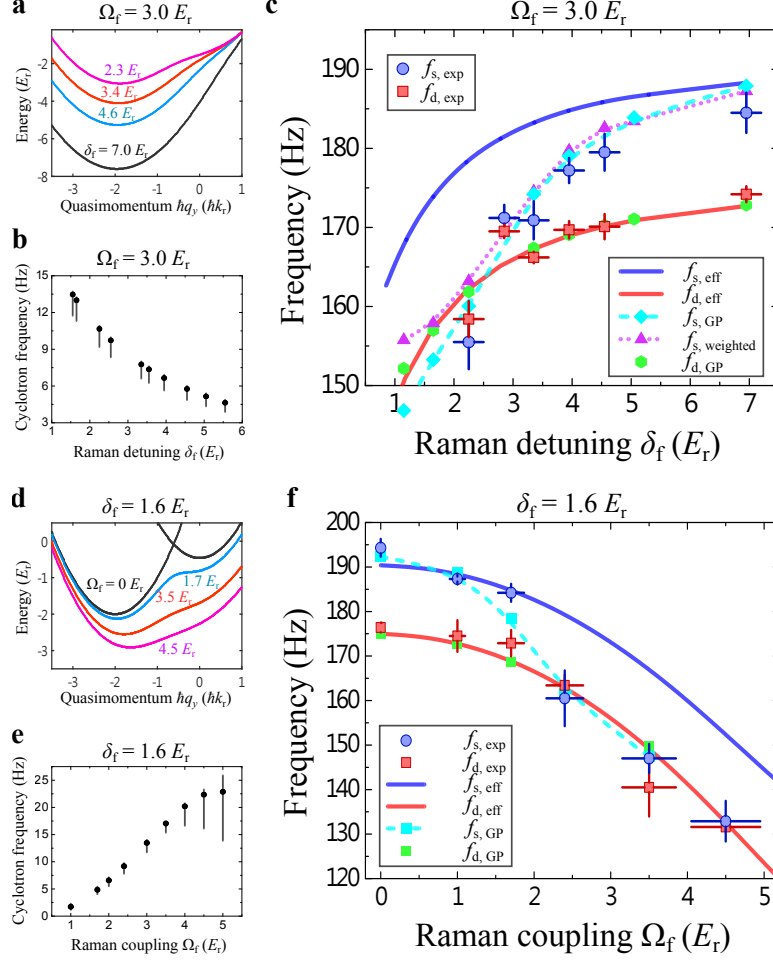


Fig. 5.7. **Experiment and GPE simulation for scissors and dipole modes at various  $\Omega_f$  and  $\delta_f$ .** (a-c) show results at various  $\delta_f$  with a fixed  $\Omega_f = 3.0 E_r$ . (d-f) show results at various  $\Omega_f$  with a fixed  $\delta_f = 1.6 E_r$ . (a) and (d) show the relevant dispersion relations calculated at the BEC's center. (b) and (e) show the calculated cyclotron frequency  $\Omega_{\text{cyc}} = \mathbf{B}^*/(2\pi m^*)$  which reflects the strength of  $\mathbf{B}^*$  at various  $\Omega_f$  and  $\delta_f$ . The dots refer to the value at the BEC's center. The vertical bars indicate the range of  $\Omega_{\text{cyc}}$  experienced by the rest part of the BEC. (c) and (f) show frequency of the scissors and dipole modes at various  $\Omega_f$  and  $\delta_f$ . Scatters are experimental data, where vertical and horizontal error bars are respectively the standard error of measurements and the statistical uncertainties of  $\delta_f$  or  $\Omega_f$ .  $f_s$  and  $f_d$  respectively refer to the frequency of the scissors and dipole modes, where the subscript “exp” means experiment, “eff” means the effective mass prediction, “GP” means GPE simulation, and “weighted” means the weighted average (see texts). The GPE simulations are performed by Chunlei Qu. The calculation of the cyclotron frequency at various Raman couplings is performed by Su-Ju Wang.

We systematically study these mode frequencies at various  $\mathbf{B}_f^*$  (determined by  $\delta_f$  and  $\Omega_f$ ). Results at  $\Omega_f = 3.0 E_r$  with various  $\delta_f$  are shown in Fig. 5.7a-c. Fig. 5.7a shows the various ground dressed bands at the BEC's center. Fig. 5.7b presents the corresponding calculated  $\mathbf{B}^*$  in terms of the cyclotron frequency  $\Omega_{\text{cyc}} \equiv \mathbf{B}^*/(2\pi m^*)$ , where black dots indicate the value at the BEC's center and the vertical lines imply the range of  $\mathbf{B}^*$  that would be experienced by the rest part of the BEC (assuming the in-situ BEC size along  $\hat{z}$  is  $10 \mu\text{m}$ ). In other words, the vertical lines show the inhomogeneity of  $\mathbf{B}^*$  experienced by a finite-size BEC. Fig. 5.7c shows the mode frequencies at  $\Omega_f = 3.0 E_r$  with various  $\delta_f$ . The scatters with error bars (circles for scissors and squares for dipole) are experimental data. The solid lines are the effective mass predictions.

We notice that the measured dipole mode's frequency ( $f_{\text{d, exp}}$ ) approximately agrees with the corresponding effective mass prediction ( $f_{\text{d, eff}}$ ), however, the measured scissors mode's frequency ( $f_{\text{s, exp}}$ ) is notably smaller than the corresponding effective mass prediction ( $f_{\text{s, eff}}$ ) at small  $\delta_f$ . Additionally, results at  $\delta_f = 1.6 E_r$  with various  $\Omega_f$  are shown in Fig. 5.7d-f. Fig. 5.7d shows the various ground dressed bands at the BEC's center. Fig. 5.7e presents the corresponding calculated  $\mathbf{B}^*$ . Fig. 5.7f reveals that the measured dipole mode's frequency ( $f_{\text{d, exp}}$ ) approximately agrees with the effective mass prediction ( $f_{\text{s, exp}}$ ), however, the measured scissors mode's frequency ( $f_{\text{s, exp}}$ ) is also notably smaller than the corresponding effective mass prediction ( $f_{\text{s, eff}}$ ) at large  $\Omega_f$ .

### 5.3.2 Simulations

To gain some physical insight, we simulate the dynamics of the BEC after the quench process using the 3D time-dependent Gross-Pitaevskii equation (GPE) with similar experimental parameters. The simulation uses a Gaussian momentum distribution for the BEC with  $N_c = 2.0 \times 10^4$  and trap frequencies  $f_z = 75 \text{ Hz}$  and

$f_x = f_y = 175$  Hz. Long-time simulations disclose that BEC's angle oscillations can exhibit beat waves, composed of two main frequency components with their relative amplitudes depending on  $\mathbf{B}^*$ . Fig. 5.8a,c,e presents examples of the tilt angle of the in-situ BEC versus  $t_{\text{hold}}$ , where the angle is obtained by fitting the simulated in-situ BECs to a rotated 2D Gaussian distribution. Similar to the analysis for the experimental data, we fit the first 2-3 cycles of the simulated angle or dipole (not shown) oscillations to a single sinusoidal function, which determines the GPE-simulated frequency of the scissors ( $f_{s, \text{GP}}$ , diamonds connected with dashed lines in Fig. 5.7cf) or dipole ( $f_{d, \text{GP}}$ , hexagons in Fig. 5.7cf) modes respectively. On the other hand, we either take the fast Fourier transform (FFT) (e.g. Fig. 5.8b,d,f respectively corresponding to Fig. 5.8a,c,e) of the angle oscillations or fit the angle oscillations to a double sinusoidal function to extract the two main frequency components ( $f_1 > f_2$ ) and their relative amplitudes ( $A_1$  and  $A_2$ ). Since these two methods give very similar results, we simply use the results from FFT to determine the “weighted average frequency” for the scissors mode as

$$f_{s, \text{weighted}} = (A_1 f_1 + A_2 f_2)/(A_1 + A_2), \quad (5.4)$$

which reflects the relative weighting of  $f_1$  and  $f_2$  and is shown as triangles connected by dotted lines in Fig. 5.7cf. We notice that  $f_1$  and  $f_2$  at given  $\Omega_f$  and  $\delta_f$  are respectively similar to the effective mass predicted frequencies of scissors and dipole modes, i.e.  $f_1 \sim f_{s, \text{eff}}$  and  $f_2 \sim f_{d, \text{eff}}$ . For example, the beat wave at  $\Omega_f = 3.0 E_r$  and  $\delta_f = 4.0 E_r$  in Fig. 5.8a has  $f_1 = 187.4$  Hz ( $\sim f_{s, \text{eff}} = 184.8$  Hz) and  $f_2 = 170.1$  Hz ( $\sim f_{s, \text{eff}} = 168.9$  Hz) with  $A_2/A_1 = 0.84$ . Besides,  $f_{s, \text{weighted}}$  and  $f_{s, \text{GP}}$  are similar and are in agreement with the experimental data  $f_{s, \text{exp}}$ . These results seem to suggest that the regular scissors and dipole modes become coupled for a SO-coupled BEC in  $\mathbf{B}^*$ , and these two modes would otherwise become uncoupled when  $\Omega = 0$  (no SOC and  $\mathbf{B}^*$ ). In other words, oscillations of angular and linear mechanical momenta are coupled.

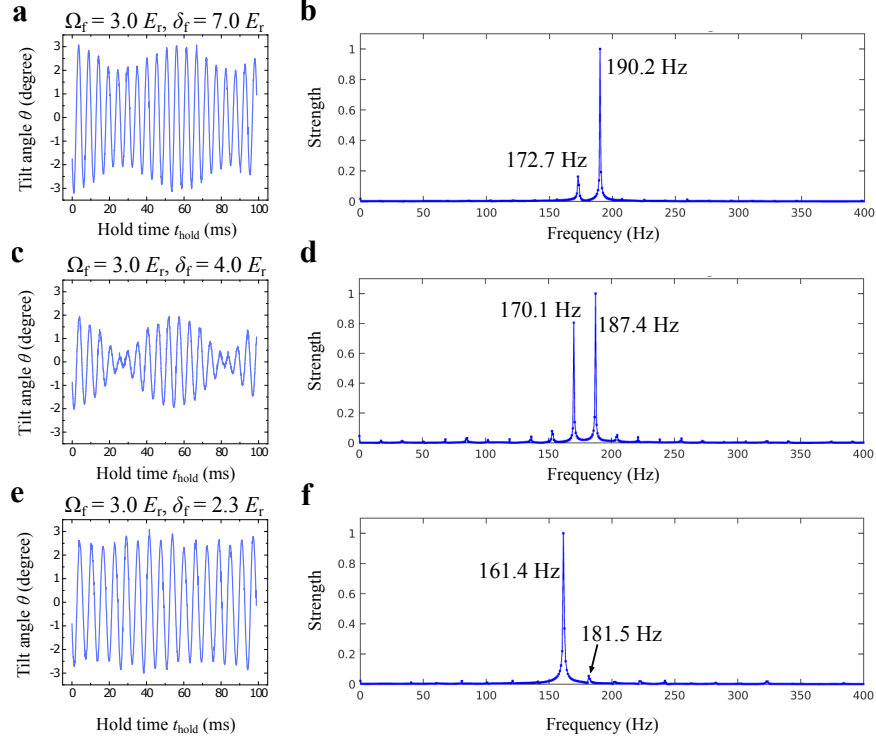


Fig. 5.8. **Beat waves of the scissors mode, revealed in GPE simulation.** (a), (c), and (e) show the tilt angle versus  $t_{\text{hold}}$  respectively at  $\delta_f = 7.0, 4.0,$  and  $2.3 E_r$  (all at a fixed  $\Omega_f = 3.0 E_r$ ). (b), (d), and (f) are the corresponding FFT analysis, disclosing the constituent frequency components. In each case, the two main frequency components  $f_1$  and  $f_2$  ( $f_1 > f_2$ ) are respectively close to the effective mass predicted frequency of the scissors and dipole modes, i.e.  $f_1 \sim f_{s, \text{eff}}$  and  $f_2 \sim f_{d, \text{eff}}$ . The relative amplitude of  $f_2$  increases with decreasing  $\delta_f$ . The GPE simulations are performed by Chunlei Qu

As  $\mathbf{B}^*$  becomes larger (by decreasing  $\delta_f$  or increasing  $\Omega_f$ , see Fig. 5.7be), the  $f_2$  ( $\sim f_{d, \text{eff}}$ ) component can become more prominent than the  $f_1$  ( $\sim f_{s, \text{eff}}$ ) component, such that both  $f_{s, \text{GP}}$  and  $f_{s, \text{weighted}}$  become notably different from  $f_{s, \text{eff}}$ . When  $\Omega_f$  approaches zero or  $\delta_f$  becomes large enough,  $f_{s, \text{exp}}, f_{s, \text{GP}}, f_{s, \text{weighted}}$ , and  $f_{s, \text{eff}}$  all become similar. In this limit, the angle oscillations almost has a single frequency component near  $f_{s, \text{eff}}$ , i.e. the scissors mode's frequency can essentially be predicted by Eq. (5.3).

We find that within the regime of parameters used in our experiment,  $f_{d, \text{exp}}$ ,  $f_{d, \text{GP}}$ , and  $f_{d, \text{eff}}$  are in agreement with one another. In other words, the dipole mode's frequency can essentially be predicted by Eq. (5.2) for our parameter regime. Note that due to the anti-trapping effect resulting from rotation [15, 34, 161], here  $\mathbf{B}^*$  would modify only the trap frequency along  $\hat{z}$  from 75 Hz to  $\sim 73.6$  Hz. Such a small modification is consistent with the observation that both the experimentally measured and GPE simulated dipole mode's frequencies along  $\hat{z}$  are similar to the trap frequency along  $\hat{z}$ . Thus, on the other hand, the anti-trapping effect cannot account for the difference between  $f_{s, \text{exp}}$  and  $f_{s, \text{eff}}$ .

#### 5.4 Discussion and conclusion

It is worth noting that the physical angular momentum of a SO-coupled BEC has a SOC-induced spin-dependent term [139], which would disappear in the absence of SOC. In our case (the SOC direction is along  $\hat{y}$ , see Eq. (5.1)), the physical (indicated by a superscript “phy”) angular momentum associated with rotation in the  $y-z$  plane is

$$\langle \hat{L}_x^{\text{phy}} \rangle = \langle y\hat{p}_z^{\text{phy}} - z\hat{p}_y^{\text{phy}} \rangle = \langle y\hat{p}_z - z(\hat{p}_y - k_r\sigma_z) \rangle = \langle \hat{L}_x^c \rangle + \langle \hat{L}_x^s \rangle. \quad (5.5)$$

Here,

$$\langle \hat{L}_x^c \rangle = \langle y\hat{p}_z - z\hat{p}_y \rangle \quad (5.6)$$

is the canonical (indicated by a superscript “c”) angular momentum and

$$\langle \hat{L}_x^s \rangle = \langle zk_r\sigma_z \rangle = \langle zk_r s_z / n \rangle \quad (5.7)$$

is the spin-dependent (indicated by a superscript “s”) contribution due to SOC, where  $s_z = n_\downarrow - n_\uparrow$  is the spin magnetization (difference between the density of  $|\downarrow\rangle$  and  $|\uparrow\rangle$  states) and  $n$  is the total density.

With SOC along the  $y$  direction, Table 5.1 shown below summarizes the expressions for the physical velocity, physical linear momentum, physical angular momentum, and their canonical and spin-dependent contributions and their relations.

Table 5.1

Physical velocity, physical linear momentum, physical angular momentum, and their canonical and spin-dependent contributions and their relations. SOC is along the  $y$  direction (see Eq. (5.1)). Physical quantities are indicated by a superscript “phy”. Canonical terms are indicated by a superscript “c”. Spin-dependent terms are indicated by a superscript “s”.  $\langle \hat{p}_x \rangle = \langle \hbar \hat{q}_x \rangle$ ,  $\langle \hat{p}_y \rangle = \langle \hbar \hat{q}_y \rangle$ ,  $\langle \hat{p}_z \rangle = \langle \hbar \hat{q}_z \rangle$  are canonical momenta (or quasi-momenta) respectively along the  $x$ ,  $y$ , and  $z$ .

Physical quantity	Canonical term	Spin-dependent term
$\langle \hat{v}_y^{\text{phy}} \rangle = \langle \hat{v}_y^{\text{c}} \rangle + \langle \hat{v}_y^{\text{s}} \rangle$	$\langle \hat{v}_y^{\text{c}} \rangle = \langle \hat{p}_y / m \rangle$	$\langle \hat{v}_y^{\text{s}} \rangle = \langle -k_r \sigma_z / m \rangle$
$\langle \hat{v}_x^{\text{phy}} \rangle = \langle \hat{v}_x^{\text{c}} \rangle + \langle \hat{v}_x^{\text{s}} \rangle$	$\langle \hat{v}_x^{\text{c}} \rangle = \langle \hat{p}_x / m \rangle$	$\langle \hat{v}_x^{\text{s}} \rangle = 0$
$\langle \hat{v}_z^{\text{phy}} \rangle = \langle \hat{v}_z^{\text{c}} \rangle + \langle \hat{v}_z^{\text{s}} \rangle$	$\langle \hat{v}_z^{\text{c}} \rangle = \langle \hat{p}_z / m \rangle$	$\langle \hat{v}_z^{\text{s}} \rangle = 0$
$\langle \hat{p}_y^{\text{phy}} \rangle = \langle \hat{p}_y^{\text{c}} \rangle + \langle \hat{p}_y^{\text{s}} \rangle$	$\langle \hat{p}_y^{\text{c}} \rangle = m \langle \hat{v}_y^{\text{c}} \rangle = \langle \hat{p}_y \rangle$	$\langle \hat{p}_y^{\text{s}} \rangle = m \langle \hat{v}_y^{\text{s}} \rangle = \langle -k_r \sigma_z \rangle$
$\langle \hat{p}_x^{\text{phy}} \rangle = \langle \hat{p}_x^{\text{c}} \rangle + \langle \hat{p}_x^{\text{s}} \rangle$	$\langle \hat{p}_x^{\text{c}} \rangle = m \langle \hat{v}_x^{\text{c}} \rangle = \langle \hat{p}_x \rangle$	$\langle \hat{p}_x^{\text{s}} \rangle = 0$
$\langle \hat{p}_z^{\text{phy}} \rangle = \langle \hat{p}_z^{\text{c}} \rangle + \langle \hat{p}_z^{\text{s}} \rangle$	$\langle \hat{p}_z^{\text{c}} \rangle = m \langle \hat{v}_z^{\text{c}} \rangle = \langle \hat{p}_z \rangle$	$\langle \hat{p}_z^{\text{s}} \rangle = 0$
$\langle \hat{L}_x^{\text{phy}} \rangle = \langle y \hat{p}_z^{\text{phy}} - z \hat{p}_y^{\text{phy}} \rangle = \langle \hat{L}_x^{\text{c}} \rangle + \langle \hat{L}_x^{\text{s}} \rangle$	$\langle \hat{L}_x^{\text{c}} \rangle = \langle y \hat{p}_z - z \hat{p}_y \rangle$	$\langle \hat{L}_x^{\text{s}} \rangle = \langle z k_r \sigma_z \rangle$
$\langle \hat{L}_y^{\text{phy}} \rangle = \langle z \hat{p}_x^{\text{phy}} - x \hat{p}_z^{\text{phy}} \rangle = \langle \hat{L}_y^{\text{c}} \rangle + \langle \hat{L}_y^{\text{s}} \rangle$	$\langle \hat{L}_y^{\text{c}} \rangle = \langle z \hat{p}_x - x \hat{p}_z \rangle$	$\langle \hat{L}_y^{\text{s}} \rangle = 0$
$\langle \hat{L}_z^{\text{phy}} \rangle = \langle x \hat{p}_y^{\text{phy}} - y \hat{p}_x^{\text{phy}} \rangle = \langle \hat{L}_z^{\text{c}} \rangle + \langle \hat{L}_z^{\text{s}} \rangle$	$\langle \hat{L}_z^{\text{c}} \rangle = \langle x \hat{p}_y - y \hat{p}_x \rangle$	$\langle \hat{L}_z^{\text{s}} \rangle = \langle -x k_r \sigma_z \rangle$

For rotation in the  $y - z$  plane, it is the  $\langle \hat{L}_x^s \rangle$  term that can cause a SO-coupled BEC's rigid-like rotation [79], which reflects the reduction of the superfluid fraction due to SOC. Similarly, the current density in the SOC direction is  $j_y = j_y^c + j_y^s$  (the corresponding velocity flow is  $v_y = j_y/n$ ), where  $j_y^c = \hbar n \nabla_y \phi / m$  corresponds to the irrotational flow, the spin-dependent term  $j_y^s = -\hbar k_r s_z / m$  corresponds to the rotational flow, and  $\phi$  is the phase of the BEC wavefunction. It is the  $j_y^s$  term that can lead to the violation of  $\nabla \times \mathbf{v} = 0$  (a defining feature for superfluids) and change the superfluid fraction [137, 138]. In our case, the scissors mode is associated with oscillations of the physical angular momentum (Eq. (5.5)), which may involve oscillations of both the canonical (Eq. (5.6)) and spin-dependent (Eq. (5.7)) contributions.

Currently, we are investigating whether the SOC-induced spin-dependent contribution (Eq. (5.7)) is related to the formation of beat waves of the scissors mode (or the seeming coupling between scissors and dipole modes). On one hand, it seems that the spin magnetization  $s_z$  in Eq. (5.7) would oscillate due to dipole oscillations along the SOC direction of a SO-coupled BEC [65]. On the other hand, because of the  $z$ -dependent  $\Omega$  (i.e. in the presence of  $\mathbf{B}^*$ ),  $s_z$  is  $z$ -dependent, such that Eq. (5.7) may be nonzero after integrating an even function of  $z$  over space (Eq. (5.7) may otherwise be zero if the integrand is an odd function of  $z$ ). Consequently,  $\langle \hat{L}_x^s \rangle$  may oscillate in time at the frequency of  $s_z$  oscillations (i.e. the frequency of dipole oscillations along the SOC direction). In other words, dipole oscillations along the SOC direction of a SO-coupled BEC in  $\mathbf{B}^*$  may induce a type of angle oscillations (associated with oscillations of  $\langle \hat{L}_x^c \rangle$ ) at the frequency of  $f_{d, \text{eff}}$ . This may be the reason for the appearance of the second frequency component in the scissors mode and the formation of beat waves. We are working on the hydrodynamic theory to understand the details of the dynamics.

## 6. FUTURE DIRECTIONS

Some future directions that may be extended from the projects presented in this thesis are summarized below.

Chapter 3 has studied the non-equilibrium spin dynamics in a quenched SO-coupled BEC. Our study provides an exemplary study of the evolution of a quantum many-body system, including the generation and decay of collective excitations, following a non-adiabatic parameter change (quench). Such quench dynamics has been of great interest to study many outstanding questions in many-body quantum systems. For example, how such a system, initially prepared in the ground state but driven out of equilibrium due to a parameter quench that drives the system across a quantum phase transition, would evolve to the new ground state or thermalize has attracted great interests (see, e.g., a recent study where coherent inflationary dynamics has been observed for BECs crossing a ferromagnetic quantum critical point [109]). Experiments on SO-coupled BECs, where many parameters can be well controlled in real time and with the potential of adding other types of synthetic gauge fields, may offer rich opportunities to study nonequilibrium materials and nonequilibrium quantum dynamics [110], such as Kibble-Zurek physics while quenching through quantum phase transitions [111], and superfluidity [63, 77] in SO-coupled systems.

Chapter 4 presents our observation of new topological phenomena absent in planar space but emerging due to manipulating the geometry of space. Direct extensions of this work include studying superfluidity on curved surfaces [118, 119], implementing a Laughlin's charge pump [132] (e.g. by making Equation (4.1) time-dependent), and exploring the fractal energy spectrum of Hofstadter butterfly as suggested in ref. [41]. Our work also paves the way to creating synthetic gauge fields in diverse geometries of spaces [42] such as a Hall torus [133]. Furthermore, increasing inter-particle interactions (e.g. by imposing strong confining potentials in  $x$  and  $z$  directions in

our case or enhancing the scattering length by Feshbach resonances) in spaces with curved geometries, for instance a Hall cylinder or torus, may allow exploring intriguing quantum many-body phases such as fractional quantum Hall states as suggested in refs. [134–136].

Chapter 5 has studied rotational properties (specifically, the scissors mode) of a SO-coupled BEC. We are trying to understand whether the observed unusual behavior of the scissors mode is related to how SO coupling modifies a BEC’s rotational and superfluid properties. In addition to GP simulations, we will work on the hydrodynamic theory to obtain a microscopic understanding of the observed phenomena.

## 6.1 Preliminary results of the ongoing projects

### 6.1.1 Charge pumping of a BEC on a synthetic Hall cylinder

One of the extensions of the cylinder project (Chapter 4) is to realize a charge pump (transport of a BEC in the real space by making the emergent lattices move). This part is still ongoing so only the ideas and preliminary results are presented below. The idea is that we can make, e.g. the Hamiltonian  $H$  in Eq. (4.1), time-dependent. This can be achieved by violating the resonance condition (Eq. (4.11)) for the cylinder such that a time-dependent term would show up in the Hamiltonian and cannot be gauged away, corresponding to a moving emergent lattice. One approach to violate Eq. (4.11) is to change the angular frequency difference between the Raman lasers from  $\Delta\omega_R$  to  $\Delta\omega'_R = \Delta\omega_R + \delta\omega_R$ , such that the lattice would move at a constant speed of  $dy/dt = 2\delta\omega_R/K = 2(\delta f)d$ , where  $\delta\omega_R/(2\pi) = \delta f$ ,  $d = \lambda/2$ , and  $\lambda$  is the wavelength of the Raman laser. Fig. 6.1 shows preliminary results of the charge pumping with a fixed  $\delta f$  at various  $t_{\text{hold}}$  or with various  $\delta f$  at a fixed  $t_{\text{hold}}$ .

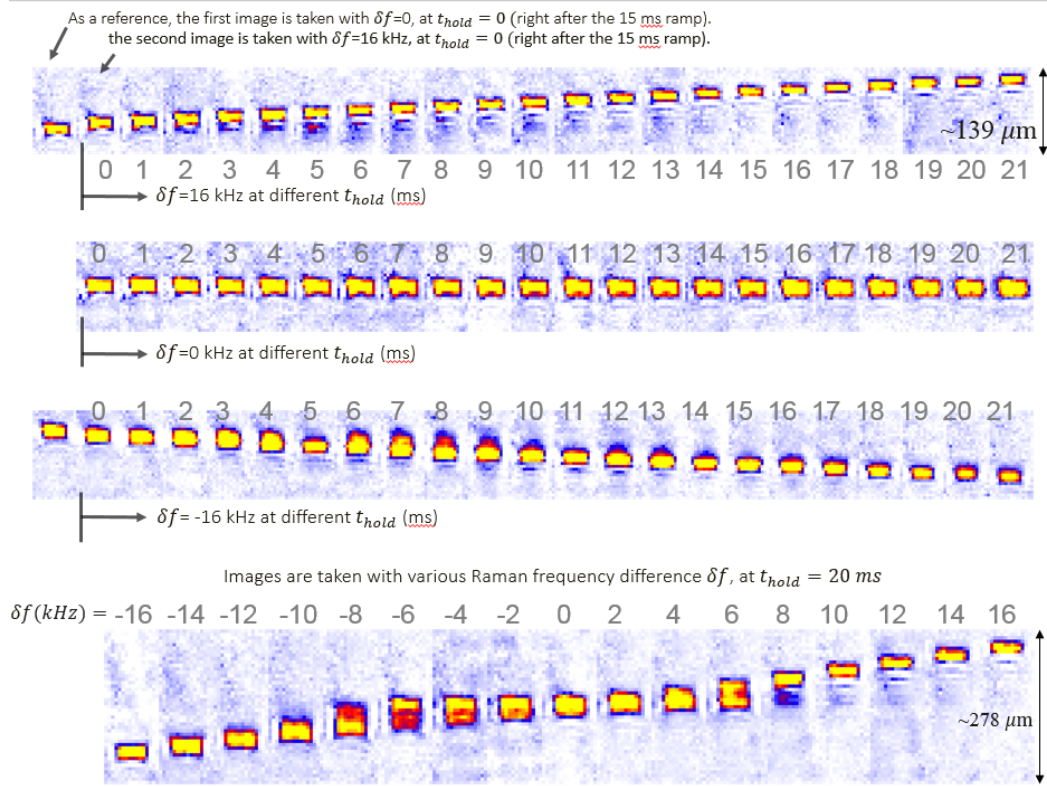


Fig. 6.1. Preliminary results for the charge pumping of a BEC on a synthetic Hall cylinder. Transport of a BEC in the real space by creating a moving emergent lattice at a constant speed.

### 6.1.2 Exploring interaction effects on the transport of a BEC in the momentum-space regular strip

Currently, we are also exploring the interaction effects on the transport of a BEC in the momentum-space regular strip (see Chapter 4). This part is still ongoing so only the ideas are introduced below. Our theory suggests that in the limit of strong particle-particle interactions (such that interaction energy becomes much larger than the gap size of the regular strip), the momentum-space regular strip can be converted to the Möbius strip because the Landau-Zener tunneling from the ground to excited bands can be greatly enhanced due to interactions. This suggests a topology change

of the band structure due to interactions. Such a phenomenon may be understood by that in the strong interaction limit, the inter-band particle interactions become much larger than the intra-band particle interactions, such that atoms tend to undergo diabatic transition to save the inter-band particle interaction energy. This phenomenon that strong inter-band particle interactions tend to prevent atoms from staying in the ground band seems analogous to a Mott insulator, in which strong on-site particle-particle interactions tend to prevent atoms from hopping. Even in the case of weak interaction (the present parameter regime), the current experimental data seem to be consistent with the weakly-interacting GP simulation as shown in Fig. 6.2 below. Fig. 6.2 shows the total mechanical momentum of *all* the atoms (rather than only the “condensate” part in the bimodal fit in Eq. (4.35)). Our GP simulation suggests that the difference between results of non-interacting GP and of weakly-interacting GP may be due to the interaction-modified Landau-Zener tunneling.

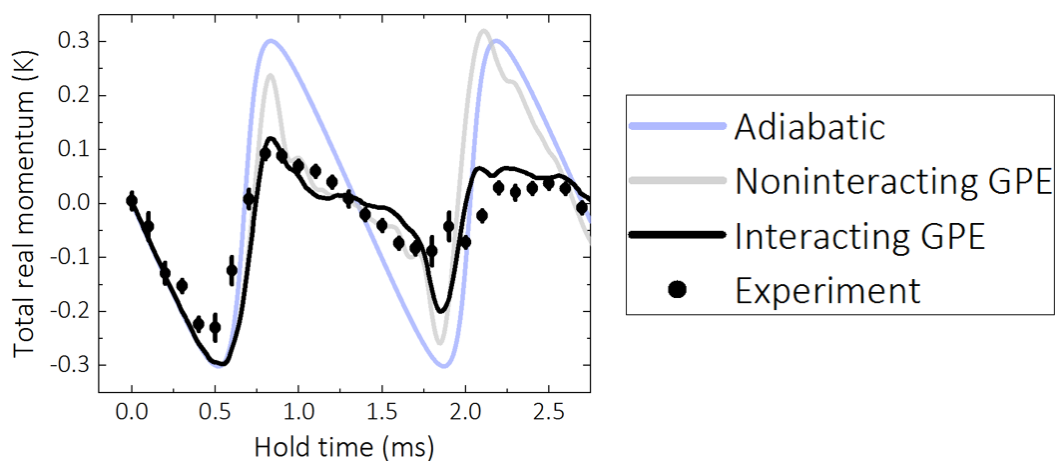


Fig. 6.2. Preliminary results for exploring interaction effects on the transport of a BEC in the momentum-space regular strip. The GPE simulations are performed by Yangqian Yan.

---

Note that the transport results presented in Chapter 4 are obtained by turning off the trap so atoms are allowed to fall under the gravity. In such cases, interaction

energy would decrease with time because the trap is off and the density of the BEC decreases. This may prevent us from exploring effects of the strong interaction, since there is only a small window of time (shorter when the interaction energy is higher) we can study the interaction effects before we lose the strong interaction. To overcome such a difficulty, we may create an accelerating lattice (with a constant acceleration) by making  $\delta\omega_R$  time-dependent (as shown in Fig. 6.3), such that in the lattice frame the atoms are subjected to a constant force and undergoing Bloch oscillations in the band structure. Here, the acceleration is  $d^2y/dt^2 = d \times d(\delta f(t))/dt = d/(2\pi) \times d(\delta\omega_R(t))/dt$ , where  $dt$  is the transport time. This may allow us to keep the trap on as well as the strong interaction during the transport of the BEC in the band structure. The first goal may be to achieve an interaction energy comparable to the gap size of the band structure.

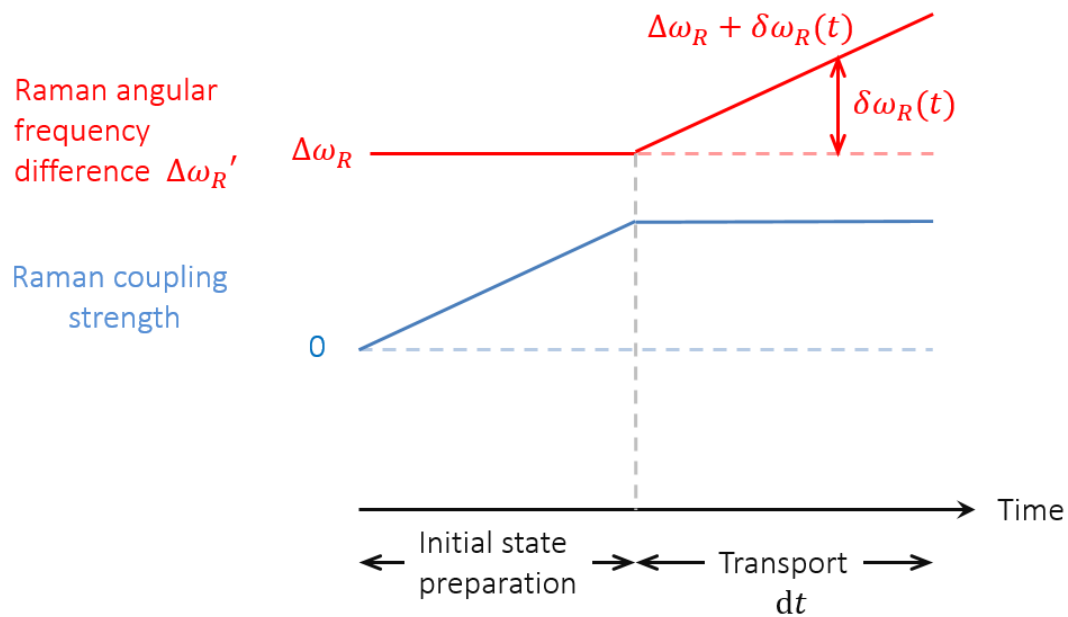


Fig. 6.3. Ideas to generate an accelerating lattice for exploring interaction effects on the transport of a BEC in the momentum-space regular strip. Such an accelerating lattice may allow us to induce transport of the BEC in the band structure while keeping the trap on as well as the strong interaction.

## LIST OF REFERENCES

- [1] W. Ketterle, D. S. Durfee, and D. M. Stamper-Kurn, “Making, probing and understanding Bose-Einstein condensates,” p. 90, 1999.
- [2] F. Dalfovo, S. Giorgini, L. P. Pitaevskii, and S. Stringari, “Theory of Bose-Einstein condensation in trapped gases,” *Rev. Mod. Phys.*, vol. 71, pp. 463–512, Apr 1999.
- [3] C. Chin, R. Grimm, P. Julienne, and E. Tiesinga, “Feshbach resonances in ultracold gases,” *Rev. Mod. Phys.*, vol. 82, pp. 1225–1286, Apr 2010.
- [4] H. Weimer, M. Müller, I. Lesanovsky, P. Zoller, and H. P. Büchler, “A Rydberg quantum simulator,” *Nature Physics*, vol. 6, pp. 382–388, Mar 2010. Article.
- [5] M. Saffman, T. G. Walker, and K. Mølmer, “Quantum information with Rydberg atoms,” *Rev. Mod. Phys.*, vol. 82, pp. 2313–2363, Aug 2010.
- [6] R. Lw, H. Weimer, J. Nipper, J. B. Balewski, B. Butscher, H. P. Bchler, and T. Pfau, “An experimental and theoretical guide to strongly interacting Rydberg gases,” *Journal of Physics B: Atomic, Molecular and Optical Physics*, vol. 45, p. 113001, May 2012.
- [7] J. Lim, H.-g. Lee, and J. Ahn, “Review of cold Rydberg atoms and their applications,” *Journal of the Korean Physical Society*, vol. 63, pp. 867–876, Aug 2013.
- [8] A. J. Olson, “The dynamics of ultracold atoms in light-induced synthetic gauge fields,” *Ph.D. thesis*, 2015.
- [9] A. J. Olson, R. J. Niffenegger, and Y. P. Chen, “Optimizing the efficiency of evaporative cooling in optical dipole traps,” *Phys. Rev. A*, vol. 87, p. 053613, May 2013.
- [10] R. P. Feynman, “Simulating physics with computers,” *International Journal of Theoretical Physics*, vol. 21, no. 6, pp. 467–488.
- [11] M. Greiner, O. Mandel, T. Esslinger, T. W. Hänsch, and I. Bloch, “Quantum phase transition from a superfluid to a Mott insulator in a gas of ultracold atoms,” *Nature*, vol. 415, no. 6867, pp. 39–44, 2002.
- [12] R. Jördens, N. Strohmaier, K. Günter, H. Moritz, and T. Esslinger, “A Mott insulator of fermionic atoms in an optical lattice,” *Nature*, vol. 455, pp. 204–207, Sep 2008.
- [13] C. Meldgin, U. Ray, P. Russ, D. Chen, D. M. Ceperley, and B. DeMarco, “Probing the Bose glass-superfluid transition using quantum quenches of disorder,” *Nature Physics*, vol. 12, pp. 646–649, Mar 2016.

- [14] S. Sugawa, F. Salces-Carcoba, A. R. Perry, Y. Yue, and I. B. Spielman, “Second Chern number of a quantum-simulated non-Abelian Yang monopole,” *Science*, vol. 360, no. 6396, pp. 1429–1434, 2018.
- [15] N. Goldman, G. Juzelinas, P. Öhberg, and I. B. Spielman, “Light-induced gauge fields for ultracold atoms,” *Reports on Progress in Physics*, vol. 77, no. 12, p. 126401, 2014.
- [16] I. Bloch, J. Dalibard, and W. Zwerger, “Many-body physics with ultracold gases,” *Rev. Mod. Phys.*, vol. 80, pp. 885–964, Jul 2008.
- [17] J. Dalibard, F. Gerbier, G. Juzeliūnas, and P. Öhberg, “*Colloquium* : Artificial gauge potentials for neutral atoms,” *Rev. Mod. Phys.*, vol. 83, pp. 1523–1543, Nov 2011.
- [18] V. Galitski and I. B. Spielman, “Spin-orbit coupling in quantum gases,” *Nature*, vol. 494, no. 7435, pp. 49–54, 2013.
- [19] Y. Li, G. I. Martone, and S. Stringari, *Spin-orbit-coupled Bose-Einstein condensates*, ch. 5, pp. 201–250.
- [20] H. Zhai, “Degenerate quantum gases with spin-orbit coupling: a review,” *Reports on Progress in Physics*, vol. 78, no. 2, p. 026001, 2015.
- [21] P.-J. Wang and J. Zhang, “Spin-orbit coupling in Bose-Einstein condensate and degenerate Fermi gases,” *Frontiers of Physics*, vol. 9, no. 5, pp. 598–612, 2014.
- [22] H. Zhai, “Spin-orbit coupled quantum gases,” *International Journal of Modern Physics B*, vol. 26, no. 01, p. 1230001, 2012.
- [23] Y.-J. Lin and I. B. Spielman, “Synthetic gauge potentials for ultracold neutral atoms,” *Journal of Physics B: Atomic, Molecular and Optical Physics*, vol. 49, no. 18, p. 183001, 2016.
- [24] P.-J. Wang and J. Zhang, “Spin-orbit coupling in Bose-Einstein condensate and degenerate Fermi gases,” *Frontiers of Physics*, vol. 9, no. 5, pp. 598–612, 2014.
- [25] Y. Zhang, M. E. Mossman, T. Busch, P. Engels, and C. Zhang, “Properties of spin-orbit-coupled Bose-Einstein condensates,” *Frontiers of Physics*, vol. 11, no. 3, p. 118103, 2016.
- [26] I. Bloch, J. Dalibard, and S. Nascimbène, “Quantum simulations with ultracold quantum gases,” *Nature Physics*, vol. 8, pp. 267–276, Apr 2012.
- [27] N. Goldman, J. C. Budich, and P. Zoller, “Topological quantum matter with ultracold gases in optical lattices,” *Nature Physics*, vol. 12, pp. 639–645, Jun 2016.
- [28] T. Ozawa and H. M. Price, “Topological quantum matter in synthetic dimensions,” *Nature Reviews Physics*, vol. 1, no. 5, pp. 349–357, 2019.
- [29] Y.-J. Lin, R. L. Compton, A. R. Perry, W. D. Phillips, J. V. Porto, and I. B. Spielman, “Bose-Einstein condensate in a uniform light-induced vector potential,” *Phys. Rev. Lett.*, vol. 102, p. 130401, Mar 2009.

- [30] N. Lundblad, M. Schlosser, and J. V. Porto, “Experimental observation of magic-wavelength behavior of  $^{87}\text{Rb}$  atoms in an optical lattice,” *Phys. Rev. A*, vol. 81, p. 031611, Mar 2010.
- [31] I. H. Deutsch and P. S. Jessen, “Quantum control and measurement of atomic spins in polarization spectroscopy,” *Optics Communications*, vol. 283, no. 5, pp. 681 – 694, 2010.
- [32] R. H. Leonard, A. J. Fallon, C. A. Sackett, and M. S. Safronova, “High-precision measurements of the  $^{87}\text{Rb}$   $D$ -line tune-out wavelength,” *Phys. Rev. A*, vol. 92, p. 052501, Nov 2015.
- [33] F. Schmidt, D. Mayer, M. Hohmann, T. Lausch, F. Kindermann, and A. Widera, “Precision measurement of the  $^{87}\text{Rb}$  tune-out wavelength in the hyperfine ground state  $F = 1$  at 790 nm,” *Phys. Rev. A*, vol. 93, p. 022507, Feb 2016.
- [34] I. B. Spielman, “Raman processes and effective gauge potentials,” *Phys. Rev. A*, vol. 79, p. 063613, Jun 2009.
- [35] Y.-J. Lin, R. L. Compton, K. Jiménez-García, W. D. Phillips, J. V. Porto, and I. B. Spielman, “A synthetic electric force acting on neutral atoms,” *Nature Physics*, vol. 7, pp. 531–534, Mar 2011.
- [36] Y.-J. Lin, R. L. Compton, K. Jiménez-García, J. V. Porto, and I. B. Spielman, “Synthetic magnetic fields for ultracold neutral atoms,” *Nature*, vol. 462, pp. 628–632, Dec 2009.
- [37] Y.-J. Lin, K. Jiménez-García, and I. B. Spielman, “Spin-orbit-coupled Bose-Einstein condensates,” *Nature*, vol. 471, pp. 83–86, Mar 2011.
- [38] S.-C. Ji, J.-Y. Zhang, L. Zhang, Z.-D. Du, W. Zheng, Y.-J. Deng, H. Zhai, S. Chen, and J.-W. Pan, “Experimental determination of the finite-temperature phase diagram of a spin-orbit coupled Bose gas,” *Nature Physics*, vol. 10, pp. 314–320, Mar 2014.
- [39] C. Hamner, C. Qu, Y. Zhang, J. Chang, M. Gong, C. Zhang, and P. Engels, “Dicke-type phase transition in a spin-orbit-coupled Bose-Einstein condensate,” *Nature Communications*, vol. 5, pp. 1–8, 2014.
- [40] M. C. Beeler, R. A. Williams, K. Jiménez-García, L. J. LeBlanc, A. R. Perry, and I. B. Spielman, “The spin Hall effect in a quantum gas,” *Nature*, vol. 498, pp. 201–204, Jun 2013.
- [41] A. Celi, P. Massignan, J. Ruseckas, N. Goldman, I. B. Spielman, G. Juzeliūnas, and M. Lewenstein, “Synthetic gauge fields in synthetic dimensions,” *Phys. Rev. Lett.*, vol. 112, p. 043001, Jan 2014.
- [42] O. Boada, A. Celi, J. Rodríguez-Laguna, J. I. Latorre, and M. Lewenstein, “Quantum simulation of non-trivial topology,” *New Journal of Physics*, vol. 17, no. 4, p. 045007, 2015.
- [43] B. Gadway, “Atom-optics approach to studying transport phenomena,” *Phys. Rev. A*, vol. 92, p. 043606, Oct 2015.

- [44] E. J. Meier, F. A. An, and B. Gadway, “Observation of the topological soliton state in the Su-Schrieffer-Heeger model,” *Nature Communications*, vol. 7, pp. 13986–, Dec 2016.
- [45] F. A. An, E. J. Meier, and B. Gadway, “Diffusive and arrested transport of atoms under tailored disorder,” *Nature Communications*, vol. 8, no. 1, p. 325, 2017.
- [46] E. J. Meier, F. A. An, A. Dauphin, M. Maffei, P. Massignan, T. L. Hughes, and B. Gadway, “Observation of the topological Anderson insulator in disordered atomic wires,” *Science*, vol. 362, no. 6417, pp. 929–933, 2018.
- [47] B. K. Stuhl, H.-I. Lu, L. M. Ayccock, D. Genkina, and I. B. Spielman, “Visualizing edge states with an atomic Bose gas in the quantum Hall regime,” *Science*, vol. 349, no. 6255, pp. 1514–1518, 2015.
- [48] M. Mancini, G. Pagano, G. Cappellini, L. Livi, M. Rider, J. Catani, C. Sias, P. Zoller, M. Inguscio, M. Dalmonte, and L. Fallani, “Observation of chiral edge states with neutral fermions in synthetic Hall ribbons,” *Science*, vol. 349, no. 6255, pp. 1510–1513, 2015.
- [49] M. Lohse, C. Schweizer, H. M. Price, O. Zilberberg, and I. Bloch, “Exploring 4D quantum Hall physics with a 2D topological charge pump,” *Nature*, vol. 553, pp. 55–58, Jan 2018.
- [50] C.-H. Li, C. Qu, R. J. Niffenegger, S.-J. Wang, M. He, D. B. Blasing, A. J. Olson, C. H. Greene, Y. Lyanda-Geller, Q. Zhou, C. Zhang, and Y. P. Chen, “Spin current generation and relaxation in a quenched spin-orbit-coupled Bose-Einstein condensate,” *Nature Communications*, vol. 10, no. 1, p. 375, 2019.
- [51] M. Z. Hasan and C. L. Kane, “Colloquium: Topological insulators,” *Rev. Mod. Phys.*, vol. 82, pp. 3045–3067, Nov 2010.
- [52] X.-L. Qi and S.-C. Zhang, “Topological insulators and superconductors,” *Rev. Mod. Phys.*, vol. 83, pp. 1057–1110, Oct 2011.
- [53] I. Žutić, J. Fabian, and S. Das Sarma, “Spintronics: Fundamentals and applications,” *Rev. Mod. Phys.*, vol. 76, pp. 323–410, Apr 2004.
- [54] D. D. Awschalom, L. C. Bassett, A. S. Dzurak, E. L. Hu, and J. R. Petta, “Quantum spintronics: Engineering and manipulating atom-like spins in semiconductors,” *Science*, vol. 339, no. 6124, pp. 1174–1179, 2013.
- [55] H. Deng, H. Haug, and Y. Yamamoto, “Exciton-polariton Bose-Einstein condensation,” *Rev. Mod. Phys.*, vol. 82, pp. 1489–1537, May 2010.
- [56] S. O. Demokritov, V. E. Demidov, O. Dzyapko, G. A. Melkov, A. A. Serga, B. Hillebrands, and A. N. Slavin, “Bose-Einstein condensation of quasi-equilibrium magnons at room temperature under pumping,” *Nature*, vol. 443, pp. 430–433, Sep 2006.
- [57] A. Bramati and M. Modugno, *Physics of Quantum Fluids: New Trends and Hot Topics in Atomic and Polariton Condensates*. Springer Berlin Heidelberg, 2013.

- [58] C. Leyder, M. Romanelli, J. P. Karr, E. Giacobino, T. C. H. Liew, M. M. Glazov, A. V. Kavokin, G. Malpuech, and A. Bramati, “Observation of the optical spin Hall effect,” *Nature Physics*, vol. 3, pp. 628–631, Jul 2007.
- [59] A. A. High, A. T. Hammack, J. R. Leonard, S. Yang, L. V. Butov, T. Ostatnický, M. Vladimirova, A. V. Kavokin, T. C. H. Liew, K. L. Campman, and A. C. Gossard, “Spin currents in a coherent exciton gas,” *Phys. Rev. Lett.*, vol. 110, p. 246403, Jun 2013.
- [60] L. J. Cornelissen, J. Liu, R. A. Duine, J. B. Youssef, and B. J. van Wees, “Long-distance transport of magnon spin information in a magnetic insulator at room temperature,” *Nature Physics*, vol. 11, pp. 1022–1026, Sep 2015.
- [61] D. A. Bozhko, A. A. Serga, P. Clausen, V. I. Vasyuchka, F. Heussner, G. A. Melkov, A. Pomyalov, V. S. L’vov, and B. Hillebrands, “Supercurrent in a room-temperature Bose-Einstein magnon condensate,” *Nature Physics*, vol. 12, pp. 1057–1062, Aug 2016.
- [62] J. Dalibard, F. Gerbier, G. Juzeliūnas, and P. Öhberg, “Colloquium: Artificial gauge potentials for neutral atoms,” *Rev. Mod. Phys.*, vol. 83, pp. 1523–1543, Nov 2011.
- [63] H. Zhai, “Degenerate quantum gases with spin-orbit coupling: a review,” *Reports on Progress in Physics*, vol. 78, no. 2, p. 026001, 2015.
- [64] L. J. LeBlanc, K. Jimnez-Garca, R. A. Williams, M. C. Beeler, A. R. Perry, W. D. Phillips, and I. B. Spielman, “Observation of a superfluid Hall effect,” *Proceedings of the National Academy of Sciences*, vol. 109, no. 27, pp. 10811–10814, 2012.
- [65] J.-Y. Zhang, S.-C. Ji, Z. Chen, L. Zhang, Z.-D. Du, B. Yan, G.-S. Pan, B. Zhao, Y.-J. Deng, H. Zhai, S. Chen, and J.-W. Pan, “Collective dipole oscillations of a spin-orbit coupled Bose-Einstein condensate,” *Phys. Rev. Lett.*, vol. 109, p. 115301, Sep 2012.
- [66] C. Qu, C. Hamner, M. Gong, C. Zhang, and P. Engels, “Observation of *Zitterbewegung* in a spin-orbit-coupled Bose-Einstein condensate,” *Phys. Rev. A*, vol. 88, p. 021604, Aug 2013.
- [67] A. J. Olson, S.-J. Wang, R. J. Niffenegger, C.-H. Li, C. H. Greene, and Y. P. Chen, “Tunable Landau-Zener transitions in a spin-orbit-coupled Bose-Einstein condensate,” *Phys. Rev. A*, vol. 90, p. 013616, Jul 2014.
- [68] Z. Wu, L. Zhang, W. Sun, X.-T. Xu, B.-Z. Wang, S.-C. Ji, Y. Deng, S. Chen, X.-J. Liu, and J.-W. Pan, “Realization of two-dimensional spin-orbit coupling for Bose-Einstein condensates,” *Science*, vol. 354, no. 6308, pp. 83–88, 2016.
- [69] A. J. Olson, D. B. Blasing, C. Qu, C.-H. Li, R. J. Niffenegger, C. Zhang, and Y. P. Chen, “Stueckelberg interferometry using periodically driven spin-orbit-coupled Bose-Einstein condensates,” *Phys. Rev. A*, vol. 95, p. 043623, Apr 2017.
- [70] D. B. Blasing, J. Pérez-Ríos, Y. Yan, S. Dutta, C.-H. Li, Q. Zhou, and Y. P. Chen, “Observation of quantum interference and coherent control in a photochemical reaction,” *Phys. Rev. Lett.*, vol. 121, p. 073202, Aug 2018.

- [71] P. Wang, Z.-Q. Yu, Z. Fu, J. Miao, L. Huang, S. Chai, H. Zhai, and J. Zhang, “Spin-orbit coupled degenerate Fermi gases,” *Phys. Rev. Lett.*, vol. 109, p. 095301, Aug 2012.
- [72] L. W. Cheuk, A. T. Sommer, Z. Hadzibabic, T. Yefsah, W. S. Bakr, and M. W. Zwierlein, “Spin-injection spectroscopy of a spin-orbit coupled Fermi gas,” *Phys. Rev. Lett.*, vol. 109, p. 095302, Aug 2012.
- [73] L. Huang, Z. Meng, P. Wang, P. Peng, S.-L. Zhang, L. Chen, D. Li, Q. Zhou, and J. Zhang, “Experimental realization of two-dimensional synthetic spin-orbit coupling in ultracold Fermi gases,” *Nature Physics*, vol. 12, pp. 540–544, Feb 2016.
- [74] S. Kolkowitz, S. L. Bromley, T. Bothwell, M. L. Wall, G. E. Marti, A. P. Koller, X. Zhang, A. M. Rey, and J. Ye, “Spin-orbit-coupled fermions in an optical lattice clock,” *Nature*, vol. 542, pp. 66–70, Dec 2016.
- [75] C.-J. Wu, I. Mondragon-Shem, and X.-F. Zhou, “Unconventional Bose-Einstein condensations from spin-orbit coupling,” *Chinese Physics Letters*, vol. 28, no. 9, p. 097102, 2011.
- [76] H. Hu, B. Ramachandhran, H. Pu, and X.-J. Liu, “Spin-orbit coupled weakly interacting Bose-Einstein condensates in harmonic traps,” *Phys. Rev. Lett.*, vol. 108, p. 010402, Jan 2012.
- [77] Q. Zhu, C. Zhang, and B. Wu, “Exotic superfluidity in spin-orbit coupled Bose-Einstein condensates,” *EPL (Europhysics Letters)*, vol. 100, no. 5, p. 50003, 2012.
- [78] Y.-C. Zhang, Z.-Q. Yu, T. K. Ng, S. Zhang, L. Pitaevskii, and S. Stringari, “Superfluid density of a spin-orbit-coupled Bose gas,” *Phys. Rev. A*, vol. 94, p. 033635, Sep 2016.
- [79] S. Stringari, “Diffused vorticity and moment of inertia of a spin-orbit coupled Bose-Einstein condensate,” *Phys. Rev. Lett.*, vol. 118, p. 145302, Apr 2017.
- [80] L. Vichi and S. Stringari, “Collective oscillations of an interacting trapped Fermi gas,” *Phys. Rev. A*, vol. 60, pp. 4734–4737, Dec 1999.
- [81] T. Kinoshita, T. Wenger, and D. S. Weiss, “A quantum Newton’s cradle,” *Nature*, vol. 440, pp. 900–903, Apr 2006.
- [82] C. Hamner, J. J. Chang, P. Engels, and M. A. Hoefer, “Generation of dark-bright soliton trains in superfluid-superfluid counterflow,” *Phys. Rev. Lett.*, vol. 106, p. 065302, Feb 2011.
- [83] A. Sommer, M. Ku, G. Roati, and M. W. Zwierlein, “Universal spin transport in a strongly interacting Fermi gas,” *Nature*, vol. 472, no. 7342, pp. 201–204, 2011.
- [84] J. H. V. Nguyen, P. Dyke, D. Luo, B. A. Malomed, and R. G. Hulet, “Collisions of matter-wave solitons,” *Nature Physics*, vol. 10, pp. 918–922, Nov 2014.
- [85] E. Fava, T. Bienaimé, C. Mordini, G. Colzi, C. Qu, S. Stringari, G. Lamporesi, and G. Ferrari, “Observation of spin superfluidity in a Bose gas mixture,” *Phys. Rev. Lett.*, vol. 120, p. 170401, Apr 2018.

- [86] I. D'Amico and G. Vignale, "Theory of spin coulomb drag in spin-polarized transport," *Phys. Rev. B*, vol. 62, pp. 4853–4857, Aug 2000.
- [87] C. P. Weber, N. Gedik, J. E. Moore, J. Orenstein, J. Stephens, and D. D. Awschalom, "Observation of spin coulomb drag in a two-dimensional electron gas," *Nature*, vol. 437, pp. 1330–1333, Oct 2005.
- [88] R. A. Duine and H. T. C. Stoof, "Spin drag in noncondensed Bose gases," *Phys. Rev. Lett.*, vol. 103, p. 170401, Oct 2009.
- [89] S. B. Koller, A. Groot, P. C. Bons, R. A. Duine, H. T. C. Stoof, and P. van der Straten, "Quantum enhancement of spin drag in a Bose gas," *New Journal of Physics*, vol. 17, no. 11, p. 113026, 2015.
- [90] R. A. Duine, M. Polini, H. T. C. Stoof, and G. Vignale, "Spin drag in an ultracold Fermi gas on the verge of ferromagnetic instability," *Phys. Rev. Lett.*, vol. 104, p. 220403, Jun 2010.
- [91] G. M. Bruun, A. Recati, C. J. Pethick, H. Smith, and S. Stringari, "Collisional properties of a polarized Fermi gas with resonant interactions," *Phys. Rev. Lett.*, vol. 100, p. 240406, Jun 2008.
- [92] S. D. Gensemer and D. S. Jin, "Transition from collisionless to hydrodynamic behavior in an ultracold Fermi gas," *Phys. Rev. Lett.*, vol. 87, p. 173201, Oct 2001.
- [93] M. Koschorreck, D. Pertot, E. Vogt, and M. Köhl, "Universal spin dynamics in two-dimensional Fermi gases," *Nature Physics*, vol. 9, pp. 405–409, May 2013.
- [94] B. DeMarco and D. S. Jin, "Spin excitations in a Fermi gas of atoms," *Phys. Rev. Lett.*, vol. 88, p. 040405, Jan 2002.
- [95] L. J. LeBlanc and J. H. Thywissen, "Species-specific optical lattices," *Phys. Rev. A*, vol. 75, p. 053612, May 2007.
- [96] Y. Castin and R. Dum, "Bose-Einstein condensates in time dependent traps," *Phys. Rev. Lett.*, vol. 77, pp. 5315–5319, Dec 1996.
- [97] S. Stringari, "Collective excitations of a trapped Bose-condensed gas," *Phys. Rev. Lett.*, vol. 77, pp. 2360–2363, Sep 1996.
- [98] M.-O. Mewes, M. R. Andrews, N. J. van Druten, D. M. Kurn, D. S. Durfee, C. G. Townsend, and W. Ketterle, "Collective excitations of a Bose-Einstein condensate in a magnetic trap," *Phys. Rev. Lett.*, vol. 77, pp. 988–991, Aug 1996.
- [99] D. S. Jin, M. R. Matthews, J. R. Ensher, C. E. Wieman, and E. A. Cornell, "Temperature-dependent damping and frequency shifts in collective excitations of a dilute Bose-Einstein condensate," *Phys. Rev. Lett.*, vol. 78, pp. 764–767, Feb 1997.
- [100] P. Maddaloni, M. Modugno, C. Fort, F. Minardi, and M. Inguscio, "Collective oscillations of two colliding Bose-Einstein condensates," *Phys. Rev. Lett.*, vol. 85, pp. 2413–2417, Sep 2000.

- [101] M. R. Matthews, D. S. Hall, D. S. Jin, J. R. Ensher, C. E. Wieman, E. A. Cornell, F. Dalfovo, C. Minniti, and S. Stringari, “Dynamical response of a Bose-Einstein condensate to a discontinuous change in internal state,” *Phys. Rev. Lett.*, vol. 81, pp. 243–247, Jul 1998.
- [102] D. S. Jin, J. R. Ensher, M. R. Matthews, C. E. Wieman, and E. A. Cornell, “Collective excitations of a Bose-Einstein condensate in a dilute gas,” *Phys. Rev. Lett.*, vol. 77, pp. 420–423, Jul 1996.
- [103] C. Wang, C. Gao, C.-M. Jian, and H. Zhai, “Spin-orbit coupled spinor Bose-Einstein condensates,” *Phys. Rev. Lett.*, vol. 105, p. 160403, Oct 2010.
- [104] T.-L. Ho and S. Zhang, “Bose-Einstein condensates with spin-orbit interaction,” *Phys. Rev. Lett.*, vol. 107, p. 150403, Oct 2011.
- [105] Y. Li, L. P. Pitaevskii, and S. Stringari, “Quantum tricriticality and phase transitions in spin-orbit coupled Bose-Einstein condensates,” *Phys. Rev. Lett.*, vol. 108, p. 225301, May 2012.
- [106] J.-R. Li, J. Lee, W. Huang, S. Burchesky, B. Shteynas, F. Ç. Top, A. O. Jamison, and W. Ketterle, “A stripe phase with supersolid properties in spin-orbit-coupled Bose-Einstein condensates,” *Nature*, vol. 543, pp. 91–94, Mar 2017.
- [107] W. Bao, D. Jaksch, and P. A. Markowich, “Numerical solution of the Gross-Pitaevskii equation for Bose-Einstein condensation,” *Journal of Computational Physics*, vol. 187, no. 1, pp. 318–342, 2003.
- [108] W. Ketterle, D. S. Durfee, and D. M. Stamper-Kurn, “Making, probing and understanding Bose-Einstein condensates,” *Preprint at <https://arxiv.org/abs/cond-mat/9904034>*, 1999.
- [109] L. Feng, L. W. Clark, A. Gaj, and C. Chin, “Coherent inflationary dynamics for Bose-Einstein condensates crossing a quantum critical point,” *Nature Physics*, vol. 14, no. 3, pp. 269–272, 2018.
- [110] A. Polkovnikov, K. Sengupta, A. Silva, and M. Vengalattore, “Colloquium: Nonequilibrium dynamics of closed interacting quantum systems,” *Rev. Mod. Phys.*, vol. 83, pp. 863–883, Aug 2011.
- [111] S. Wu, Y. Ke, J. Huang, and C. Lee, “Kibble-Zurek scalings of continuous magnetic phase transitions in spin-1 spin-orbit-coupled Bose-Einstein condensates,” *Phys. Rev. A*, vol. 95, p. 063606, Jun 2017.
- [112] R. J. Niffenegger, “Experiments with synthetic spin-orbit coupling and spin transport in Bose Einstein condensates.,” *Ph.D. thesis*, 2015.
- [113] C.-H. Li, Y. Yan, S. Choudhury, D. B. Blasing, Q. Zhou, and Y. P. Chen, “A Bose-Einstein condensate on a synthetic Hall cylinder,” *Preprint at <https://arxiv.org/abs/1809.02122>*, 2018.
- [114] S. M. Carroll, *Spacetime and geometry: An introduction to general relativity*. Addison-Wesley, 2004.
- [115] N. Schine, A. Ryou, A. Gromov, A. Sommer, and J. Simon, “Synthetic Landau levels for photons,” *Nature*, vol. 534, pp. 671–675, Jun 2016.

- [116] A. J. Kollár, M. Fitzpatrick, and A. A. Houck, “Hyperbolic lattices in circuit quantum electrodynamics,” *Nature*, vol. 571, no. 7763, pp. 45–50, 2019.
- [117] H. Kleinert, *Gauge Fields in Condensed Matter*. World Scientific, 1989.
- [118] T.-L. Ho and B. Huang, “Spinor condensates on a cylindrical surface in synthetic gauge fields,” *Phys. Rev. Lett.*, vol. 115, p. 155304, Oct 2015.
- [119] N.-E. Guenther, P. Massignan, and A. L. Fetter, “Quantized superfluid vortex dynamics on cylindrical surfaces and planar annuli,” *Phys. Rev. A*, vol. 96, p. 063608, Dec 2017.
- [120] X. G. Wen and Q. Niu, “Ground-state degeneracy of the fractional quantum Hall states in the presence of a random potential and on high-genus Riemann surfaces,” *Phys. Rev. B*, vol. 41, pp. 9377–9396, May 1990.
- [121] S.-L. Zhang and Q. Zhou, “Manipulating novel quantum phenomena using synthetic gauge fields,” *Journal of Physics B: Atomic, Molecular and Optical Physics*, vol. 50, no. 22, p. 222001, 2017.
- [122] M. W. Ray, E. Ruokokoski, S. Kandel, M. Möttönen, and D. S. Hall, “Observation of Dirac monopoles in a synthetic magnetic field,” *Nature*, vol. 505, pp. 657–660, Jan 2014.
- [123] L. F. Livi, G. Cappellini, M. Diem, L. Franchi, C. Clivati, M. Frittelli, F. Levi, D. Calonico, J. Catani, M. Inguscio, and L. Fallani, “Synthetic dimensions and spin-orbit coupling with an optical clock transition,” *Phys. Rev. Lett.*, vol. 117, p. 220401, Nov 2016.
- [124] M. E. Tai, A. Lukin, M. Rispoli, R. Schittko, T. Menke, D. Borgnia, P. M. Preiss, F. Grusdt, A. M. Kaufman, and M. Greiner, “Microscopy of the interacting Harper-Hofstadter model in the two-body limit,” *Nature*, vol. 546, pp. 519–523, Jun 2017.
- [125] D. L. Campbell, G. Juzeliūnas, and I. B. Spielman, “Realistic Rashba and Dresselhaus spin-orbit coupling for neutral atoms,” *Phys. Rev. A*, vol. 84, p. 025602, Aug 2011.
- [126] H. Miyake, G. A. Siviloglou, C. J. Kennedy, W. C. Burton, and W. Ketterle, “Realizing the Harper Hamiltonian with laser-assisted tunneling in optical lattices,” *Phys. Rev. Lett.*, vol. 111, p. 185302, Oct 2013.
- [127] M. Aidelsburger, M. Atala, M. Lohse, J. T. Barreiro, B. Paredes, and I. Bloch, “Realization of the Hofstadter Hamiltonian with ultracold atoms in optical lattices,” *Phys. Rev. Lett.*, vol. 111, p. 185301, Oct 2013.
- [128] A. A. Burkov, “Topological semimetals,” *Nature Materials*, vol. 15, pp. 1145–1148, Oct 2016.
- [129] K. Shiozaki, M. Sato, and K. Gomi, “ $Z_2$  topology in nonsymmorphic crystalline insulators: Möbius twist in surface states,” *Phys. Rev. B*, vol. 91, p. 155120, Apr 2015.
- [130] J. H. Han, J. H. Kang, and Y. Shin, “Band gap closing in a synthetic Hall tube of neutral fermions,” *Phys. Rev. Lett.*, vol. 122, p. 065303, Feb 2019.

- [131] M. Ben Dahan, E. Peik, J. Reichel, Y. Castin, and C. Salomon, “Bloch oscillations of atoms in an optical potential,” *Phys. Rev. Lett.*, vol. 76, pp. 4508–4511, Jun 1996.
- [132] R. B. Laughlin, “Quantized Hall conductivity in two dimensions,” *Phys. Rev. B*, vol. 23, pp. 5632–5633, May 1981.
- [133] Y. Yan, S.-l. Zhang, S. Choudhury, and Q. Zhou, “Emergent periodic and quasiperiodic lattices on surfaces of synthetic Hall tori and synthetic Hall cylinders,” *Preprint at <https://arxiv.org/abs/1810.12331>*, 2018.
- [134] S. Barbarino, L. Taddia, D. Rossini, L. Mazza, and R. Fazio, “Magnetic crystals and helical liquids in alkaline-earth fermionic gases,” *Nature Communications*, vol. 6, p. 8134, Sep 2015. Article.
- [135] M. Lacki, H. Pichler, A. Sterdyniak, A. Lyras, V. E. Lembessis, O. Al-Dossary, J. C. Budich, and P. Zoller, “Quantum Hall physics with cold atoms in cylindrical optical lattices,” *Phys. Rev. A*, vol. 93, p. 013604, Jan 2016.
- [136] L. Taddia, E. Cornfeld, D. Rossini, L. Mazza, E. Sela, and R. Fazio, “Topological fractional pumping with alkaline-earth-like atoms in synthetic lattices,” *Phys. Rev. Lett.*, vol. 118, p. 230402, Jun 2017.
- [137] Y.-C. Zhang, Z.-Q. Yu, T. K. Ng, S. Zhang, L. Pitaevskii, and S. Stringari, “Superfluid density of a spin-orbit-coupled Bose gas,” *Phys. Rev. A*, vol. 94, p. 033635, Sep 2016.
- [138] X.-L. Chen, J. Wang, Y. Li, X.-J. Liu, and H. Hu, “Quantum depletion and superfluid density of a supersolid in Raman spin-orbit-coupled Bose gases,” *Phys. Rev. A*, vol. 98, p. 013614, Jul 2018.
- [139] C. Qu and S. Stringari, “Angular momentum of a Bose-Einstein condensate in a synthetic rotational field,” *Phys. Rev. Lett.*, vol. 120, p. 183202, May 2018.
- [140] M. R. Matthews, B. P. Anderson, P. C. Haljan, D. S. Hall, C. E. Wieman, and E. A. Cornell, “Vortices in a Bose-Einstein condensate,” *Phys. Rev. Lett.*, vol. 83, pp. 2498–2501, Sep 1999.
- [141] K. W. Madison, F. Chevy, W. Wohlleben, and J. Dalibard, “Vortex formation in a stirred Bose-Einstein condensate,” *Phys. Rev. Lett.*, vol. 84, pp. 806–809, Jan 2000.
- [142] J. R. Abo-Shaer, C. Raman, J. M. Vogels, and W. Ketterle, “Observation of vortex lattices in Bose-Einstein condensates,” *Science*, vol. 292, no. 5516, pp. 476–479, 2001.
- [143] S. Stringari, “Moment of inertia and superfluidity of a trapped Bose gas,” *Phys. Rev. Lett.*, vol. 76, pp. 1405–1408, Feb 1996.
- [144] O. M. Marag, G. Hechenblaikner, E. Hodby, S. A. Hopkins, and C. J. Foot, “The moment of inertia and the scissors mode of a Bose-condensed gas,” *Journal of Physics: Condensed Matter*, vol. 14, no. 3, p. 343, 2002.
- [145] S.-C. Ji, L. Zhang, X.-T. Xu, Z. Wu, Y. Deng, S. Chen, and J.-W. Pan, “Softening of roton and phonon modes in a Bose-Einstein condensate with spin-orbit coupling,” *Phys. Rev. Lett.*, vol. 114, p. 105301, Mar 2015.

- [146] M. A. Khamehchi, Y. Zhang, C. Hamner, T. Busch, and P. Engels, “Measurement of collective excitations in a spin-orbit-coupled Bose-Einstein condensate,” *Phys. Rev. A*, vol. 90, p. 063624, Dec 2014.
- [147] J. F. Annett, *Superconductivity, Superfluids, and Condensates*. Oxford University Press, 2004.
- [148] M. Bartenstein, A. Altmeyer, S. Riedl, S. Jochim, C. Chin, J. H. Denschlag, and R. Grimm, “Collective excitations of a degenerate gas at the BEC-BCS crossover,” *Phys. Rev. Lett.*, vol. 92, p. 203201, May 2004.
- [149] J.-Y. Zhang, S.-C. Ji, Z. Chen, L. Zhang, Z.-D. Du, B. Yan, G.-S. Pan, B. Zhao, Y.-J. Deng, H. Zhai, S. Chen, and J.-W. Pan, “Collective dipole oscillations of a spin-orbit coupled Bose-Einstein condensate,” *Phys. Rev. Lett.*, vol. 109, p. 115301, Sep 2012.
- [150] E. van der Bijl and R. A. Duine, “Anomalous Hall conductivity from the dipole mode of spin-orbit-coupled cold-atom systems,” *Phys. Rev. Lett.*, vol. 107, p. 195302, Nov 2011.
- [151] A. Sommer, M. Ku, G. Roati, and M. W. Zwierlein, “Universal spin transport in a strongly interacting Fermi gas,” *Nature*, vol. 472, no. 7342, pp. 201–204, 2011.
- [152] L. J. LeBlanc, K. Jimnez-Garca, R. A. Williams, M. C. Beeler, A. R. Perry, W. D. Phillips, and I. B. Spielman, “Observation of a superfluid Hall effect,” *Proceedings of the National Academy of Sciences*, vol. 109, no. 27, pp. 10811–10814, 2012.
- [153] O. Maragò, G. Hechenblaikner, E. Hodby, and C. Foot, “Temperature dependence of damping and frequency shifts of the scissors mode of a trapped Bose-Einstein condensate,” *Phys. Rev. Lett.*, vol. 86, pp. 3938–3941, Apr 2001.
- [154] N. L. Iudice and F. Palumbo, “New isovector collective modes in deformed nuclei,” *Phys. Rev. Lett.*, vol. 41, pp. 1532–1534, Nov 1978.
- [155] D. Guéry-Odelin and S. Stringari, “Scissors mode and superfluidity of a trapped Bose-Einstein condensed gas,” *Phys. Rev. Lett.*, vol. 83, pp. 4452–4455, Nov 1999.
- [156] O. M. Maragò, S. A. Hopkins, J. Arlt, E. Hodby, G. Hechenblaikner, and C. J. Foot, “Observation of the scissors mode and evidence for superfluidity of a trapped Bose-Einstein condensed gas,” *Phys. Rev. Lett.*, vol. 84, pp. 2056–2059, Mar 2000.
- [157] M. Modugno, G. Modugno, G. Roati, C. Fort, and M. Inguscio, “Scissors mode of an expanding Bose-Einstein condensate,” *Phys. Rev. A*, vol. 67, p. 023608, Feb 2003.
- [158] M. Cozzini, S. Stringari, V. Bretin, P. Rosenbusch, and J. Dalibard, “Scissors mode of a rotating Bose-Einstein condensate,” *Phys. Rev. A*, vol. 67, p. 021602, Feb 2003.
- [159] I. Ferrier-Barbut, M. Wenzel, F. Böttcher, T. Langen, M. Isoard, S. Stringari, and T. Pfau, “Scissors mode of dipolar quantum droplets of dysprosium atoms,” *Phys. Rev. Lett.*, vol. 120, p. 160402, Apr 2018.

- [160] N. Q. Burdick, Y. Tang, and B. L. Lev, “Long-lived spin-orbit-coupled degenerate dipolar Fermi gas,” *Phys. Rev. X*, vol. 6, p. 031022, Aug 2016.
- [161] L. J. LeBlanc, K. Jimnez-Garca, R. A. Williams, M. C. Beeler, W. D. Phillips, and I. B. Spielman, “Gauge matters: observing the vortex-nucleation transition in a Bose condensate,” *New Journal of Physics*, vol. 17, no. 6, p. 065016, 2015.

## VITA

**Chuan-Hsun Li**

Email: li841@purdue.edu; chuanhsun@gmail.com

**EDUCATION**

**Ph.D., Purdue University**, West Lafayette, IN, USA. Aug. 2011 - Aug. 2019

*Major:* School of Electrical and Computer Engineering

*Ph.D. Thesis:* Bose-Einstein Condensates in Synthetic Gauge Fields and Spaces: Quantum Transport, Dynamics, and Topological States

*Adviser:* Prof. Yong P. Chen

**M.S., National Tsing Hua University**, Hsinchu, Taiwan. Sept. 2007 - July 2009

*Major:* Institute of Photonics Technologies/Department of Electrical Engineering

*M.S. Thesis:* Pulsed Sodium-yellow Intracavity Raman Laser

*Adviser:* Prof. Yen-Chieh Huang

**B.S., National Tsing Hua University**, Hsinchu, Taiwan. Sept. 2003 - June 2007

*Major:* Electrical Engineering

**RESEARCH INTERESTS**

Experimental atomic, molecular, and optical physics: cold atoms/quantum gases (Bose-Einstein condensates, light-matter interaction, quantum simulation), and quantum photonics

**HONORS AND AWARDS**

2019, First Place in Poster Session Award, International Symposium of Quantum Science and Technology at Purdue University, USA

2017, Conference Travel Award, College of Engineering, Purdue University, USA

2017, Conference Travel Award, Department of Physics, Purdue University, USA  
 2009, Masters Thesis of the Year, Taiwan Photonics Society  
 2009, Honorary member of The Phi Tau Phi Scholastic of The Republic of China  
 2007, Outstanding Graduate Student Award, Institute of Photonics Technologies Department of Electrical Engineering, National Tsing Hua University, Taiwan  
 2004, Academic Achievement Award, National Tsing Hua University, Taiwan

## PUBLICATIONS

[J7] **Chuan-Hsun Li** *et. al.* , “Scissors mode and rotational properties of a spin-orbit-coupled Bose-Einstein condensate”, in preparation.

[J6] **Chuan-Hsun Li**, Yangqian Yan, Sayan Choudhury, David B. Blasing, Qi Zhou, and Yong P. Chen, “A Bose-Einstein Condensate on a Synthetic Hall Cylinder”, submitted. Preprint at arXiv:1809.02122.

[J5] **Chuan-Hsun Li**, Chunlei Qu, Robert J. Niffenegger, Su-Ju Wang, Mingyuan He, David B. Blasing, Abraham J. Olson, Chris H. Greene, Yuli Lyanda-Geller, Qi Zhou, Chuanwei Zhang, Yong P. Chen, “Spin Current Generation and Relaxation in a Quenched Spin-Orbit Coupled Bose-Einstein Condensate”, **Nature Communications** 10, 375 (2019).

Related news story: [“New quantum system could help design better spintronics”](#) by *Purdue News*.

[J4] David B. Blasing, Jess Prez-Ros, Yangqian Yan, Sourav Dutta, **Chuan-Hsun Li**, Qi Zhou, Yong P. Chen, “Observation of Quantum Interference and Coherent Control in a Photo-Chemical Reaction”, **Physical Review Letters** 121, 073202 (2018).

[J3] Abraham J. Olson\*, David B. Blasing\*, Chunlei Qu, **Chuan-Hsun Li**, Robert J. Niffenegger, Chuanwei Zhang, and Yong P. Chen, “Stueckelberg interferometry using periodically driven spin-orbit-coupled Bose-Einstein condensates” (\*equal contribution), **Physical Review A** 95, 043623 (2017).

[J2] A. J. Olson, S. J. Wang, R. J. Niffenegger, **C. H. Li**, C. H. Greene, Y. P. Chen,

“Tunable Landau-Zener transitions in a spin-orbit coupled Bose-Einstein condensate”, **Physical Review A** 90, 013616 (2014).

[J1] **Chuan-Hsun Li** and Yen-Chieh Huang, “Pulsed Sodium-yellow Intracavity Raman Laser”, issue 109, quarterly published by Taiwan Photonics Society, March, 2010.

## PRESENTATIONS

[P22] **Chuan-Hsun Li**, Yangqian Yan, Sayan Choudhury, David Blasing, Qi Zhou, Yong P. Chen, “A Bose-Einstein Condensate on a Synthetic Hall Cylinder”. Talk at 2019 American Physical Society DAMOP Meeting in Milwaukee, Wisconsin, USA.

[P21] **Chuan-Hsun Li**, Yangqian Yan, Sayan Choudhury, David Blasing, Qi Zhou, Yong P. Chen, “Transport and Dynamics of a Bose-Einstein Condensate (BEC) on a Synthetic Hall Cylinder”. Poster at 2019 American Physical Society DAMOP Meeting in Milwaukee, Wisconsin, USA.

[P20] H. Esat Kondakci, David Blasing, **Chuan-Hsun Li**, Yong P. Chen, “Coherent control of a photo-chemical reaction with ultracold atoms in quantum superposition”. Talk at 2019 American Physical Society DAMOP Meeting in Milwaukee, Wisconsin, USA.

[P19] **Chuan-Hsun Li**, Yangqian Yan, Sayan Choudhury, David Blasing, Qi Zhou, Yong P. Chen, “A Bose-Einstein Condensate on a Synthetic Hall Cylinder”. Talk (presented by Yangqian Yan) at 2019 American Physical Society March Meeting in Boston, Massachusetts, USA.

[P18] **Chuan-Hsun Li**, Yangqian Yan, Sayan Choudhury, David Blasing, Qi Zhou, Yong P. Chen, “A Bose-Einstein Condensate on a Synthetic Hall Cylinder”. Talk at 2018 Midwest Cold Atom Workshop in Champaign, Illinois, USA.

[P17] **Chuan-Hsun Li**, Chunlei Qu, David Blasing, Yong P. Chen, “Scissors mode and rotational properties of a spin-orbit coupled Bose-Einstein condensate”. Talk at 2018 American Physical Society DAMOP Meeting in Lauderdale, Florida, USA.

[P16] David Blasing, Jesus Perez-Rios, Yangqian Yan , **Chuan-Hsun Li**, Sourav Dutta, Qi Zhou , Yong P. Chen, “Effects of quantum superposition and interference in spin-dependent photoassociation of  $^{87}\text{Rb}$  Bose-Einstein condensates”. Talk at 2018 American Physical Society DAMOP Meeting in Lauderdale, Florida, USA.

[P15] **Chuan-Hsun Li**, David Blasing, Yong P. Chen, “Spin Excitations and dynamics in a Spin-orbit Coupled BEC”. Poster at 2017 Midwest Cold Atom Workshop in Ann Arbor, Michigan, USA.

[P14] **Chuan-Hsun Li**, David Blasing, Yong P. Chen, “Damping of spin-dipole mode and generation of quadrupole mode excitations in a spin-orbit coupled Bose-Einstein condensate”. Talk at 2017 American Physical Society DAMOP Meeting in Sacramento, California, USA.

[P13] **Chuan-Hsun Li**, Robert Niffenegger, David Blasing, Abraham Olson, Yong P. Chen, “Experimental studies of collective excitations of a BEC in light-induced gauge fields”. Poster at 2016 Midwest Cold Atom Workshop in Chicago, Illinois, USA.

[P12] **Chuan-Hsun Li**, Robert Niffenegger, David Blasing, Abraham Olson, Yong P. Chen, “Experimental studies of collective excitations of a BEC in light-induced gauge fields”. Poster at 2015 Midwest Cold Atom Workshop in Madison, Wisconsin, USA.

[P11] **Chuan-Hsun Li**, Robert Niffenegger, David Blasing, Abraham Olson, Yong P. Chen, “Experimental studies of collective excitations of a BEC in light-induced gauge fields”. Poster at 2015 Purdue Quantum Center Kickoff International Workshop in West Lafayette, Indiana, USA.

[P10] **Chuan-Hsun Li**, Robert Niffenegger, David Blasing, Abraham Olson, Yong P. Chen, “Experimental studies of collective excitations of a BEC in light-induced gauge fields”. Talk at 2015 American Physical Society DAMOP Meeting in Columbus, OH, USA.

[P9] **Chuan-Hsun Li**, Robert Niffenegger, David Blasing, Abraham Olson, Yong P. Chen, “Experimental studies of scissors mode and dipole oscillation in a BEC in light-induced gauge fields”. Poster at 2014 Midwest Cold Atom Workshop at Argonne

National Lab, Argonne, IL, USA.

[P8] **Chuan-Hsun Li**, David Blasing, Abraham Olson, Robert Niffenegger, Yong P. Chen, “Experimental studies of excitations in a BEC in light-induced gauge fields”. Poster at 2014 American Physical Society DAMOP Meeting in Madison, Wisconsin, USA.

[P7] Robert Niffenegger, Abraham Olson, **Chuan-Hsun Li**, Yong P. Chen, “Spin Transport in Spin Orbit Coupled Bose Einstein Condensates”. Talk at 2014 American Physical Society March Meeting, Denver, Colorado, USA.

[P6] Robert Niffenegger, **Chuan-Hsun Li**, Abraham Olson, Yong P. Chen, “Transport in BECs with Spin Orbit Coupling and Synthetic Gauge Fields”. Poster at 2013 Midwest Cold Atom Workshop in West Lafayette, IN, USA.

[P5] Yong P. Chen, Robert Niffenegger, Abraham Olson, **Chuan-Hsun Li**, David Blasing, “Experimental studies of transport and dynamics of BEC in synthetic gauge fields and spin-orbit coupling”. Poster at 2013 American Physical Society DAMOP Meeting in Quebec City, Canada.

[P4] A.J. Olson, S.J. Wang, **C.H. Li**, R.J. Niffenegger, C.H. Greene, Y.P. Chen, “Observation of Landau-Zener transitions in spin-orbit coupled Bose-Einstein condensates”. Talk at 2013 American Physical Society DAMOP Meeting in Quebec City, Canada.

[P3] A.J. Olson, Robert Niffenegger, Sourav Dutta, **Chuan-Hsun Li**, Y.P. Chen “BEC with gauge fields, spin-orbit coupling, and photo-association”. Talk at 2012 Midwest Cold Atom Workshop, U of Illinois at Urbana-Champaign, USA.

[P2] **Chuan-Hsun Li** and Yen-Chieh Huang, “Pulsed Intracavity Frequency-Doubled  $\text{CaWO}_4$  Raman Laser for Narrow-Line Sodium-Yellow Radiation”, JTuD112, CLEO/QELS (The Conference on Lasers and Electro-Optics / Quantum Electronics and Laser Science Conference), May 16-21, 2010, San Jose, California, USA.

[P1] **Chuan-Hsun Li** and Yen-Chieh Huang, “Diode-pumped, Pulsed  $\text{Nd:YVO}_4/\text{CaWO}_4/\text{LBO}$  Intracavity Frequency-doubled Raman Laser for Narrow-line Sodium-Yellow Radia-

tion,” OPT (Optics and Photonics Taiwan), oral presentation CO123, December 11-12, 2009, Taipei, Taiwan, R.O.C.

## **ACADEMIC EXPERIENCE**

**Graduate Mentors**, 2015 - Aug. 2019

Mentoring several graduate and undergraduate students and summer interns, Purdue University

**Graduate Research Assistant**, Jan. 2012 - Aug. 2019

School of Electrical and Computer Engineering, Purdue University

**Graduate Research Assistant**, Sept. 2009 - July 2010

Department of Physics, National Tsing Hua University

**Graduate Research Assistant**, Sept. 2007 - July 2009

Institute of Photonics Technologies/Department of Electrical Engineering, National Tsing Hua University

**Teaching Assistant**, Electrodynamics II, graduate course, 2010

Department of Physics, National Tsing Hua University

**Teaching Assistant**, Electrodynamics I, graduate course, 2009

Department of Physics, National Tsing Hua University

**Teaching Assistant**, Nonlinear Optics, graduate course, 2008

Institute of Photonics Technologies, National Tsing Hua University

**Teaching Assistant**, Optoelectronic Engineering, undergraduate course, 2007

Department of Electrical Engineering, National Tsing Hua University